



# Electrodéposition de couches minces métalliques à partir de solutions de liquides ioniques pour des applications électroniques.

Tomin Liu

## ► To cite this version:

Tomin Liu. Electrodéposition de couches minces métalliques à partir de solutions de liquides ioniques pour des applications électroniques.. Physique Atomique [physics.atom-ph]. Université de Bordeaux; Universidade nova de Lisboa. Faculdade de ciências e tecnologia (Lisboa, Portugal), 2014. Français. NNT : 2014BORD0170 . tel-01142699

**HAL Id: tel-01142699**

**<https://theses.hal.science/tel-01142699>**

Submitted on 15 Apr 2015

**HAL** is a multi-disciplinary open access archive for the deposit and dissemination of scientific research documents, whether they are published or not. The documents may come from teaching and research institutions in France or abroad, or from public or private research centers.

L'archive ouverte pluridisciplinaire **HAL**, est destinée au dépôt et à la diffusion de documents scientifiques de niveau recherche, publiés ou non, émanant des établissements d'enseignement et de recherche français ou étrangers, des laboratoires publics ou privés.

THÈSE EN COTUTELLE PRÉSENTÉE  
POUR OBTENIR LE GRADE DE  
**DOCTEUR DE**  
**L'UNIVERSITÉ DE BORDEAUX**  
**ET DE L'UNIVERSITÉ DE LISBONNE**

INSTITUT DES SCIENCES MOLÉCULAIRES  
INSTITUTO DE CIÊNCIA E ENGENHARIA DE MATERIAIS E SUPERFÍCIES  
SPÉCIALITÉ : PHYSICO-CHIMIE DE LA MATIÈRE CONDENSÉE

**LIU, TOMIN**  
**ELECTRODEPOSITION OF METALLIC THIN FILMS**  
**FROM IONIC LIQUID SOLUTIONS**  
**FOR**  
**ELECTRONIC APPLICATIONS**

Directeur de thèse : M. Rui Mario CORREIA DA SILVA VILAR  
M. Joseph GRONDIN

Soutenue le : VENDREDI 18 Juillet 2014

Membres du jury :

**M. R. M. A. ALMEIDA**, *Professeur, Université de Lisbonne*  
**M. F. J. M. MONTEIRO**, *Professeur, FEUP, Université de Porto*  
**Mme. C. M. R. ARCHILA**, *Chercheur principal, LNEG Lisbonne*  
**M. J. M. P. CORREIA**, *Chercheur principal, Université de Lisbonne*  
**M. Y. DANTEN**, *Chargé de Recherche 1 CNRS, Université de Bordeaux*  
**M. R. M. C. VILAR**, *Professeur, University de Lisbonne*  
**M. J. GRONDIN**, *Professeur, Université de Bordeaux*

**Président**  
**Rapporteur**  
**Rapporteur**  
**Examineur**  
**Examineur**  
**Directeur**  
**Directeur**



**Titre:** Electrodeposition de couches minces métalliques à partir de solutions de liquides ioniques pour des applications électroniques.

## **Résumé**

Les mécanismes d'électrodeposition réalisés à partir d'électrolytes à base de liquides ioniques ne sont pas très bien compris en raison de l'organisation structurale complexe de ces électrolytes. Dans cette thèse, nous étudions les relations qui existent entre la morphologie des films, les propriétés électrochimiques ainsi que la structure de l'électrolyte liquide ionique. Plusieurs solutions ont été étudiées: CuCl, CuCl<sub>2</sub> et CuSO<sub>4</sub> dans 1-éthyl-3-méthylimidazolium éthyl-sulfate [EMIM] [EtSO<sub>4</sub>]; AgTFSI, CuTFSI<sub>2</sub> et AlTFSI<sub>3</sub> en 1-éthyl-3-méthylimidazolium bis(trifluorométhylsulfonyl)imide [EMIM] [TFSI]. Des mesures de cyclovoltammétrie montrent que les réductions de l'argent et du cuivre sont quasi-réversibles et se produisent par une réaction de transfert mono-électronique {(Ag (I) → Ag (0), (Cu (II) → Cu (I)) et (Cu (I) → Cu (0))}. La réduction de l'aluminium est irréversible. Les coefficients de diffusion augmentent avec la température de l'électrolyte et sont également influencés par l'état d'oxydation du métal et des anions en solution. Des films minces métalliques ont été obtenus pour toutes les solutions, sauf pour AlTFSI<sub>3</sub>. L'analyse par XRD et EDX montrent que les films sont cristallins et sont principalement constitués de cuivre ou d'argent pur. Leur morphologie est contrôlée par la température, du temps et du potentiel d'électrodeposition. D'une manière générale, l'élévation du temps de dépôt et de la température augmente la couverture du film et de la taille des particules, tandis que l'augmentation du potentiel de dépôt diminue la taille des particules. La structure des électrolytes a été étudiée par Raman et IR spectroscopies et interprétée à l'aide de méthodes théoriques de chimie quantique. Pour AgTFSI-[EMIM][TFSI], le cation d'argent est solvato par trois anions TFSI<sup>-</sup>. Pour CuCl<sub>2</sub>-[EMIM][EtSO<sub>4</sub>], le cation de cuivre est solvato par deux anions de chlore et deux anions EtSO<sub>4</sub><sup>-</sup>.

**Mots-clés:** électrodeposition, liquides ioniques, films minces, argent, cuivre, aluminium, [EMIM] [TFSI], [EMIM] [EtSO<sub>4</sub>], spectroscopie Raman, spectroscopie infrarouge



**Title:** Electrodeposition of metallic thin films from ionic liquid solutions for electronic applications

### **Abstract**

Deposition mechanisms from ionic liquid-based electrolytes are not fully understood due to difficulties in probing the electrolyte structure. In this study, we investigate the links between films morphology, electrochemical properties of the electrolyte and electrolyte structure. Several solutions were investigated: CuCl, CuCl<sub>2</sub> and CuSO<sub>4</sub> in 1-ethyl-3-methylimidazolium ethylsulphate [EMIM][EtSO<sub>4</sub>]; AgTFSI, CuTFSI<sub>2</sub> and AlTFSI<sub>3</sub> in 1-ethyl-3-methylimidazolium bis(trifluoromethylsulfonyl)imide [EMIM][TFSI]. Cyclic-voltammetry shows that silver and copper reductions are quasi-reversible and occur by one-electron transfer reaction {(Ag(I)→Ag(0), (Cu(II)→Cu(I)) and (Cu(I)→Cu(0))}. Aluminium reduction is irreversible. The diffusion coefficients increase with electrolyte temperature, and are also influenced by the metal oxidation state and anions in solution. Metallic thin films were obtained for all the solutions except AlTFSI<sub>3</sub>. XRD and EDX analysis show that the films are crystalline and consist mainly of pure copper or silver. Their morphology is controlled by the deposition temperature, time and potential. In general, increasing the deposition time and temperature increases the film coverage and particle size, whereas increasing the deposition potential decreases the particle size. The electrolytes structure was investigated by Raman and IR spectroscopies, supported by theoretical calculations. For the AgTFSI-[EMIM][TFSI], silver cation is solvated by three TFSI<sup>-</sup>. For the CuCl<sub>2</sub>-[EMIM][EtSO<sub>4</sub>], copper cation is solvated by two chlorines and two EtSO<sub>4</sub><sup>-</sup>.

**Keywords:** electrodeposition, ionic liquids, thin films, silver, copper, aluminium, [EMIM][TFSI], [EMIM][EtSO<sub>4</sub>], Raman spectroscopy, infrared spectroscopy

**Titre:** Electrodeposition de couches minces métalliques à partir de solutions de liquides ioniques pour des applications électroniques.

## **Le sommaire**

Les couches minces fonctionnelles sont importantes dans nos appareils électroniques de tous les jours, et leur utilisation est en constante expansion dans bien d'autres domaines d'applications. L'électrodeposition à partir de liquides ioniques présente l'avantage d'être une méthode peu coûteuse et efficace pour la création de ces films minces. Cependant, les mécanismes d'électrodeposition au sein d'électrolytes à base de liquides ioniques ne sont pas très bien compris en raison du gap qui existe entre la connaissance à un niveau théorique de pointe et la pratique industrielle. Cette lacune résulte de la complexité structurale de l'électrolyte. Dans cette étude, nous avons pour objectif de parfaire nos connaissances en établissant les relations qui existent entre la morphologie des films, les propriétés électrochimiques de l'électrolyte et de la nature des interactions au sein de l'électrolyte liquide ionique.

Cette étude a été menée sur des solutions  $\text{CuCl}$ ,  $\text{CuCl}_2$  et  $\text{CuSO}_4$  dans 1-ethyl-3-methyl-imidazolium ethylsulfate [EMIM][EtSO<sub>4</sub>] et des solutions AgTFSI, CuTFSI<sub>2</sub> et AlTFSI<sub>3</sub> dans 1-ethyl-3-methyl bis(trifluorométhylsulfonyl)imide [EMIM][TFSI].

La compréhension de l'organisation structurale complexe de l'électrolyte liquide ionique s'avère une propriété importante qui gouverne la solubilité du sel dans la solution, la conductivité ionique, la réaction de transfert de charge ainsi que la morphologie des films déposés. La structure des complexes métalliques formés dans ces solutions a été étudiée par les méthodes de spectroscopie de vibration (diffusion Raman et absorption infrarouge) et les spectres mesurés ont été interprétés à l'aide de calculs basés sur la théorie de la fonctionnelle densité (DFT). Dans ce contexte, seules les solutions  $\text{CuCl}_2$  dans [EMIM] [EtSO<sub>4</sub>] et AgTFSI dans [EMIM] [TFSI] ont pu être étudiés, en raison de l'extrême faiblesse de la solubilité des autres sels étudiés pour induire des modifications dans les signatures spectrales qui soient détectables. Dans la solution AgTFSI dans [EMIM] [TFSI], le cation d'argent est solvato par trois anions TFSI et interagît avec un des atomes d'oxygène des groupements SO<sub>2</sub> les plus proches. Ainsi, la première couche de solvation de l'argent possède une structure de type  $[\text{Ag}(\text{TFSI})_3]^{2-}$ . Dans la solution  $\text{CuCl}_2$  dans [EMIM] [TFSI], des nouvelles bandes à 997, 1045 et 1298  $\text{cm}^{-1}$  sont associés aux modes d'élongation S-O, induites par interaction entre le cation de cuivre et les anions EtSO<sub>4</sub><sup>-</sup> environnants. De même, une nouvelle bande à 312  $\text{cm}^{-1}$

est induite par le mode d'élongation asymétrique inter-ionique Cl-Cu-Cl. Le complexe de cuivre implique deux anions de chlore et deux  $\text{EtSO}_4^-$  anions, situées à deux distances de séparation distincts. La première couche de solvatation de cuivre a la structure  $[\text{CuCl}_2(\text{EtSO}_4)_2]^{2-}$ .

Les liquides ioniques [EMIM] [EtSO<sub>4</sub>] et [EMIM] [TFSI] s'avèrent être de bons solvants pour l'électrodéposition, même si l'électrolyte [EMIM] [TFSI] présente de bien meilleures propriétés. Les cyclovoltammogrammes montrent que les réductions de l'argent et du cuivre dans ces liquides ioniques sont quasi-réversibles et se produisent par un processus de transfert mono-électronique:  $\text{Ag(I)} \rightarrow \text{Ag(0)}$ ,  $\text{Cu(II)} \rightarrow \text{Cu(I)}$  et  $\text{Cu(I)} \rightarrow \text{Cu(0)}$ . La réduction de l'aluminium à partir de la solution de  $\text{AlTFSI}_3$  est irréversible et se produit par le biais d'un processus en une seule étape conduisant au dépôt de l'aluminium. Les coefficients de diffusion des espèces de l'argent et du cuivre dans les liquides ioniques augmentent comme prévu avec la température et avec des valeurs tout à fait typiques d'un électrolyte liquide ionique de viscosité comparable. Cependant, le coefficient de diffusion de l'aluminium dans [EMIM] [TFSI] est six fois inférieur à celui de l'argent et du cuivre dans ce même liquide ionique. Pour les solutions de cuivre dans [EMIM] [EtSO<sub>4</sub>], l'état d'oxydation du cuivre en solution et la nature de l'anion des sels affectent les propriétés électrochimiques. Dans les solutions de sels ayant le même anion mais pour différents états d'oxydation du cuivre ( $\text{CuCl}$  et  $\text{CuCl}_2$ ), il y a un déplacement des pics de potentiel correspondant à la même réaction observée par cyclovoltammétrie. Les pics de la solution de  $\text{CuCl}_2$  sont situés à un potentiel plus négatif que ceux de la solution de  $\text{CuCl}$ . Pour les solutions contenant des sels de cuivre ayant le même état d'oxydation, mais avec un anion différent ( $\text{CuCl}_2$  et  $\text{CuSO}_4$ ), on observe une différence significative des coefficients de diffusion du cation. Les coefficients de diffusion de l'espèce de cuivre sont d'un ordre de grandeur plus élevés pour les solutions de chlorure par rapport à ceux de la solution de sulfate. Ceci est cohérent avec l'énergie d'activation élevée de la réduction de  $\text{Cu(II)}$  en  $\text{Cu(I)}$  dans la solution de sulfate de cuivre ( $\text{CuSO}_4$ ) par rapport à celle d'une solution de chlorure de cuivre(II) ( $\text{CuCl}_2$ ). L'influence de l'état d'oxydation du cuivre ou de l'anion des sels peut être expliquée à partir des complexes métalliques qui sont formés dans chacune de ces solutions.

Des films minces d'argent et de cuivre peuvent être obtenus par électrodéposition à partir des solutions de  $\text{CuCl}_2$ ,  $\text{CuCl}$  et  $\text{CuSO}_4$  dans [EMIM] [EtSO<sub>4</sub>] et des solutions  $\text{AgTFSI}$  et  $\text{CuTFSI}_2$  dans [EMIM] [TFSI]. Cependant, aucun film d'aluminium n'a pu être déposé à partir d'une solution  $\text{AlTFSI}_3$ , ce qui est pleinement compatible avec les très faibles

coefficients de diffusion des espèces d'aluminium par rapport à ceux de l'argent et du cuivre. L'analyse des films par EDX et DRX montre qu'ils sont cristallins et constitués principalement de l'argent pur ou de cuivre, avec des traces d'oxygène et de soufre. La morphologie des films change avec la température de l'électrolyte, le potentiel et le temps de dépôt. En général, la continuité des films et la taille des particules augmente avec la température de l'électrolyte de 35 à 85 °C. L'augmentation de la durée de déposition de 900 à 1800 s améliore de façon marginale la continuité des films. Si les tendances générales sont semblables, il existe aussi des différences dans la morphologie des films déposés avec des paramètres d'électrodéposition similaires:

- Les films déposés à partir de la solution  $\text{CuCl}_2$  dans [EMIM] [EtSO<sub>4</sub>] ont des particules plus grosses et sont discontinus. Les meilleurs films ont été obtenus pour des températures d'électrolyte de 35 et 50 °C, le potentiel de dépôt de 1,8 V et un temps de dépôt de 900 s.
- Les films déposés à partir de la solution  $\text{CuCl}$  dans [EMIM] [EtSO<sub>4</sub>] étaient continus même avec un temps de dépôt de 900 s et constitués de très petites particules globulaires agrégées en amas. L'augmentation du temps de dépôt à 1800 s conduit à une surcroissance de ces films et une augmentation de leur rugosité, en raison de la formation d'une structure de type 'chou-fleur'.
- Des films continus pouvaient être préparés à partir de la solution  $\text{CuSO}_4$  dans [EMIM] [EtSO<sub>4</sub>] avec des potentiels de dépôt de -1,6 et -1,8 V à toutes températures et avec un potentiel de -1,2 V à la température de 85 °C. La structure des films est formée à partir d'agrégats nanométriques constitués des particules de formes irrégulières.
- Des films d'argent denses et continus ont été obtenus à partir de la solution  $\text{AgTFSI}$  dans [EMIM] [TFSI]. Cependant, les films obtenus à 85 °C étaient très rugueux, avec une croissance de grosses particules dirigée vers l'extérieur de la surface du film. La rugosité a été réduite avec l'augmentation du temps de dépôt. Les meilleurs films ont été obtenus à 35 et 50 °C, et avec un potentiel de -0,4 V. La dureté des films d'argent était de  $2,0 \pm 0,40$  GPa et une valeur du module de Young réduit de  $176 \pm 23$  GPa.
- A 35 °C, la morphologie des films de cuivre déposés à partir de la solution  $\text{CuTFSI}_2$  dans [EMIM] [TFSI] était indépendante du potentiel et du temps d'électrodéposition. La taille des particules n'est que légèrement augmentée avec l'élévation du temps de dépôt et la diminution du potentiel. L'analyse EDX montre qu'à 85 °C, les films ont été contaminés par

l'argent, probablement à partir du fil d'argent utilisé comme électrode de référence. Les particules d'argent et de cuivre étaient très petites, allant de 10 à 50 nm. Les particules d'argent sont légèrement plus grandes que celles de cuivre.

La stabilité des complexes métalliques avec la concentration des ions en solution et de la température de l'électrolyte n'a été que partiellement étudiée. Une brève analyse a montré que les électrolytes dans lesquels le liquide ionique et le sel métallique partage le même anion (solutions AgTFSI et CuTFSI<sub>2</sub> dans [EMIM] [TFSI]) sont plus stables. Ceci a été également révélé à partir des mesures cyclovoltammétriques qui sont stables dans un large domaine de température et avec absence de pics supplémentaires. Les morphologies des films déposés à partir de ces solutions sont également tout à fait similaires dans un large domaine de potentiels et de temps d'électrodéposition et de températures de l'électrolyte liquide ionique.

#### **Unité de recherche :**

1. Institut des Sciences Moléculaires  
Université Bordeaux  
CNRS UMR 5255  
Bâtiment A12, 351 cours de la libération  
33405 TALENCE cedex  
France
  
2. Departamento de Engenharia Química  
Instituto Superior Técnico  
Universidade de Lisboa  
Av. Rovisco Pais  
1049-001 Lisboa  
Portugal

## Acknowledgements

Doing a PhD can be challenging at times, and as one of the first guinea pigs of the IDS-FunMat program, I have faced my fair share of challenges. However, the love, encouragement and support shown by many people have helped to make this PhD endeavour both possible and enjoyable and I would like to thank them here.

First and foremost, I would like to thank both my supervisors, Prof. Rui Vilar and Prof. Joseph Grondin for their guidance and wisdom. Coordinating my work between different institutions can be very challenging and Prof. Vilar has done a great job ensuring my work can go as smoothly as possible. His stories and “everything is possible” attitude have been very motivational and have been useful when all hopes seemed lost. Prof. Grondin has spent countless hours teaching me the ins and outs of both Raman and infrared spectroscopies. Through our countless time shared, I have also managed to pick up some of his philosophy on science and I feel this has made me into a better scientist.

I am also extremely grateful to my predecessor, Dr. Sónia Eugénio for her advices, her countless hours of help with many of my experiments at IST and her input to solve the unfinished paper from hell. Sónia has an extremely busy schedule managing her work and her young child and I am extremely sorry for unbalancing her life. I am also grateful to Dr. Yann Danten, my co-supervisor at Université Bordeaux 1. Yann assisted me with all the theoretical calculation work and has been very approachable with any problems I have in both work and life. I would also like to thank Isabel Nogueira who taught and helped me with the scanning electron microscope, Dr. Sahendra Pal Sharma who helped me with the transmission electron microscope and my buddy, Bruno Nunes who helped me with the atomic force microscope.

I would like to give a special mention to Audrey Sidobre for her creative and superhuman effort to solve many of my administrative issues that was critical to the success of my PhD. Prof. Amelia Almeida and Alexander Jarques were also instrumental in solving my various administrative problems at IST; and Prof. Laurent Servant and Thierry Tassaing who helped me with any issues at UB1.

To all my colleagues at IST, UB1 and IDS-FunMat, I am very appreciative for their support and the times that we shared together. Their names in semi-alphabetical order are Alex, Carol, Elisabeth, Felipe, Gonçalo, Jaroslaw, Laura, Liliana, Lo, Tuyen, Annie, Aude, Elise, Edgar, Enora, Flavio, Hanbin, Jinzhu, Mathilde, Nguyen, Uyxing, Tamez, Tatiana, Yi-Shiang, Aline, Daniel, Diana, Henu, Ji, Mariel,

Naresh, Nilson, Poussin, Ragu, Tri and Zilin. Special mentions to Natacha and Narayanan for letting me stay at their place when I was homeless.

I am also very appreciative of the company of Prof. Mauro, Arthur and Helen for showing me places with good food and for having lunch with me during my first year. I would also like to thank my friends Ram, Oat, Feng and Shaolong for coming to my place on many weekends and cooking delicious meals. To Mikolas, Angel and Nestor, I would like to thank them for the enjoyable time during my stay in the Baldaques Residence.

Finally, I would like to thank my parents for their love and undying support. They have always believed in my abilities even when sometimes, I do not.

This work is financially supported by the European Commission under the Erasmus Mundus IDS-FunMat project n° 2010-08. Although the ride has been extremely bumpy at times, I am extremely grateful for the opportunity to have this unique experience.

## List of Symbols

$a$	Polarisability
$a_i$	Activity of species i
$A$	Area
$A_r$	Displacement area
$A_p$	Projected area
$A_\lambda$	Absorbance
$\alpha$	Adsorption coefficient
$B$	Peak width at half maximum in radians
$B_F$	Magnetic field
$\beta$	Geometrical constant
$c_0$	Speed of light in vacuum
$c_i$	Concentration of species i
$C$	Capacity
$C_\infty$	Initial concentration of the reductant
$C_1$	Cisoid transformation
$C_2$	Transoid transformation
$d$	Distance between atomic plane
$D$	Diffusion coefficient
$D_{2d}$	Distorted tetrahedral
$\epsilon$	Permittivity
$E$	Potential
$E_a$	Activation energy
$E_{op}$	Open circuit potential
$E_i$	Initial potential
$E_f$	Final potential
$E_F$	Electric field
$E_r$	Reduced Young's Modulus
$E_{max}$	Maximum potential value
$E_{min}$	Minimum potential value
$E_{ph}$	Energy of a photon
$E_p$	Peak potential
$E_{p/2}$	Potential when the current density is half of the peak value
$E_{p,a}$	Oxidation peak potential
$E_{p,c}$	Reduction peak potential
$\Delta E$	Difference between two energy state
$E_0$	Maximum amplitude
$E_{cell}$	Potential of a cell
$E^\circ$	Standard electrode potential
$E^\phi$	Formal Potential
$\Delta G$	Free energy
GC	Glassy carbon



$h_c$	Difference in penetration depth between loaded & unloaded conditions
H	Hardness
$\Delta H^*$	Activation enthalpy
i	Current density
I	Current
$I_{VV}$	Raman vertically polarised spectra
$I_{HV}$	Raman horizontally polarised spectra
$I_0$	Intensity of incident radiation
$I_x$	Intensity of exiting radiation
$I_{pA}$	Maximum peak current of oxidation
$I_{pC}$	Maximum peak current of reduction
$J_i$	Flux of the species i
k	Rate
$k_0$	Kinetics of electrode process
m	Mass
M	Metal
$\mu$	Permeability
$\mu_i$	Chemical potential of species i
$\mu^\theta$	Chemical potential in the standard state
n	Number of electrons
N	Number of atoms
$\eta$	Viscosity
$\eta_v$	Overpotential
$\eta$	Current efficiency
$[O]^*$	Concentration of the oxidant
$\rho$	Dipole moment
P	Load
$P_{max}$	Maximum load
$\rho$	Depolarisation ratio
q	Charge
r	Radius
R	Resistance
$[R]^*$	Concentration of the reductant
S	Stiffness
$\Delta S^*$	Activation entropy
t	Time
T	Temperature
$T_d$	Decomposition temperature
$T_g$	Glass transition temperature
$T_m$	Melting temperature
$T_\lambda$	Transmittance
u	Propagation speed
v	Frequency

$v$	Sweep rate
$v_s$	Poisson ratio of the sample
$v_i$	Poisson ratio of the indenter
$V$	Potential
$\nu_i$	Stoichiometric number of species i
$\gamma_i$	Activity coefficient of species i
$Z$	Valence of ionic species
$\theta$	Bragg angle
$\phi$	Electrostatic potential
$\sigma$	Ionic conductivity
$\nabla$	Laplace operator
$\lambda$	Wavelength

## Acronyms and abbreviations

ATR-IR	Attenuated total reflectance infrared spectroscopy
BEI	Backscattered electron imaging
BF	Bright field
CCD	Charge coupled diode
CV	Cyclic voltammogram
CVD	Chemical vapour deposition
C.S.	Current source
DFT	Density Functional Theory
DPCP	Diphenylcyclopropenone
EC	Electrochemical cell
EDX	Energy dispersive X-ray
EIS	Electrochemical impedance spectroscopy
FMHW	Full width at half maximum
FT-IR	Fourier transformed infrared spectroscopy
GA-XRD	Glancing angle X-ray diffraction
HOPG	Highly oriented pyrolytic graphite
IL	Ionic liquid
IR	Infrared
IHP	Inner Helmholtz layer
IST	Instituto Superior Tecnico
ITO	Indium tin oxide
JCPDS	Joint Committee on Powder Diffraction Standards
MNDO	Modified neglect of diatomic overlap
NMR	Nuclear magnetic resonance
OHP	Outer Helmholtz layer
PS	Polystyrene
PVD	Physical vapour deposition
QRE	Quasi reference electrode
SAD	Selected area diffraction
SEI	Secondary electron imaging
SEM	Scanning electron microscopy
SERS	Surface enhanced Raman scattering
SFGS	Sum frequency generation vibrational spectroscopy
SHE	Standard hydrogen electrode
TEM	Transmission electron microscopy
ToF-SIMS	Time-of-flight secondary ion mass spectrometry
UB1	Universite Bordeaux 1
ULWD	Ultra-long working distance
XRD	X-ray diffraction

## Ionic liquid abbreviations

[Ag(eth-hex-en) <sub>2</sub> ]	bis(N-2-ethylhexylethyl-enediamine)silver(I)
[Ag(hex-en) <sub>2</sub> ]	bis(N-hexylethylenediamine)silver(I)
[BMIM]	1-butyl-3-methyl imidazolium
[BMPyr]	1-butyl-1-methylpyrrolidinium
[BPyr]	1-butylpyridinium
[3-BPyr]	3-butylpyridinium
[BTMA]	benzyltrimethylammonium
(BuPyCl)	N-butylpyridinium chloride
[C <sub>2-4</sub> MIM]	1-ethyl/1-propyl/1-butyl -3-methyl imidazolium
DIMCARB	Dimethylammonium dimethylcarbamate
[EAN]	ethylammonium nitrate
[EMIM]	1-ethyl-3-methyl imidazolium
(EtPyBr)	N-ethylpyridinium bromide
[Et <sub>3</sub> N]	triethylammonium
[(MeOEt) <sub>2</sub> NH]	bis(2-methoxyethyl)ammonium
[MIMSBu]	1-methyl-2-butylthiolonium
[MoeMIM]	1-(2-methoxyethyl)-3-methylimidazolium
[TMHA]	trimethyl-n-hexylammonium
[TMPAC]	AlCl <sub>3</sub> -trimethylphenylammonium chloride
[TOMA]	trioctylmethylammonium
[TFSM]	tris((trifluoromethyl)sulfonyl)methanide
[PFSI]	Bis(pentafluoroethanesulfone)imide
[AcOH]	acetate
[AlCl <sub>3</sub> ]	tetrachloroaluminate
[Al <sub>2</sub> Cl <sub>7</sub> ]	heptachloroaluminate
[CF <sub>3</sub> COO]	trifluoroacetate
[CF <sub>3</sub> SO <sub>3</sub> ]	trifluoromethanesulfonate
[BF <sub>4</sub> ]	tetrafluoroborate
[Br]	bromide
[Cl]	chloride
[DCA]	dicyanamide
[EtSO <sub>4</sub> ]	ethylsulphate
[FeCl <sub>4</sub> ]	tetrachloroferrate
[I]	iodide
[MeSO <sub>4</sub> ]	methylsulfonate
Me <sub>2</sub> NH	N-methylmethanamine
[NO <sub>3</sub> ]	nitrate
[PF <sub>6</sub> ]	hexafluorophosphate
[TFSI]	Bis(trifluoromethylsulfonyl)imide
[TFO]	trifluoromethanesulfonate

## Physical constants

$c$	velocity of light	$2.99792458 \times 10^7 \text{ m s}^{-1}$
$e$	unit of electron charge	$1.60217646 \times 10^{-19} \text{ C}$
$F$	Faraday constant	$9.6485 \times 10^4 \text{ C mol}^{-1}$
$h$	Planck constant	$6.62608 \times 10^{-34} \text{ J s}$
$k_B$	Boltzmann constant	$1.3806503 \times 10^{-23} \text{ m}^2 \text{ kg s}^{-2}$
$N_a$	Avogadro number	$6.02214 \times 10^{23} \text{ mol}^{-1}$
$\pi$	Pi	3.14159
$R$	ideal gas constant	$8.31451 \text{ J K}^{-1} \text{ mol}^{-1}$

## Lists of Figures

Figure 1.1: Photoluminescent semiconductors of $\text{Ge}_x\text{Si}_{1-x}$ deposited from ionic liquids. [1].	2
Figure 1.2: <b>a)</b> SEM micrographs of Ti–Al alloy deposits at 70 °C by using a deposition potential of -2.5 V [2]. <b>b)</b> Template-free electrodeposition of hexagonal CuSn tubes [3].	2
Figure 1.3: <b>a)</b> SEM micrographs of free-standing aluminium nanowires obtained by electrodeposition with a polycarbonate template [4]. <b>b)</b> Inversed opal structure of germanium obtained after applying a constant potential of -1.7 V from [EMIM] [TFSI] [5].	2
Figure 2.1: <b>a)</b> An electrochemical cell and <b>b)</b> Circuit diagram representing an electrochemical cell [6]. Where <b>C.S.</b> is the current source, <b>R</b> is an Ohmic resistance, <b>V</b> a voltmeter, <b>A</b> an ammeter, <b>EC</b> the electrochemical cell, <b>B</b> the circuit breaker.	6
Figure 2.2: Relationship between the energy levels of the electron and the molecular levels in the ions in solution during <b>a)</b> reduction and <b>b)</b> oxidation reaction [7].	7
Figure 2.3: Structure of the solution in an electrochemical cell during an electrochemical reaction.	9
Figure 2.4: Kinetics of the oxidation and reduction reaction near the electrode/electrolyte surface [8].	13
Figure 2.5: Potential step to obtain the diffusion limited current of the electroactive species [8].	15
Figure 2.6: <b>a)</b> A conceptual structure of an electrolyte double-layer. (1) is the Inner Helmholtz layer (IHP), (2) Outer Helmholtz layer (OHP), (3) Diffuse layer, (4) Solvated ions, (5) Specifically adsorbed ions and (6) Solvent molecule [9]. <b>b)</b> Change in the electrostatic potential between the interfacial region and bulk solution [8].	18
Figure 2.7: Phase diagram representing the two components inside a first-generation ionic liquid showing the importance of composition to the melting temperature in a eutectic system	20
Figure 2.8: Structure of the cations and anions used in the air and water stable ionic liquids [10,11].	22
Figure 2.9: A representation of an electromagnetic wave [12].	33
Figure 2.10: The electromagnetic spectrum showing the relationship between wavelength, frequency and energy [13].	33
Figure 2.11: Energy states of a diatomic molecule [14].	34
Figure 2.12: Examples of different modes of molecular vibration [12]. Stretching modes: symmetric and asymmetric stretching; bending modes: deformation, rocking, wagging and twisting; out of plane and in plane mode of bending.	35
Figure 2.13: Relationship between molecular processes, radiation wavelength range [12].	36

Figure 2.14: The absorption process showing the atom in the ground state being promoted to an excited state due to interaction with a photon with the correct energy. Adapted from [15].	37
Figure 2.15: Spontaneous emission of a photon when an atom decays from an excited state to the ground state [15].	37
Figure 2.16: Energy levels of infrared and Raman spectroscopy [16].	39
Figure 3.1: The UniLab, MBraun glove box system used at Instituto Superior Técnico [11].	44
Figure 3.2: Experimental setup for the electrochemical characterisation and electrodeposition experiments.	46
Figure 3.3: <b>a)</b> The variation of the potential with time for one full cycle of a cyclic voltammogram [8]. <b>b)</b> A cyclic voltammogram for a simple reversible reaction involving a one oxidation and one reduction process. $\text{Fc}^+/\text{Fc}$ couple of ferrocene in [BMIM] $[\text{BF}_4]$ ionic liquid adapted from [11].	47
Figure 3.4: <b>a)</b> Potential step to obtain the diffusion limited current of the electroactive species [8]. <b>b)</b> Chronoamperograms showing a typical current response.	51
Figure 3.5: Schematic representation of a scanning electron microscope [17].	52
Figure 3.6: Interactions observed between the electron beam and a sample [18,11].	53
Figure 3.7: The interaction volume showing the region from which the various signals may reach the detectors.	54
Figure 3.8: Schematic representation of a Transmission Electron Microscope [11,19].	56
Figure 3.9: The interplay between the objective and intermediate lens in <b>a)</b> imaging mode and <b>b)</b> diffraction mode [20].	56
Figure 3.10: The two common geometries used in X-ray diffraction experiments. <b>a)</b> Bragg-Brentano Geometry and <b>b)</b> Glancing Angle Geometry [11].	58
Figure 3.11: A typical load-displacement curve obtained from a nanoindentation experiment [21].	59
Figure 3.12: Parameters describing the relationship between the contact geometry on the sample surface during loading and unloading [22].	59
Figure 3.13: Schematic showing a typical attenuated total reflectance (ATR) cell.	61
Figure 4.1: Raman spectrum of pure [EMIM] [TFSI] ionic liquid in the spectral region $200\text{--}3250\text{ cm}^{-1}$ . The bands from the C-H stretching region ( $2700\text{--}3250\text{ cm}^{-1}$ ) are magnified for clarity. Vibrational modes are indicated with the symbols: $\nu$ = stretching; $\delta$ = bending; $\rho$ = rocking; $s$ = symmetric; $as$ = asymmetric.	64
Figure 4.2: Mid-IR ( $400\text{--}3250\text{ cm}^{-1}$ ) and far-IR ( $190\text{--}460\text{ cm}^{-1}$ ) spectra of pure [EMIM] [TFSI] ionic liquid. The bands from the C-H stretching ( $2700\text{--}3250\text{ cm}^{-1}$ ) and far-IR ( $190\text{--}460\text{ cm}^{-1}$ ) regions are magnified for clarity. Vibrational modes are indicated by the same symbols as in Figure 4.1.	64

Figure 4.3: Chemical structures of cation and anion species in the [EMIM] [TFSI].	65
Figure 4.4: Calculated eigenvectors for the breathing mode of [TFSI] anion ( $742\text{ cm}^{-1}$ ) for the $C_2$ <b>(a)</b> and $C_1$ <b>(b)</b> symmetry extracted from Herstedt et al. [23].	65
Figure 4.5: Polarised $I_{VV}$ and depolarised $I_{VH}$ Raman spectra of pure [EMIM] [TFSI] ionic liquid ( $200\text{--}1600\text{ cm}^{-1}$ ). The ‘breathing’ mode is observed at $742\text{ cm}^{-1}$ .	66
Figure 4.6: Evolution with the AgTFSI concentration of the Raman spectra of the AgTFSI/[EMIM] [TFSI] solutions measured in the region $200\text{--}3250\text{ cm}^{-1}$ . The spectra of the solutions have been shifted upward for clarity.	68
Figure 4.7: Evolution with AgTFSI concentration of the Raman spectra of the AgTFSI/[EMIM] [TFSI] solutions measured in the region $400\text{--}1600\text{ cm}^{-1}$ . The spectra of the solutions have been shifted upwards for clarity.	69
Figure 4.8: Raman spectrum of the pure [EMIM] [EtSO <sub>4</sub> ] in the spectral region $200\text{--}3300\text{ cm}^{-1}$ . The spectrum in the region $2700\text{--}3250\text{ cm}^{-1}$ is magnified for clarity. Vibrational modes are indicated with symbols: $\nu$ = stretching; $\delta$ = bending; $\rho$ = rocking ; $s$ = symmetric ; $as$ = asymmetric.	70
Figure 4.9: Mid-infrared ( $400\text{--}3300\text{ cm}^{-1}$ ) and far-infrared ( $200\text{--}500\text{ cm}^{-1}$ ) spectra of pure [EMIM] [EtSO <sub>4</sub> ]. The intensity in the far-IR region has been magnified. Vibrational modes are indicated by the same symbols in Figure 4.8.	70
Figure 4.10: Chemical structure of cation and anion species in [EMIM] [EtSO <sub>4</sub> ].	71
Figure 4.11: Evolution of the Raman spectra of CuCl <sub>2</sub> /[EMIM] [EtSO <sub>4</sub> ] solutions in the region $200\text{--}1600\text{ cm}^{-1}$ with the salt concentration.	73
Figure 4.12: Evolution of the IR spectra of CuCl <sub>2</sub> /[EMIM] [EtSO <sub>4</sub> ] solutions in the region $200\text{--}1600\text{ cm}^{-1}$ with the salt concentration.	73
Figure 4.13: Structure of the Ag-complex formed with TFSI <sup>-</sup> anions calculated at the [B3LYP/6-31+G(d,p):MQZVP(S):DGDZVP(Ag)] level. Two cations have been considered in the calculation of this structure.	75
Figure 4.14: Evolution with the AgTFSI concentration of the Raman spectra of the AgTFSI/[EMIM] [TFSI] solutions measured in the region of the ‘breathing’ modes of TFSI. The evolution of the normalised intensity with the concentration [AgTFSI] is displayed in the inset of this figure.	77
Figure 4.15: Evolution with the AgTFSI concentration of the IR spectra of the AgTFS/[EMIM] [TFSI] solutions measured in the region of the asymmetric S-N-S stretching mode.	78
Figure 4.16: Evolution with the AgTFSI concentration of the IR spectra of the AgTFS/[EMIM] [TFSI] solutions measured in the region of the asymmetric S-O stretching mode.).	79
Figure 4.17: Structure of the Cu-complex formed with Cl <sup>-</sup> and EtSO <sub>4</sub> <sup>-</sup> anions calculated at the [B3LYP/6-31+G(d,p):MQZVP(S,Cu)] level. Two EMIM cations have been considered in the geometry optimization of this structure.	80



Figure 4.18: Evolution with the concentration of the $\text{CuCl}_2$ salt of the IR spectra of the $\text{CuCl}_2/[\text{EMIM}][\text{EtSO}_4]$ solutions measured in the region of the asymmetric O-S-O stretches ( $1150\text{-}1350\text{ cm}^{-1}$ ). ..	81
Figure 4.19: Evolution with the concentration of the $\text{CuCl}_2$ salt of the IR spectra of the $\text{CuCl}_2/[\text{EMIM}][\text{EtSO}_4]$ solutions measured in the region of the symmetric O-S-O stretches. The new bands are located at $997$ and $1045\text{ cm}^{-1}$ . ..	82
Figure 4.20: Evolution with the concentration of the $\text{CuCl}_2$ salt of the Raman spectra of the $\text{CuCl}_2/[\text{EMIM}][\text{EtSO}_4]$ solutions measured in the far IR spectral region $200\text{-}500\text{ cm}^{-1}$ . The new band obtained upon the dissolution of the $\text{CuCl}_2$ salt is located at $313\text{ cm}^{-1}$ . ..	84
Figure 4.21: Evolution with the $\text{CuCl}_2$ concentration the far-IR spectra ( $200\text{-}500\text{ cm}^{-1}$ ) showing the new band at $312\text{ cm}^{-1}$ . The relationship between the intensity of the band at $312\text{ cm}^{-1}$ and concentration of the $\text{CuCl}_2$ salt is given in the inset. ....	84
Figure 5.1: Cyclic voltammogram showing the electrochemical window of the pure $[\text{EMIM}][\text{EtSO}_4]$ between $-2.5$ to $1.5\text{ V}$ . The working electrode was a GC disc. The experimental temperature was $35^\circ\text{C}$ and the scan rate was $50\text{ mV s}^{-1}$ . ....	87
Figure 5.2: Cyclic voltammogram (3 cycles) of $0.1\text{ M CuCl}$ solution in $[\text{EMIM}][\text{EtSO}_4]$ at $35^\circ\text{C}$ . The working electrode was a GC disc and the scan rate was $50\text{ mV s}^{-1}$ . The potential of the cathodic and anodic peaks are shown in the accompanying table. ....	88
Figure 5.3: Cyclic voltammograms of $0.1\text{ M CuCl}$ solution in $[\text{EMIM}][\text{EtSO}_4]$ at $35^\circ\text{C}$ using different reversal potentials. The working electrode was a GC disc and the scan rate was $50\text{ mV s}^{-1}$ . The potential of the cathodic and anodic peaks are shown in the accompanying table. ....	89
Figure 5.4: Cyclic voltammograms of $0.1\text{ M CuCl}_2$ solution in $[\text{EMIM}][\text{EtSO}_4]$ at $35^\circ\text{C}$ . The working electrode was a GC disc and the scan rate was $50\text{ mV s}^{-1}$ . The potential of the cathodic and anodic peaks are shown in the accompanying table. ....	90
Figure 5.5: Cyclic voltammograms of $0.1\text{ M CuCl}_2$ solution in $[\text{EMIM}][\text{EtSO}_4]$ at $35^\circ\text{C}$ using different cathodic reversible potentials. The working electrode was a GC disc and the scan rate was $50\text{ mV s}^{-1}$ . The potential of the cathodic and anodic peaks are shown in the accompanying table. ....	91
Figure 5.6: Cyclic voltammogram (3 cycles) of $0.1\text{ M CuSO}_4$ solution in $[\text{EMIM}][\text{EtSO}_4]$ at $35^\circ\text{C}$ . The working electrode was a GC disc and the scan rate was $50\text{ mV s}^{-1}$ . The potential of the cathodic and anodic peaks are shown in the accompanying table. ....	91
Figure 5.7: Cyclic voltammograms of $0.1\text{ M CuSO}_4$ solution in $[\text{EMIM}][\text{EtSO}_4]$ at $35^\circ\text{C}$ using different cathodic reversible potentials. The working electrode was a GC disc and the scan rate was $50\text{ mV s}^{-1}$ . The potential of the cathodic and anodic peaks are shown in the accompanying table. ....	92
Figure 5.8: Cyclic voltammograms of $0.1\text{ M CuCl}_2$ solution in $[\text{EMIM}][\text{EtSO}_4]$ at $85^\circ\text{C}$ using different potential scan rates between $0.01$ and $1.00\text{ V s}^{-1}$ . The working electrode was a GC disc. ....	93
Figure 5.9: <b>a)</b> The anodic peak current ( $A_1$ ) and <b>b)</b> cathodic peak current ( $C_1$ ) as a function of scan rate for the $0.1\text{ M CuCl}_2$ solution in $[\text{EMIM}][\text{EtSO}_4]$ at $85^\circ\text{C}$ shown in Figure 5.8. ....	94

Figure 5.10: Cyclic voltammograms of 0.1 M CuCl <sub>2</sub> solution in [EMIM] [EtSO <sub>4</sub> ] at <b>a)</b> 35, <b>b)</b> 50 and <b>c)</b> 85 °C. The working electrode was a GC disc and the scan rate was 50 mV s <sup>-1</sup> . The potential of the cathodic and anodic peaks are shown in the accompanying tables. ....	95
Figure 5.11: Cyclic voltammograms of 0.1 M CuSO <sub>4</sub> solution in [EMIM] [EtSO <sub>4</sub> ] at <b>a)</b> 35, <b>b)</b> 50 and <b>c)</b> 85 °C. The working electrode was a GC disc and the scan rate was 50 mV s <sup>-1</sup> . The potential of the cathodic and anodic peaks are shown in the accompanying tables. ....	96
Figure 5.12: Change in the current density of peak C1 with temperature for 0.1 M CuCl, CuCl <sub>2</sub> and CuSO <sub>4</sub> solutions in [EMIM] [EtSO <sub>4</sub> ]. The working electrode was a GC disc and the scan rate was 50 mV s <sup>-1</sup> . ....	97
Figure 5.13: A plot of the current density of peak C1 versus the electrolyte temperature. A linear relationship shows that Equation 5.2 is satisfied. ....	98
Figure 5.14: <b>a)</b> Chronoamperograms of 0.1 M CuCl, CuSO <sub>4</sub> and CuCl <sub>2</sub> solutions obtained at 35 °C with a GC disc electrode, using potential steps of -1.0, -0.7 and -0.3 V, respectively; <b>b)</b> respective variation of the current density with t <sup>-1/2</sup> . ....	99
Figure 5.15: SEM micrographs at <b>a)</b> lower magnification and <b>b)</b> higher magnification of films electrodeposited from 0.1 M CuCl solution at -0.8 V. Deposition temperature: 35 °C. Deposition time: 900 s. ....	101
Figure 5.16: SEM micrographs (lower magnification) of films electrodeposited from 0.1 M CuCl solution at -1.6 V. Deposition temperatures: 35, 50 and 85 °C. Deposition times: 900 and 1800 s. ....	102
Figure 5.17: SEM micrographs (higher magnification) of films electrodeposited from 0.1 M CuCl solution at -1.6 V. Deposition temperatures: 35, 50 and 85 °C. Deposition times: 900 and 1800 s. ....	103
Figure 5.18: SEM micrographs of films electrodeposited from 0.1 M CuCl solution at -1.8 V for 900 s. Deposition temperatures: 35, 50 and 85 °C. ....	104
Figure 5.19: SEM micrographs (lower magnification) of films electrodeposited from 0.1 M CuCl <sub>2</sub> solution at -1.6 V. Deposition temperatures: 35, 50 and 85 °C. Deposition times: 900 and 1800 s. ....	105
Figure 5.20: SEM micrographs (higher magnification) of films electrodeposited from 0.1 M CuCl <sub>2</sub> solution at -1.6 V. Deposition temperatures: 35, 50 and 85 °C. Deposition times: 900 and 1800 s. ....	106
Figure 5.21: SEM micrographs of films electrodeposited from 0.1 M CuCl <sub>2</sub> solution at -1.8 V for 900 s. Deposition temperatures: 35 and 85 °C. ....	107
Figure 5.22: SEM micrographs at <b>a)</b> lower magnification and <b>b)</b> higher magnification of films electrodeposited from 0.1 M CuSO <sub>4</sub> solution at -1.2 V. Deposition temperature: 85 °C. Deposition time: 900 s. ....	108

Figure 5.23: SEM micrographs (lower magnification) of films electrodeposited from 0.1 M CuSO <sub>4</sub> solution at -1.6 V. Deposition temperatures: 35, 50 and 85 °C. Deposition times: 900 and 1800 s. ....	109
Figure 5.24: SEM micrographs (higher magnification) of films electrodeposited from 0.1 M CuSO <sub>4</sub> solution at -1.6 V. Deposition temperatures: 35, 50 and 85 °C. Deposition times: 900 and 1800 s. ....	110
Figure 5.25: SEM micrographs of films electrodeposited from 0.1 M CuSO <sub>4</sub> solution at -1.8 V for 900 s. Deposition temperatures: 35, 50 and 85 °C. ....	111
Figure 5.26: XRD patterns of copper films electrodeposited at -1.8 V for 900 s from <b>a)</b> 0.1 M CuSO <sub>4</sub> and <b>b)</b> 0.1 M CuCl solutions in [EMIM] [EtSO <sub>4</sub> ] at 85 °C. ....	112
Figure 5.27: TEM micrographs of films electrodeposited with -1.8 V for 900 s from <b>a)</b> 0.1 M CuCl <sub>2</sub> solution with <b>b)</b> the corresponding selected area diffraction pattern and <b>c)</b> 0.1 M CuSO <sub>4</sub> solution with <b>d)</b> the corresponding selected area diffraction pattern. ....	114
Figure 6.1: Cyclic voltammograms of pure [EMIM] [TFSI] between -2.5 to 2.5 V using <b>(a)</b> a GC disc and <b>(b)</b> a Pt disc working electrode. The electrolyte temperature was 35 °C and the scan rate was 0.05 V s <sup>-1</sup> . ....	117
Figure 6.2: Cyclic voltammogram (3 cycles) of 0.05 M AgTFSI solution in [EMIM] [TFSI] at 35 °C. The working electrode was a GC disc and the scan rate was 50 mV s <sup>-1</sup> . The potential of the cathodic and anodic peaks are shown in the accompanying table. ....	118
Figure 6.3: Cyclic voltammogram (3 cycles) of 0.05 M AgTFSI solution in [EMIM] [TFSI] at 35 °C. The working electrode was a Pt disc and the scan rate was 50 mV s <sup>-1</sup> . The potential of the cathodic and anodic peaks are shown in the accompanying table. ....	119
Figure 6.4: Cyclic voltammograms of 0.05 M AgTFSI solution in [EMIM] [TFSI] at 35, 50 and 85 °C. The working electrode was a GC disc and the scan rate was 50 mV s <sup>-1</sup> . The potential of the cathodic and anodic peaks are shown in the accompanying table. ....	120
Figure 6.5: Relationship between current density of C1 with temperature. The working electrode was a GC disc and the scan rate was 50 mV s <sup>-1</sup> . ....	120
Figure 6.6: Cyclic voltammograms of 0.05 M AgTFSI solution in [EMIM] [TFSI] using different potential scan rates between 0.01 and 1.00 V s <sup>-1</sup> at <b>a)</b> 35 °C on GC, <b>b)</b> 35 °C on Pt, <b>c)</b> 50 °C on GC, <b>d)</b> 50 °C on Pt, <b>e)</b> 85 °C on GC and <b>f)</b> 85 °C on Pt. ....	121
Figure 6.7: <b>a)</b> The anodic peak current (A1) and <b>b)</b> cathodic peak current (C1) as a function of scan rate for the 0.05 M AgTFSI solution in [EMIM] [TFSI] using a GC working electrode. ....	123
Figure 6.8: <b>a)</b> The anodic peak current (A1) and <b>b)</b> cathodic peak current (C1) as a function of scan rate for the 0.05 M AgTFSI solution in [EMIM] [TFSI] using a Pt working electrode. ....	123

Figures 6.9: <b>a)</b> Chronoamperograms of 0.05 M AgTFSI solution obtained at 35, 50 and 85 °C on a GC disc electrode with potential steps of -0.39, -0.31 and -0.28 V, respectively; and <b>b)</b> respective variation of the current density with $t^{-1/2}$ . .....	124
Figure 6.10: <b>a)</b> Chronoamperograms of 0.05 M AgTFSI solution obtained at 35, 50 and 85 °C on a Pt disc electrode with potential steps of -0.34, -0.22 and -0.24 V, respectively; and <b>b)</b> respective variation of the current density with $t^{-1/2}$ . .....	125
Figure 6.11: Cyclic voltammogram (3 cycles) of 0.05 M CuTFSI <sub>2</sub> solution in [EMIM] [TFSI] at 35 °C. The working electrode was a GC disc and the scan rate was 50 mV s <sup>-1</sup> . The potential of the cathodic and anodic peaks are shown in the accompanying table. ....	125
Figure 6.12: Cyclic voltammogram (3 cycles) of 0.05 M CuTFSI <sub>2</sub> solution in [EMIM] [TFSI] at 35 °C. The working electrode was a Pt disc and the scan rate was 50 mV s <sup>-1</sup> . The potential of the cathodic and anodic peaks are shown in the accompanying table. ....	126
Figure 6.13: Cyclic voltammograms of 0.05 M CuTFSI <sub>2</sub> solution in [EMIM] [TFSI] at 50 °C using different cathodic reversible potentials. The working electrode was a GC disc and the scan rate was 50 mV s <sup>-1</sup> . The potential of the cathodic and anodic peaks are shown in the accompanying tables. ....	127
Figure 6.14: The variation in current density with temperature for the 0.05 M CuTFSI <sub>2</sub> solution in [EMIM] [TFSI] obtained on a Pt working electrode. The potential of the cathodic and anodic peaks are shown in the accompanying tables. ....	128
Figure 6.15: Relationship between current density of C1 with temperature. The working electrode was a GC disc and the scan rate was 50 mV s <sup>-1</sup> . ....	128
Figure 6.16: Cyclic voltammograms of 0.05 M CuTFSI <sub>2</sub> solution in [EMIM] [TFSI] using different potential scan rates between 0.01 and 1.00 V s <sup>-1</sup> at <b>a)</b> 35 °C on GC, <b>b)</b> 35 °C on Pt, <b>c)</b> 50 °C on GC, <b>d)</b> 50 °C on Pt, <b>e)</b> 85 °C on GC and <b>f)</b> 85 °C on Pt. ....	129
Figure 6.17: <b>a)</b> The anodic peak current (A1) and <b>b)</b> cathodic peak current (C1) as a function of scan rate for the 0.05 M CuTFSI <sub>2</sub> solution in [EMIM] [TFSI] using a GC working electrode. ....	130
Figure 6.18: <b>a)</b> The anodic peak current (A1) and <b>b)</b> cathodic peak current (C1) as a function of scan rate for the 0.05 M CuTFSI <sub>2</sub> solution in [EMIM] [TFSI] using a Pt working electrode. ....	130
Figure 6.19: <b>a)</b> Chronoamperograms of 0.05 M CuTFSI <sub>2</sub> solutions obtained on a GC disc electrode with potential steps of -0.30, -0.30 and -0.24 V, respectively; and <b>b)</b> respective variation of the current density with $t^{-1/2}$ . ....	131
Figure 6.20: <b>a)</b> Chronoamperograms of 0.05 M CuTFSI <sub>2</sub> solutions obtained on a Pt disc electrode with potential steps of -0.1 V; and <b>b)</b> respective variation of the current density with $t^{-1/2}$ . ....	131
Figure 6.21: Cyclic voltammogram (3 cycles) of 0.50 M AlTFSI <sub>3</sub> solution in [EMIM] [TFSI] at 35 °C. The working electrode was a GC disc. The scan rate was 50 mV s <sup>-1</sup> . ....	132

Figure 6.22: Cyclic voltammogram (3 cycles) of 0.50 M AlTFSI <sub>3</sub> solution in [EMIM] [TFSI] at 35 °C. The working electrode was a Pt disc. The scan rate was 50 mV s <sup>-1</sup> . The potential of the cathodic and anodic peaks are shown in the accompanying table. ....	133
Figure 6.23: <b>a)</b> Variation in current density with temperature for the 0.50 M AlTFSI <sub>3</sub> solution in [EMIM] [TFSI] using a GC working electrode. <b>b)</b> Colour change after electrochemical characterisation experiments for the 0.50 M and 1.00 M AlTFSI <sub>3</sub> solution. ....	133
Figure 6.24: <b>a)</b> Cyclic voltammograms of 0.50 M AlTFSI <sub>3</sub> solution in [EMIM] [TFSI] at 50 °C using different potential scan rates between 0.01 and 0.50 V s <sup>-1</sup> . The working electrode was a GC disc. <b>b)</b> Corresponding cathodic peak current of C1 as a function of scan rate. ....	134
Figure 6.25: <b>a)</b> Chronoamperograms of 0.50 M AlTFSI <sub>3</sub> solutions obtained with a GC disc electrode and potential steps of -0.1 V; <b>b)</b> respective variation of the current density with t <sup>-1/2</sup> . ....	134
Figure 6.26: SEM micrographs (low magnification) of films electrodeposited from 0.05 M AgTFSI solution at 35 °C. Deposition potential: -0.2 and -0.5 V. Deposition time: 900, 1800 and 3600 s. ....	136
Figure 6.27: SEM micrographs (high magnification) of films electrodeposited from 0.05 M AgTFSI solution at 35 °C. Deposition potential: -0.2 and -0.5 V. Deposition time: 900, 1800 and 3600 s. ....	137
Figure 6.28: SEM micrographs (low magnification) of films electrodeposited from 0.05 M AgTFSI solution at 50 °C. Deposition potential: -0.2 and -0.4 V. Deposition time: 900, 1800 and 3600 s. ....	138
Figure 6.29: SEM micrographs (high magnification) of films electrodeposited from 0.05 M AgTFSI solution at 50 °C. Deposition potential: -0.2 and -0.4 V. Deposition time: 900, 1800 and 3600 s. ....	139
Figure 6.30: SEM micrographs of films electrodeposited from 0.05 M AgTFSI solution at 85 °C and -0.2 V. ....	140
Figure 6.31: SEM micrographs (low magnification) of films electrodeposited from 0.05 M CuTFSI <sub>2</sub> solution at 35 °C. Deposition potentials: -0.7 and -1.7 V. Deposition times: 900, 1800 and 3600 s. ....	142
Figure 6.32: SEM micrographs (high magnification) of films electrodeposited from 0.05 M CuTFSI <sub>2</sub> solution at 35 °C. Deposition potentials: -0.7 and -1.7 V. Deposition times: 900, 1800 and 3600 s. ....	143
Figure 6.33: SEM micrographs (low magnification) of films electrodeposited from 0.05 M CuTFSI <sub>2</sub> solution at 50 °C. Deposition potentials: -0.7 and -1.7 V. Deposition times: 900, 1800 and 3600 s. ....	144
Figure 6.34: SEM micrographs (high magnification) of films electrodeposited from 0.05 M CuTFSI <sub>2</sub> solution at 50 °C. Deposition potentials: -0.7 and -1.7 V. Deposition times: 900, 1800 and 3600 s. ....	145

Figure 6.35: SEM micrographs (low magnification) of films electrodeposited from 0.05 M CuTFSI <sub>2</sub> solution at 85 °C. Deposition potentials: -0.7 and -1.7 V. Deposition times: 900, 1800 and 3600 s. ....	147
Figure 6.36: SEM micrographs (high magnification) of films electrodeposited from 0.05 M CuTFSI <sub>2</sub> solution at 85 °C. Deposition potentials: -0.7 and -1.7 V. Deposition times: 900, 1800 and 3600 s. ....	148
Figure 6.37: <b>a)</b> EDX analysis of silver film deposited from 0.05 M AgTFSI solution at 50 °C, -0.4 V and 3600 s. <b>b)</b> SEM image of the site where the spectrum was collected. ....	149
Figure 6.38: <b>a)</b> EDX analysis of a copper film deposited from 0.05 M CuTFSI <sub>2</sub> solution at 35 °C, -0.7 V for 3600 s. <b>b)</b> TEM image of the site where the spectrum was collected. ....	149
Figure 6.39: <b>a)</b> EDX analysis of a copper-silver film deposited from 0.05 M CuTFSI <sub>2</sub> solution at 85 °C, -0.7 V for 3600 s. <b>b)</b> TEM image of the site where the spectrum was collected. ....	150
Figure 6.40: TEM micrographs of films electrodeposited from 0.05 M AgTFSI solution at <b>a)</b> -0.2 V for 900 s at 50 °C with <b>b)</b> the corresponding selected area diffraction pattern. ....	150
Figure 6.41: TEM micrographs of films electrodeposited from 0.05 M AgTFSI solution <b>a)</b> at -0.4 V for 3600 s at 85 °C <b>b)</b> the corresponding selected area diffraction pattern. ....	151
Figure 6.42: <b>a)</b> TEM micrographs of films electrodeposited from 0.05 M CuTFSI <sub>2</sub> solution at -0.7 V for 3600 s at 35 °C and <b>b)</b> the selected diffraction patterns. ....	151
Figure 6.43: <b>a)</b> TEM micrographs of films electrodeposited from 0.05 M CuTFSI <sub>2</sub> solution at -0.7 V for 3600 s at 85 °C and <b>b)</b> the selected diffraction patterns. ....	152
Figure 6.44: The load-displacement curves for nano-indentation tests carried out on silver films deposited at <b>a)</b> 35 °C, -0.2 V for 1800 s and <b>b)</b> 50 °C, -0.2 V for 900 s. ....	152
Figure 2.3: Structure of the solution in an electrochemical cell during an electrochemical reaction. ....	164
Figure 7.1: <b>a)</b> Structure of the copper complex in the CuCl <sub>2</sub> solutions in [EMIM] [EtSO <sub>4</sub> ] reproduced from Figure 4.17 and <b>b)</b> Structure of the silver complex in the AgTFSI solutions in [EMIM] [TFSI] reproduced from Figure 4.13. ....	165
Figure 7.2: Schematic of a combined electrochemical cell and surface enhanced Raman spectroscopy experimental setup required to probe the double layer structure near the electrode/electrolyte in ionic liquids. ....	171
Figure A1.1: Double cation-anion pair model (IP <sub>2</sub> ) for the [EMIM] [EtSO <sub>4</sub> ] ionic liquid. ....	193
Figure A1.2: Double cation-anion pair model (IP <sub>2</sub> ) for the [EMIM] [TFSI] ionic liquid. ....	193
Figure A1.3: A copper ion is bidentately coordinated by two EtSO <sub>3</sub> <sup>-</sup> anions and two EMIM cations. ....	194

Figure A1.4: A copper ion is bidentately coordinated by two  $\text{EtSO}_3^-$  anions, two chloride anions and two EMIM cations. .... 194

Figure A1.5: A silver ion is tridentately coordinated by two  $\text{TFSI}^-$  anions and two EMIM cations.  
.....195

## Lists of Tables

Table 2.1: Standard electrode potential of various metal reduction reactions [8].	11
Table 2.2: Boundary conditions for chronoamperometry.	15
Table 2.3: Melting temperature ( <b><i>T<sub>m</sub></i></b> ), glass transition temperature ( <b><i>T<sub>g</sub></i></b> ) and thermal decomposition temperature ( <b><i>T<sub>d</sub></i></b> ) for several different ionic liquids.	24
Table 2.4: The viscosity of several [EMIM] and [BMIM] based ionic liquids.	25
Table 2.5: The electrochemical window of several different EMIM based ionic liquids.	26
Table 3.1: Electrolytes used in this study.	43
Table 3.2: Colour of the copper salts used in System 1 electrolytes before and after the drying process.	44
Table 3.3: Composition of the electrolytes used in the electrochemical and electrodeposition experiments.	45
Table 3.4: Composition of the solutions used for Raman and IR spectroscopies.	45
Table 4.1: Assignment of the IR and Raman bands of pure [EMIM] [TFSI] in the 200 to 1600 cm <sup>-1</sup> range. Assignments are only given for the anion vibrational mode due to their importance in the interactions between these anions and the metal cation.	67
Table 4.2: Assignments of the vibrational bands in the 200 to 1600 cm <sup>-1</sup> region of the IR and Raman [EMIM] [EtSO <sub>4</sub> ] ionic liquid spectra.	72
Table 4.3: Main vibrational transitions involved in the Ag complex formation with TFSI anions evaluated from the structure AgTFSI+(TFSI <sup>-</sup> EMI) <sub>2</sub> calculated at the [B3LYP/6-31+G(d,p):MQZVP(S):DGDVZP(Ag)] level.	76
Table 4.4: Main vibrational transitions of the complex Cu(Cl <sub>2</sub> )-(EthOSO <sub>3</sub> <sup>-</sup> EMI)\ <sub>2</sub> calculated at the [B3LYP/ 6-31+G(d,p):MQZVP(S,Cu)] level.	85
Table 5.1: Calculated activation energy of the Cu(II) to Cu(I) reduction reaction for the three solutions.	98
Table 5.2: Diffusion coefficient of the copper species in the three EMIM-EtSO <sub>4</sub> solutions calculated from chronoamperometry data.	99
Table 5.3: Summary of the electrodeposition results obtained under different experimental conditions.	100
Table 6.1: Diffusion coefficient of the silver species in [EMIM] [TFSI] solutions calculated from chronoamperometry data.	125
Table 6.2: Diffusion coefficient of the copper species in [EMIM] [TFSI] solutions calculated from chronoamperometry data.	132



Table A1.1: Assignments of the vibrational bands of [EMIM] [EtSO <sub>4</sub> ] in the 200 to 1600 cm <sup>-1</sup> region obtained from the experimental IR and Raman spectra in conjunction with the theoretical DFT calculated spectra based on the structure in Figure A1.1. ....	196
Table A1.2: Assignments of the vibrational bands of [EMIM] [EtSO <sub>4</sub> ] in the 2700-3200 cm <sup>-1</sup> C-H region obtained from the experimental IR and Raman spectra in conjunction with the anharmonic calculation of the spectra using DFT calculation, based on the structure in Figure A1.1. ....	197
Table A1.3: Assignments of the vibrational bands of [EMIM] [TFSI] in the 200 to 1600 cm <sup>-1</sup> region obtained from the experimental IR and Raman spectra in conjunction with the theoretical DFT calculated spectra based on the structure in Figure A1.2. ....	198
Table A1.4: Assignments of the vibrational bands of [EMIM] [EtSO <sub>4</sub> ] + CuCl <sub>2</sub> solution in the 200 to 1600 cm <sup>-1</sup> region obtained from the experimental IR and Raman spectra in conjunction with the theoretical spectra calculated using DFT calculation based on the structure in Figure A1.4. ....	200
Table A1.5: Assignments of the vibrational bands of [EMIM] [EtSO <sub>4</sub> ] + CuCl <sub>2</sub> solution in the 2700-3200 cm <sup>-1</sup> C-H region obtained from the experimental IR and Raman spectra in conjunction with DFT calculation based on the structure in Figure A1.4. ....	202
Table A1.6: Assignments of the vibrational bands of [EMIM] [TFSI] + AgTFSI solution in the 200 to 1600 cm <sup>-1</sup> region obtained from the experimental IR and Raman spectra in conjunction with the theoretical spectra calculated using DFT calculation based on the structure in Figure A1.5. ....	203

## Table of Contents

Acknowledgements.....	vii
List of Symbols .....	ix
Acronyms and abbreviations .....	xii
Ionic liquid abbreviations.....	xiii
Physical constants .....	xiv
Lists of Figures.....	xv
Lists of Tables.....	xxv
1 Introduction and Objective .....	1
2 Backgrounds, Principles and Bibliographic Review.....	5
2.1 History and challenges of electrodeposition .....	5
2.2 Basic principle of electrodeposition.....	6
2.2.1 Faraday's law of electrolysis .....	8
2.2.2 Structure and mechanism during an electrochemical reaction.....	9
2.2.3 Thermodynamics of the electrochemical reaction .....	10
2.2.4 Kinetics of the electrochemical reaction .....	12
2.2.5 Mass transport in the electrolyte .....	14
2.2.6 Electrolyte double-layer region .....	17
2.3 Limitations of water-based electrodeposition.....	18
2.4 What is an Ionic liquid?.....	20
2.4.1 First-generation ionic liquid .....	20
2.4.2 Second-generation ionic liquid .....	21
2.5 Properties of ionic liquids .....	22
2.5.1 Thermal properties .....	22
2.5.2 Viscosity .....	25
2.5.3 Electrochemical properties .....	26
2.6 Electrodeposition from ionic liquids .....	26
2.6.1 Silver.....	27
2.6.2 Copper.....	29
2.6.3 Aluminium.....	30
2.7 Basic principle of spectroscopy.....	32
2.7.1 What is electromagnetic radiation?.....	32
2.7.2 Energy states in matter .....	34

2.7.3	Normal modes of molecular vibrations .....	35
2.7.4	Interaction between electromagnetic radiation and matter.....	36
2.7.5	Infrared and Raman Spectroscopies .....	38
2.7.6	Interpretation of IR and Raman spectra: Complicating factors .....	39
2.8	Structural characterisation of ionic liquid.....	40
3	Materials and Experimental Methods .....	43
3.1	Experimental materials .....	43
3.2	Environmental control .....	43
3.3	Preparation of the materials.....	44
3.3.1	Metallic salts preparation .....	44
3.3.2	Solution preparation .....	44
3.4	Electrochemical characterisation of the solution .....	46
3.4.1	Cyclic voltammetry.....	47
3.4.2	Chronoamperometry .....	50
3.5	Electrodeposition experiments.....	51
3.5.1	Pre-electrodeposition substrate treatment.....	51
3.5.2	Electrodeposition experimental parameters .....	52
3.5.3	Post-electrodeposition film treatment .....	52
3.6	Characterisation of the films.....	52
3.6.1	Scanning electron microscope (SEM).....	52
3.6.2	Transmission electron microscope (TEM).....	55
3.6.3	Glancing angle X-ray Diffraction (GA-XRD) .....	57
3.6.4	Nano-indentation.....	58
3.7	Structural characterisation of the solution .....	60
3.7.1	Fourier transformed infrared (IR) spectroscopy .....	60
3.7.2	Raman spectroscopy .....	61
4	Vibrational Spectroscopy of Ionic Liquid-based Electrolytes.....	63
4.1	[EMIM] [TFSI] ionic liquid system .....	63
4.1.1	Raman and infrared spectra of pure [EMIM] [TFSI].....	63
4.1.2	Raman and IR spectra of [EMIM] [TFSI] solutions .....	67
4.2	[EMIM] [EtSO <sub>4</sub> ] ionic liquid system .....	69
4.2.1	Infrared and Raman spectra of pure [EMIM] [EtSO <sub>4</sub> ] .....	69
4.2.2	IR and Raman spectra of [EMIM] [EtSO <sub>4</sub> ] solution.....	72
4.3	Discussion of the results .....	74

4.3.1	Modelling the Vibrational Spectra of the metal complexes .....	74
4.3.2	Vibrational Analysis of the Spectra (AgTFSI/[EMIM] [TFSI] solution) .....	74
4.3.4	Vibrational Analysis of the Spectra of the solutions CuCl <sub>2</sub> /[EMIM] [EtSO <sub>4</sub> ] .....	80
4.4	Summary .....	86
5	Electrochemical Results of EMIM EtSO <sub>4</sub> -based Electrolytes.....	87
5.1	Electrochemical stability window of the [EMIM] [EtSO <sub>4</sub> ] ionic liquid.....	87
5.2	Electrochemical characterisation of the electrolyte solutions .....	88
5.2.1	Cyclic voltammograms of the [EMIM] [EtSO <sub>4</sub> ] solutions .....	88
5.2.2	Mechanism of the electrochemical reaction .....	93
5.2.3	Stability of the solutions .....	94
5.2.4	Activation Energy of Cu(II) to Cu(I) .....	97
5.2.5	Diffusion Coefficient .....	98
5.3	Electrodeposition .....	100
5.3.1	Microstructure of the films.....	100
5.3.2	Synthesis of the film microstructure observations.....	112
5.3.3	Current Efficiency.....	113
5.3.4	Composition of the film .....	113
5.4	Summary .....	115
6	Electrochemical Results of EMIM TFSI-based Electrolytes .....	117
6.1	Electrochemical window of [EMIM] [TFSI] ionic liquid .....	117
6.2	Electrochemical characterisation of the electrolyte solutions .....	118
6.2.1	Cyclic Voltammogram of AgTFSI in [EMIM] [TFSI] solution .....	118
6.2.2	Cyclic Voltammogram of CuTFSI <sub>2</sub> in [EMIM] [TFSI] solution.....	125
6.2.3	Cyclic Voltammogram of AlTFSI <sub>3</sub> in [EMIM] [TFSI] solution.....	132
6.3	Electrodeposition .....	135
6.3.1	Microstructure of the films.....	135
6.4	Chemical analysis of the films.....	149
6.5	Mechanical properties of the films.....	152
6.6	Summary .....	153
7	Discussion.....	155
7.1	Suitability of the electrodeposition solvents .....	155
7.1.1	Electrochemical window .....	155
7.1.2	Solubility of the metal salts.....	155
7.1.3	Mobility of the ionic species .....	157

7.1.4	Stability of the solution .....	158
7.1.5	Morphology of the films .....	161
7.1.6	Summary .....	163
7.2	Complex formation in the ionic liquid electrolytes.....	164
7.2.1	Effect of the complexes on the deposition mechanism .....	164
7.2.2	Structure of the metal complexes .....	165
7.2.3	Stability of the complexes.....	167
7.2.4	Summary .....	170
7.3	Future works .....	171
8	Conclusion.....	173
9	References .....	177
1	Annex 1 .....	193
1.1	Density Functional Theory (DFT) calculations.....	193
1.2	Full assignment .....	196
1.2.1	Pure [EMIM] [EtSO <sub>4</sub> ].....	196
1.2.2	Pure [EMIM] [TFSI] .....	198
1.2.3	[EMIM] [EtSO <sub>4</sub> ] + CuCl <sub>2</sub> solution.....	200
1.2.4	[EMIM] [TFSI] + AgTFSI solution.....	203

# 1 Introduction and Objective

Electrodeposition currently occupies a niche position in industry, mainly in the plating of metals for aesthetic purposes and for corrosion resistance applications. The main electrolytes used in industry are aqueous solutions, but these solutions are technologically limited due to the evolution of hydrogen gas during film formation, adversely affecting the film morphology and properties [10]. These drawbacks have so far limited the use of electrodeposition for high-tech applications. When a film with a well-defined microstructure and properties is needed, the main deposition techniques used are chemical vapour deposition (CVD) and physical vapour deposition (PVD). An example is the creation of high quality functional thin films used to make integrated circuits in the microelectronic industry.

Electrodeposition has the potential to create these functional thin films more cheaply than the CVD and PVD techniques. To realise this potential, investigations have been carried out to find a solvent with superior electrochemical properties capable of replacing water. Some of the most promising candidates investigated are ionic liquids, which are a class of salts that exist as a liquid at room temperature. Ionic liquids have a large potential window and zero vapour pressure, thus they can be used to create high quality films that do not suffer from gas embrittlement, unlike films deposited from aqueous solution [10]. Moreover, they are non-volatile and non-flammable [10]. Besides that, a wide range of possible ionic liquids may be created from the various cations and anions, allowing them to be designed and tailored for specific applications [10,24]. Hence, ionic liquids can be designed to be non-toxic, recyclable and reusable, consequently saving on cost as well as reducing pollution to the environment.

The potentials of ionic liquids in the field of electrodeposition have been shown from studies reported in the literature. One of the best examples which shows the accurate control of electrodeposition on the microstructure and grain size of the film is a study carried out by Al-Salman et al [1]. The authors electrodeposited germanium-silicon semiconductors and demonstrated that the range of particle size can be accurately controlled by varying the deposition potential. As a consequence, the colour of the films changed, which clearly illustrated the photoluminescence effect (Figure 1.1), making their films suitable for optical applications. The large electrochemical windows as well as narrower range of deposition potentials between different metals in ionic liquids allow for the deposition of alloy films, which is not possible in aqueous solutions. An example of this is the titanium-aluminium film deposited by Pradhan et al. [2] (Figure 1.2 a). Besides smooth and compact films, electrodeposition from ionic liquids can also be used to make three-dimensional film structures. This is shown by Hsieh et al. [3] who electrodeposited copper-tin hexagonal tubes (Figure 1.2 b). The structure of the films can also be manipulated by using templates. Nanowires can be created by electrodeposition using polycarbonate or alumina templates, followed by etching of the templates, for example, the aluminium nanowires created by El Abedin et al. [4] (Figure 1.3 a). Similarly, three-dimensional ordered macro-porous nanostructures can be created by electrodeposition by using polycarbonate spheres followed by etching of the spheres. An example of this is the inversed opal structure of germanium obtained by Meng et al. [5] (Figure 1.3 b).

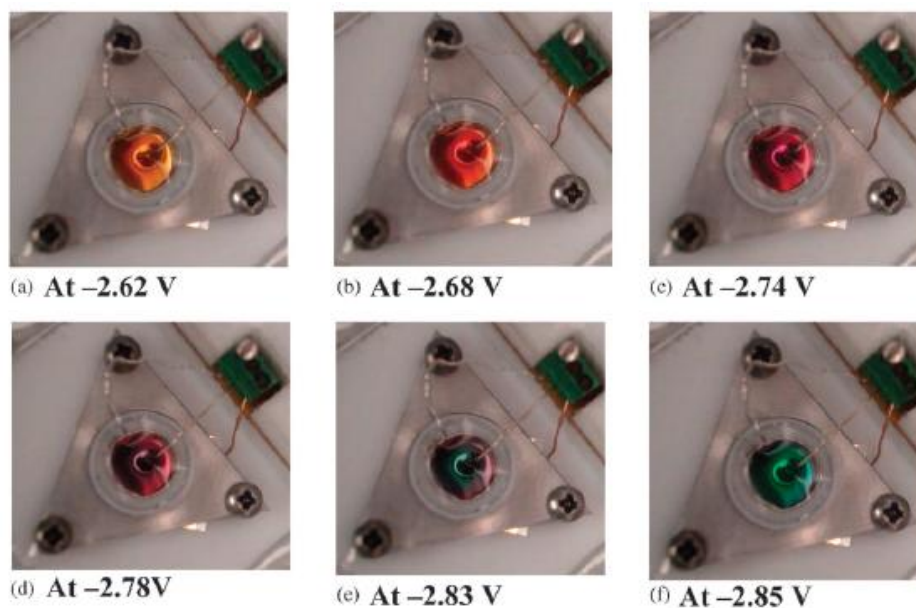


Figure 1.1: Photoluminescent semiconductors of  $\text{Ge}_x\text{Si}_{1-x}$  deposited from ionic liquids. [1].

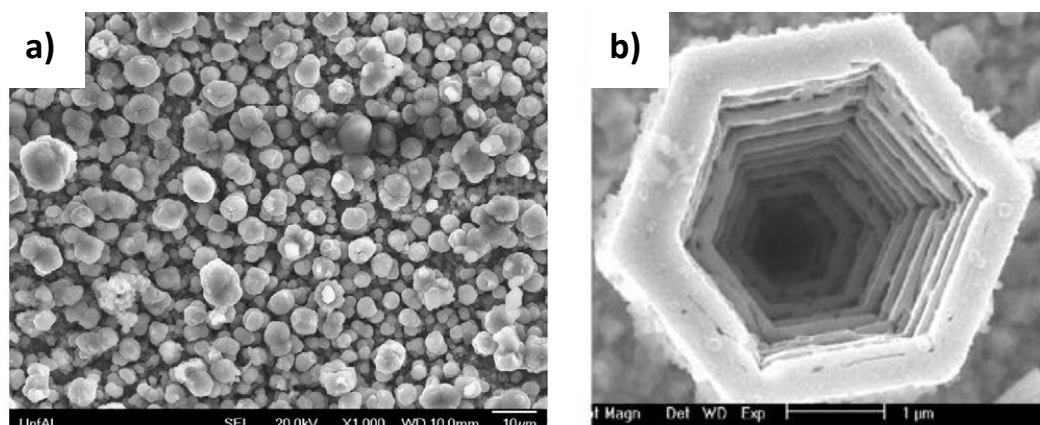


Figure 1.2: **a)** SEM micrographs of Ti-Al alloy deposits at 70 °C by using a deposition potential of -2.5 V [2]. **b)** Template-free electrodeposition of hexagonal CuSn tubes [3].

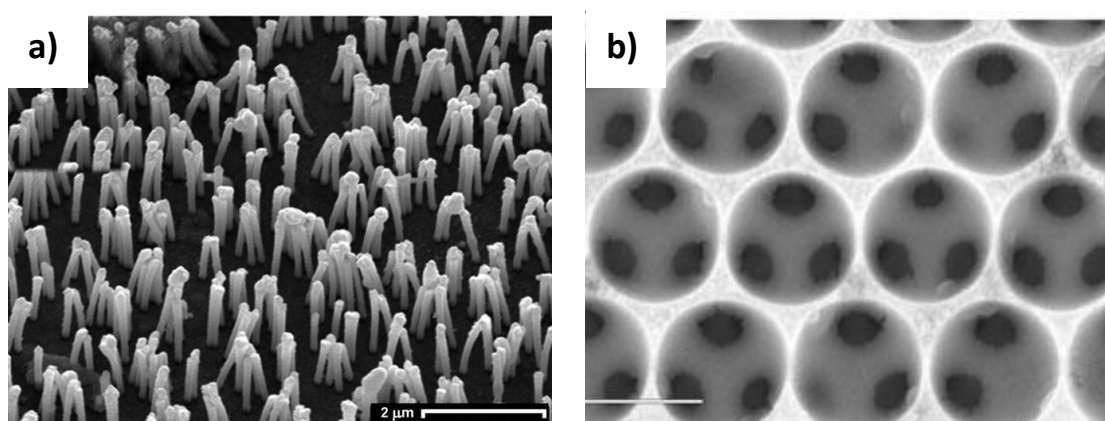


Figure 1.3: **a)** SEM micrographs of free-standing aluminium nanowires obtained by electrodeposition with a polycarbonate template [4]. **b)** Inversed opal structure of germanium obtained after applying a constant potential of -1.7 V from [EMIM] [TFSI] [5].

However, electrodeposition from an ionic liquid solution (or any other solvent) is currently an inexact science. This is not an insult to the known laws existing in electrochemistry, many of which are very exact and theoretically rigorous. The main reason lies in the large gap between fundamental knowledge and industrial practice still existing in this field. Electrodeposition experiments to create new coatings from ionic liquids are easy to do; and many of them have been done over the last two decades. In contrast, experiments to probe the underlying mechanism for electrodeposition are much harder to perform and analyse, and not many of these have been carried out. This leaves many gaps between high level theory and practical experiment, as discussed in many existing electrochemistry books [25,6,10]. The biggest of these is the complete lack of knowledge of the structure of the ionic liquid electrolyte, both in the bulk solution and near the solution-substrate interface and how these structures affect the morphology of the films. Other smaller gaps include the nucleation and growth mechanism of the films, mass transport mechanism in solution, diffusion and adsorption mechanism on the substrate.

The main objective for this study is to explore the factors affecting the morphology and properties of the thin film electrodeposited from ionic liquid. The ionic liquids used are 1-ethyl-3-methyl imidazolium [EMIM]-based ionic liquid of 1-ethyl-3-methyl imidazolium bis(trifluoromethylsulfonyl)imide, [EMIM] [TFSI] and 1-ethyl-3-methyl imidazolium ethylsulphate, [EMIM] [EtSO<sub>4</sub>]. Deposited films of copper and silver were obtained and their morphologies and properties were studied. Electrochemical studies on the electrolyte solutions were performed to determine their electrochemical properties. Additionally, vibrational analyses of the bulk electrolyte solutions were performed to give a better understanding of the complex formation.

With this study, we hope to slightly narrow the existing knowledge gap in electrodeposition. When a complete theory is completed in the future, the ideal goal is that the exact properties of functional films can be predicted just from knowing the properties of the starting materials. Even if this lofty goal is never achieved, we hope that at least a more systematic approach will be used to choose the starting materials, in contrast to the current shooting-in-the-dark approach.





## 2 Backgrounds, Principles and Bibliographic Review

### 2.1 History and challenges of electrodeposition

The history of electrodeposition can be first traced back to the invention of the Voltaic pile by Alessandro Volta in the 1790's. The pile consisted of repeating pairs of copper and zinc plates, each pair separated by a pad soaked in aqueous electrolyte. For the first time in history, the Voltaic pile allowed the creation of low voltage continuous current, making it the world first electric battery. The first electrodeposition experiment was performed in 1805 by a colleague of Volta at the University of Pavia, Professor Luigi Brugnatelli [26]. He electrodeposited gold on a silver substrate with what is now known as the electrochemical cell, which he described in his correspondence with Brussels on how he "recently gilt in a perfect manner two large silver medals, by bringing them into communication, by means of a steel wire, with the negative pole of a Voltaic pile, and keeping them, one after the other, immersed in ammoniuret of gold newly made and well saturated" [26]. This process was later improved by an English doctor by the name of John Wright, who discovered that potassium cyanide was an excellent electrolyte for the electroplating of gold and silver. This improvement also allowed the creation of thicker and more adherent films [26,10]. This discovery paved the way for the first commercialisation of the electrodeposition process when Henry and George Richard Elkington bought the rights to John Wright's process for 300 pound. The Elkingtons applied the electrodeposition process to the gilding of jewellery and other decorative items, thereby creating a successful monopoly over the electroplating industry for many years. By the 1850's, electrodeposition was expanded to include metals other than silver and gold, and commercial deposition of the so-called non decorative metals such as nickel, brass, tin and zinc.

With the rise of the industrial age, the electrodeposition process was widely used across different industries [10]. The main types of metals deposited were Cr, Ni, Cu, Au, Ag, Zn and Cd. Presently, electrodeposition processes in industry are almost exclusively based on aqueous solutions. Electrodeposition processes used in industries can be placed into four main groups: Electrowinning, electrorefining, electroforming and electroplating. Electrowinning is the extraction of metals by electrodeposition from their ores in molten or solution form. A famous example of this is the extraction of aluminium using the Hall-Héroult process. Electrorefining is the purification of metals by electrolysis, where the impure metal is used as the anode and the refined metal is deposited on the cathode. The applications of electrorefining are: to obtain metal of very high purity, to recycle metals from waste products and to remove toxic metals from waste products before disposal. Electroforming is the production of thin metal parts by electrodeposition. Electroplating is the deposition of thin films and coatings on a substrate without modifying the properties of the bulk material. The main applications are surface finishes aesthetics and protection of corrosion and wear. Although the application of electrodeposition increased over time, very little has changed in the actual physical process of electrodeposition since its invention.

The impetus for change only occurred with the rise of the electronic industry, where new sets of challenges could not be met by using existing deposition technologies. The electronic industry requires the use of many exotic metals and alloys, many of which cannot be deposited by using current electrodeposition technology based on aqueous electrolytes. As electronic components get smaller and become more complex in architectural design, there is a greater need for an electrodeposition process that has better control over the dimension, structure and properties of

the coatings [10]. There is also an increasing awareness of the pollution and toxicity of existing electrolyte baths, the need for stricter control over hazardous materials and a stronger drive to develop greener and more environmentally friendly process [10].

In response to these new challenges, many new types of deposition processes and materials have been proposed and studied. Currently, the most widely used deposition processes to overcome these problems are physical and chemical vapour deposition (PVD and CVD). They can be used to deposit many different types of metals and alloys. In addition, they allow the deposition of metals on most substrates and are less harmful to the environment. Although they can solve many of the above problems, these processes cannot be used to deposit thick coatings. Furthermore, they require a very high capital investment, consequently they are only used in high value- added niche applications.

In this study, we seek to solve this problem through the electrodeposition of metals and alloys by using ionic liquid based electrolytes. Studies on electrodeposition from ionic liquids have been intensifying in the last 15 years. In this chapter, we will discuss the limitations of current deposition technologies, properties of ionic liquids and their solutions and we will analyse the state of the art of electrodeposition from ionic liquid-based electrolytes.

## 2.2 Basic principle of electrodeposition

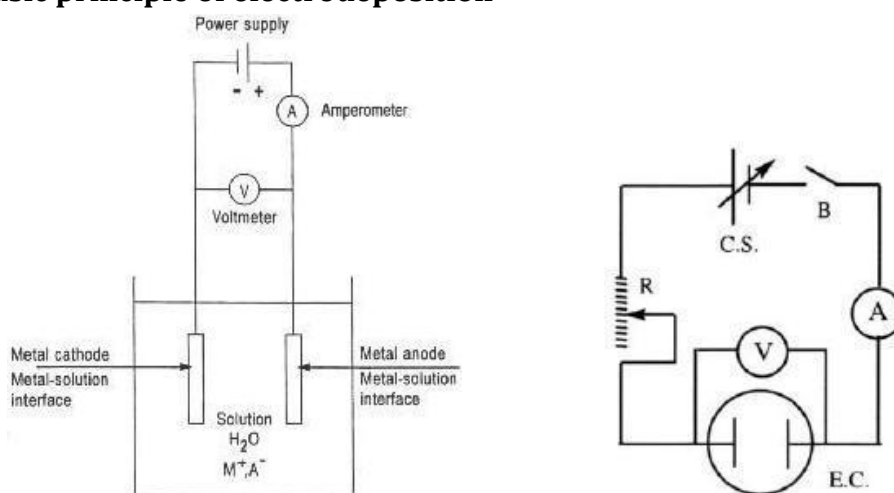


Figure 2.1: **a)** An electrochemical cell and **b)** Circuit diagram representing an electrochemical cell [6]. Where **C.S.** is the current source, **R** is an Ohmic resistance, **V** a voltmeter, **A** an ammeter, **EC** the electrochemical cell, **B** the circuit breaker.

Electrodeposition is the process of growing a metallic film onto a conductive substrate through the reduction of metal ions in an electrolyte. Electrodeposition is usually carried out by using an electrochemical cell via an electrolysis process. The cell consists of a working electrode which is the conductive substrate material that will be coated with the film and a counter electrode. Both electrodes are immersed in an electrolyte, which consists of the solute which are the metal salts and the solvent which in this study, is an ionic liquid. The two electrodes are connected to an external power supply which can be used to change the deposition potential. The electrochemical cell can also be represented by a circuit diagram. There are two parts to the electrochemical circuit: The

metallic conductor which carries the charge by free conducting electrons and the ionic conductor where the charge is conducted by ions in solution.

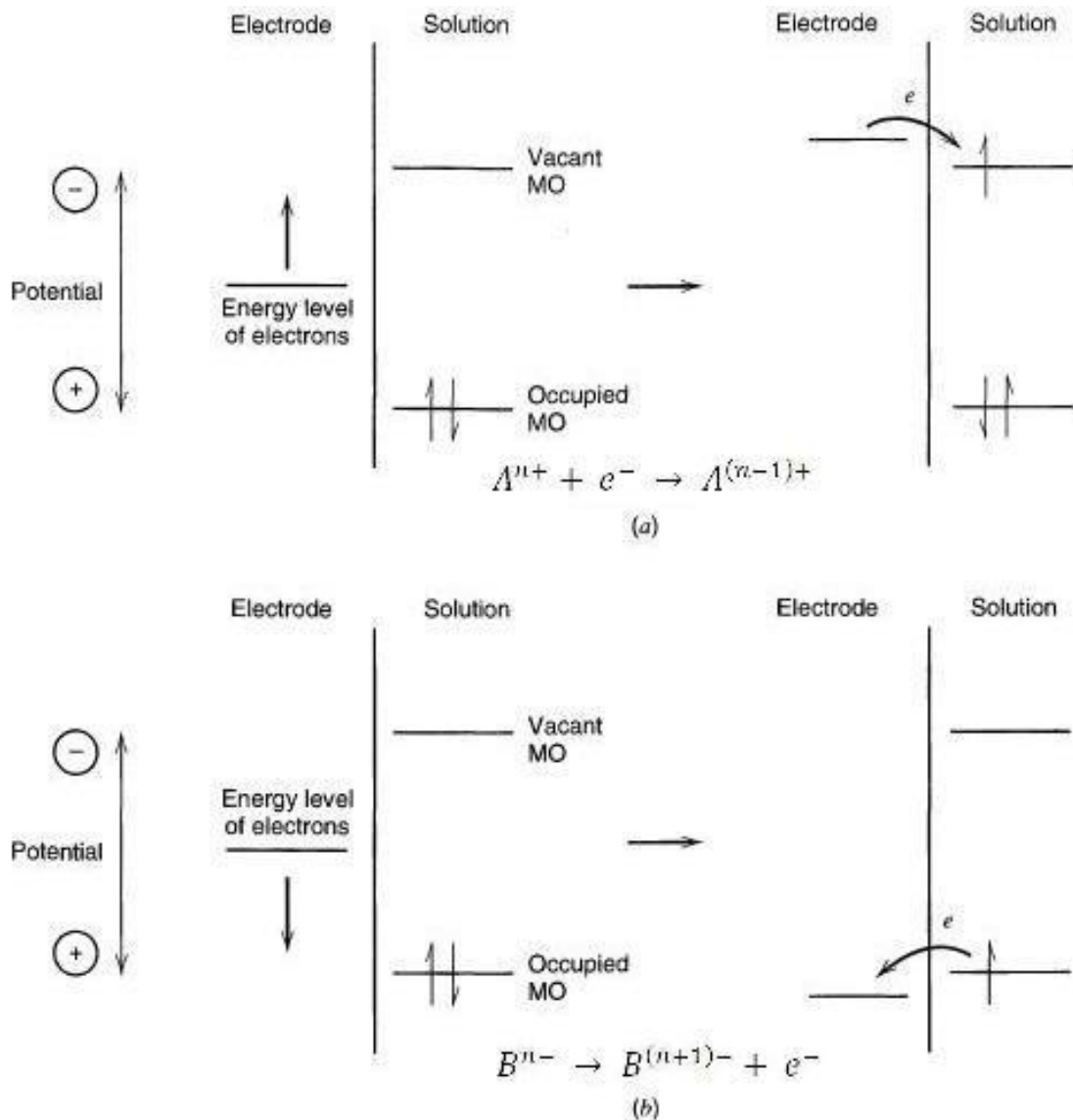


Figure 2.2: Relationship between the energy levels of the electron and the molecular levels in the ions in solution during **a)** reduction and **b)** oxidation reaction [7].

When a potential difference is applied across the circuit, the electrons will flow from the higher potential (negative pole) to the lower potential (positive pole) of the circuit. In the first part of the metallic conductor connected to the negative pole of the power supply, free conduction electrons will flow until they reach the cathode surface. The electrons build up at the surface of the cathode, which acts as an electron source. This attracts the cations in the electrolyte solution near the interface towards the surface of the cathode. For a steady current to flow through the circuit, the charge needs to go through the electrode/electrolyte interface. This involves a change in the charge carrier at the interface from the free conducting electrons in the electrode to the cations in the electrolyte. This change in charge carrier is facilitated by an electrochemical reaction known as a reduction reaction:



$A^{n+}$  are the cations in solution. This reaction only occurs if the free conduction electrons in the cathode have a high enough energy to overcome the work required to fill the vacant molecular orbital in the cations species in solution. The driving force of this reaction is the high negative potential provided by the power supply. If the negative potential is high enough, the electrons will transfer into a vacant electronic state on species in the electrolyte.

As the anode is connected to the positive pole of the power supply, electrons will be attracted to this positive pole and there is a build-up of holes near the anode surface. This attracts the anions in the electrolyte solutions near the interface towards the surface of the anode. The positive potential reduces the maximum energy of the lowest unoccupied orbital at the anode surface. If the deposition potential is high enough, the acceptance level of the anode will be lower than the lowest occupied molecular orbital in the solution, allowing the transfer of electrons from the solution to the electrode via the chemical reaction:



$B^{n-}$  are the anions in solution. The free conduction electrons will flow from the anode to the positive pole of the circuit.

Usually in electrodeposition, we are only interested in the process at either the anode or the cathode. Because of this, it is sometimes more convenient to designate the electrodes as working and counter electrodes; where the working electrode is the electrode where the process of interest occurs and the counter electrode is the electrode is where no process of interest occurs as it merely serves to carry the current flowing through the cell [27].

Instead of the electrochemical cell configuration shown in Figure 2.1, more often cells used in electrochemical studies present a three electrode setup. In a two electrode cell, it is sometimes difficult to maintain a constant potential difference between the electrodes, in particularly while passing the current.

### 2.2.1 Faraday's law of electrolysis

In Equations 2.1 and 2.2, the electrons transfer is directly proportional to the product formed. This is because all reactions involving electron transfer must obey the mass and charge conservation laws, a cornerstone of chemistry. For the specific cases where a solid metallic film is formed by electrodeposition ( $M^{n+} + ne \rightarrow M$ ), the mass of the film is related to the charge according to Faraday's Law, given by:

$$m = \frac{ItM}{nF} \eta \quad \text{Eq. 2.3}$$

$m$  is the mass of the substance deposited/liberated at an electrode,  $I$  is the current of the reaction,  $t$  is the total time the current is applied,  $n$  is the charge transfer per mole of the reaction product and  $F$  is Faraday's constant.

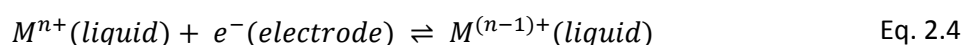
One of the practical uses of Faraday's Law is to determine the current efficiency of an electrodeposition cell,  $\eta$ . This is done by comparing the actual mass of product deposited in the

experiment with the theoretical mass value calculated from the total charge that flows in the experiment.

## 2.2.2 Structure and mechanism during an electrochemical reaction

In the previous sections, we described the general workings of an electrochemical cell, with only a brief explanation of the charge transfer mechanism in solution. The whole charge transfer mechanism is quite complex and it involves multiple steps. Equations 2.1 and 2.2 only describe the last step. It is important to understand these mechanism as they affect the film morphology and properties [10]. In this section, we will discuss the process starting from the solvation of the metal ions until the final stage of charge transfer.

We consider these mechanisms using as example, a single-charge transfer electrochemical reduction reaction occurring at the working electrode:



$M$  is a metal dissolved into the electrolyte from a metallic salt.

To help describe the reaction mechanism, a representation of the molecular structure in solution during an electrochemical reaction is given in Figure 2.3.

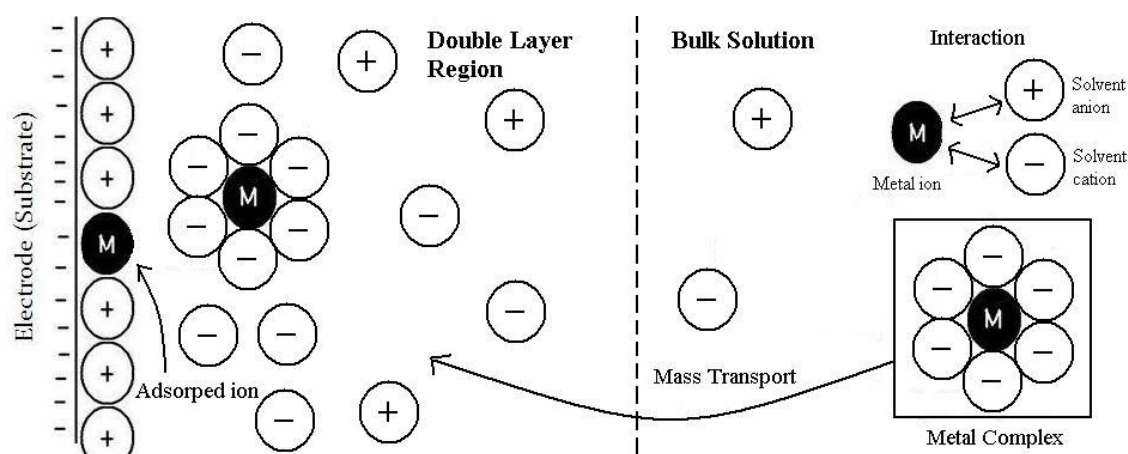


Figure 2.3: Structure of the solution in an electrochemical cell during an electrochemical reaction.

When a metal salt is added to a solvent below the solubility limit, it will be dissolved. The solubility will depend on the physical and chemical properties of both the solvent and salt. To be more specific, the two important parameters are the bond strength between the cations and anions of both the solvent and salt and the ability of the solvent ions to break the bonds between the salt ions. These parameters are affected by changes in the environment, such as temperature and pressure. At the molecular level, the metallic ions do not exist independently; rather, they are solvated by the solvent ions to form metal complexes. The metal cations will usually be the central atom coordinated by one or more ligands (usually the solvent anions) which acts as a Lewis base (donating a lone pair of electrons) [28]. Studying the metal complexes is important because they affect the electrodeposition process. A more detailed discussion can be found in Section 2.8. One of the methods to study the metal complexes is by vibrational spectroscopy, discussed in Section 2.7.

During electrodeposition, the metal complexes must be transported from the bulk solution to the electrode/electrolyte interface before any charge transfer can occur. The dominant mechanism for this mass transport is diffusion, although other mechanisms of mass transport such as convection may occur. For a spherical particle moving through a solution at low Reynolds number, the diffusion coefficient can be described by the Stokes-Einstein equation, as follows:

$$D = \frac{RT}{N_a} \frac{1}{6\pi\eta r} \quad \text{Eq. 2.5}$$

$D$  is the diffusion coefficient,  $R$  is the ideal gas constant,  $T$  is the temperature,  $N_a$  is Avogadro's number,  $\eta$  is the viscosity of the solution and  $r$  is the radius of the particle. From this relationship, we can see that the important factors affecting the rate of diffusion are the temperature of the electrolyte, the viscosity of the solution and the size of the diffusing particle. A more detailed discussion of the mass transport is given in Section 2.2.5 and the viscosities of various ionic liquids are presented in Section 2.5.2.

When the metal complex is close to the electrode/electrolyte interface, it will experience forces due to the electric field of the electrode. This causes a change to the metal complex as the metal ion is attracted to the electrode while the opposite charge ligands experience repulsive forces. Concurrently, the existing solvent ions near the electrode/electrolyte interface will also rearrange themselves due to the effect of the electric field. This structure is known as the electrolyte double-layer region and it is very different from the structure of the bulk solution. A more detailed discussion of the double-layer structure can be found in Section 2.2.6. As the metal complex approaches the electrode surface, it becomes energetically more favourable for the metal ion to dissociate from the complex and be adsorbed at the substrate. From there, the charge transfer mechanism shown in Equation 2.4 will proceed as discussed in the previous sections.

### 2.2.3 Thermodynamics of the electrochemical reaction

Thermodynamics can tell us whether a reaction such as Equation 2.4 can occur or not. This is done by calculating the free energy variation that accompanies the transformation of the reactants into the products of a reaction. If the free energy variation is negative, the products are more stable than the reactants and this provides the driving force for the reaction to occur. In electrolysis, the potentials at which electrode reactions occur are related to this free energy variation. However, measuring these potentials is tricky as the exact values are dependent on many factors such as the electrode materials, electrolyte, temperature, etc.

In order to compare the critical potentials at which the main oxidation and reduction processes occur for different ionic species, they must be compared with a standard. For electrodeposition from aqueous solutions, the reference used is known as the standard hydrogen electrode (SHE). The potentials measured relative to the SHE are known as the standard electrode potential  $E^\circ$ .

For electrode reactions in equilibrium condition, the total cell potential,  $E_{cell}$  can be calculated from the Nernst equation [8]:

$$E_{cell} = E^\circ - \frac{RT}{nF} \sum v_i \ln Q \quad \text{Eq. 2.6}$$

Similarly, the half-cell reduction potential,  $E_{red}$  is given by [8]:

$$E_{red} = E_{red}^o - \frac{RT}{nF} \sum v_i \ln \frac{a_{red}}{a_{ox}} \quad \text{Eq. 2.7}$$

$E$  is the equilibrium electrode potential,  $E^o$  is the standard electrode potential,  $R$  is the ideal gas constant,  $T$  is the absolute temperature,  $n$  is the moles of electron transferred,  $F$  is Faraday constant,  $v_i$  is the stoichiometric numbers,  $a_{red}$  is activity of the reductant,  $a_{ox}$  is activity of the oxidant and  $Q$  is the reaction quotient

In general, the electrolyte is considered an ideal solution and the activity of a species is substituted by its concentration. The activity of a species is related to its concentration by:

$$a_i = \gamma_i c_i \quad \text{Eq. 2.8}$$

$c_i$  is the concentration of species  $i$  and  $\gamma_i$  is the activity coefficient of species  $i$ . For an ideal solution  $\gamma_i = 1$ .

The Nernst equation can be rewritten in the form:

$$E = E^\phi - \frac{RT}{nF} \sum v_i \ln c_i \quad \text{Eq. 2.9}$$

$E^\phi$  is known as the formal potential.  $E^\phi$  takes into account the changes to  $E^o$  when activity is replaced by concentration [27].

For aqueous solution, the standard potential of many substances have been calculated and a few examples can be seen in Table 2.1.

Table 2.1: Standard electrode potential of various metal reduction reactions. [8].

Electrode reaction	Standard potentials, V
$\text{Li}^+ + \text{e}^- \rightarrow \text{Li}$	-3.045
$\text{K}^+ + \text{e}^- \rightarrow \text{K}$	-2.925
$\text{Mg}^{2+} + 2\text{e}^- \rightarrow \text{Mg}$	-2.363
$\text{Al}^{3+} + 3\text{e}^- \rightarrow \text{Al}$	-1.662
$\text{Zn}^{2+} + 2\text{e}^- \rightarrow \text{Zn}$	-0.763
$\text{Cr}^{3+} + 3\text{e}^- \rightarrow \text{Cr}$	-0.744
$\text{Fe}^{2+} + 2\text{e}^- \rightarrow \text{Fe}$	-0.440
$\text{Ni}^{2+} + 2\text{e}^- \rightarrow \text{Ni}$	-0.250
$\text{Cu}^{2+} + 2\text{e}^- \rightarrow \text{Cu}$	0.337
$\text{Cu}^+ + \text{e}^- \rightarrow \text{Cu}$	0.521
$\text{Ag}^+ + \text{e}^- \rightarrow \text{Ag}$	0.799
$\text{Au}^{3+} + 3\text{e}^- \rightarrow \text{Au}$	1.498
$\text{Au}^+ + \text{e}^- \rightarrow \text{Au}$	1.691

When two or more anodic and cathodic reactions are thermodynamically possible during electrodeposition, the reactions with the lowest equilibrium potential difference will, in general, take place first. This means that at the cathode, the reaction with the highest equilibrium reduction



potential will take place first, and at the anode, the reaction with the highest equilibrium oxidation potential (lowest equilibrium reduction potential) will take place first.

Knowing the equilibrium electrode potential of the half reactions for both electrodes in the electrochemical cell, the cell potential can be calculated by the difference between the equilibrium oxidation potential and the equilibrium reduction potential:

$$E_{cell} = E_{right} - E_{left} \quad \text{Eq. 2.10}$$

By convention,  $E_{right}$  is the equilibrium oxidation reaction potential and  $E_{left}$  is the equilibrium reduction reaction potential at their respective electrodes calculated from the Nernst equation.

From the cell potential, the maximum energy ( $\Delta G$ ) that can be supplied by the cell is given by:

$$\Delta G = -nFE_{cell} \quad \text{Eq. 2.11}$$

### 2.2.4 Kinetics of the electrochemical reaction

Thermodynamics only tells us half the story on whether a reaction will actually occur or not in the real world. In a reaction, the products may be energetically more stable than the reactants but the reaction still may not occur if the rate of reaction is very slow. This shows the importance of kinetics which takes into consideration the rate of the reaction.

As all electrochemical reactions are thermally activated, their rate constant varies with temperature according to an Arrhenius equation. For a first order half reaction of the form  $O + ne^- \rightarrow R$  that occurs at an electrode, the rate of the electrode reaction,  $k$ , is given by [8]:

$$k = A \exp \left[ \frac{-\Delta H^*}{RT} \right] \quad \text{Eq. 2.12}$$

$\Delta H^*$  is the activation enthalpy and  $A$  is the pre-exponential factor.

Due to the change in the ionic atmosphere around the active species during the electron transfer reaction, it is important to include the activation entropy  $\Delta S^*$ . The rate is then [8]:

$$k = A' \exp \left[ \frac{-(\Delta H^* - T\Delta S^*)}{RT} \right] \quad \text{Eq. 2.13}$$

$$k = A' \exp \left[ \frac{-\Delta G^*}{RT} \right] \quad \text{Eq. 2.14}$$

$\Delta G^*$  is the activation energy of the reaction.

When an electrode reaction,  $O + ne^- \rightleftharpoons R$  occurs in equilibrium, the forward and backward reaction rate must be equal. As the reaction is first order, we have [8]:

$$k_c[O]^* = k_a[R]^* \quad \text{Eq. 2.15}$$

$[O]^*$  and  $[R]^*$  are the concentrations of  $O$  and  $R$  very close to the electrode. If  $[O]^* = [R]^*$ , the potential is  $E^\phi$ , the formal potential.

This means that [8]:

$$k_c = k_a = k_0 \quad \text{Eq. 2.16}$$

$$k_c = k_0 \exp \left[ \frac{-\alpha_c n F (E - E^{\phi'})}{RT} \right] \quad \text{Eq. 2.17}$$

$$k_a = k_0 \exp \left[ \frac{\alpha_a n F (E - E^{\phi'})}{RT} \right] \quad \text{Eq. 2.18}$$

From this, we may obtain the Butler-Volmer equation. The electric current which controls the kinetics of the electrode reactions is proportional to the difference between the rates of the oxidation and reduction reactions at the electrode surface and is given by [8]:

$$I = A i_0 \left\{ \exp \left[ \frac{\alpha_a n F (E - E^{\phi'})}{RT} \right] - \exp \left[ \frac{-\alpha_c n F (E - E^{\phi'})}{RT} \right] \right\} \quad \text{Eq. 2.19}$$

$$I = n F A (k_a [R]_* - k_c [O]_*) \quad \text{Eq. 2.20}$$

To fully understand how the kinetics of a particular reaction is controlled, we need to know the mechanism behind it. A reaction may involve multiple steps, each of these steps occurring at a different rate. The overall reaction rate will be controlled by the step with the slowest rate, known as the rate determining step. The mechanism involved in an electrochemical reaction is shown in Figure 2.3 and discussed in Section 2.2.2. In this section, we give the rates of some of the important steps. The important steps and the mechanisms involved are shown once again as Steps 1-5 in Figure 2.4.

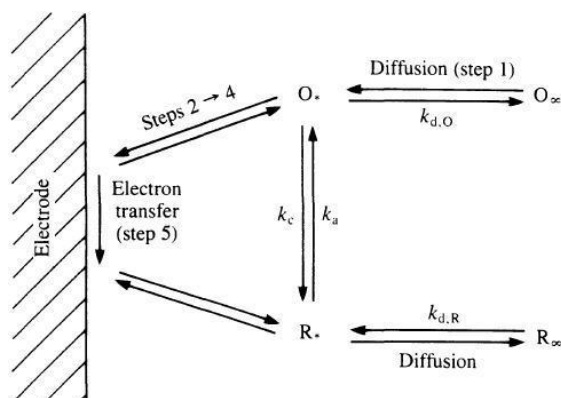


Figure 2.4: Kinetics of the oxidation and reduction reaction near the electrode/electrolyte surface [8].

Step 1 is the mass transport of metal complexes from the bulk solution to the vicinity of the working electrode/electrolyte interface. As diffusion is the main transport mechanism, the rate is mostly described by the diffusion coefficient,  $D$  and characterised by a differential kinetics constant,  $k_d$ .

Steps 2 to 4 occur in the electrode/electrolyte interface.

In step 2, the ionic species from both the solvent and solute will rearrange themselves in the presence of the electric field of the electrode. This process will be discussed in more details in the

section on the electrolyte double-layer region. This rearrangement takes about  $10^{-8}$  s, and does not significantly affect the overall kinetics.

In step 3, the solvent molecules near the electrode/electrolyte interface are affected by the electric field and interactions with other charged particles. As these molecules are often non-symmetrical and have dipole moments, they will orientate themselves to maintain charge neutrality and maintain a lower energy, more stable configuration of the liquid at the vicinity of the electrode surface. This process typically takes  $10^{-11}$  s.

In step 4, changes occur to the metal complexes when they approach the electrode. There is an increase in distance between the central  $M^{n+}$  ion and the ligands of the metal complex as  $M^{n+}$  is adsorbed onto the surface. The process takes around  $10^{-14}$  s, so its influence on the overall kinetics is also negligible

Step 5 involves the electron transfer from the electrode surface to the adsorbed  $M^{n+}$  ion, turning it into a  $M^{(n-1)+}$  ion which completes the electrochemical reaction. The electron transfer process is on the order of  $10^{-16}$  s. After step 5, the  $M^{(n-1)+}$  ion will undergo the 'reverse' process, i.e. it is desorbed from the electrode surface and transported back to the bulk solution.

As we can see from Figure 2.4, steps 2 to 5 are included in the kinetics of the electrode process,  $k_0$ . As the rate of the electron transfer process is much higher than all the other processes, the electron transfer obeys the Franck Condon principle, which postulates that the nucleus processes are much slower than the electron processes; hence, the nucleus will appear static in relation to the electron.

## 2.2.5 Mass transport in the electrolyte

In most electrodeposition experiments, the kinetics of the electrode reactions is much faster than the mass transport of the ionic species from the bulk solution to the electrode/electrolyte interface. This makes it important to understand the mass transport as it is the overall rate determining step. Knowledge of the mass transport is fundamental to understand the electrochemical and structural properties of the electrolyte as well as the factors effecting the movement of different ions in solution. There are three ways in which ions in solution can move from the bulk solution to the interface: diffusion, migration and convection.

### 2.2.5.1 Diffusion

Diffusion affects all charged and neutral species in solution. It is the most important mass transport mechanism as it is always present and many electrodeposition experiments are carried out in conditions where kinetics is diffusion controlled and other types of mass transport have a negligible effect on the overall deposition kinetics. Diffusion is due to the thermal movement of species in solution independently of an electric field. The driving force for diffusion is due to a difference in chemical potential of the species in solution, resulting from a difference in concentration of the active species. The chemical potential is related to the concentration of the active species by [8]:

$$a_i = \exp\left(\frac{\mu_i - \mu^\theta}{RT}\right) \quad \text{Eq. 2.21}$$

$a_i$  is the activity of the ionic species  $i$ ,  $\mu_i$  is the chemical potential of the ionic species in the current environment and  $\mu^0$  is the chemical potential of the ionic species in the standard state.

From Section 2.2.3, we know that the activity is the effective concentration of the ionic species and is related to concentration by Equation 2.7. Mass transport by diffusion is governed by Fick's laws, which relate the mass transport with the diffusion coefficient and concentration of the active species.

For an electrolyte in steady state, the diffusion in a one-dimensional system is described by Fick's first law, given by:

$$J_i = -D \frac{\partial c_i}{\partial x} \quad \text{Eq. 2.22}$$

$J_i$  is the flux of species  $i$  in direction  $x$ , and  $\partial c_i / \partial x$  is the concentration gradient in the same direction.  $D$  is the proportionality factor between flux and concentration gradient, known as the diffusion coefficient.

For more general cases where the concentration of the active species changes with time, diffusion is described by Fick's second law:

$$\frac{\partial c_i}{\partial t} = D \frac{\partial^2 c_i}{\partial x^2} \quad \text{Eq. 2.23}$$

So far, we have only considered diffusion in a single direction. For a three-dimensional system, the diffusion in all three directions of Euclidean space must be considered. This can be done by replacing the unidirectional term with the Laplace operator to give Fick's second law in three dimensional spaces:

$$\frac{\partial c_i}{\partial t} = D \nabla^2 c_i \quad \text{Eq. 2.24}$$

One case where Fick's second law is of paramount importance is the chronoamperometry experiment, which is used to determine the diffusion-limited current. Chronoamperometry involves a step change in the potential applied to an electrochemical cell, as described below.

Initially, a potential is applied to the solution that contains the oxidised and reduced species such that no electrode reactions occur. At  $t=0$ , the potential is stepped up to a level where the electroactive species will react. This will give rise to a change in diffusion-limited current with time. This change in potential step is shown in Figure 2.5. The boundary conditions are summarised in Table 2.2.

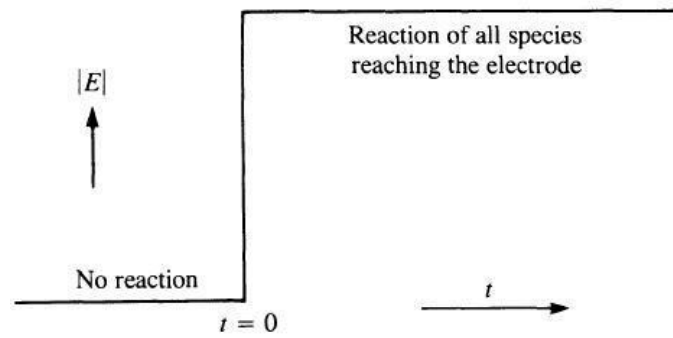


Figure 2.5: Potential step to obtain the diffusion limited current of the electroactive species [8].

Table 2.2: Boundary conditions for chronoamperometry.

$t = 0$	$c_0 = c_\infty$	no electrode reaction
$t \geq 0$	$\lim_{x \rightarrow \infty} c = c_\infty$	bulk solution
$t \geq 0, x = 0$	$c_0 = 0$	Diffusion limited current, $I_d$

$c_0$  represents the concentration at the electrode and  $c_\infty$  the concentration in bulk solution.

Solving the Equation 2.23 by considering these boundary conditions and using a planar electrode geometry, we get:

$$I(t) = \frac{nFAD^{\frac{1}{2}}c_\infty}{\pi t^{\frac{1}{2}}} \quad \text{Eq. 2.25}$$

This equation is known as Cottrell equation [8]. This equation describes the changes in current resulting from a potential step experiment over a time period. It can be used to estimate the diffusion coefficient of the ionic species in solution, which can be used to compare the mass transport rate of different ionic species.

### 2.2.5.2 Migration

Migration is the movement of charged species due to an applied electric field. The driving force for migration is the electric potential gradient that exists between the two electrodes.

In an applied electric field characterised by  $\partial\phi/\partial x$ ,

$$J_i = -D_i \frac{\partial c_i}{\partial x} - \frac{Z_i F}{RT} c_i \frac{\partial \phi}{\partial x} \quad \text{Eq. 2.26}$$

The second term on the right- hand side represents migration [8].

### 2.2.5.3 Convection

Convection is the transport of the active species in solution due to fluid flow generated by the action from external forces. Convection in an electrolyte can take two forms. The first is natural convection which is present in all solutions, arising from variations in the density due to changes in the temperature and/or solute concentration in solution.

The other type of convection is known as the forced convection. Forced convection is due to mechanical agitation or externally-induced fluid flow. An example of this is magnetic stirring using an inert magnetic bar.

#### 2.2.5.4 General equation for mass transport

Combining the effects of diffusion, migration and convection, the total mass transport in solution can be described by the Nernst-Planck equation, as follows [8]:

$$J_i(x) = -D_i \frac{\partial c_i(x)}{\partial x} - \frac{Z_i F}{RT} D_i c_i \frac{\partial \phi(x)}{\partial x} + c_i v(x) \quad \text{Eq. 2.27}$$

In a more general form:

$$J_i = -D_i \nabla c_i - \frac{Z_i F}{RT} D_i c_i \nabla \phi + c_i v \quad \text{Eq. 2.28}$$

$D$  is the diffusivity of the chemical species,  $c$  is their concentration, and  $v$  is velocity of the fluid,  $Z$  is the valence of ionic species,  $e$  is the elementary charge,  $R$  is ideal gas constant and  $T$  is temperature.

#### 2.2.6 Electrolyte double-layer region

The environment near the electrode/electrolyte interface is very different from the environment in the bulk solution. This difference in environment affects the processes that occur at the electrode/electrolyte interface, such as the adsorption of charged species, nucleation and growth of films, types of reaction that take place, electron transfer reaction, concentration of the various ionic species, arrangement of the various ionic species and diffusion of charged species from the bulk solution to the electrode/electrolyte interface. In general, a small double-layer region is preferable to reduce their effect on the various properties. Conditions that favour a small interfacial region are: i) the presence of a large quantity of inert electrolyte that does not interfere with the electrode reaction, ii) a low concentration of the electroactive species and iii) efficiency of the chosen electrolyte to conduct electric current.

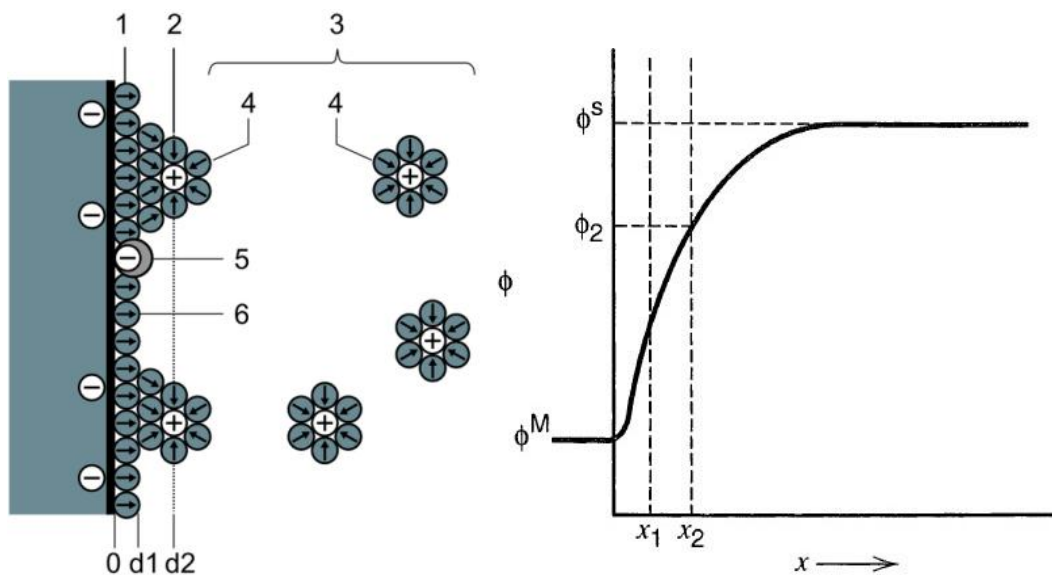


Figure 2.6: **a)** A conceptual structure of an electrolyte double-layer. (1) is the Inner Helmholtz layer (IHP), (2) Outer Helmholtz layer (OHP), (3) Diffuse layer, (4) Solvated ions, (5) Specifically adsorbed ions and (6) Solvent molecule [9]. **b)** Change in the electrostatic potential between the interfacial region and bulk solution [8].

In the interfacial region, the electrostatic potential,  $\phi$ , is different from that in the bulk solution. The change in electrostatic potential at the vicinity of the electrode is shown in Figure 2.6 **b**. This difference in electrostatic potential results in a strong interaction between ionic species and molecule in solution near the interfacial region. The conceptual structure of the electric double-layer is shown in Figure 2.6 **a**. In order to neutralise the electrostatic charge on the electrode surface, ionic species of positive or negative charge arrange themselves in ordered stacking of alternating layers of the opposite charges, which is known as the double-layer.

One of the models proposed to explain the structure of the double-layer is the Helmholtz model [29]. According to this model, the layer closest to the electrode, known as the compact, Stern or inner Helmholtz layer is composed of solvent molecules and other ionic or molecular species that are specifically adsorbed on the electrode surface. An ion is considered to be specifically adsorbed when the short range interaction between it and the interfacial layer becomes important, usually when in contact with the substrate surface, but not necessarily [27]. The locus of the electrical centres of the specifically adsorbed ions is called the inner Helmholtz plane (IHP). The solvated ions (metal complex) cannot enter the IHP. The locus of centres of the solvated ions nearest to the substrate is called the outer Helmholtz plane (OHP). The interaction of the solvated ions with the charged metal cations involves only long-range electrostatic forces, so their interaction is essentially independent of the chemical properties of the ions. These ions are said to be non-specifically adsorbed [27]. Because of thermal agitation in the solution, the non-specifically adsorbed ions are distributed in a three-dimensional region called the diffuse layer, which extends from the OHP to the bulk of the solution.

This model of the interface is analogous to a parallel-plate capacitor, where one plate is the electrode/electrolyte surface and the other plate is formed by the ionic species of opposite charge from solution. By analogy with a capacitor, the capacity would be:

$$C = \frac{q}{E} \quad \text{Eq. 2.29}$$

$q$  is the charge stored in the capacitor (in coulombs, **C**),  $E$  is the potential across the capacitor (in volts, **V**), and **C** is its capacitance (in farads, **F**).

One of the methods to probe the structure of the electrolyte double-layer region as well as the general bulk solution is by spectroscopy. The basic principles of spectroscopy are presented in Section 2.7 and the structural characterisation of the electrolyte is discussed in Section 2.8.

## 2.3 Limitations of water-based electrodeposition

Throughout the history of electrodeposition, electroplating from water-based electrolyte has been the dominant process in industry [10]. Aqueous solutions have many advantages that made them good electrolytes for electrodeposition. These advantages include:

- Low cost
- Non-flammable
- High solubility of electrolytes
- High conductivity
- High solubility of metal salts
- High rate of mass transfer

Despite their popularity, aqueous solvents suffer from several major drawbacks, which limit their application. One of their main disadvantages is the small electrochemical window of water (around 1.23 V). This means that many technologically important reactive metals cannot be electrodeposited from aqueous solutions as water will breakdown before the difference in potential is high enough to provide the driving force for the desired reduction reaction. Another major disadvantage of aqueous solutions is the gas evolution at the electrodes. At the cathode hydrogen gas evolves due to the reduction reaction  $2\text{H}^+ + 2\text{e}^- \rightarrow \text{H}_2(\text{g})$ , while oxygen gas evolves at the anode due to the oxidation reaction  $2\text{H}_2\text{O}(\text{l}) \rightarrow \text{O}_2(\text{g}) + 4\text{H}^+ + 4\text{e}^-$ . This gas evolution leads to the incorporation of bubbles in the film during deposition, leading to porosity in the films and poor mechanical properties. An example of this is hydrogen embrittlement. Moreover, many types of aqueous electrolytes include toxic agents such as cyanides in their composition in order to increase the deposition efficiency or to change the metallic complex in solution to improve the properties of the deposited films. These complexing agents are difficult to dispose of, are toxic and have negative impacts on the environment.

With the advent of the electronic age, there is a need for better and more refined control over the electrodeposition process in order to create coatings with exact properties and well-defined microstructures. The development of many new types of electronic and opto-electronic devices also requires the use of new types of exotic and rare earth metals, alloys and semiconductors, many of which cannot be deposited by current electrodeposition technologies. Tighter regulation and better awareness of the effect of chemicals on the environment and health of the population also drives a need for cleaner and greener deposition technologies to replace the existing processes based on aqueous solutions. Another major driver for better electrodeposition technology is the increasing demand to deposit refractory metals which have excellent thermal and corrosion resistance properties, such as titanium, aluminium and tungsten. However, electrodepositions of these metals are difficult due to passivation as their oxides are extremely stable.

Among the new types of solvents considered for these new electrodeposition methods are ionic liquids. They are superior to aqueous solutions due to their wide electrochemical windows (4.0 to 4.5 V for the [EMIM]-based ionic liquids used in the present study) that allows the deposition of a wide range of reactive metals, including water reactive metals such as magnesium. Ionic liquids have high thermal stability and zero vapour pressure, which ensures a higher quality coating as they do not suffer from hydrogen embrittlement [10]. Deposition potentials of metals are also much closer in ionic liquids, thereby making alloy deposition possible [10]. Besides that, the ionic liquids can be tailored to make them more environmentally friendly, thus removing the need for toxic baths [10]. This also makes them easier to recover and recycle [10]. The main drawback of ionic liquid is their greater cost compared to aqueous solution. However, thin film deposition from ionic liquids can potentially be cheaper than alternative thin film deposition techniques, such as chemical vapour deposition (CVD) and physical vapour deposition (PVD) [10].



## 2.4 What is an Ionic liquid?

An ionic liquid can be roughly defined as an ionic material that exists as a liquid at an unusually low temperature, generally accepted by consensus to be around 100 °C or below [10]. The 100 °C cut-off point was probably chosen because some of the earliest discovered ionic liquids have melting points close to this temperature and this value is easily recognisable as it is also the boiling point of water. In this regard, one can think of ionic liquids as a class of molten salts. Historically, the term ionic liquid was coined in order to distinguish them from inorganic molten salts with high melting temperatures. The high melting temperature of inorganic salts requires large energy consumption to keep the salts in liquid form, thus limiting their application in electrodeposition due to the high cost involved in such operations. Ionic liquids have no such limitations, thereby opening up many new potential applications.

### 2.4.1 First-generation ionic liquid

Historically, ionic liquids have been classified into first- and second-generation ionic liquids [10]. First-generation ionic liquids are usually mixtures of two different salt compounds which contain a haloaluminate ( $\text{Al X}_3$ , where  $\text{X} = \text{Cl, Br, I}$ ) based anion and their mixture form a eutectic system. For this class of ionic liquids, the melting point depends on the composition ratio of two compounds. At a certain composition, there exists a minimum melting point at which both compounds will simultaneously melt from their solid phases, forming a homogeneous liquid. This point is known as the eutectic point, as shown in Figure 2.7.

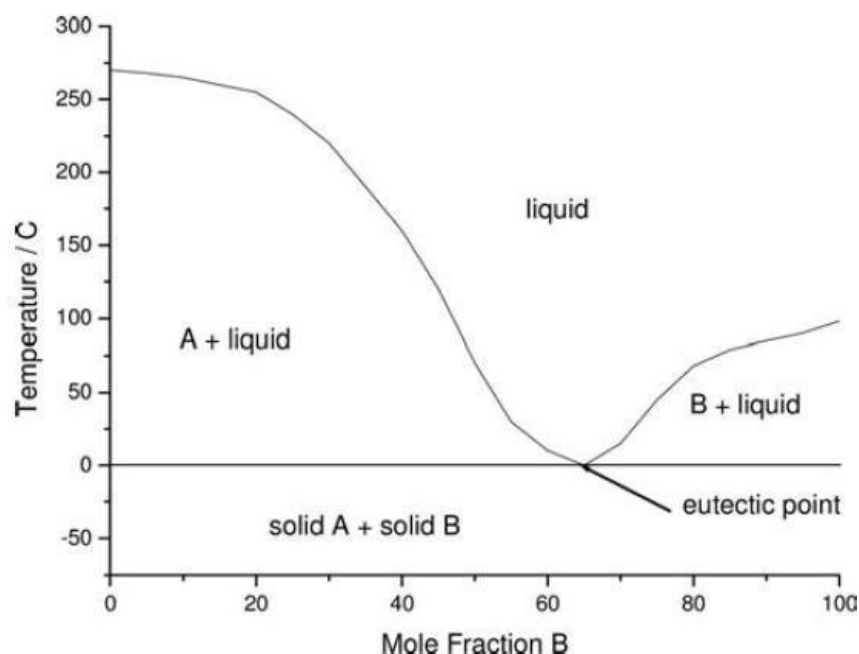


Figure 2.7: Phase diagram representing the two components inside a first-generation ionic liquid showing the importance of composition to the melting temperature in a eutectic system [10].

Eutectic-based ionic liquids were widely studied in order to further reduce their melting temperature as well as increasing their electrochemical stability. The main application of this principle was to

develop aluminium containing ionic liquids for room temperature deposition of aluminium. The first eutectic-based ionic liquid was created by Hurley and Wier in 1951 [30]. It was a mixture of N-ethylpyridinium bromide (EtPyBr) and  $\text{AlCl}_3$ , with a eutectic composition of 1:2 [10,30]. The authors noticed that this liquid had an unusually low melting temperature at the eutectic point and carried out studies on its potential application as a solvent for electrodeposition of aluminium at room temperature. They found that this system was not suitable for electrodeposition because it could only exist as a liquid at an exact composition of 1:2. This ionic liquid was improved by Osteryoung et al. [31,32] by replacing the EtPyBr cation with N-butylpyridinium chloride (BuPyCl). For the composition range of  $X(\text{AlCl}_3) = 0.66$  to  $0.43$ , this mixture existed as a liquid at room temperature. The change from bromide to chloride also improved the electrochemical stability. Further improvements were made with the discovery of more stable ionic liquids by improving the cations. In 1982, Wilkes et al. [33] did a modified neglect of diatomic overlap (MNDO) calculations on various different types of organic cations and they found that *N,N*-dialkylimidazolium cation were more stable than the *N*-butylpyridinium cation due to the higher electron affinity of these cation. The composition range at which the ionic liquid remained as liquid was also enlarged and for the 1-ethyl-3-methyl-imidazolium chloride/ $\text{AlCl}_3$  mixtures, the liquid range was extended from  $X(\text{AlCl}_3) = 0.66$  to  $0.30$  [34]. Currently, most ionic liquids have their cation based on pyridinium and imidazolium groups. Although almost all the research on eutectic-based ionic liquids from the 1950 to the 1990 had focused on the  $\text{AlCl}_3$  type anion, there were also some studies on the formation of eutectic-based ionic liquid with other types of metal groups, for example, the use of eutectic-based ionic liquids containing zinc halide and quaternary halides which have been shown to have a melting point close to room temperature [35-38].

#### 2.4.2 Second-generation ionic liquid

Second-generation ionic liquids have discrete anions and are generally considered to be air- and water-stable ionic liquids. First-generation ionic liquids have one major drawback: they are very hygroscopic such that a small amount of water can significantly change their electrochemical properties [10]. This has limited their application and the development of any application would require the use of expensive environmentally controlled glove box. In order to overcome this limitation, Wilkes et al. [39] tried to create a new type of ionic liquid by using less reactive anions instead of haloaluminate anions found in first-generation ionic liquids. Five different anions were paired with 1-ethyl-3-methyl-imidazolium [EMIM] cation. They were nitrate  $[\text{NO}_3]^-$ , nitrite  $[\text{NO}_2]^-$ , sulphate  $[\text{SO}_4]^{2-}$ , methyl carbonate  $[\text{CH}_3\text{CO}_2]^-$  and tetrafluoroborate  $[\text{BF}_4]^-$ . Only the [EMIM]  $[\text{CH}_3\text{CO}_2]^-$  and [EMIM]  $[\text{BF}_4]^-$  were found to have a melting temperature below  $100^\circ\text{C}$ . However, [EMIM]  $[\text{CH}_3\text{CO}_2]^-$  was too reactive to be used in electrochemical applications, leaving [EMIM]  $[\text{BF}_4]^-$  as the first air- and water-stable ionic liquid. This was quickly followed by the creation of the 1-Ethyl-3-methylimidazolium hexafluorophosphate [EMIM]  $[\text{PF}_6]$  ionic liquid, which was found to have a melting point of around  $60^\circ\text{C}$  [40], and later by the creation of 1-butyl-3-methylimidazolium hexafluorophosphate [BMIM]  $[\text{PF}_6]$  and 1-butyl-3-methylimidazolium tetrafluoroborate [EMIM]  $[\text{BF}_4]^-$  which are both liquid at room temperature [41]. The creation of the 1-Ethyl-3-methylimidazolium bis(trifluoromethylsulfonyl)amide [EMIM] [TFSI] ionic liquid started from investigations of lithium bis(trifluoromethylsulfonyl)amide  $\text{Li}[\text{TFSI}]$  as a possible component in battery electrolyte [42]. The structure of some of the more common anions for air- and water-stable ionic liquid is shown in Figure 2.8.

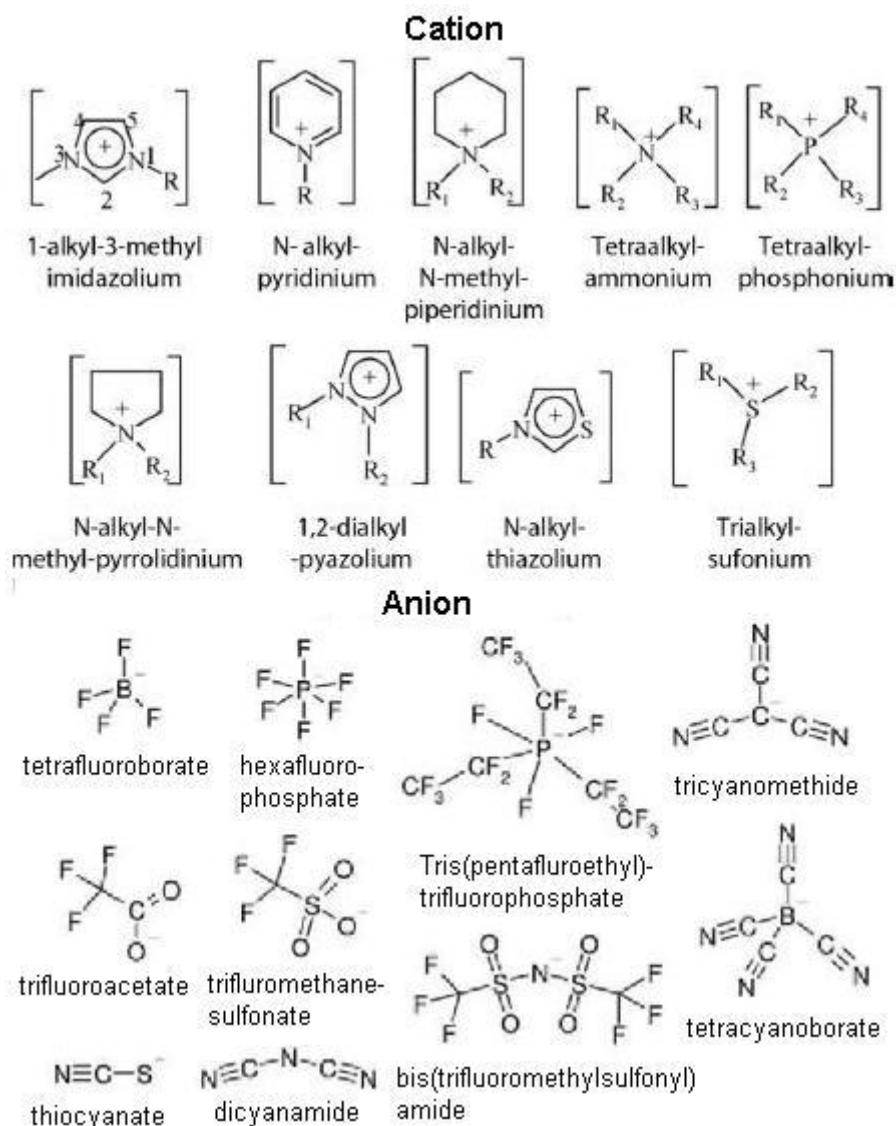


Figure 2.8: Structure of the cations and anions used in the air and water stable ionic liquids [10,11].

## 2.5 Properties of ionic liquids

From the previous sections, we can see that a small change in the cationic and anionic structures of the ionic liquid can significantly affect the ionic liquid properties such as the melting point, electrochemical stability, thermal stability, solubility of the metal salts, etc. In order to design an ionic liquid that is suitable for specific application, it is vital to understand the relationship between the structures of an ionic liquid and their properties.

### 2.5.1 Thermal properties

Since ionic liquids are defined as molten salts with melting temperature lower than 100 °C, it is important that they are thermally stable over a wide temperature range and there is no loss in its electrochemical properties due to temperature changes. To achieve this, it is important to keep the melting temperature as low as possible and the thermal degradation temperature as high as possible. Another important thermal property is the glass transition temperature, which affects the

viscosity of the ionic liquid. In this section, we will discuss the influence of the ionic liquids structures on their thermal properties.

The melting temperatures of inorganic salts are usually very high. For example, sodium chloride (NaCl) has a melting temperature of 801 °C. This is because the cations and anions of inorganic salts form strong ionic bonds and the ions are arranged in a very stable crystal structure. On the other hand, ionic liquids must incorporate several structural features that keep their melting temperature low.

Firstly, both the cations and anions of an ionic liquid contain organic groups. Unlike the strong ionic bonds in inorganic salts, the bond strength in organic salts is much weaker due to the larger organic cations and anions in ionic liquids. The larger ions impose limitations to the ionic packing and increase the surface area of the ions, leading to a decrease in the surface charge density. This, in turns, leads to a weaker electrostatic interaction between the cations and anions. Most organic cations and anions are also asymmetrical and this further prevents a compact coordination between the cations and anions.

The cations of most current ionic liquids are based on quaternary onium cation such as imidazolium, pyridinium, ammonium, phosphonium, sulfonium, etc. They usually contain a five-or-six-atom aromatic ring with two or more elements present in the ring. The delocalised  $\pi$  electron orbitals in the aromatic rings affect the electrostability of the cation and have the effect of reducing its effective charge. Most of the quaternary onium cations used in ionic liquids usually contain one or two alkyl side-groups. This has the effect of increasing the ionic radius and the asymmetry of the cation, thereby further weakening the bond between cations and anions. For ionic liquid with similar structure, increasing the alkyl side-chain length will initially lower the melting point. An example of this is [CMIM][BF<sub>4</sub>], where the melting temperature decreases when the carbon atom number, **C** increases between 2 and 9 [43]. As the alkyl side-chain length is increased with a **C** value of 10 or greater, the melting temperature will rise again. This is because as the chain length increases, the entropy of the system increases and the chains undergo reptation [41]. This increases the chance for different chains to interact with each other, and consequently increasing the probability of chain entanglement. A further increase of the **C** value will increase the surface area of the alkyl side-chain, thereby increasing the Van der Waals forces between the chains and, consequently, the melting temperature. For cations that contain two alkyl side-chains, the cation with an asymmetric side-chain will have a lower melting temperature compared to the cation with a symmetric side-chain. This is because structures with higher symmetry will pack more efficiently than those with lower symmetry, thus increasing the interaction surface.

Compared to the cations, there is a much wider range of anions that can be used to create ionic liquids. Some of the most common types of anions are those based on halogens. Ionic liquids based on pure halogens have a relatively high melting point, as shown in Table 2.3. The melting temperatures of pure chloride-based ionic liquids are higher than those based on pure bromide and iodide, due to the much higher electronegativity of the chloride ion. Anions that contain halides as side-groups have a much lower melting temperature as can be seen from the examples of BF<sub>4</sub><sup>-</sup>, PF<sub>6</sub><sup>-</sup> and TFSI<sup>-</sup> in Figure 2.8 above. This is because the electron withdrawing effect of the halogen helps to stabilise the anion by delocalising the negative charge of the anion. Anions that do not contain

halides can also have a low melting point through a suitable structural design that is capable of lowering the anionic charge density.

Table 2.3: Melting temperature (***T<sub>m</sub>***), glass transition temperature (***T<sub>g</sub>***) and thermal decomposition temperature (***T<sub>d</sub>***) for several different ionic liquids.

Ionic liquid		Temperature		
Cation	Anion	<i>T<sub>m</sub></i> / °C	<i>T<sub>g</sub></i> / °C	<i>T<sub>d</sub></i> / °C
[EMIM] <sup>+</sup>	[Cl] <sup>-</sup>	89 [44]	—	285 [44]
	[Br] <sup>-</sup>	79 [44]	—	311 [44]
	[I] <sup>-</sup>	79 [44]	—	303 [44]
	[BF <sub>4</sub> ] <sup>-</sup>	11 [44], 15 [45]	-86 [45]	420 [46]
	[PF <sub>6</sub> ] <sup>-</sup>	62 [44], 58 [40]	—	375 [44]
	[NO <sub>3</sub> ] <sup>-</sup>	11 [47], 38 [39]	—	—
	[TFSI] <sup>-</sup>	-15 [47]	-98[48,49,47]	455 [44], 440 [50]
	[DCA] <sup>-</sup>	-21 [51]	-104 [51]	—
	[EtSO <sub>4</sub> ] <sup>-</sup>	—	-78 [52]	—
	[AcOH] <sup>-</sup>	45 [44]	—	—
	[CF <sub>3</sub> COO] <sup>-</sup>	-14 [50]		150 [53]
	[MeSO <sub>4</sub> ] <sup>-</sup>	39 [54]		
	[CF <sub>3</sub> SO <sub>3</sub> ] <sup>-</sup>	-9 [50]		440 [53]
[BMIM] <sup>+</sup>	[PFSI] <sup>-</sup>	-1 [44]		423 [44]
	[TFSM] <sup>-</sup>	39 [44]		450 [44]
	[(CN) <sub>3</sub> C] <sup>-</sup>	-11 [55]	-95 [55]	—
	[Cl] <sup>-</sup>	65 [53]	—	250 [56]
	[Br] <sup>-</sup>	—	-50 [56]	273 [57]
	[I] <sup>-</sup>	-72 [58]	—	265 [44]
	[BF <sub>4</sub> ] <sup>-</sup>	-81 [59]	-97 [56]	403 [56]
	[PF <sub>6</sub> ] <sup>-</sup>	-8 [53], 10 [54]	-80 [56]	349 [56]
	[NO <sub>3</sub> ] <sup>-</sup>			
	[TFSI] <sup>-</sup>	-4 [53]	-87 [60]	439 [58,56]
	[DCA] <sup>-</sup>	-6 [55]	-90 [56]	300 [56]
	[AcOH] <sup>-</sup>			220 [61]
	[CF <sub>3</sub> COO] <sup>-</sup>	—	-78 [57]	176 [57]
	[MeSO <sub>4</sub> ] <sup>-</sup>			
	[CF <sub>3</sub> SO <sub>3</sub> ] <sup>-</sup>	16 [53]	—	409 [57]
	[PFSI] <sup>-</sup>			402 [57]
	[TFSM] <sup>-</sup>	—	-65 [56]	413 [56]
	[(CN) <sub>3</sub> C] <sup>-</sup>			

The glass transition temperature is defined as the reversible transition from a molten state to an amorphous solid. The glass transition temperature is always lower than the melting temperature, and in many ionic liquids, it is almost equal to two-thirds of the melting temperature in degrees Kelvin. For an ionic liquid, the glass transition temperature affects the viscosity and ionic conductivity.

For most applications, the thermal decomposition temperature of ionic liquids is much higher than the working temperature. For applications that require a high working temperature, knowing the thermal decomposition temperature is important. Moreover, ionic liquids can also decompose at

temperatures below the thermal decomposition temperature, depending on the rate and duration of heating. Ionic liquids that have a non-halogen containing anion usually have very high thermal decomposition temperature, up to 400 °C. For ionic liquids with pure halogen anions, the thermal decomposition temperature is slightly lower than that of ionic liquid with an anion that contains halogen as a side-group. Some studies have also been done to investigate the effect of the alkyl side-groups of the cations on the thermal decomposition temperature and the results show that alkyl side-groups have very little effect on the thermal decomposition temperature [10].

The melting temperature, glass transition temperature and decomposition temperature of several imidazolium based ionic liquids are shown in Table 2.3.

## 2.5.2 Viscosity

Due to the strong electrostatic forces in the ionic liquids, the viscosity of ionic liquid is usually 10 to 100 times greater than that of water [10]. As viscosity is directly affected by the electrostatic interaction, it is affected by the structure of cation and anion present in solution. Ionic liquid that are composed of larger ions as well as a delocalised charge should have lower viscosity. Increasing the alkyl side-chain on the cation of an ionic liquid also increases its viscosity due to reptation and chain entanglement.

The viscosity of an ionic liquid is also affected by temperature. As the process is thermally activated, the temperature dependence is governed by an Arrhenius equation, given by [10]:

$$\ln \eta = \ln \eta_0 + \frac{E_n}{RT} \quad \text{Eq. 2.30}$$

$E_n$  is the activation energy viscous flow and  $\eta_0$  is a constant.

Increasing the temperature decreases the viscosity of the ionic liquid. The viscosity of several imidazolium based ionic liquids is given in Table 2.4.

Table 2.4: The viscosity of several [EMIM] and [BMIM] based ionic liquids.

		Viscosity / cP
Water		0.89
[EMIM] <sup>+</sup>	[BF <sub>4</sub> ] <sup>-</sup>	43 [47]
	[PF <sub>6</sub> ] <sup>-</sup>	15 (80 °C) [47]
	[TFSI] <sup>-</sup>	34 [50], 28 [47]
	[DCA] <sup>-</sup>	21
	[EtSO <sub>4</sub> ] <sup>-</sup>	78 (30 °C) [62]
	[(CF <sub>3</sub> SO <sub>2</sub> ) <sub>2</sub> N] <sup>-</sup>	
	[(C <sub>2</sub> F <sub>5</sub> SO <sub>2</sub> ) <sub>2</sub> N] <sup>-</sup>	61 [47]
	[CF <sub>3</sub> SO <sub>3</sub> ] <sup>-</sup>	45 (30°C) [63]
[BMIM] <sup>+</sup>	[BF <sub>4</sub> ] <sup>-</sup>	219 [58]
	[PF <sub>6</sub> ] <sup>-</sup>	450 [58]
	[TFSI] <sup>-</sup>	52 [50], 69 [58]
	[DCA] <sup>-</sup>	33
	[(C <sub>2</sub> F <sub>5</sub> SO <sub>2</sub> ) <sub>2</sub> N] <sup>-</sup>	77 [63]
	[CF <sub>3</sub> SO <sub>3</sub> ] <sup>-</sup>	93 [64]

### 2.5.3 Electrochemical properties

Table 2.5: The electrochemical window of several different EMIM based ionic liquids.

Cation	Anion	Working electrode	Reference electrode	Potential window (V)
EMIM	BF <sub>4</sub>	GC	Al/Al <sup>3+</sup>	>2.1 [65]
		Pt	Al/Al <sup>3+</sup>	4.4 [65]
			I <sup>-</sup> /I <sub>3</sub> <sup>-</sup>	4.4 [66]
			Ag wire	4.4 [67]
	DCA	Pt	Ag wire	3.0 [68]
	TFA	Pt	I <sup>-</sup> /I <sub>3</sub> <sup>-</sup>	3.2 [50]
	TFO	Pt	I <sup>-</sup> /I <sub>3</sub> <sup>-</sup>	3.8 [50]
	TFSI	Pt	I <sup>-</sup> /I <sub>3</sub> <sup>-</sup>	4.2 [50]
		GC	Ag wire	4.1 [47]

The electrochemical window is governed by the structure and composition of an ionic liquid, and by the electrode materials, reference electrode, potential scan rate, temperature, atmosphere, impurities and other factors. All ionic liquids usually have a large potential window when compared to water. The electrochemical windows of several EMIM based ionic liquids are shown in Table 2.5.

## 2.6 Electrodeposition from ionic liquids

Recent advances in the field of ionic liquids have increased their potential application in electrodeposition [69], catalysis [70,71], chemical synthesis [70,72], and as electrolytes in batteries and fuel cells [73] as well as in separation technology [72]. In this study, we will concentrate on the application of ionic liquids in electrodeposition. Electrodeposition from ionic liquids can be split into two eras, depending on the type of ionic liquid used: first- or second-generation ionic liquids (as mentioned earlier in Section 2.4).

The beginning of for the electrodeposition from ionic liquid started in 1951, with the electrodeposition of aluminium from a N-ethylpyridium bromide (EtPyBr) and AlCl<sub>3</sub> ionic liquid at a eutectic composition of 1:2 [10,30]. These first-generation ionic liquids were known as chloroaluminated ionic liquids as they are based on AlCl<sub>3</sub>. Although most studies carried out were on electrodeposition of aluminium [10,74-79], studies were also performed on the electrodeposition of lithium [10,80,81], gallium [10,82], tin [10,83], antimony [10,84,85] and tellurium [10,86]. These ionic liquids were, however, not widely studied because expensive glove boxes were required, due to the hygroscopic nature of these liquids [10]. Besides that, electrodeposition of metals other than aluminium also suffer from problems associated with co-deposition of aluminium from the chloroaluminate [10].

In light of the drawbacks of chloroaluminated ionic liquids, new air- and water-stable ionic liquids were created in the early nineties by substituting the chloroaluminated anion with a more hydrophobic anion [87,10]. This led to the creation of second-generation ionic liquids such as 1-Ethyl-3-methylimidazolium tetrafluoroborate [EMIM] [BF<sub>4</sub>] [39], 1-Ethyl-3-methylimidazolium hexafluorophosphate [EMIM] [PF<sub>6</sub>] [88], 1-Ethyl-3-methylimidazolium bis(trifluoromethylsulfonyl)amide [EMIM] [TFSI] [89] and many others. Due to their increased stability, electrodeposition from second-generation ionic liquid solutions have become more

widespread and studies have been carried out on a wide variety of metals such as zinc [10,90-93], copper [10,94-97], cadmium [10,98,99], chromium [10,100], palladium [10,101-103], silver [10,15,104-107], platinum [10,108], antimony [10,109], aluminium [10,110-112], magnesium [10,113-116], lithium [10,117,118], tantalum [10,119] and titanium [10,120].

In the following sections, a more in-depth review of the electrodeposition of silver, copper and aluminium from ionic liquid based electrolytes is carried out.

### 2.6.1 Silver

Thin films of silver have traditionally been used in jewellery, although in recent times they have been applied in microelectronics, electrochemical sensors [121,122], coating on electrode surface for analytical spectroscopy [106] and as anti-bacterial coatings [123].

The electrodeposition of silver from first-generation ionic liquids was not widely studied due to the hygroscopic nature of these liquids, although there are several papers on the topic. For example, Xu et al. [124] electrodeposited silver on several different electrodes from  $(\text{AlCl}_3) - [\text{EMIM}] [\text{Cl}]$  ionic liquid. The authors found that underpotential deposition occurred on a gold electrode. A similar study was carried out by Zell et al. [125] on the electrodeposition of silver on annealed (111) gold substrate. Xu et al. [124] also found that a large nucleation overpotential was needed to deposit silver on tungsten and glassy carbon electrodes. This behaviour was also observed for silver deposited on highly oriented pyrolytic graphite (HOPG) from a  $(\text{AlCl}_3) - [\text{EMIM}] [\text{Cl}]$  ionic liquid solution containing 0.05 mol/L AgCl [126]. Furthermore, Abbott et al. [127] performed galvanic electroless deposition of silver from a choline chloride based ionic liquid and they were able to obtain films with thickness of several microns. The silver deposit grew in two phases: the first phase produced a thin but relatively dense layer and the second phase produced a very rough surface interpenetrated by the ionic liquid solution. The wear resistance of these silver coatings was improved by switching to a solution of AgCl in ethylene glycol-choline chloride ionic liquid mixture [128].

The advent of more air- and water-stable ionic liquids has increased the research on the electrodeposition of silver from ionic liquids. He et al. [106] electrodeposited silver from  $[\text{BMIM}] [\text{PF}_6]$  and  $[\text{BMIM}] [\text{BF}_4]$  and found that the resulting films were suitable for electrodes used in surface enhanced Raman scattering (SERS). The authors found that the silver produced from  $[\text{BMIM}] [\text{PF}_6]$  solution was formed by instantaneous nucleation [106]. Those produced from  $[\text{BMIM}] [\text{BF}_4]$  solution was formed by progressive nucleation [106], in agreement with the results of Bomparola et al. [129], who showed that only a small overpotential was required to initiate silver deposition. On the other hand, the opposite result was obtained by Basile et al. [130], who found that the nucleation of silver was instantaneous, although the presence of water in solution significantly affected the mechanism and morphology of the films. In another study, Tsai et al. [122] were able to obtain silver nanoparticles with diameters between 5 to 35 nm on indium tin oxide (ITO) from  $[\text{BMIM}] [\text{BF}_4]$  solution, which could be used for the detection of dissolved oxygen upon further processing. Silver was also deposited from various  $[\text{TFSI}]$  base ionic liquids. Many other similar studies have also been carried out. Serizawa et al. [131] electrodeposited silver from  $[\text{BMPyr}] [\text{TFSI}]$  ionic liquid containing Ag(TFSI) salt. Fukui et al. [132] electrodeposited silver from  $[\text{TMHA}] [\text{TFSI}]$ ,  $[\text{BMPyr}] [\text{TFSI}]$  and  $[\text{BMIM}] [\text{TFSI}]$ , while Basile et al. [130] electrodeposited silver from  $[\text{BMPyr}] [\text{TFSI}]$ . Besides the direct deposition of the film, Reyna-Gonzalez et al. [133] showed that silver could be first extracted from



an aqueous solution using a thick [MIMSBu] [TFSI] ionic liquid film adhered to an electrode. This extracted silver could then be directly electrodeposited onto the electrode. A similar study was conducted on the [3-BPyr][TFSI] ionic liquid [134]. The silver nucleation mechanism changed from progressive to instantaneous when the applied potential was increased to a more negative potential, an effect attributed to the increased water content in the liquid [134]. Silver was also electrodeposited from [EMIM] [TFO] by Ispas et al. [135] and from ethylammonium nitrate [EAN], triethylammonium methylsulfonate [Et<sub>3</sub>N] [MeSO<sub>4</sub>], and bis(2-methoxyethyl)ammonium acetate [(MeOEt)<sub>2</sub>NH] [AcOH] onto glassy carbon, gold and indium tin oxide-coated glass substrates by Suryanto et al. [136].

Besides pure silver, various silver alloy films were also electrodeposited from ionic liquid electrolytes. Grishina et al. [137] deposited silver bromide Ag(Br) films on a silver electrode from solutions of Ag(Br) in [BMIM][Br]. The film properties depended on the composition of the solution. Tai et al. [138] deposited a palladium-silver alloy film from [EMIM] [Cl] [BF<sub>4</sub>] ionic liquid. The reduction of Ag(I) occurred prior to the reduction of Pd(II) and an overpotential was required to start nucleation. The composition of the Ag-Pd alloy could be varied by changing the deposition potential and concentrations of Ag(I) and Pd(II) in solution.

Various physical and chemical methods were used to control the morphology and structure of the silver films. Dobbs et al. [139] electrodeposited particles of silver by using a template made from ionic liquid-crystal precursors. They found that the supra molecular structure of the liquid-crystal phase could be used to control silver nanoparticles morphology deposited by electrochemical reduction. Yeh et al. [140] showed that porous silver film could be obtained by electrodeposition of a silver-zinc alloy from ZnCl<sub>2</sub>-[EMIM] [Cl] ionic liquid on a silver substrate, followed by electrochemical etching of zinc. The structure of the film could be controlled by the deposition temperature and potential as well as the concentration of zinc. Kazeminezhad et al. [141] electrodeposited silver wires from a commercial nuclear track-etched polycarbonate template in [BMIM] [PF<sub>6</sub>] solution using silver electrochemically dissolved from the anode. The nanowires have a very high aspect ratio with an average diameter of 80 nm and length of 5 μm. A similar study was performed by Abedin et al. [142] using a [EMIM] [TFO] ionic liquid. They obtained nanowires with average diameter of 200 nm and length of 3 μm. Tsai et al. [121] electrodeposited macroporous silver films using a template formed by polystyrene (PS) spheres assembled on indium tin oxide (ITO) electrodes. The authors found that [BMPyr] [DCA] formed better macroporous films than [BMPyr] [TFSI] as it exhibited a better wetting of the PS spheres.

Due to the low solubility of silver salts in ionic liquids, attempts were also made to modify the structure of the electrolyte in order to increase deposition efficiency and improve the quality of the coating. For example, Iida et al. [143] created two different silver containing ionic liquids of bis(N-2-ethylhexylethyl-enediamine)silver(I) nitrate [Ag(eth-hex-en)<sub>2</sub>] [NO<sub>3</sub>] and bis(N-hexylethylenediamine)silver(I) hexafluorophosphate [Ag(hex-en)<sub>2</sub>] [PF<sub>6</sub>]. Uniformly sized silver nanoparticles in water were created by the reduction of the [Ag(eth-hex-en)<sub>2</sub>] [NO<sub>3</sub>] with aqueous NaBH<sub>4</sub> but not so for [Ag(hex-en)<sub>2</sub>] [PF<sub>6</sub>]. In a separate study, Bhatt et al. [144] showed that nanoparticles of silver could be obtained through electrodeposition from the 'distillable' ionic liquid DIMCARB. DIMCARB was synthesised from Me<sub>2</sub>NH and CO<sub>2</sub> in a 1.8:1 ratio according to the reaction: CO<sub>2</sub> + Me<sub>2</sub>NH ↔ Me<sub>2</sub>NHCOOH + Me<sub>2</sub>NH ↔ [Me<sub>2</sub>NH<sub>2</sub>]<sup>+</sup> [Me<sub>2</sub>NCOO]<sup>-</sup>. In another study, Fu et al. [145] electrodeposited silver from [BMIM] [PF<sub>6</sub>] using two different emulsions, one of water in the ionic

liquid (W/IL) and the other of ionic liquid in water (IL/W). They found that silver deposited from the (W/IL) system had a nano-granular structure, while silver deposited from the (IL/W) system were pretty much featureless. Furthermore, Brooks et al. [146] created several mixed-ligand metal-containing ionic liquids where the cations consisted of two-coordinated silver(I) centres ligated by two different N-alkylimidazole ligands and the anion was (TFSI). They showed that the silver complex-ionic liquid had a low melting point. Further studies by Schaltin et al. [147] showed that silver coating could be obtained through high current density electrodeposition from these ionic liquids.

### 2.6.2 Copper

Copper is one of the most widely used metals in the semiconductor industry. Almost all the connections in semiconductor chips are made from copper because of the low electrical resistance and good oxidation resistance of this metal [10].

The electrochemical behaviour of Cu(I) solutions in [EMIM][BF<sub>4</sub>] was studied by Chen and Sun [148]. The authors showed that the Cu(I) ions in [EMIM][BF<sub>4</sub>]-copper (I) chloride solutions could be oxidised to Cu(II) or reduced to metallic copper in appropriate conditions, and that fairly dense copper films could be electrodeposited from these solutions. The required potential depended on the substrate material: underpotential deposition occurred for platinum while an overpotential was required to initiate deposition on glassy carbon. Murase et al.[149] studied the redox behaviour of Cu(I) and Cu(II) salts solutions in [TMHA] [TFSI] to evaluate the applicability of this ionic liquid in copper deposition and concluded that copper thin films could be produced from Cu(I) salts solutions. The process involved a single-electron reduction reaction with a current efficiency of almost 100%. The electrodeposition of copper from [BMPyr] [TFSI] based electrolytes at several temperatures was studied by Zein El Abedin et al. [150]. The authors found that the solubility of Cu salts in this ionic liquid was limited, which reduced the suitability of this electrolyte for Cu deposition. However, they could introduce Cu(I) ions in solution by anodic dissolution of a copper electrode, then depositing copper as a thin film by an appropriate variation of the applied potential. The films deposited on gold substrates were found to have a nanocrystalline structure with an average particle size of 50 nm.

An alternative approach to create ionic liquid based electrolytes with high concentration of copper is by carefully selecting the ionic liquid. Leong et al [151] showed that the solubility of CuCl and CuCl<sub>2</sub> in [EMIM] [DCA] are 1.1M and 0.9M respectively, allowing the preparation of electrolytes with high concentration of copper suitable for electrodeposition. Moreover, [EMIM] [DCA] had lower viscosity than other similar ionic liquids, which improved mass transport in the liquid and accelerating the electrodeposition kinetics. The authors showed that continuous nanocrystalline copper films could be obtained at low overpotential by electrodeposition from solution of CuCl in [EMIM] [DCA]. The films were formed by a three-dimensional progressive nucleation and growth process. On the other hand, Brooks et al. [152] achieved high copper electrodeposition rate by using specially designed ionic liquids containing the metal cation. The authors deposited copper at current densities greater than 25 Adm<sup>-2</sup> from an ionic liquid containing Cu(I) and the TFSI anion ([Cu(CH<sub>3</sub>CN)<sub>n</sub>][TFSI], n=2,4), thus overcoming the limitations observed in previous work. Furthermore, Abbot et al. [153] used 0.1 M CuCl<sub>2</sub>·2H<sub>2</sub>O in an ionic liquid consisting of choline chloride and hydrogen bond donors such as urea or ethylene glycol to deposit copper and copper-based composites reinforced with Al<sub>2</sub>O<sub>3</sub> and SiC. Assaker et al. [154] electrodeposited copper from a mixture of [TOMA] [Cl] ionic liquid and

chloroform. They found that the copper films were moderately dense and contained fine crystallites with average sizes of about 1  $\mu\text{m}$ .

The electrodeposition of copper alloys was also studied. Hsieh et al. [155] obtained free standing hexagonal copper-tin tube arrays by electrodeposition from [EMIM] [DCA] ionic liquid without using a template. Chen et al. [156] co-electrodeposited copper-manganese alloy coatings from [BMPyr] [TFSI] ionic liquid. The coatings were compact and adherent. The composition and surface morphology of the coatings depended on deposition potential and on the concentration ratio of Cu(I) to Mn(II).

### 2.6.3 Aluminium

Aluminium undergoes passivation by reacting with oxygen. Passivation is due to the formation of a dense and extremely thin film of aluminium oxide. This gives aluminium a high corrosion resistance, making it an ideal coating for corrosion protection of other metals. However, due to its high reactivity (-1.7 V vs SHE), aluminium cannot be electrodeposited from aqueous solutions. Hence there is a huge driving force to electrodeposit aluminium from ionic liquid based electrolytes.

Many studies were carried out on the electrodeposition of aluminium from haloaluminate-based ionic liquids [10,74-79]. One of the first was the electrodeposition of aluminium on platinum and glassy carbon from  $\text{AlCl}_3$  - [BPyr][Cl] ionic liquid by Robinson et al. [74]. A similar experiment was carried out with the same electrolyte on tungsten and brass where aluminium films with thicknesses up to 15  $\mu\text{m}$  were obtained [75]. The deposition occurred at potential of -0.43 V. Aluminium were also deposited from the imidazolium-based ionic liquid solution,  $\text{AlCl}_3$  - [EMIM] [Cl] by Lai et al. [76]. The authors found that aluminium deposited on glassy carbon at a potential of -0.2 V, while an initial potential of -0.65 V was required to deposit aluminium on tungsten, although this potential subsequently dropped below -0.2 V. Aluminium were also deposited on copper from  $\text{AlCl}_3$  - [EMIM] [Cl] ionic liquid, yielding films with a thickness of 24-30  $\mu\text{m}$  [77]. The addition of benzene to the electrolyte was required to obtain adherent and shiny films.

Several studies were carried out to investigate the corrosion resistance of the aluminium coatings. Jiang et al. [157,158] obtained dense, continuous and well adherent aluminium films on tungsten from 2:1 molar ratio  $\text{AlCl}_3$  - [EMIM][Cl] and  $\text{AlCl}_3$ -trimethylphenylammonium chloride [TMPAC]. A similar result was obtained by Liu et al. on AZ31 magnesium alloy [159] and mild steel [160] substrates. Caporali et al. [161] also obtained thick aluminium films (10-40  $\mu\text{m}$ ) with good corrosion resistance on carbon steel from [BMIM] [ $\text{Al}_2\text{Cl}_7$ ] and a similar result with the same electrolyte was obtained by Bardi et al. [162] on P90 lithium-aluminium alloy substrates. The corrosion resistance was further improved by oxidative post-treatment of the aluminium coating [163]. Besides pure aluminium, several studies were also carried out on the deposition of aluminium alloys from haloaluminate-based ionic liquids. Rostom Ali et al. [164] deposited aluminium-chromium alloy with good corrosion resistance from 2: 1 molar ratio  $\text{AlCl}_3$  / [BPyr] [Cl] solution. The composition and microstructure of the film depended on the deposition parameters. Abbott et al. [78] electrodeposited aluminium and aluminium-platinum alloy from  $\text{AlCl}_3$  - benzyltrimethylammonium chloride [BTMA] [Cl] solution. The deposited films were generally uniform, adherent and pore-free, making them suitable for corrosion prevention. They found that the  $\text{AlCl}_3$  - [BTMA] [Cl] ionic liquid was more hygroscopic, thermally stable and easier to purify than  $\text{AlCl}_3$  - [BPyr] [Cl] and  $\text{AlCl}_3$ -[EMIM] [Cl] based ionic liquids.

Electrodeposition of three-dimension nanostructures of aluminium by using templates was also investigated. Perre et al. [165] electrodeposited aluminium nanorods from a eutectic mixture of  $\text{AlCl}_3$  - [EMIM] [Cl] at a 2:1 ratio by using an alumina template. The authors were able to obtain uniform free standing aluminium pillars with dimensions directly controlled by the template. Pomfret et al. [166] carried out a similar study using a polycarbonate template and obtained aluminium nanorods with diameters ranging from 10 to 30 nm and length of around 5  $\mu\text{m}$ . Improvements on the nanowire architecture was carried out by El Abedin et al. [4] through careful control of the electrodeposition process. They were able to obtain different nanowire architectures such as free-standing nanowires, vertically aligned tree-shaped arrays, and bunched nanowire films. Gandhi et al. [167] electrodeposited an aluminium antimonide semiconductor from a 3:2 molar ratio of  $\text{AlCl}_3$  - [EMIM] [Cl] with addition of  $\text{SbCl}_3$  using a  $\text{TiO}_2$  nanotubular template. The films were predominantly amorphous in as-deposited condition but after annealing at 350  $^\circ\text{C}$  for 2 hours in an argon atmosphere, it was transformed into a crystalline phase.

The influence of the electrolyte structure on the aluminium coating properties was also investigated. Abbott et al. [168] deposited aluminium films from chloroaluminate based ionic liquids and studied the influence of toluene and LiCl on the morphology of the deposited films. They found that toluene changed the speciation in solution, leading to a decrease in underpotential deposition and changing the morphology of the aluminium films to more mirror-like finish. Addition of LiCl increased the underpotential deposition and led to the formation of larger crystallites and grey deposits. El Abedin et al. [169] electrodeposited nanocrystalline aluminium from 3:2 molar ratio of  $\text{AlCl}_3$  and 1-(2-methoxyethyl)-3-methylimidazolium chloride [MoeMIM][Cl] ionic liquid. They found that the methoxy group in the side-chain of the imidazolium cation influenced the electrodeposition pathway of Al in comparison to [EMIM]Cl- $\text{AlCl}_3$  systems. Shiny Al layers with an average crystallite size of about 40 nm were obtained. Pradhan et al. [170] analysed the effects of electrode surface modification and cathode overpotential on the characteristics of aluminium deposited from 1.65:1 molar ratio of  $\text{AlCl}_3$ : [EMIM][Cl] ionic liquid and concluded that the electrode surface modification and cathode overpotential are key to prevent dendritic formation in the aluminium films.

Studies have also been carried out on the electrodeposition of aluminium from second-generation ionic liquids. El Abedin et al. [171] electrodeposited nanocrystalline aluminium films from [BMPyr] [TFSI] ionic liquid saturated with  $\text{AlCl}_3$ . Below 80  $^\circ\text{C}$ , this liquid separated into two immiscible phases when the  $\text{AlCl}_3$  concentration was above 1.6 M, namely a white upper phase and a denser colourless phase. Aluminium could only be deposited from the white upper phase. Rocher et al. [172] found that for concentration of  $\text{AlCl}_3$  larger than 3.3 M, aluminium could only be deposited from the denser phase. The deposits obtained were generally nanocrystalline, uniform, dense, shining and adherent to the substrate. Moustafa et al. [173] also carried out a similar study using [BMPyr] [TFSI] and [EMIM] [TFSI] saturated with  $\text{AlCl}_3$ . Similar to [BMPyr] [TFSI], [EMIM] [TFSI] electrolytes also separated into two phases when the concentration of  $\text{AlCl}_3$  was above 2.5 M at room temperature. Underpotential deposition was observed for the deposition of aluminium from this solution. The films consisted of coarse cubic-shaped aluminium particles with sizes in the micrometre range. El Abedin et al. [174] electrodeposited aluminium from [trihexyl-tetradecyl-phosphonium] [TFSI]. It was found that aluminium could only be electrodeposited when the concentration of  $\text{AlCl}_3$  in the liquid exceeded 4 M and the deposition temperature was at 150  $^\circ\text{C}$ . A very thin, mirror-like aluminium film consisting of very fine crystallites of about 20 nm was obtained.

## 2.7 Basic principle of spectroscopy

Spectroscopy is the study of the interaction between electromagnetic radiation and matter.

### 2.7.1 What is electromagnetic radiation?

Electromagnetic radiation has a split personality. Sometimes it behaves like a wave and sometimes it behaves like a particle. Whether it exhibits wave-like properties or particle-like properties will depend on the type of phenomena being observed. In quantum mechanics, this behaviour is known as the wave-particle duality, which postulates that all particles exhibit both wave and particle properties.

The wave-like properties of electromagnetic radiation are described by Maxwell's equations from the classical theory of electromagnetism. From Maxwell's equation, we can derive the homogeneous electromagnetic wave equation in three dimensions. For an electric field:

$$\left( \nabla^2 - \mu\epsilon \frac{\delta^2}{\delta t^2} \right) E_F = 0 \quad \text{Eq. 2.31}$$

Similarly for a magnetic field:

$$\left( \nabla^2 - \mu\epsilon \frac{\delta^2}{\delta t^2} \right) B_F = 0 \quad \text{Eq. 2.32}$$

$\nabla$  is the Laplace operator,  $\mu$  and  $\epsilon$  are the permeability and permittivity of the medium,  $E_F$  and  $B_F$  are the electric and magnetic field.

The speed of light,  $c$  is given by:

$$c = \frac{1}{\sqrt{\mu\epsilon}} \quad \text{Eq. 2.33}$$

It can be shown that the electric field of a monochromatic plane wave is given by:

$$E(x, t) = E_0 \sin \left[ 2\pi\nu \left( \frac{x}{u} - t \right) \right] \quad \text{Eq. 2.34}$$

$E_0$  being the maximum amplitude,  $\nu$  the wave frequency and  $u$  is the propagation speed.

The electromagnetic radiation consists of planes of electric and magnetic fields that are in phase but perpendicular to each other, both fields propagating in the same direction. An illustrative diagram of a linear polarised electromagnetic wave is shown in Figure 2.9.

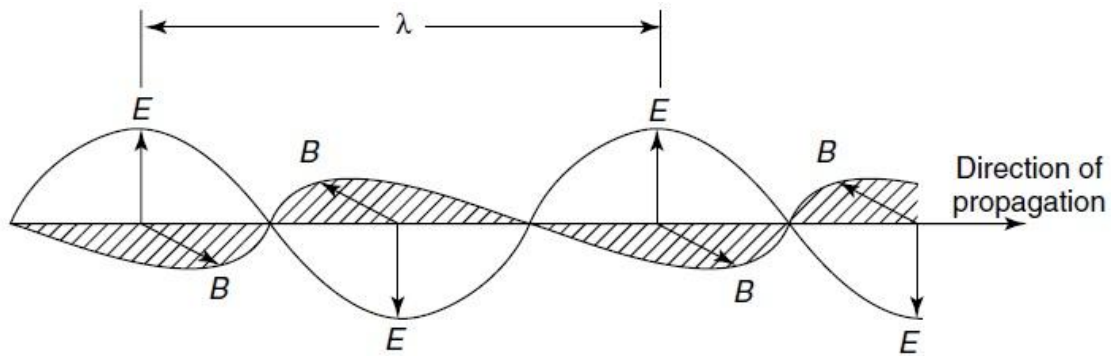


Figure 2.9: A representation of an electromagnetic wave [12].

Since the speed of light in vacuum  $c_0$  is a constant, the wavelength  $\lambda$ , is inversely proportional to the frequency  $\nu$ :

$$c_0 = \nu \lambda \quad \text{Eq. 2.35}$$

The particle of electromagnetic radiation is known as a photon. The energy of a photon  $E_{ph}$ , is quantised and is given by:

$$E_{ph} = h\nu = \frac{hc}{\lambda} \quad \text{Eq. 2.36}$$

$h$  is the Planck's constant.

This shows that the energy of the photon is directly proportional to its frequency and inversely proportional to its wavelength.

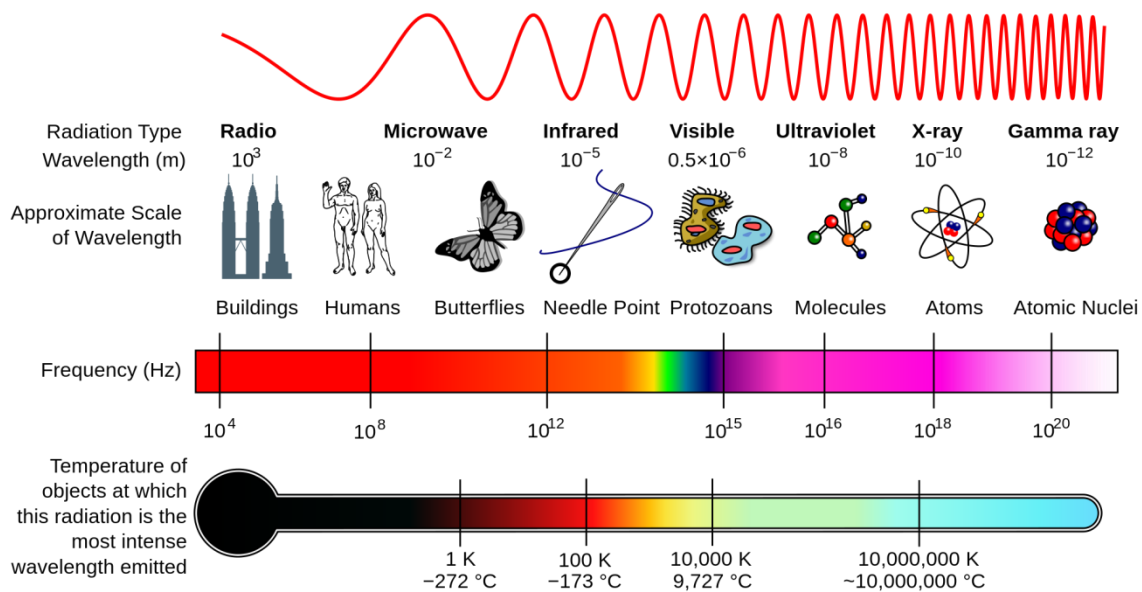


Figure 2.10: The electromagnetic spectrum showing the relationship between wavelength, frequency and energy [13].

## 2.7.2 Energy states in matter

The total energy  $E_{total}$  of a molecule is made up of two components: the translational energy and the internal energy. The translation energy is the kinetic energy possessed by the molecule due to translational motion. The internal energy  $E_{internal}$  is the sum of three different components: the electronic, vibrational and rotational energies. The electronic energy is the energy required to excite an electron from one atomic or molecular orbital to another. In a molecule, it is the energy required to break the chemical bonds within the molecule. The vibrational energy is much smaller than the electronic energy. It is the energy associated with the atomic vibrations within the molecule. For a diatomic molecule, the vibrational energy can be understood from the classical Newtonian model of two masses connected by a spring-like bond. The vibrational energy of the molecule can be thought as the elastic energy stored in the spring. The rotational energy is even smaller than the vibrational energy and is related to the rotation of the molecule as a whole. Thus, the energy of a molecule is:

$$E_{total} = \Sigma E_{translation} + E_{electronic} + E_{vibration} + E_{rotation} \quad \text{Eq. 2.37}$$

$$E_{internal} = E_{electronic} + E_{vibration} + E_{rotation} \quad \text{Eq. 2.38}$$

According to the laws of quantum mechanics, the electronic, vibrational and rotational energies are all quantised. The relationship between the electronic, vibrational and rotational energies can be understood from the energy versus distance plots for a diatomic molecule, shown in Figure 2.8. The two curves correspond to two different electronic states of the molecule, in this case the ground state and the first excited state, defined by the principal quantum numbers  $n = 0$  and  $n = 1$ . The electronic energy corresponds to the minimum value of each curve. In each of the electronic states, the molecule may take up different quantised states that do not involve electron transfers between orbitals. These new states are vibrational states and they are described by the vibrational quantum number ( $v'$ ). Between two vibrational states, the molecule may assume several discrete energy states known as the rotational states, described by the rotational quantum number ( $v''$ ) as shown in Figure 2.8.

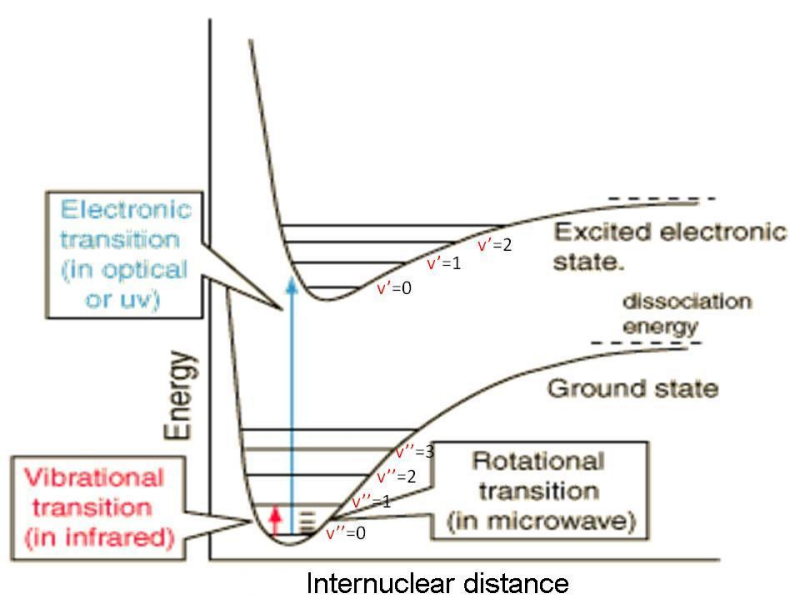


Figure 2.11: Energy states of a diatomic molecule [14] .

### 2.7.3 Normal modes of molecular vibrations

In the previous sections, we only looked at the energy levels associated with the molecular vibrations and rotations. These energy levels are associated with physical processes involving changes in the shape, length and motion of the intermolecular bonds. A basic classical model describes a molecule as a system of masses joined by bonds with spring-like properties [12]. In general, a molecule with  $N$  number of atoms will have a number of normal vibrational modes given by:

$$3N - 6 \quad \text{Eq. 2.39}$$

However, for a linear molecule the number of normal modes of vibration is given by:

$$3N - 5 \quad \text{Eq. 2.40}$$

Molecular vibrations can be classified into two types. The first is a change in the bond length known as stretching mode and the second is a change in the angles between bonds, known as bending mode[12]. When there are two or more vibrations within a molecule, they can either be in phase or out of phase with each other [12]. Examples of the different type of stretching and bending modes are shown in Figure 2.12.

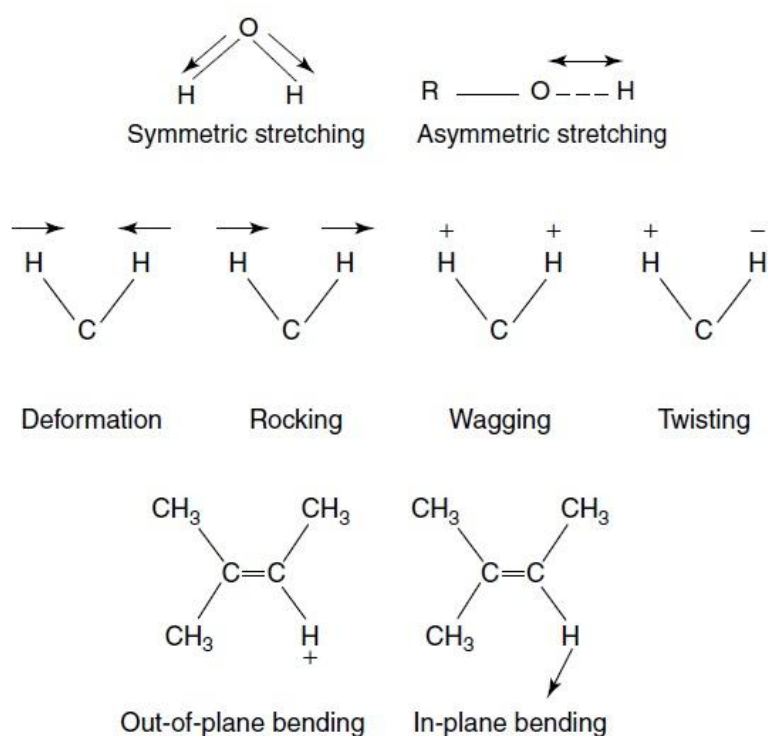


Figure 2.12: Examples of different modes of molecular vibration [12]. Stretching modes: symmetric and asymmetric stretching; bending modes: deformation, rocking, wagging and twisting; out of plane and in plane mode of bending.



## 2.7.4 Interaction between electromagnetic radiation and matter

In the previous section, it was shown that the molecular energy levels are discrete and each energy state is described by a set of quantum numbers. Interaction between electromagnetic radiation and molecules only occurs when the photon energy is equal to the difference between two different energy states ( $\Delta E$ ):

$$\Delta E = h\nu \quad \text{Eq. 2.41}$$

When a photon induces a molecular state transition, we can calculate the frequency ( $\nu$ ) of the photon using Equation 2.38. Performing this calculation for all the electronic, vibrational and rotational energy states, one can demonstrate that the different energy transitions correspond to different radiation frequencies across the electromagnetic spectrum. The electronic state transitions correspond to the visible and ultraviolet spectral range, while the vibrational state transitions are in the infrared range and the rotational state transitions are in the microwave range. One important consequence is that varying the frequency of the incident electromagnetic radiation allows one to probe the various atomic and molecular processes that may occur in matter. This is the basis for all spectroscopy techniques. A list of these relationships is shown in Figure 2.13.

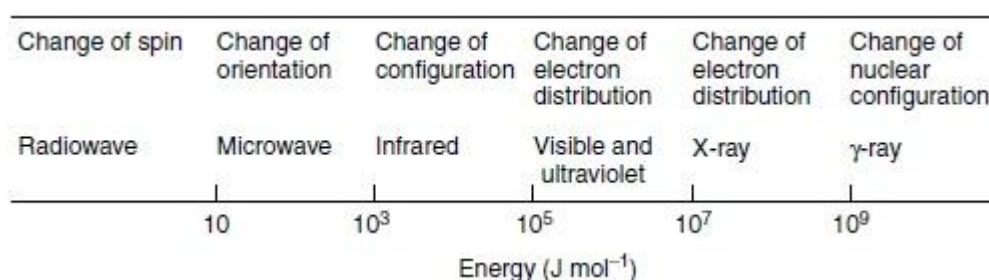


Figure 2.13: Relationship between molecular processes, radiation wavelength range [12].

The interaction between electromagnetic radiation and matter usually involves four types of mechanism:

- Transmission occurs when the electromagnetic radiation does not interact with matter. In general, the transmission is only partial and is characterised by the transmittance ( $T_\lambda$ ), given by:

$$T_\lambda = \frac{I_x}{I_0} \quad \text{Eq. 2.42}$$

$I_0$  is the intensity of the incident radiation and  $I_x$  is the intensity of the radiation exiting the matter. The transmittance is also described by Beer-Lambert law, given by:

$$I_x = I_0 \exp(-\alpha x) \quad \text{Eq. 2.43}$$

$\alpha$  is the adsorption coefficient of the substance and  $x$  is the distance the light travels through the substance.

The transmittance is also related to the absorbance ( $A_\lambda$ ), given by:

$$A_\lambda = \frac{I_0 - I}{I_0} \quad \text{Eq. 2.44}$$

$$A_{\lambda} = -\log_{10} T_{\lambda} \quad \text{Eq. 2.45}$$

- Absorption occurs when photons with the proper energy are absorbed by particles, promoting the transition from a lower energy to higher energy states. There are certain rules deduced from quantum mechanics that govern which transitions are allowed or forbidden. These are called the selection rules. The selection rule for absorption states that the transition dipole moment must be non-zero. The oscillating field associated with a radiation must be able to induce a dipole oscillating in the molecule, such that it leads to the transition between two states.

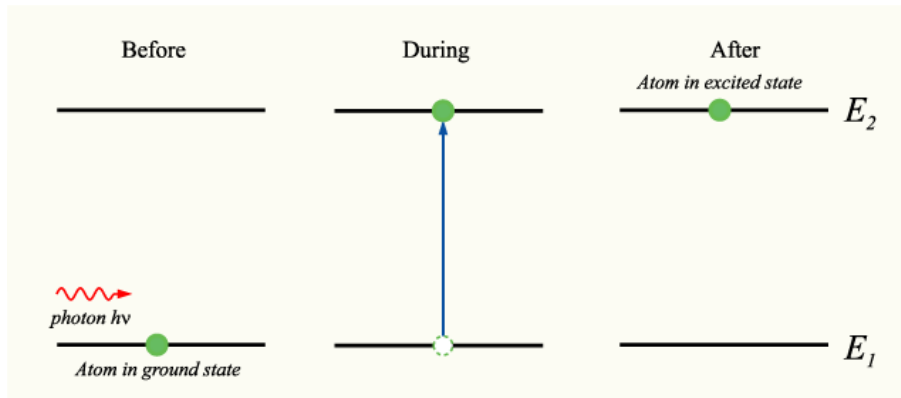


Figure 2.14: The absorption process showing the atom in the ground state being promoted to an excited state due to interaction with a photon with the correct energy. Adapted from [15].

- Emission occurs when a particle undergoes a transition from a higher energy to a lower energy state. A photon with energy similar to the energy difference between the two states is released. Emission can occur by two different mechanisms: spontaneous emission and stimulated emission. In spectroscopy, we are only concerned with spontaneous emission.

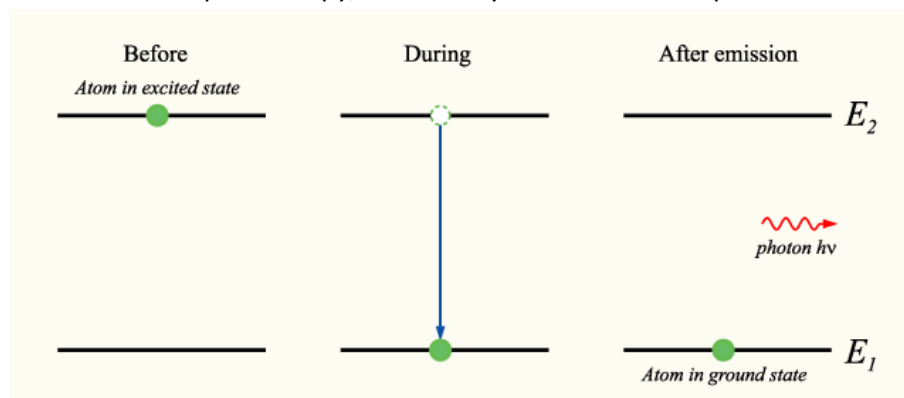


Figure 2.15: Spontaneous emission of a photon when an atom decays from an excited state to the ground state [15].

- Scattering occurs when photons interact with electrons in matter. This interaction causes a change in direction of the photon. Scattering is due to the interaction between the oscillating electric field of the electromagnetic wave acting on the charge of individual particles. Scattering phenomena may be elastic in which the wavelength of the incident radiation do not change or inelastic in which changes in the wavelength occur.

### 2.7.5 Infrared and Raman Spectroscopies

Infrared (IR) and Raman spectroscopies are used to obtain information on the structure and environment of atoms or molecules. This is done by studying the vibration state of different bonds in the molecule. The interaction mechanisms that occur in IR and Raman spectroscopies are indicated in Figure 2.16.

For IR spectroscopy, the main interaction mechanism is radiation absorption. A photon with wavelength in the IR spectral range is absorbed by a molecule, promoting it from a vibrational state with a lower energy to a vibrational state with a higher energy. During this transition, the electric dipole moment of the molecule must change. This is the selection rule for IR, which can be stated mathematically as:

$$\left(\frac{\partial p}{\partial x}\right) \neq 0 \quad \text{Eq. 2.46}$$

$p$  is the dipole moment and  $x$  is the distance.

The interaction mechanism in Raman spectroscopy is the inelastic scattering of the photons as they interact with the electron clouds of a molecule. When a particle is irradiated by a monochromatic radiation, most photons will undergo Rayleigh scattering. Rayleigh scattering is the elastic scattering of electromagnetic radiation by particles with sizes that are much smaller than the wavelength of the electromagnetic radiation. In an energy level diagram, this can be thought of as the promotion of the particle from a lower vibrational energy state to a virtual energy state and then a demotion back to the original lower vibrational energy state. This changes the direction of the photon but does not change its wavelength, hence the energy of the photon and the vibrational energy state of the molecule remain the same. However, a very small fraction of photons (around  $10^{-7}$ ) will undergo inelastic scattering, known as Raman scattering. Raman scattering occurs in two forms, known as Stokes and anti-Stokes. In Stokes Raman scattering, the photon will have longer wavelength (and lower energy) after the scattering process. The vibrational state of the particle also changes as there is a transition from a lower to a higher vibrational energy states. In anti-Stokes Raman scattering, the photon will have a shorter wavelength after the scattering process, and there is a transition from a higher to lower vibrational energy states in the particle. For both the Raman Stokes and anti-Stokes scatterings, the polarisability ( $\alpha$ ) in a molecule is changed during the normal vibration. This is the selection rule for Raman which can be mathematically stated as:

$$\left(\frac{\partial \alpha}{\partial Q}\right) \neq 0 \quad \text{Eq. 2.47}$$

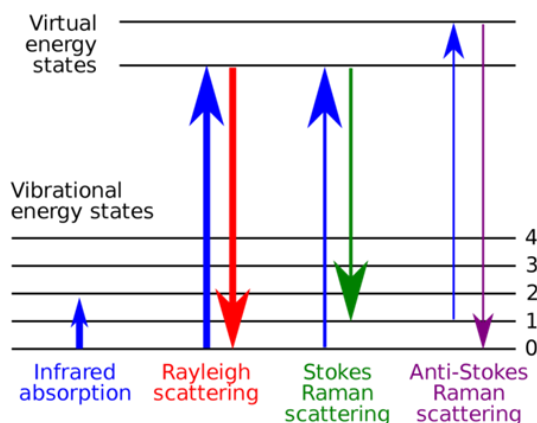


Figure 2.16: Energy levels of infrared and Raman spectroscopies [16].

IR spectroscopy can only detect vibrational transitions that involve changes in the dipole moment of the molecule whereas Raman spectroscopy can only detect vibrational transitions that involve a change in the polarisability of the molecule. Thus, IR and Raman spectroscopies are complimentary and they are often used in conjunction with each other.

## 2.7.6 Interpretation of IR and Raman spectra: Complicating factors

When interpreting IR or Raman spectra, several factors can complicate the assignment of the vibrational bands. The three main complicating factors are: Overtone and combination bands, Fermi resonance and coupling.

### 2.7.6.1 Overtone and combination bands

The fundamental vibration frequency of a molecule occurs when there is a transition from a vibrational state corresponding to  $\nu = 0$  to another state at  $\nu = 1$ , where  $\nu$  is the vibrational quantum number. The overtone bands can be described as the multiple of the fundamental vibration frequency [12]. The first overtone corresponds to the transition from  $\nu = 0$  to  $\nu = 2$ , the second overtone from  $\nu = 0$  to  $\nu = 3$  and etc. In the spectra, the first overtone band will show up at a wavenumber around twice the wavenumber of the fundamental band.

When two or more fundamental vibrations are excited simultaneously, they may form a combination band [12]. The combination band will appear at the wavenumber corresponding to the sum of the wavenumbers of all the fundamental vibrations involved.

### 2.7.6.2 Fermi resonance

When two different bands have wavenumbers that are similar, the wave function of the two bands can combine. This causes a shift in the wavenumber of the two bands and the equalisation of their IR or Raman intensities. The two shifted vibrational bands are known as a Fermi doublet [12]. The most common occurrence of a Fermi doublet is between a fundamental band and an overtone or combination band. It is impossible to determine the actual wavenumber and intensities from the original two vibrations due to the mixed wave function.

### 2.7.6.3 Coupling

When a molecule has a backbone, such as hydrocarbon chains, the vibration of the bonds in the molecular backbone can be coupled together, especially when all the bonds in the localised area experience the same type of motion [12]. This causes the energy levels to mix and the bands can no longer be assigned to one bond.

## 2.8 Structural characterisation of ionic liquid

Although the electrochemical and physical properties of ionic liquids are described extensively in literature, very little information is known on the actual structure and mechanism during electrodeposition from ionic liquid because of the complex interaction between cations and anions in an ionic liquid [10]. In order to fully understand the electrodeposition process, it is important to study the effect of speciation on the mechanism and growth of the film as well as the double-layer structure at the electrode-solution interface [10]. In other words, we must study the structure of the pure ionic liquid (solvent) and ionic liquid solution (solvent and solute) in the absence of an electric field, as well as the structure between the electrolyte and electrode in the presence of the electrode's electric field. Knowledge of these structures is essential for the selection and design of suitable ionic liquid [10]. Unlike a solid solution, the structure of the ionic liquid cannot be observed by direct methods such as microscopy and must be inferred indirectly. The most efficient method used to probe the structure of ionic liquid is through vibrational spectroscopy, such as Raman and infrared spectroscopies. These structures can be inferred from their molecular vibration as discussed in Section 2.7. Due to the complexity of the structures and interactions in ionic liquids, theoretical calculations, such as calculations based on the density functional theory (DFT) are usually carried out to compliment the information obtained from vibrational spectroscopies [175].

In the last two decades, vibrational spectroscopy has been used to characterise the structure of many common imidazolium based ionic liquids such as Imidazolium hexafluorophosphate [C<sub>2-4</sub>MIM] [PF<sub>6</sub>] [176-178], Imidazolium tetrafluoroborate [C<sub>2-4</sub>MIM] [BF<sub>4</sub>] [178-181], Imidazolium trifluoromethanesulfonate [C<sub>2-4</sub>MIM] [TFO] [182], Imidazolium ethylsulfate [C<sub>2-4</sub>MIM] [EtSO<sub>4</sub>] [183,184], and Imidazolium bis(fluorosulfonyl)imide [C<sub>2-4</sub>MIM] [TFSI] [185,176,186,183]. As the ionic liquids used in this study are [EMIM] [TFSI] and [EMIM] [EtSO<sub>4</sub>], a more detailed discussion about their structure is given below.

Many studies have been carried out on ionic liquids with the [TFSI] based anion in view of their potential application as electrolytes for lithium ion batteries due to the large availability of lithium bis(trifluoromethylsulfonyl)amide (LiTFSI) [10]. By combining infrared and Raman spectroscopies with theoretical calculation, it has been shown that the TFSI<sup>-</sup> anion exists as two conformers: the transoid (C<sub>2</sub>) conformer and the cisoid (C<sub>1</sub>) conformer. The former is predicted to be more energetically favourable than the latter [185,23,187-189]. In an ionic liquid, the conformation of [TFSI] depends on the structure of the imidazolium ring [190]. In most cases, the transoid form is slightly more energetically favourable than the cisoid form, in line with the theoretical prediction. Quantum mechanical calculation for metal-[TFSI] based solid salt showed that the transoid is more stable by 2.7 kJ mol<sup>-1</sup> [191] and for the [EMIM] [TFSI] ionic liquid, it is more stable by about 3.5 [192], 4.5 [193] or 3.4-5.0 [66] kJ mol<sup>-1</sup>. Lassegues et al. [191] found that the population of the transoid form of [TFSI]

is around 75%. They also found that the vibrational bands of [TFSI] anion are influenced by both the ionic interaction and conformational effects.

Ionic liquids based on the [EtSO<sub>4</sub>] anion have not been widely studied. Nevertheless, Raman and infrared spectroscopies for the [EMIM] [EtSO<sub>4</sub>] ionic liquid were carried out by Kiefer et al. [183]. The data of these authors was later analysed by Dhumal et al. [184] using theoretical ab-initio calculations, and the structure of [EMIM] [EtSO<sub>4</sub>] and vibrational peaks assignment were deduced from these calculations.

Aside from the anions, many studies have been carried out on the [EMIM] cation. For example, Umebayashi et al. [176] carried out vibrational spectroscopy and density functional theory (DFT) calculations on four different ionic liquids to study the effects of the anion on the EMIM ion. They showed that EMIM ion in 1-Ethyl-3-methylimidazolium base ionic liquid existed as non-planar or planar conformers in equilibrium in its liquid salts and the influence of the anionic environment on the equilibrium was minimum [176]. The nature of the bond between the [EMIM] cation and various anions was investigated and some studies showed that these bonds were electrostatically active, while others suggested the possible existence of H-bonds [194,195]. Lassegues et al. [196] investigated the C-H stretching region in imidazolium based ionic liquids with weakly coordinating anions and they proposed a new assignment for the peak at 3105 cm<sup>-1</sup> as the combination and overtone of the ring mode in Fermi resonance, previously assigned as the stretching of the C<sub>(2)</sub>H in the imidazolium ring [182,197]. This was confirmed by Grondin et al. [194], who revisited the vibrational assignments in imidazolium based ionic liquids obtained from the Raman and infrared spectroscopies. Vibrational analysis of the imidazolium based ionic liquids in the spectra range of 2-300 cm<sup>-1</sup> showed that intermolecular interactions were the main contributor for the spectra in this region and such analysis can be used to probe the interaction between the imidazolium cation and the anions [198-203].

Besides the structure of pure ionic liquids, the structure involving a mixture of several substances with ionic liquids has also been explored by spectroscopy, supported by theoretical calculations. Probe molecules have also been used to investigate the structure of some ionic liquids. The solvation of Li<sup>+</sup> in [TFSI] based ionic liquids has been investigated by Raman and IR spectroscopies with the help of DFT calculations, in view of their potential application in lithium ion batteries [204-207]. The results showed that Li<sup>+</sup> ion was most likely coordinated by two bidentate [TFSI] anions [204-207]. Q.G. Zhang et al. [208] investigated the hydrogen bonds between [EMIM] [EtSO<sub>4</sub>] and water, and Sarkar et al. [209] studied the interactions between [EMIM] [EtSO<sub>4</sub>] and water or alcohol. Miki et al. [210] showed that unusual water configurations were observed in 1-butyl-3-methylimidazolium tetrachloroferrate [BMIM] [FeCl<sub>4</sub>] exposed to atmosphere by using Raman spectroscopy. Fujisawa et al. [211] determined the acceptor number of various ionic liquids at room temperature by using diphenylcyclopropanone (DPCP) and phenol blue (PB) as probe molecules. Stricker et al. [212] studied the interaction between [TFSI] based ionic liquids and salts based on Cu(TFSI) and Ag(TFSI) in order to determine their reactivity and structural properties. They found that the [TFSI] anions served as ligands in the metal complexes, contrary to their original assumption that [TFSI] would be weakly coordinated to the metal cation due to its structure. The strong bonds formed with the metal ions involved the nitrogen atom on the [TFSI] anion. A similar study was carried out by Eiden et al. [213] on 1.6 M AlCl<sub>3</sub> solutions in [BMPyr] [TFSI] and [EMIM] [TFSI], which was used in their previous study on the electrodeposition of aluminium [171]. The authors found that both mixtures separated

into two liquid phases, the lower phase contained octahedral complex of  $\text{Al}(\text{TFSI})_3$  with free TFSI ions, and the upper phase contained solids of  $[\text{BMPyr}][\text{AlCl}_4]$  and  $[\text{EMIM}][\text{AlCl}_4]$  respectively, with trace amounts of  $\text{Al}(\text{TFSI})_3$  and free  $[\text{TFSI}]$  ions. Sarkar et al. [214] investigated the photon-induced electron transfer of  $[\text{EMIM}][\text{EtSO}_4]$  ionic liquid binary mixtures with water, methanol and 2-Propanol in order to determine the changes in molecular interactions and resulting properties. A similar study was carried out by Noack et al. [215] on the binary mixture of  $[\text{EMIM}][\text{EtSO}_4]$  ionic liquid with water, methanol and ethanol.

The structure of the double-layer region in ionic liquids has only been studied quite recently. These structures cannot be described by using models established for aqueous solutions [216,217] and new models supported by DFT calculations have been proposed [218,219]. One study carried out on  $[\text{EMIM}][\text{BF}_4]$  and  $[\text{EMIM}][\text{TFSI}]$  proposed a model where the cations and anions were arranged in alternating multiple layers [217]. These types of studies require the integration of both electrochemistry and spectroscopy setups. One of the first of these studies was carried out by Baldelli et al. [220-222] which probed the arrangement of the ions of  $[\text{BMIM}][\text{BF}_4]$ ,  $[\text{BMIM}][\text{PF}_6]$  and  $[\text{BMIM}][\text{DCA}]$  at a Pt electrode by sum frequency generation vibrational spectroscopy (SFG), electrochemical impedance spectroscopy (EIS), and the vibrational Stark effect [220-222]. The vibrational Stark effect is the shifting and splitting of the vibrational frequency due to the presence of the electric field [220,221]. The Stark effect can be used to probe the local electric field, which in turn can be used to estimate the thickness of the double-layer by using CO molecules adsorbed on the electrode as a probe. Baldelli et al. [221,220] found that the imidazolium rings orientated themselves such that they were almost parallel to the electrode, although the exact orientation was influenced by the anion. They concluded that the ions of  $[\text{EMIM}][\text{BF}_4]$  were organised in a single-ion thick Helmholtz layer on the Pt electrode surface while for  $[\text{EMIM}][\text{DCA}]$ , a five-ion thick layer was formed [220-222]. Baldelli et al. [223] further investigated the effect of different substrates on the double-layer structure with  $[\text{EMIM}][\text{BF}_4]$ . They used different dielectric, semiconductors and metallic electrodes and found that the double-layer followed a Helmholtz type model due to charge neutralisation on the surface [223]. They found no evidence of double- or multilayer structure for  $[\text{EMIM}][\text{BF}_4]$  [223]. The results for  $[\text{BMIM}][\text{PF}_6]$  were validated by Santos et al. [224], using surface enhanced Raman spectroscopy (SERS) on a silver electrode. They found that the  $[\text{BMIM}]$  cations were adsorbed on silver when the potential was more negative than -0.4 V vs Pt QRE. From -0.4 to -1.0 V, the Raman spectra of  $[\text{BMIM}][\text{PF}_6]$  were similar to those of the same liquid in the absence of an electric field, but above -1.0 V the  $[\text{BMIM}]$  cations arranged themselves such that the imidazolium rings were parallel to the substrate surface [224]. Similar experiments were also carried out by Yuan et al. [225] on  $[\text{BMIM}][\text{BF}_4]$  and  $[\text{BMIM}][\text{Br}]$  on a copper electrode. The authors found that the  $[\text{EMIM}]$  cation lay parallel to the substrate [225].

### 3 Materials and Experimental Methods

#### 3.1 Experimental materials

In this study, two different ionic liquid-based systems were used as shown in Table 3.1. The first system was based on the 1-ethyl-3-methylimidazolium ethylsulfate [EMIM] [EtSO<sub>4</sub>] with three different copper salts, namely, copper (I) chloride (CuCl), copper (II) chloride (CuCl<sub>2</sub>·2H<sub>2</sub>O) and copper (II) sulphate pentahydrate (CuSO<sub>4</sub>·5H<sub>2</sub>O). The second system was based on the 1-ethyl-3-methylimidazolium bis(trifluoromethylsulfonyl)imide [EMIM] [TFSI] with three specially designed metallic salts provided by the industrial partner of this study, Solvionic: Silver (I) bis(trifluoromethylsulfonyl)imide (AgTFSI), copper (II) bis(trifluoromethylsulfonyl)imide (Cu(TFSI)<sub>2</sub>) and aluminium (III) bis(trifluoromethylsulfonyl)imide (Al(TFSI)<sub>3</sub>).

Table 3.1: Electrolytes used in this study.

	Materials	Formula & abbreviation	Grade
System 1	1-ethyl-3-methylimidazolium ethylsulfate	[EMIM] [EtSO <sub>4</sub> ]	for synthesis, Merck ≥99%
	copper (I) chloride	CuCl	
	copper (II) chloride	CuCl <sub>2</sub> ·2H <sub>2</sub> O	
	copper (II) sulfate	CuSO <sub>4</sub> ·5H <sub>2</sub> O	
	Anhydrous copper (II) chloride	CuCl <sub>2</sub>	Sigma-Aldrich ≥99%
System 2	1-ethyl-3-methylimidazolium bis(trifluoromethylsulfonyl)imide	[EMIM] [TFSI]	Solvionic 99.9%
	Silver (I) bis(trifluoromethylsulfonyl)imide	AgTFSI	Solvionic 99.5%
	copper (II) bis(trifluoromethylsulfonyl)imide	Cu(TFSI) <sub>2</sub>	Solvionic 99.5%
	aluminium (III) bis(trifluoromethylsulfonyl)imide	Al(TFSI) <sub>3</sub>	Solvionic 99.5%

#### 3.2 Environmental control

Water contamination in the electrolyte can have a big impact on the electrolyte properties as well as on the electrodeposited film. As both the ionic liquids and metallic salts are hygroscopic, there was a need to provide a controlled water-free environment in order to obtain consistent, reproducible results. For this reason, the material preparation and experiments were carried out in a glove box.

In Instituto Superior Técnico (IST, Lisbon), the glove box system used was a UniLab, MBraun (Figure 3.1) and in University Bordeaux 1 (UB1, Bordeaux), the glove box system used was a MBRAUN MB150-GI. In both cases, the working environment was high purity argon gas constantly circulated through a H<sub>2</sub>O / O<sub>2</sub> purifier column. The purity of the working atmosphere was periodically checked by using a water and oxygen analyser to ensure that the oxygen and water contents were kept below 1 ppm. To ensure the efficiency of the purification system, the purifier column was periodically regenerated by using a gas mixture of 95% argon and 5% hydrogen. The pressure inside



the glove box was kept at a value between 5 to 6 bars, in comparison to the atmospheric pressure of 1 bar. This is to ensure that no atmospheric contamination can occur.

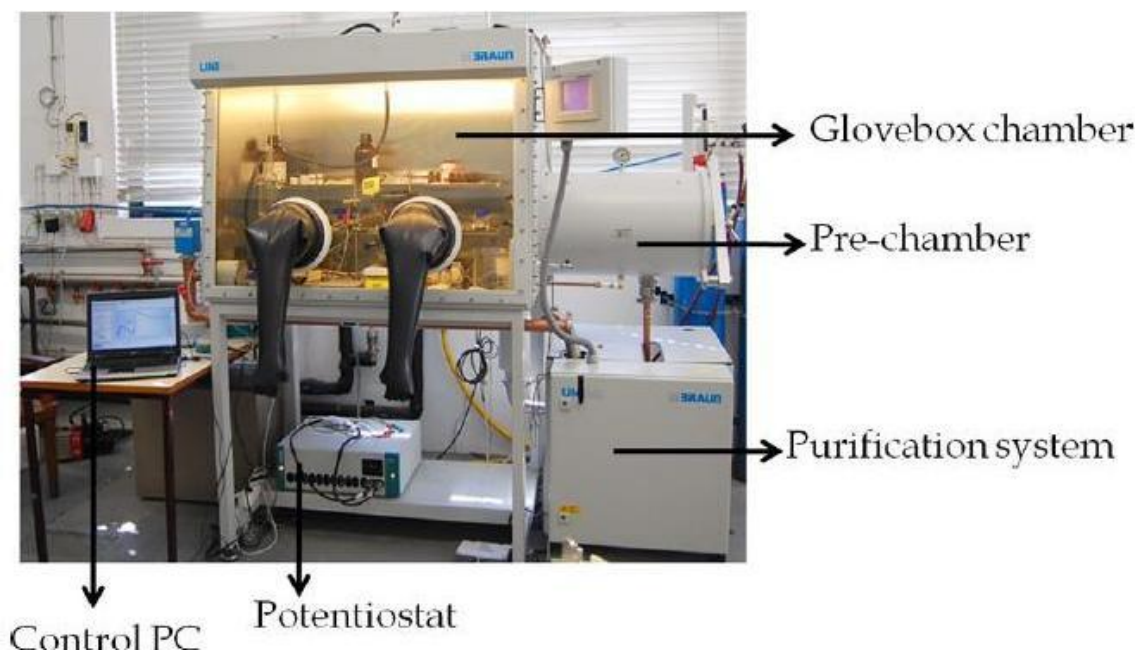


Figure 3.1: The UniLab, MBraun glove box system used at Instituto Superior Técnico [11].

### 3.3 Preparation of the materials

#### 3.3.1 Metallic salts preparation

As the copper salts used in System 1 (Table 3.1) were not anhydrous and were initially exposed to the atmosphere, they had to be dried in order to reduce the water content. The  $\text{CuCl}$ ,  $\text{CuCl}_2 \cdot 2\text{H}_2\text{O}$  and  $\text{CuSO}_4 \cdot 5\text{H}_2\text{O}$  salts were placed in an oven at a temperature above  $100^\circ\text{C}$  and for a period of at least 72 hours. Table 3.2 shows the changes in the colour of the salts as a result of the drying process. The salts of  $\text{AgTFSI}$ ,  $\text{Cu(TFSI)}_2$  and  $\text{Al(TFSI)}_3$  used in system 2 were anhydrous so no further preparations were done. All the salts were kept in the glove box.

Table 3.2: Colour of the copper salts used in System 1 electrolytes before and after the drying process.

Metallic Salts	Colour before drying	Colour after drying	Anhydrous salt colour in literature
$\text{CuCl}$	Light green	Pale green	White
$\text{CuCl}_2 \cdot 2\text{H}_2\text{O}$	Light blue	Coffee brown	Yellowish brown
$\text{CuSO}_4 \cdot 5\text{H}_2\text{O}$	Dark blue	Pale blue	Greyish white

#### 3.3.2 Solution preparation

For the electrochemical and electrodeposition experiments done in IST, further treatment was carried out on both the  $[\text{EMIM}][\text{EtSO}_4]$  and  $[\text{EMIM}][\text{TFSI}]$  in order to reduce their water content. The ionic liquids were heated to  $80^\circ\text{C}$  and dried under vacuum for 72 hours in the glove box. For

Raman and infrared (IR) spectroscopy experiments done in UB1, both the [EMIM] [EtSO<sub>4</sub>] and [EMIM] [TFSI] were used as received.

The electrolytes were prepared by dissolving the salts into the ionic liquid. For the electrochemical characterisation and electrodeposition experiments, only small concentrations of salts were needed in order to obtain a working electrolyte, as shown in Table 3.3. The required mass of the salt was accurately measured and dissolved in a fixed volume of ionic liquid.

For Raman and IR spectroscopies, higher concentrations of the salts were required compared to the electrodeposition experiments in order to obtain detectable changes in the spectra signature. Various concentrations of the ionic liquid solutions were prepared by accurately weighting the metal salts and ionic liquids, as shown in Table 3.4. The two were mixed together, according to the molar ratio calculated by (1-x) [ionic liquid]-(x) [metal salt], where x the mole fraction was set at a range of 0<x<0.2. To ensure the complete dissolution of the salts, the solutions were mechanically agitated by using a magnetic stirrer at a temperature of 35 °C for at least 24 hours.

Table 3.3: Composition of the electrolytes used for the electrochemical and electrodeposition experiments.

Solvent	Volume (mL)	Salt	Concentration (M)
[EMIM] [EtSO <sub>4</sub> ]	10	CuCl	<0.1
	10	CuCl <sub>2</sub>	0.1
	10	CuSO <sub>4</sub>	<0.1
[EMIM] [TFSI]	1	Ag(TFSI)	0.05
	1	Cu(TFSI) <sub>2</sub>	0.01
	1	Cu(TFSI) <sub>2</sub>	0.05
	1	Al(TFSI) <sub>3</sub>	0.05

Table 3.4: Composition of the solutions used for Raman and IR spectroscopies.

System 1		System 2	
Solvent (mole fraction)	Salt (mole fraction)	Solvent (mole fraction)	Salt (mole fraction)
[EMIM] [EtSO <sub>4</sub> ]	CuCl <sub>2</sub>	[EMIM] [TFSI]	Ag(TFSI)
1	0	1	0
0.98	0.02	0.95	0.05
0.95	0.05	0.925	0.075
0.925	0.075	0.90	0.10
0.90	0.10	0.875	0.125
0.85	0.15	0.85	0.15
0.825	0.175	0.80	0.20
0.80	0.20		

### 3.4 Electrochemical characterisation of the solution

The experimental setup for our electrochemical characterisation experiments is shown in Figure 3.2. All electrochemical experiments were carried out inside the glove box, using an AutoLAB PGSTAT100 potentiostat with Nova 1.5 software. The potentiostat was connected to the electrochemical cell in the glove box and a computer with the control software outside of the glove box. An electrochemical cell with a three-electrode configuration was used. The working electrode is where the reaction that we would like to analyse took place. The potentiostat was used to control the potential at the working electrode, by varying it with respect to the potential at the reference electrode. The reference electrode is an electrode with a stable potential. As no current flows through the reference electrode, a counter electrode was needed to pass all the current through the electrochemical cell. The temperature of the electrolyte was controlled by a heater connected to a thermometer. The cell is provided with a magnetic stirrer to mechanically agitate the electrolyte.

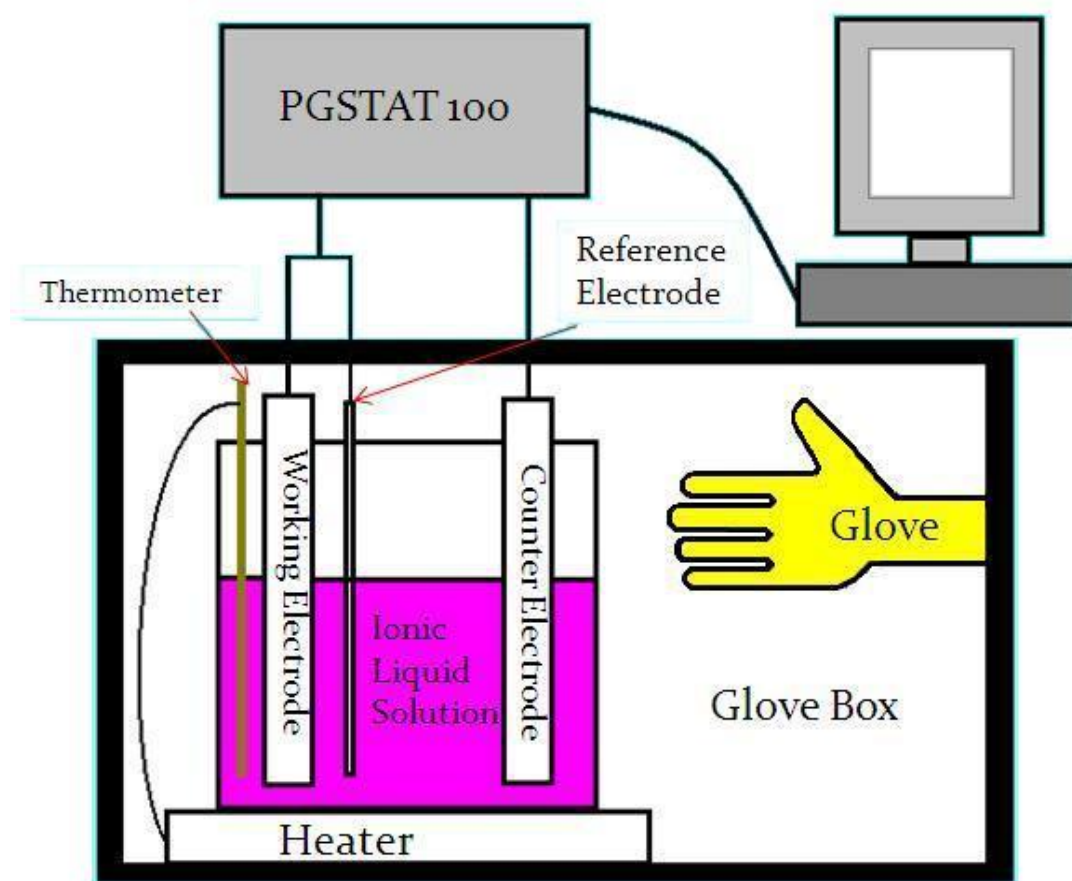


Figure 3.2: Experimental setup for the electrochemical characterisation and electrodeposition experiments.

For system 1 (Table 3.1), a three-electrode Metrohm electrochemical cell was used. The cell had a capacity of 50 mL although in our typical electrochemical experiments, only 10 mL of electrolyte volume was used. The working electrode was a glassy carbon disc (Metrohm) with an area of 0.071 cm<sup>2</sup>. The counter electrode was a platinum foil (Metrohm) with an area of 1.0 cm<sup>2</sup>. A platinum wire was used as a quasi-reference electrode (QRE).

For system 2 (Table 3.1), a three-electrode BASi low volume C-2 electrochemical cell was used. The cell could hold a minimum electrolyte volume of 0.2 mL and between 0.2 to 0.3 mL of electrolyte was used for each test. The working electrodes were a glassy carbon (BASi) and platinum (BASi) discs with an area of 0.071 and 0.020 cm<sup>2</sup>, respectively. The counter electrode was a platinum wire (BASi) with a 0.5 mm diameter. A silver wire was used as a QRE.

After each experiment, the working, counter and reference electrodes were thoroughly rinsed with copious amount of tap water and dried. The electrodes were then wiped down with acetone and placed in an ultrasonic bath for 15 minutes in acetone. Finally, they were rinsed with distilled water and blow-dried.

### 3.4.1 Cyclic voltammetry

Cyclic voltammetry is a potential sweep method whereby a continuously varying potential is applied to the working electrode and the resulting change in the electrical current with respect to the potential is recorded [29,8]. The current-potential graph obtained is known as a cyclic voltammogram. For a full cycle cyclic voltammogram, the change in electrical current is recorded by first sweeping the potential in the cathodic direction from the open-circuit potential ( $E_{op}$ ) to a predetermined highest potential value ( $E_{max}$ ) and then in the anodic direction up to a predetermined lowest potential value ( $E_{min}$ ) and finally back to the starting potential (Figure 3.3 a). The process can be repeated if more than one cycle is needed. The potential of the cyclic voltammogram can also be swept in the opposite direction.

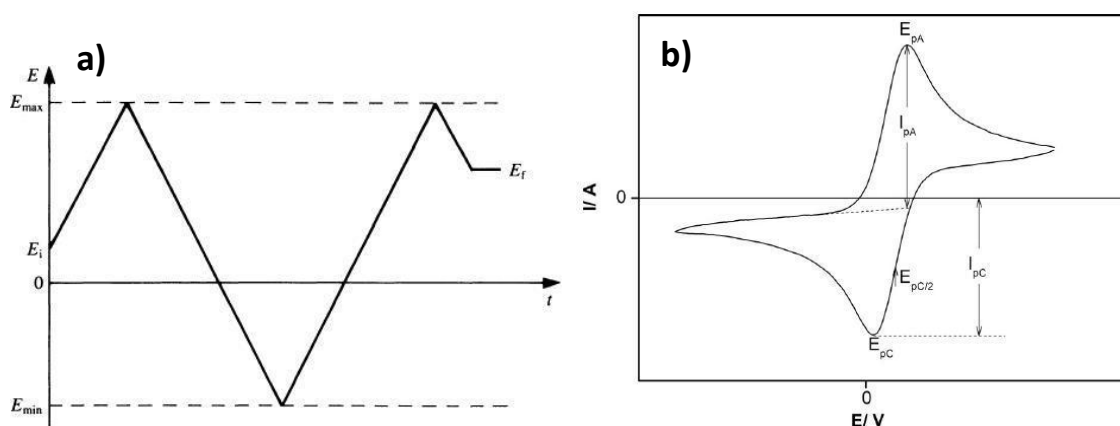


Figure 3.3: **a)** The variation of the potential with time for one full cycle of a cyclic voltammogram [8]. **b)** A cyclic voltammogram for a simple reversible reaction involving a one oxidation and one reduction process.  $Fc^+/Fc$  couple of ferrocene in [BMIM]  $[BF_4]$  ionic liquid, adapted from [11].

An example of a cyclic voltammogram involving a simple reversible one-electron transfer reaction,  $O + ne^- \rightarrow R$ , is shown in Figure 3.3 b. The redox couple is made of  $O$ , the oxidant, and  $R$ , the reductant. Initially in the electrolyte solution, there is only the oxidant  $O$ . As the potential is swept to the negative direction, only a very low current will flow as the potential is not high enough to cause the electron transfer reaction affecting species  $O$ . Thus, this current flow is due the capacitive current, where the electrode and electrolyte act as a capacitor [8]. As the potential becomes more negative, at a certain point the potential is high enough for the reduction of species  $O$  to occur. This causes

the current to increase until it reaches a maximum peak current of reduction ( $I_{pc}$ ). The rate of this reaction is governed by the Nernst equation, given by [29,8]:

$$E = E^\circ - \frac{RT}{nF} \sum v_i \ln \frac{[O]}{[R]} \quad \text{Eq. 3.1}$$

$E$  is the equilibrium electrode potential,  $E^\circ$  is the standard electrode potential,  $v_i$  is the stoichiometric numbers and  $a_i$  is the activity of the species  $i$ .

The concentration of the oxidant  $O$  at the vicinity of the electrode surface decreases and the concentration of reductant  $R$  increases as the potential becomes more negative. For a reversible process, the electron transfer rate is very rapid. The current,  $i$ , measured as the potential decreases, is directly related to diffusion rate of the oxidised species to the electrode surface from the bulk solution, governed by Fick's law.

$$\frac{\partial [O]}{\partial t} = D_O \frac{\partial^2 [O]}{\partial x^2} \quad \text{Eq. 3.2}$$

$$\frac{\partial [R]}{\partial t} = D_R \frac{\partial^2 [R]}{\partial x^2} \quad \text{Eq. 3.3}$$

The continuous consumption of the electroactive species  $O$  means that the concentration gradient between the bulk and interface will increase. At a certain potential, just before the potential corresponding to the maximum peak current, the supply of the electroactive species falls as the diffusion rate of species  $O$  cannot keep up with the electron transfer reaction. The current will then start to decay until the potential reaches the minimum pre-determined potential value ( $E_{min}$ ). This peak is known as the reduction peak.

As the potential starts to sweep in the positive direction, the potential is still large enough for the electron transfer reaction of species  $O$  to proceed but the current decreases as the potential becomes more positive. At a certain potential, the current switches signs, indicating that the opposite reaction is occurring ( $R - ne^- \rightarrow O$ ). The potential then reaches a certain positive value that is high enough for the oxidation reaction of species  $R$  to occur. The current increases until it reaches a maximum value analogous to what happened in the reduction process but in the opposite direction. This is the maximum peak current of oxidation ( $I_{pA}$ ). As the electroactive species  $R$  is further depleted, the current will decrease until the potential reach the maximum pre-determined potential value ( $E_{max}$ ).

The important experimental parameters that can be varied in a cyclic voltammetry experiment are [8]:

- Initial and final potential,  $E_i$  and  $E_f$   
It is important to choose  $E_i$  and  $E_f$  in a region in which reduction or oxidation reactions do not occur, as the reduction and oxidation peaks might not be shown.
- The initial sweep direction  
For quasi-reversible and irreversible reactions, the sweep direction affects the peak current so it is important to have the cyclic voltammogram in both directions.
- The sweep rate,  $v$

The sweep rate has a huge impact on the reversibility of a reaction.

- The predetermined minimum and maximum potential,  $E_{min}$  and  $E_{max}$

It is important to choose  $E_{min}$  and  $E_{max}$  values that are within the electrochemical window of the solvent, as well as in the correct range to observe the reaction of the electroactive species under study.

- Number of cycles

The shape of the cyclic voltammogram in the first cycle may be different from the shape in subsequent cycles, due, for example, to the initial processes on the electrode surface. Changes in the shape of the cyclic voltammogram in the subsequent cycles may also indicate that the electrolyte is not stable within the potential range used.

Cyclic voltammetry is a very useful technique that can be used to characterise an unknown electrolyte system. It can be used to obtain information on the electroactive species behaviour in the system, the type of reactions and mechanisms, the kinetics of these reactions and formation mechanism of new phases deposited on the surface of the electrode [8].

The identity of the electroactive species and the reaction type can be determined from the oxidation and reduction peak potentials,  $E_{pA}$  and  $E_{pC}$  of the cyclic voltammogram, such as the ones in Figure 3.3 **b**. As explained above, the sign of the peak's current in the cyclic voltammogram corresponds to the direction of the reaction, which allows us to determine whether a reaction is a reduction or an oxidation. For a cyclic voltammogram with multiple oxidation and reduction peaks, the peaks may be caused by different phenomena. One possibility is when there are more than one electroactive species in the electrolyte. Each peak corresponds to a reaction affecting a particular electroactive species [8]. The second possibility is that one of the electroactive species has more than one electrovalent state. Each peak then corresponds to the transition from one valence state to another [8]. This is very common when a transition metal is one of the electroactive species. An example is copper, which usually has two reduction peaks and two oxidation peaks corresponding to the oxidation and reduction of copper (II) to copper (I) and copper (I) to copper (0).

Cyclic voltammograms can also be used to study the mechanism controlling the electrochemical reaction kinetics. The two common mechanisms are known as the reversible (diffusion controlled) and irreversible (electron transfer kinetic controlled) process. For a reversible process, the rate of electron transfer is much faster than the rate of mass transport of the electroactive species from the bulk solution to the electrode/electrolyte interface. Hence the electrochemical reaction kinetic is said to be controlled by the diffusion of the electroactive species in the liquid [8]. For an irreversible process, the rate of mass transport is much faster than the rate of electron transfer [8]. So the electrochemical process is controlled by the kinetics of the reaction. From the shape of the cyclic voltammogram, we can tell whether a process is reversible, quasi-reversible or irreversible. The reversibility of the electrochemical reaction is heavily influenced by the sweep rate ( $\nu$ ) and the standard rate constant ( $k$ ). For stationary planar electrodes, this relationship is given by [29,8]:

- Reversible reaction,  $k \gg 0.3\nu^{1/2}$
- Quasi-reversible reaction,  $0.3\nu^{1/2} > k > 2 \times 10^{-5} \nu^{1/2} \text{ cm s}^{-1}$
- Irreversible reaction,  $k < 2 \times 10^{-5} \nu^{1/2} \text{ cm s}^{-1}$

Some of the data recorded from the cyclic voltammogram can be used to identify a reversible reaction. They are [29,8]:

- $I_p = v^{1/2}$  Eq. 3.4

- $E_p$  is independent of  $v$
- $|E_p - E_{p/2}| = 2.2RT/nF$  Eq. 3.5

- $E_{p,a} - E_{p,c} = 2.3RT/nF$  ( $E_\lambda \leq E_{p,c}$  or  $E_\lambda \geq E_{p,a}$ ) Eq. 3.6

- $|I_{p,a}/I_{p,c}| = 1$  Eq. 3.7

$I_p$  is the peak current density,  $E_p$  is the peak potential,  $E_{p/2}$  is the potential when the current density is half of the peak current density,  $E_{p,a}$  is the oxidation peak potential,  $E_{p,c}$  is the reduction peak potential,  $I_{p,a}$  is the oxidation peak current density and  $I_{p,c}$  is the reduction peak current density.

The criteria for an irreversible reaction are not as well defined as that for a reversible reaction, although there are a few indications that can help with the identification [8]:

- The anodic and cathodic peaks are separated over a large distance and are independent of each other
- There is a current decay when the sweeping direction is inverted
- The peaks are usually located at a large overpotential
- Changing the sweep rate ( $v$ ) will change  $E_p$
- The larger the sweep rate ( $v$ ), the broader and lower are the peaks

Due to the slower rate of electron transfer compared to the rate of mass transport in irreversible electrochemical reactions, a large kinetic barrier must be overcome. This is usually achieved by applying extra energy to the system, which manifests itself as a larger potential difference when compared to the case of a reversible reaction. The extra potential is known as the overpotential,  $\eta_v$ . The rate of the electrochemical reaction can be related to overpotential by the Tafel equation:

$$I = nFk \exp\left(\pm \alpha F \frac{\eta_v}{RT}\right) \quad \text{Eq. 3.8}$$

The plus sign relates to the anodic reaction and the minus sign relates to the cathodic reaction.  $\alpha$  is the current exchange coefficient.

### 3.4.2 Chronoamperometry

Chronoamperometry is a technique whereby initially, a potential at which no electrode reactions occur is applied to the solution (This potential was applied for 25 seconds for all chronoamperometry experiments in this study). Then, the potential is stepped up to a potential where specific electroactive species will react at its peak rate, and the change in diffusion-limited current over a 30 s time period is recorded. The potential step and a typical current response are shown in Figure 3.4.

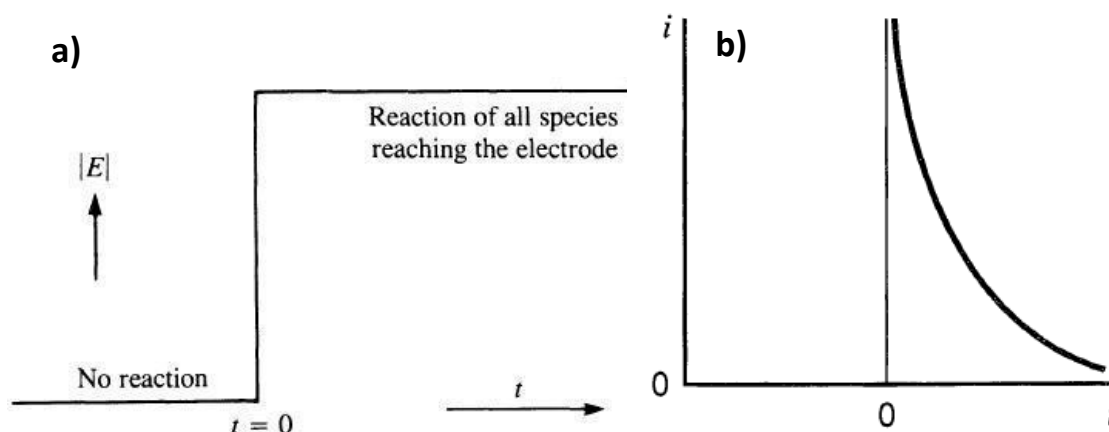


Figure 3.4: **a)** Potential step to obtain the diffusion limited current of the electroactive species [8]. **b)** Chronoamperograms showing a typical current response.

We can extract the data from the chronoamperometry curve to build a plot of the current density versus  $(\text{time})^{-1/2}$ . Rearranging the Cottrell equation [8,7], we have:

$$i(t) = \frac{nFAD^{1/2}C_{\infty}}{\pi}(t)^{-1/2} \quad \text{Eq. 3.8}$$

$i$  is the current,  $n$  is the number of electrons per mole of reaction,  $F$  is the Faraday constant,  $A$  is the electrode area,  $D$  is the diffusion coefficient,  $C$  is the initial concentration of the electroactive species undergoing reduction and  $t$  is the time

The diffusion coefficient of the ionic species in solution can be determined from the slope of the current density versus  $(\text{time})^{-1/2}$  curve.

### 3.5 Electrodeposition experiments

All electrodeposition experiments were carried out by using the fixed potential method over a period of time. The electrodeposition experiment setup was similar to that used in the electrochemical characterisation, except that nickel plates (Goodfellow, 99.99%) with a thickness of 0.125 mm were used as the working electrode. For system 1, Ni plates with a working area of 5 x 5 mm<sup>2</sup> were used and for system 2 the working area was 3 x 3 mm<sup>2</sup>. The rest of the fixed parameters were similar to those mentioned in Sections 3.1-3.3. Almost every aspect of the electrodeposition setup had an influence on the morphology and properties of the deposited films, thus it was important to fix some of the parameters.

#### 3.5.1 Pre-electrodeposition substrate treatment

Our nickel plates were polished by 800-grits SiC paper for 30 minutes, followed by a diamond paste polish (3 μm particle size) for 15 minutes. The Ni plates were then cut to the correct dimensions and ultra-sonicated for 15 minutes in distilled water. A subsequent ultra-sonication for 15 minutes in acetone was used for degreasing. The surfaces were activated by immersion in 33% vol. of H<sub>2</sub>SO<sub>4</sub> acid for 5 minutes. After activation, the substrates were thoroughly rinsed with distilled water and blow-dried.



### 3.5.2 Electrodeposition experimental parameters

In this study, the films were deposited by controlling three experimental parameters: the deposition potential, time and temperature. Appropriate values of the deposition potential were obtained by consulting the cyclic voltammogram of each individual system and performing trial runs to observe changes in the film structure. The deposition time was fixed at 900, 1800 and 3600 s. These provide a good window to see the morphological evolution of the films, from the first glimpse of the deposit to the final structure of a thick film. The deposition temperature was fixed at 35, 50 and 85 °C.

### 3.5.3 Post-electrodeposition film treatment

After each of our electrodeposition experiments, the substrates were rinsed with deionised water and ultra-sonicated for 5 minutes in order to wash away the excess electrolyte. The films were then dried and prepared for characterisation.

## 3.6 Characterisation of the films

The films obtained by electrodeposition were characterised by using several techniques. In this section, we will give a brief description on the basic principle and the role of each technique used.

### 3.6.1 Scanning electron microscope (SEM)

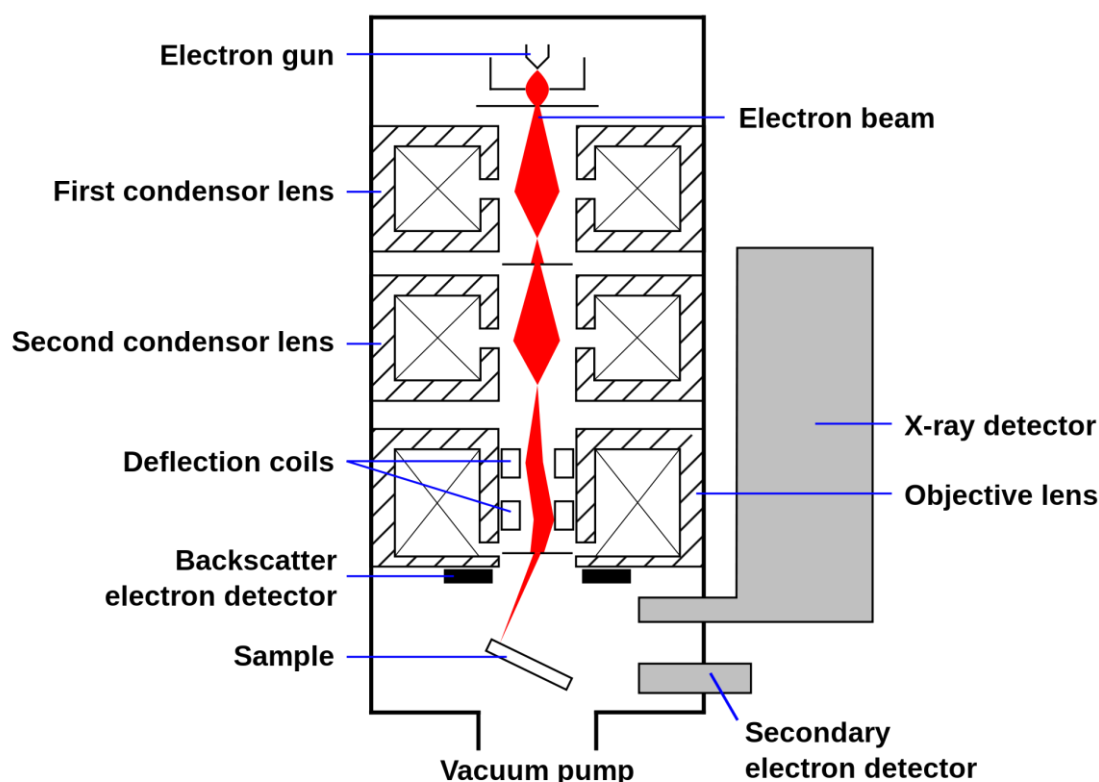


Figure 3.5: Schematic representation of a scanning electron microscope [17].

The microstructure, surface topography and elemental composition of the deposited films were analysed by scanning electron microscopy (SEM) and energy dispersive X-ray spectroscopy (EDX)

using a Hitachi S-2400 and JEOL JSM-7001F scanning electron microscopes. This information was obtained by detecting the signals from the interaction between the high energy electron beam and the sample. The schematic representation of the SEM is shown in Figure 3.5. The electrons are generated using either a thermionic electron gun (Hitachi S-2400) or a field emission gun (JEOL JSM-7001F) and accelerated towards the sample up to a voltage of 30 keV [226,20]. Most of the SEM observation in this study was carried out with an acceleration voltage of 15 keV. The electron beam passes through two or three condenser lenses which control the diameter of the beam as it is accelerated towards the sample [226,20]. The beam is then scanned across the sample by deflection coils in a raster-like pattern [226,20]. The electrons and radiation emitted due to the interaction between the electron beam and the samples are collected by various detectors. The intensity of the detected signals as a function of the position of the incident beam are used to form the images [11]. The equipment operates under vacuum to prevent the interaction of electrons with air molecules and sample oxidation [226].

The products of the interaction between the electron beam and the atoms in the sample are shown in Figure 3.6. The main interaction phenomena are elastic and inelastic scattering of the incident electrons. Elastic scattering is a process where the direction of the primary electrons is changed without a detectable change in their kinetic energy [20]. Inelastic scattering is a process where there is a loss of energy from the primary electrons [20]. The interaction products include secondary and backscattered electrons, Auger electrons, characteristic and continuum (*bremstrahlung*) X-rays, electromagnetic radiation in the ultraviolet, visible and infrared ranges, electron-hole pairs, lattice vibrations (phonons) and electron oscillations (plasmons) [11]. The interaction volume between the primary electrons and the sample has a pear shape and the region where signals from the secondary effect may reach the detectors are shown in Figure 3.7.

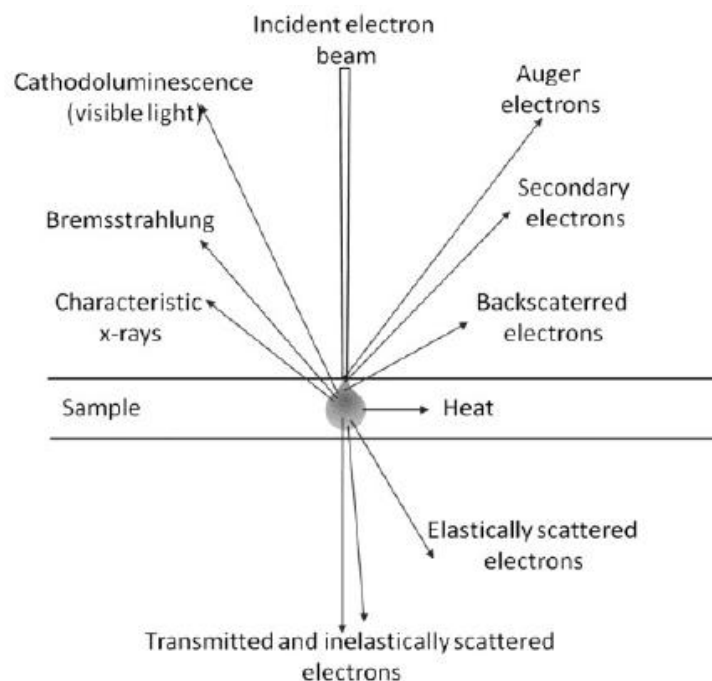


Figure 3.6: Interactions observed between the electron beam and a sample [18,11].

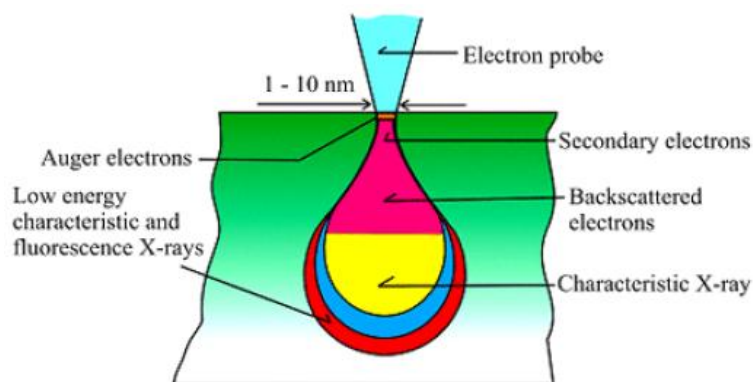


Figure 3.7: The interaction volume showing the region from which the various signals may reach the detectors.

### 3.6.1.1 Secondary electron imaging (SEI)

Secondary electrons are valence electrons that gain energy after interacting with inelastically scattered primary electrons. A small part of the acquired energy is used to break the bonds between the valence electron and the nucleus and the rest of this energy will be converted into kinetic energy when the valence electron is ejected from the atom. These secondary electrons will undergo inelastic scattering themselves until they escape from the sample surface or are reabsorbed within the sample. As the kinetic energy of the secondary electrons is very low (a typical value is below 100 eV), only electrons coming from 1-2 nm below the surface can escape from the sample, as shown in Figure 3.7 [226,20]. Hence secondary electrons provide information about the surface morphology of the sample rather than the underlying bulk structure. Images obtained by using this technique are said to provide a topographical contrast [226,20].

### 3.6.1.2 Backscattered electron imaging (BEI)

Backscattered electrons are primary electrons that undergo elastic scattering in the sample with only a small loss in energy [226]. Backscattered electrons can be distinguished from secondary electrons by their much higher kinetic energy [226]. The intensity of the backscattered signal carries information about the chemical composition of the sample, because the backscattering coefficient is proportional to the atomic number of the atoms in the interaction volume [226,11]. Hence, images obtained by using backscattered electron imaging will present contrast for different chemical composition, whereby areas with heavier elements appearing brighter than those containing lower atomic number.

### 3.6.1.3 Energy-dispersive X-ray spectroscopy (EDX)

As the highly energetic primary electrons interact with the atoms in the interaction volume, they may excite and eject an electron from the inner shell of an atom. This creates a vacancy, thereby leaving the atom in an excited state. As this vacancy is filled by an electron from the outer shell, the difference in energy between the outer shell and the inner shell (usually K, L and M) can be released as a photon, which usually has energy that lies in the X-ray portion of the electromagnetic spectrum. As the difference in energies between the different outer and inner shells of each element is unique

due to their unique atomic structure, the energy of the X-ray released can be used to identify the element. Hence, X-rays released this way are known as characteristic X-rays.

In this study, characteristic X-rays were detected by using an Oxford 70 X-ray spectrometer attached to a JEOL JSM-7001F FEG-SEM. Qualitative and semi-qualitative analyses of the EDX spectra were performed by using Oxford's INCA software, the peak positions in the spectra being compared with a database for elemental identification. The quantification included correction for the effect of atomic number, absorption and fluorescence (ZAF correction) according to the equation[18,11]:

$$c = ZAFK \quad \text{Eq. 3.9}$$

**Z**, **A** and **F** are factors related to the average atomic number of the sample, absorption of the X-ray radiation and fluorescence of the matrix respectively and **K** is the ratio of the concentrations between the specimen and a standard measured under the same experimental conditions [11].

### 3.6.2 Transmission electron microscope (TEM)

TEM observation was carried out with a Hitachi 8100 LaB6 transmission electron microscope at a 200 kV acceleration voltage. Similar to the SEM, the underlying mechanism is based on the interaction between a primary electron beam and the sample. However unlike the SEM, only the electrons that have been transmitted through the sample are used to form the images (Figure 3.6). Hence, very thin samples with thickness less than 150 nm are required for this technique [11,227]. In this study, the TEM samples were prepared by detaching fragments of the electrodeposited films from the substrate with a scalpel and placing these fragments on a formvar-coated 200 mesh Cu grid.

A schematic representation of a TEM is shown in Figure 3.8. Like the SEM, TEM columns operate in a vacuum to prevent the interaction between electrons and air molecules [226,11]. The electrons are generated by using thermionic and field-emission guns similar to those found in the SEM but at a much higher acceleration voltage, typically between 40-400 keV [20]. The primary electron beam is then focused onto the specimen by using a number of condenser lenses [226,20]. The interplay between the objective and intermediate lenses can then be used to show the sample object in real space via imaging or in reciprocal space via diffraction patterns, such as the one shown in Figure 3.9 [226,20,11]. The images or diffraction patterns are then magnified and projected onto a fluorescent screen and captured by using a charge coupled diode (CCD) sensor [11].

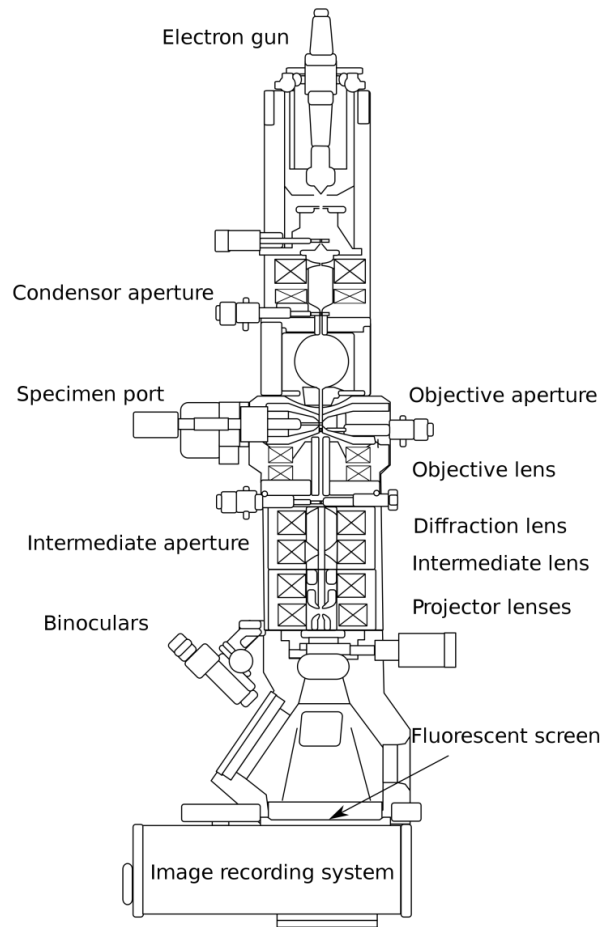


Figure 3.8: Schematic representation of a Transmission Electron Microscope [11,19].

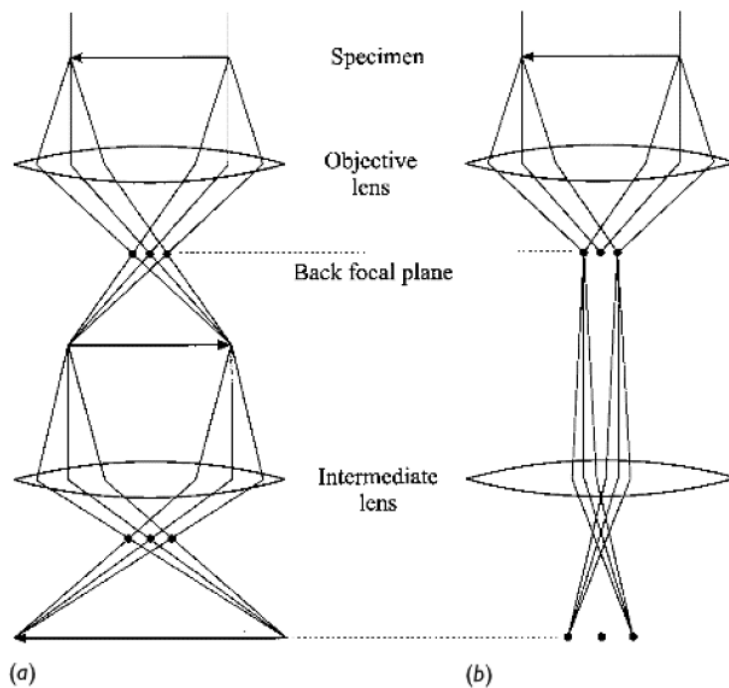


Figure 3.9: The interplay between the objective and intermediate lens in **a)** imaging mode and **b)** diffraction mode [20].

### 3.6.2.1 Imaging modes

In this study, the TEM images were acquired in bright-field (BF) mode, where only electrons from the unscattered transmitted beam were used to form the image [20]. After the electron beam was transmitted through the sample, the objective lens formed an intermediate image as shown in Figure 3.10 a. When the lenses were focused in this image plane, the image was magnified by the intermediate and projector lenses, and projected onto a screen [20]. In imaging mode, the contrast arose from differences in the average atomic mass of the sample constituents (mass contrast), non-uniform distribution of the sample thickness (thickness contrast) and diffraction contrast resulting from diffraction of the incident electron beam by the crystallographic structure of the material [226,11,227].

### 3.6.2.2 Diffraction mode

The electron diffraction patterns were obtained by using the selected area diffraction (SAD) mode, where an area of the sample was chosen by using an aperture that blocks out the electron beam from other unwanted areas [20]. The diffraction information was located in the back focal plane as shown in Figure 3.10 b. When the intermediate lenses were focused on the back focal plane of the objective, the diffraction pattern was projected onto the screen [226]. In diffraction mode, the electrons were diffracted by the atoms organised in a crystallographic structure to form a pattern which could be analysed to retrieve information on its crystallographic structure and defects [11,227].

## 3.6.3 Glancing angle X-ray Diffraction (GA-XRD)

The basic principle of X-ray diffraction is based on the arrangement of the atoms in a material. A solid composed of atoms arranged in a periodic pattern in three dimensions is known as a crystal [228]. When X-rays are diffracted by a crystal, it scatters in both a constructive and destructive manner [228]. Constructive interference only occurs at a specific wavelength ( $\lambda$ ) and incident angle of the X-rays, such that a very large peak can be observed in the diffracted X-ray pattern. The diffraction angle is given by Bragg's law, which relates the distance between atomic planes ( $d$ ) with the angle of incident radiation ( $\theta$ ) [228]:

$$n\lambda = 2d \sin\theta \quad \text{Eq. 3.10}$$

The phases in the electrodeposited films and their crystallographic structures were studied by using X-ray diffraction. Since the films were very thin, with thicknesses of a few microns or less, glancing angle geometry was employed by using a Siemens D5000 diffractometer and Cu K $\alpha$  radiation. The angle was fixed at 1° in relation to the sample surface (Figure 3.10 b) and the diffractometer scanned over a 2 $\theta$  angle between 40° to 80° by moving the detector over the goniometer [11]. This configuration had a lower penetration depth than the Bragg-Brentano geometry (Figure 3.10 a) [11]. A diffractogram showing the diffracted intensity of the X-rays over the 2 $\theta$  angle was obtained. For multiphase materials, the diffractogram would be a weighted average of the individual diffraction patterns of each phase, proportional to their volume fraction and taking into consideration other factors affecting the diffracted intensity, such as textures and the configuration and crystallographic structure of the phases [11]. Phase identification was performed by using the Hanawalt method [228,11], where the position of the three most intense peaks in the diffractogram were compared

with a database containing known diffractograms of pure substances (Joint Committee on Powder Diffraction Standards (JCPDS) database [11]).

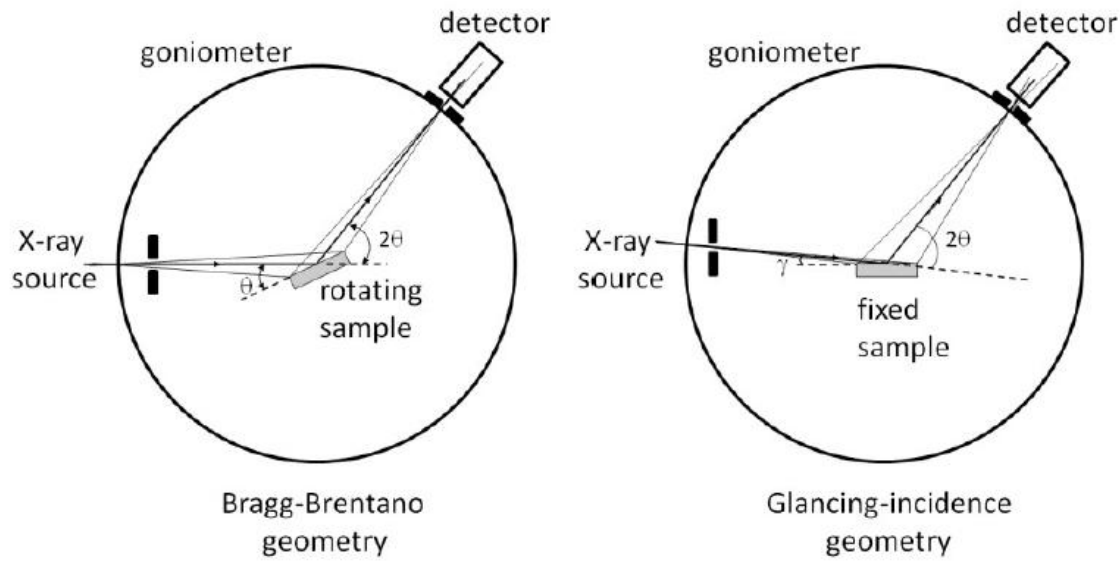


Figure 3.10: The two common geometries used in X-ray diffraction experiments. **a)** Bragg-Brentano Geometry and **b)** Glancing Angle Geometry [11].

The film crystallite size of the electrodeposited films can be estimated from the diffraction peak broadening using Scherrer's equation, given by:

$$t = \frac{0.9\lambda}{B \cos \theta} \quad \text{Eq. 3.11}$$

$\lambda$  is the wavelength of the incident X-rays in nm,  $B$  is the peak width at half maximum (FWHM) in radians, and  $\theta$  is the Bragg angle in radians.

### 3.6.4 Nano-indentation

Nano-indentation experiments were carried out by using a Micro Materials Ltd NanoTest system equipped with a Berkovich diamond indenter. The indentation rig is located inside a specially designed chamber to shield it against vibration, acoustic noise, temperature variations and air draughts [229]. The indentation area was selected by using an optical microscope. A typical nano-indentation experiment was carried out by using a loading and unloading cycle, with a typical load displacement curve as shown in Figure 3.11. Initially, an increasing load was applied until the maximum load was reached [229]. At this maximum, the load was held over a specified period of time (dwell period) to allow the material to flow [229]. Unloading was then performed after the dwell period. In order to reduce the statistical error, at least 80 measurements were carried out for each sample.

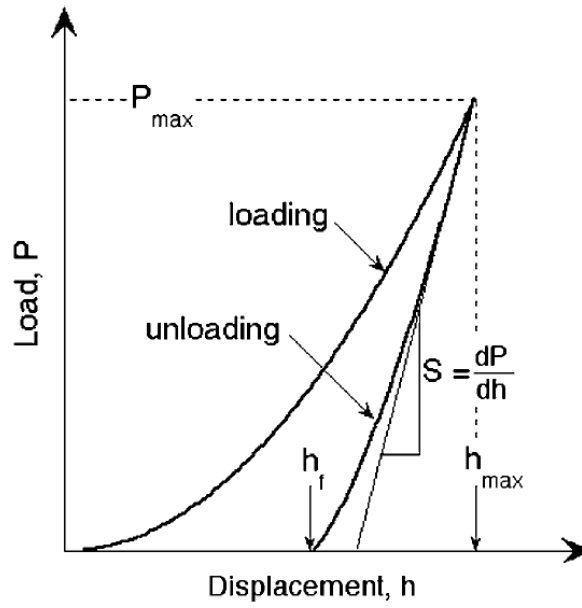


Figure 3.11: A typical load-displacement curve obtained from a nanoindentation experiment [21].

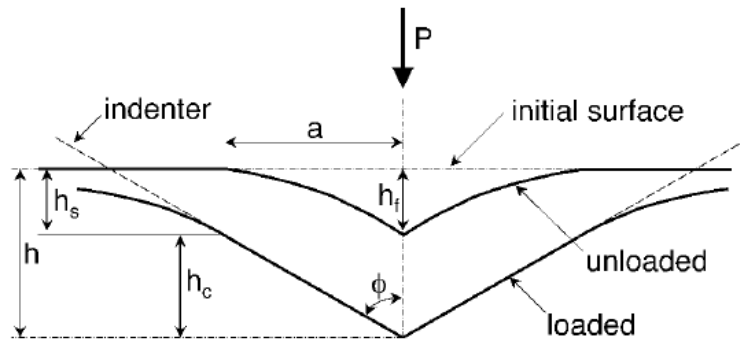


Figure 3.12: Parameters describing the relationship between the contact geometry on the sample surface during loading and unloading [22].

The hardness of the electrodeposited thin films were measured by load control, where the maximum test force and number of load increments were set [229]. In order to reduce the influence from the substrate, a suitable maximum load ( $P_{max}$ ) with a penetration depth less than 20% of the film thickness was chosen for each experiment. Using the known geometry of the Berkovich tip, the displacement area ( $A_r$ ) can be determined and the hardness ( $H$ ) of the films is given by [229]:

$$H = \frac{P_{max}}{A_r} \quad \text{Eq. 3.12}$$

During unloading, the slope of the initial part of the unloading curve corresponding to the elastic deformation of the material could be used to determine the stiffness ( $S$ ) of the contact, given by:

$$S = \frac{dP}{dh} \quad \text{Eq. 3.13}$$

$P$  is the load and  $h$  is the displacement.

The reduced Young's Modulus ( $E_r$ ) can be obtained from the stiffness by using:



$$E_r = \frac{1}{\beta} \frac{\sqrt{\pi}}{2} \frac{S}{\sqrt{A_p}} \quad \text{Eq. 3.14}$$

$\beta$  is the geometrical constant and  $A_p$  is the projected area, which for a Berkovich indenter is given by:

$$A_p = 4.896 h_c^2 \quad \text{Eq. 3.15}$$

$h_c$  is difference in penetration depth in the loaded and unloaded conditions, as shown in Figure 3.12.

The indentation modulus ( $E_{IT}$ ), which provides similar values to the Young's modulus for the sample is given by[229]:

$$E_{IT} = \frac{1 - (v_s)^2}{\frac{1}{E_r} - \frac{1 - (v_i)^2}{E_i}} \quad \text{Eq. 3.16}$$

$s$  and  $i$  refer to the properties of the sample and indenter, respectively, and  $\nu$  is the Poisson's ratio.

### 3.7 Structural characterisation of the solution

Information on the molecular interactions and chemical environment in the pure ionic liquids and their solution were studied by Raman and IR spectroscopies. These were done by studying the molecular vibrations in the liquid, which had energy ranges corresponding to the far-infrared region of 200 to 400  $\text{cm}^{-1}$  and the mid-infrared region of 400 to 4000  $\text{cm}^{-1}$ . Due to the complexities in the ionic liquid structure and interactions, density functional theory (DFT) calculations were also carried out to provide additional help for the assignment of the vibrational spectra.

#### 3.7.1 Fourier transformed infrared (IR) spectroscopy

IR experiments were performed in transmission mode from the far-IR range between 50 to 650  $\text{cm}^{-1}$  and the mid-IR range between 400 to 4000  $\text{cm}^{-1}$  in transmission mode by using a Nicolet 6700 FT-IR spectrometer. For the far-IR and mid-IR regions, polyethylene (PE) and potassium bromide (KBr) windows were used to encapsulate the ionic liquid samples. Great care was taken in order to ensure an even spreading of the sample solutions between the two windows. The "thickness" of the sample solutions between the windows was also controlled in order to obtain spectra with a detectable signal. Sample preparations were done in a glove box in order to minimise exposure to the atmosphere.

Correction for the reflective index was needed for the ATR-IR spectra obtained in this study before a comparison can be made with the IR spectra in the literature, which were usually obtained in the transmission mode. The ATR-IR spectra were corrected by using the OMNIC software with the refractive index values of the ionic liquids given by the suppliers. For [EMIM] [TFSI], the refractive index is 1.42 (Solvionic) and for [EMIM] [EtSO<sub>4</sub>], the refractive index is 1.48 (Sigma Aldrich). These reflective indices for the ionic liquids were also checked by using the Abbe Refractometer NAR-1Tsolid and they were found to be in good agreement with the values provided by the suppliers. The

corrected ATR spectra were compared with the IR spectra obtained in transmission mode and they were found to be in good agreement.

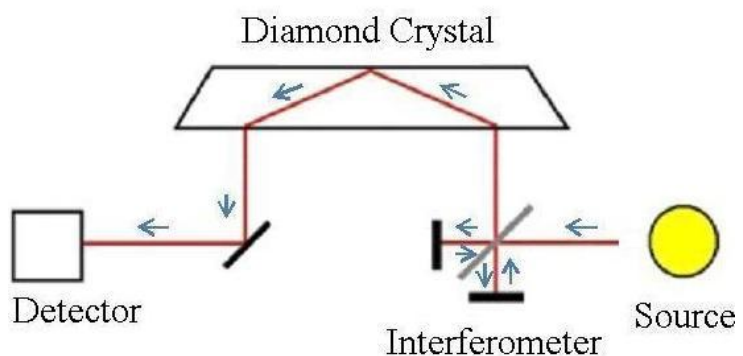


Figure 3.13: Schematic showing a typical attenuated total reflectance (ATR) cell.

The IR spectra for both the [EMIM] [TFSI] and [EMIM] [EtSO<sub>4</sub>] solutions had to be normalised to compare the changes in the spectra due to the increasing concentration of the metal salts. The far-IR spectra were normalised by fitting the intensity of the band at 343 cm<sup>-1</sup> which corresponded to the bending of the CNCH<sub>2</sub> group in the cation. The mid-IR spectra were normalized by fitting the intensity of the band at 1574 cm<sup>-1</sup> which corresponded to the vibration of the ring of EMIM cation. These bands were chosen as previous studies have shown that they remain relatively unchanged from the perturbation due to the anion [194].

### 3.7.2 Raman spectroscopy

Raman experiments were performed from 200 to 3500 cm<sup>-1</sup> on a Labram 800 Jobin Yvon Horiba spectrometer using a Kr laser with wavelength of 752.45 nm. This wavelength was selected in order to avoid fluorescence. The laser was focused with an ultra-long working distance (ULWD) 50x lens onto the ionic liquid solution sample. The scattered light was focused onto the slit of the spectrometer which had a 600 groove mm<sup>-1</sup> grating, giving a spectral resolution of around 2 cm<sup>-1</sup>. The spectrally resolved Raman signal was detected using an air cooled charge coupled device (CCD) detector ANDOR.

The Raman spectra were normalized by fitting the Raman intensity of the band at 960 cm<sup>-1</sup> which corresponded to the vibration of the ethyl group of the EMIM cation. Previous studies have shown that this band remained relatively unchanged from any perturbation due to the metal complex formation in ionic liquids [194].

The depolarisation ratio  $\rho$  was obtained from the Raman vertically polarised spectra,  $I_{VV}$ , and horizontally polarised spectra,  $I_{HV}$ . The polarisations of the incident light were controlled using a half-wave plate. The depolarisation ratio is given by the formula:

$$\rho = \frac{I_{HV}}{I_{VV}} \quad \text{Eq. 3.17}$$

The depolarisation ratio helps with the assignment of peaks, as it provides information on the symmetry of the molecule. A depolarisation ratio of  $0 \leq \rho < 0.75$  indicates a symmetric vibration mode while a depolarisation ratio of 0.75 indicates that other modes of vibration are present.

## 4 Vibrational Spectroscopy of Ionic Liquid-based Electrolytes

The solvation mechanisms of metal salts in an ionic liquid (IL) electrolyte are not well-understood. This is due to the complexity of their structural organisation induced by the nano-segregation phenomenon in polar and non-polar domains [10,190]. Understanding the interactions involved in the solvation mechanisms is important in order to understand the electrodeposition behaviour and, in turn, help with the design electrochemical baths which would allow the deposition of films with optimised composition and deposition efficiency. Solvation of the metal salts in IL leads to the formation of metal complexes, in which the structures of the metal complexes have a great effect on the electrodeposition properties, such as the diffusion of the charge carriers, the film nucleation and growth process as well as the structure and morphology of the film [10]. In this context, vibrational spectroscopies (infrared (IR) absorption and Raman scattering) are well-adapted to the task of probing the interactions between the metallic cations and anions in solution, as well as probing the composition of the first shell of neighbours in ionic liquids and their solutions [107,230,231,182,232,192,198,193,203,233,234,105,200,235,29].

In this chapter, we report our investigation on the physico-chemical properties of ionic liquid electrolytes used in our study. The investigation was carried out by means of vibrational spectroscopy. Our objectives were to determine the nature of interactions between the species of the ionic liquid-based electrolyte and metal ions from the dissolution of the metal salts. From this, the structure and organisation of the first shell of solvation would be deduced from the changes in the vibrational spectral signatures. In our experiments, vibrational spectroscopic measurements were only carried out for the solutions of  $\text{CuCl}_2$  / [EMIM]  $[\text{EtSO}_4]$  and  $\text{AgTFSI}$  / [EMIM] [TFSI] because the salts in other solutions investigated in our study did not provide detectable spectral signatures because of their low solubility. The vibrational spectra were obtained over a large spectral range ( $200\text{--}4000\text{ cm}^{-1}$ ), and their evolution with the concentration of salt was investigated. Any new vibrational bands and perturbations in the spectral were interpreted in terms of the complexes formed by the metal ion with the ionic liquid species in solution. Interpretation of the experimental IR absorption and Raman spectra was aided by theoretical calculations based on Density Functional Theory (DFT).

### 4.1 [EMIM] [TFSI] ionic liquid system

#### 4.1.1 Raman and infrared spectra of pure [EMIM] [TFSI]

Our experimental Raman and IR spectra of pure 1-ethyl-3-methyl-imidazolium bis(trifluoromethylsulfonyl)imide [EMIM] [TFSI] are shown in Figures 4.1 and 4.2. These spectra are in good agreement with those reported in the literature [185,176,186,183,196].

The information recovered from the Raman scattering and IR absorption spectra is complimentary because of the distinct selection rules of these spectroscopic techniques. The vibrational spectra of [EMIM] [TFSI] ionic liquid has been widely reported in literature [185,176,186,183,187]. A complete assignment of the spectra for pure [EMIM] [TFSI] can be carried out based on the findings of these studies which are summarised in Annex 1 (Table A1.3). The complete assignment of the spectra was also verified in our study. Both spectra show two distinct regions: the region of C-H stretching modes ( $2700\text{--}3250\text{ cm}^{-1}$ ) and the region of other internal modes, below  $1650\text{ cm}^{-1}$ .

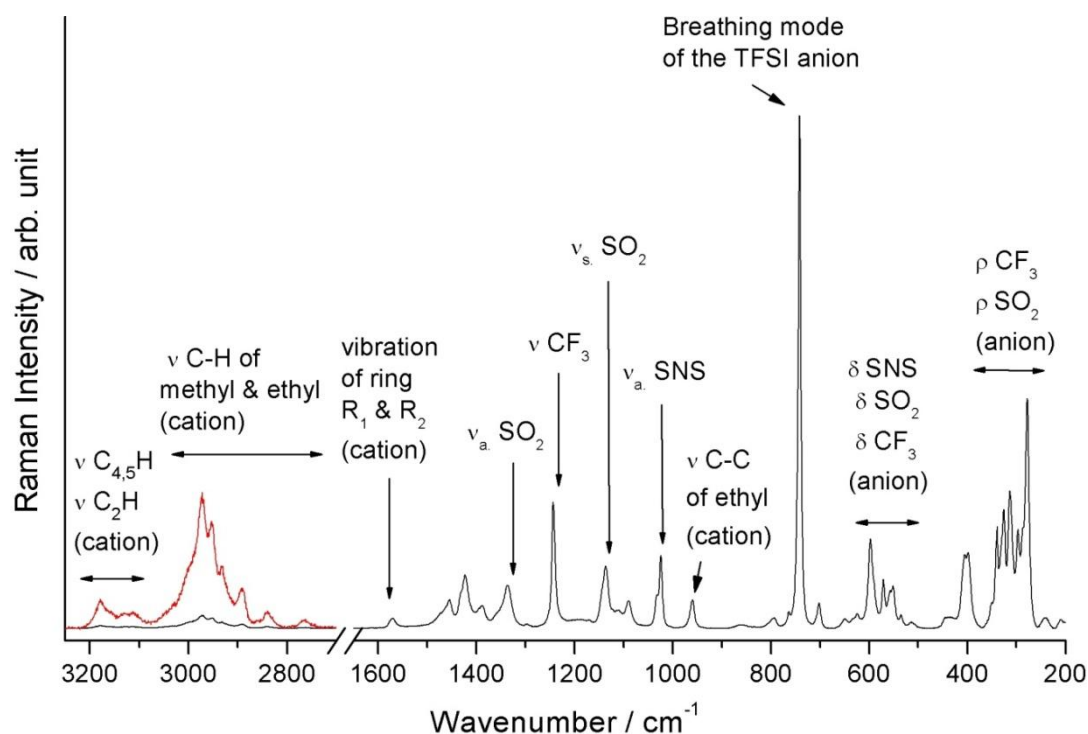


Figure 4.1: Raman spectrum of pure [EMIM] [TFSI] ionic liquid in the spectral region 200-3250  $\text{cm}^{-1}$ . The bands from the C-H stretching region (2700-3250  $\text{cm}^{-1}$ ) are magnified for clarity. Vibrational modes are indicated with the symbols:  $\nu$  = stretching;  $\delta$  = bending;  $\rho$  = rocking;  $s$  = symmetric;  $as$  = asymmetric.

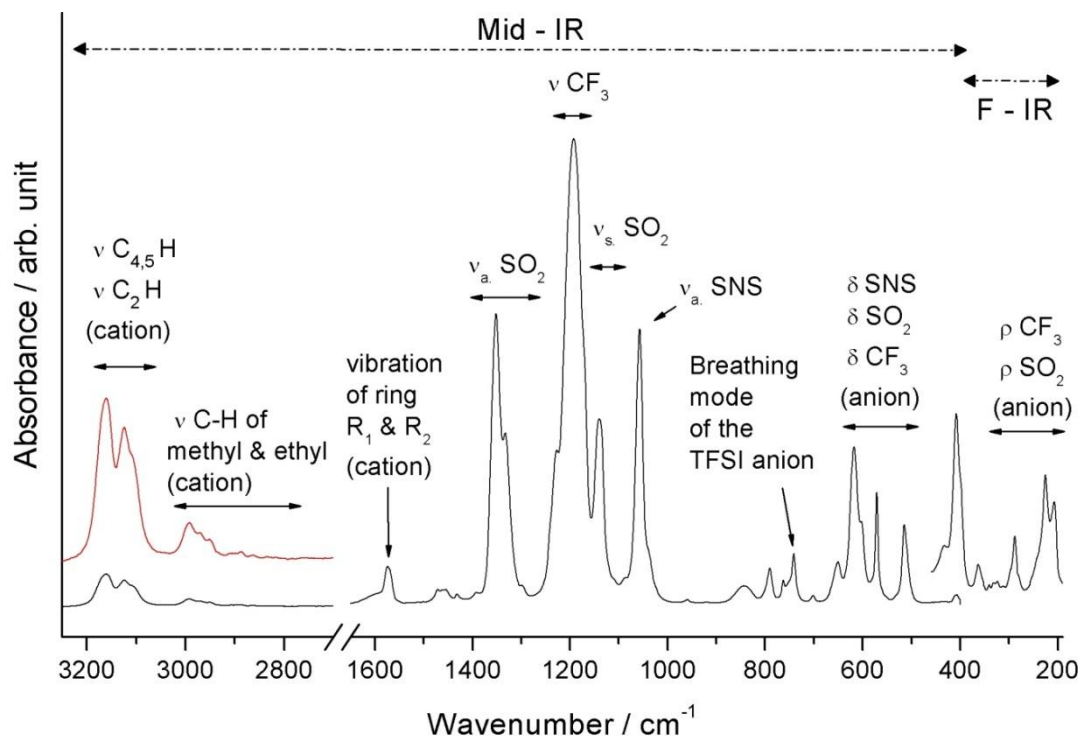


Figure 4.2: Mid-IR (400-3250  $\text{cm}^{-1}$ ) and far-IR (190-460  $\text{cm}^{-1}$ ) spectra of pure [EMIM] [TFSI] ionic liquid. The bands from the C-H stretching (2700-3250  $\text{cm}^{-1}$ ) and far-IR (190-460  $\text{cm}^{-1}$ ) regions are magnified for clarity. Vibrational modes are indicated by the same symbols as in Figure 4.1.

The spectral region at  $2700\text{--}3300\text{ cm}^{-1}$  is associated with C-H stretching (anharmonic) modes. The IR and Raman spectral features observed in this range are very specific to imidazolium based ionic liquids as reported in literature [185,176,186,183,187,23]. The bands located in the spectral region at  $2700\text{--}3050\text{ cm}^{-1}$  have been assigned to the symmetric and asymmetric stretching of the  $\text{CH}_2$  and  $\text{CH}_3$  groups of the cations (Figure 4.3). Above  $3050\text{ cm}^{-1}$ , the profiles are a convolution of peaks corresponding to three different vibrations in the imidazolium ring: the asymmetric stretching of  $\nu_{\text{C}_{(4,5)}\text{H}}$  (HCCH), the symmetric stretching of  $\nu_{\text{C}_{(4,5)}\text{H}}$  (HCCH) and the stretching  $\nu_{\text{C}_2\text{H}}$ . It must be emphasised that an additional vibrational transition (at about  $3105\text{ cm}^{-1}$ ) was also reported in this region and assigned to the combination and overtone of the ring mode in Fermi resonance [196].

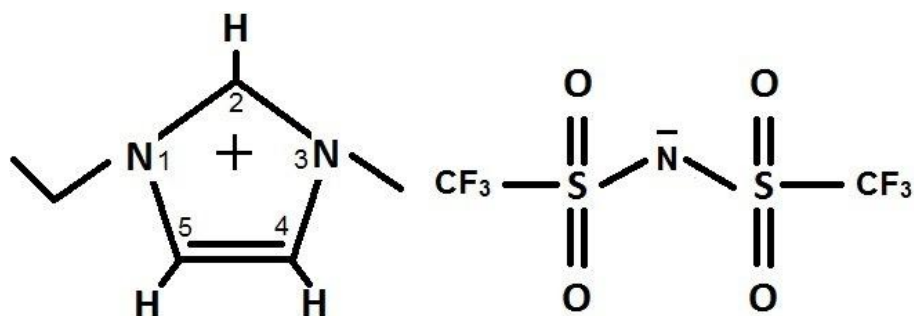


Figure 4.3: Chemical structures of cation and anion species in the [EMIM] [TFSI].

In the spectral region below  $1650\text{ cm}^{-1}$ , the bands associated with the cation modes exhibit a weak intensity [236,198]. The IR and Raman profiles are mainly dominated by the vibrational modes of the anions, as displayed in Figures 4.1 and 4.2. In the IR spectrum, the most intense bands correspond to the stretching modes of  $\text{SO}_2$ ,  $\text{CF}_3$  and  $\text{SNS}$  groups. In the Raman spectrum, the most intense band at  $742\text{ cm}^{-1}$  is due to the ‘breathing’ mode of the TFSI anion. This mode is caused by the collective motion of all the atoms of the [TFSI] anion as displayed in Figure 4.4, and is sometimes defined as an ‘expansion-contraction’ mode [23].

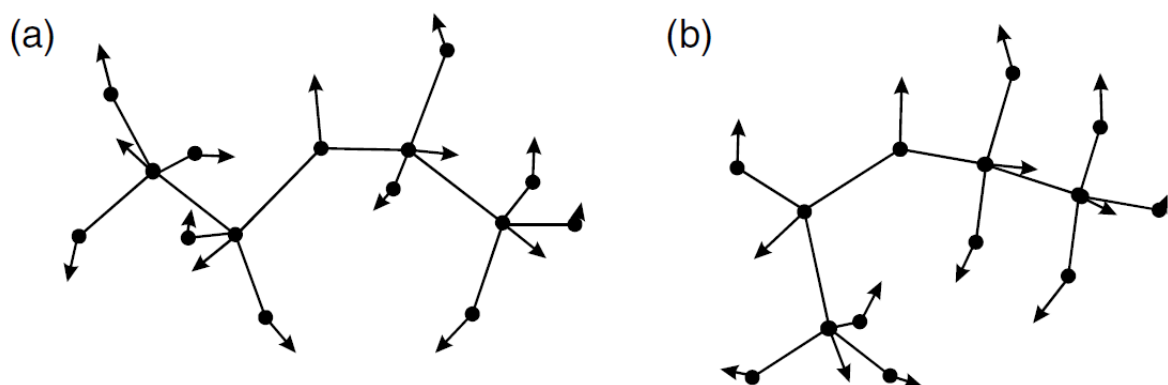


Figure 4.4: Calculated eigenvectors for the breathing mode of [TFSI] anion ( $742\text{ cm}^{-1}$ ) for the  $\text{C}_2$  (a) and  $\text{C}_1$  (b) symmetry extracted from Herstedt et al. [23].

In Raman scattering, this band is strongly polarised as shown by the comparison between polarised ( $I_{\text{VV}}$ ) and depolarized ( $I_{\text{VH}}$ ) spectra in Figure 4.5.

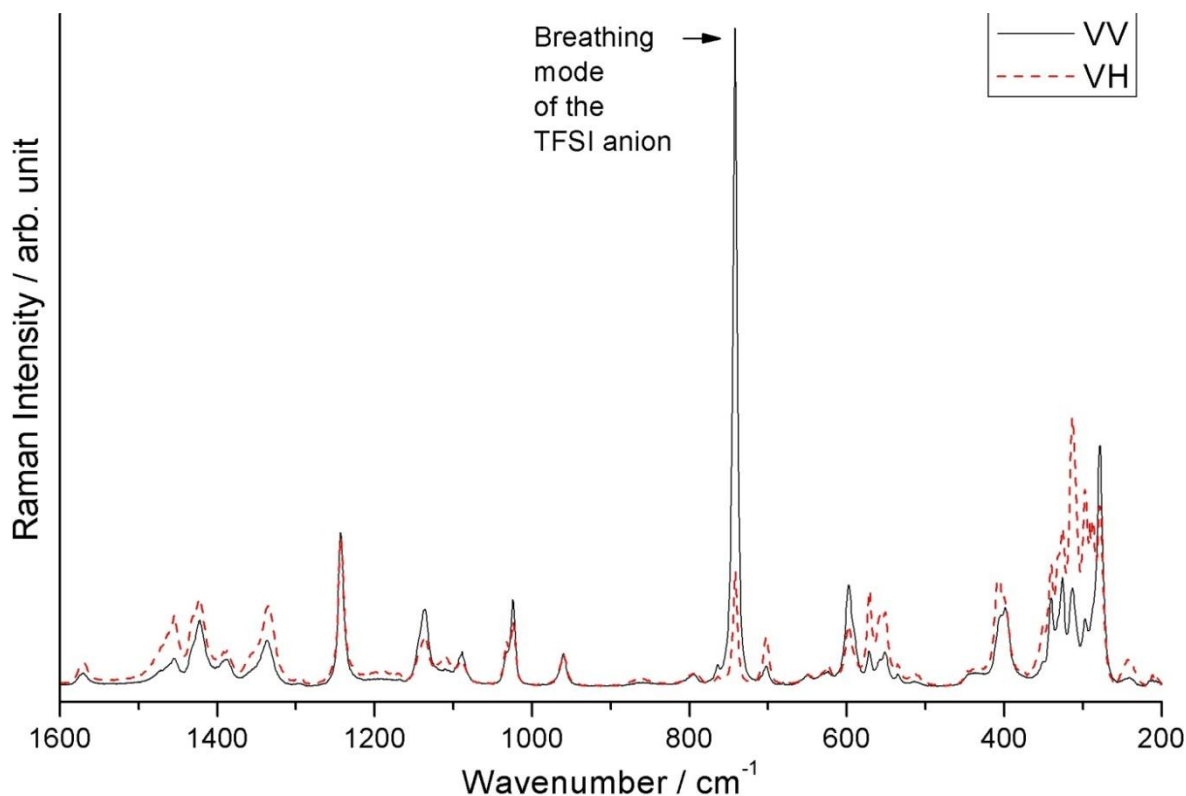


Figure 4.5: Polarised  $I_{VV}$  and depolarised  $I_{VH}$  Raman spectra of pure [EMIM] [TFSI] ionic liquid (200-1600  $\text{cm}^{-1}$ ). The ‘breathing’ mode is observed at 742  $\text{cm}^{-1}$ .

In the spectral region of 200-450- $\text{cm}^{-1}$ , the vibrational transitions are associated with complicated modes due to couplings with other modes involving both  $\text{CF}_3$  and  $\text{SO}_2$  groups of the [TFSI] anion (Mainly the rocking ( $\rho$ ) motions in Figures 4.1 and 4.2). The analysis of Raman spectra in this region shows two distinct conformations of the [TFSI] anion in [EMIM] [TFSI] [192,193]. The TFSI anion exhibits:

- A cisoid conformation labelled ( $C_1$ ) (where both the  $\text{CF}_3$  groups are on the same side of the S-N-S plane).
- A transoid conformation labelled ( $C_2$ ) (where the  $\text{CF}_3$  groups are on far most opposite sides of the S-N-S plane).

At room temperature, the cisoid and transoid conformers coexist with populations about 25% and 75% respectively in ionic liquid [EMIM] [TFSI] [236].

The results published in the literature show that changes in the vibrational spectra upon the dissolution of a metal salt in [EMIM] [TFSI] are mainly induced by the interactions between the metal cations and TFSI anions. Due to this, we focused mainly on the modification of the spectra associated with modes of the [TFSI] anion. Consequently, we only provided the assignment of the vibrational transitions due to TFSI anions in pure [EMIM] [TFSI] in Table 4.1 and the full assignment is shown in Annex 1 (Table A1.3).

Table 4.1: Assignment of the IR and Raman bands of pure [EMIM] [TFSI] in the 200 to 1600  $\text{cm}^{-1}$  range. Assignments are only given for the anion vibrational mode due to their importance in the interactions between these anions and the metal cations.

Experimental bands ( $\text{cm}^{-1}$ )		Assignment
IR	Raman.	
	245	rocking. $\rho(\text{CF}_3, \text{SO}_2)$
	279	rocking. $\rho(\text{CF}_3, \text{SO}_2)$
287	288	rocking. $\rho(\text{SO}_2)$
	296	rocking. $\rho(\text{CF}_3)$
314	311	rocking. $\rho(\text{CF}_3)$
324	328	bending $\delta \text{N-S-CF}_3$
517	513	bending $\delta(\text{SO}_2)$
531	534	asymmetric bending $\delta_{\text{as}}(\text{CF}_3)$ and bending $\delta(\text{SO}_2)$
553	551	asymmetric bending $\delta_{\text{as}}(\text{CF}_3)$
	556	asymmetric bending $\delta_{\text{as}}(\text{CF}_3)$
573	571	asymmetric bending $\delta_{\text{as}}(\text{CF}_3)$ and bending $\delta(\text{SO}_2)$
	589	bending $\delta \text{S-N-S}$ , bending $\delta \text{O-S-O}$
743	741	'breathing' mode of the [TFSI] anion.
1059		asymmetric stretching $\nu_{\text{as}}(\text{S-N-S})$ symmetric stretching $\nu_{\text{s}}(\text{S-O})$ and symmetric bending $\delta_{\text{s}}(\text{CF}_3)$ $\text{CF}_3$
1141	1136	asymmetric stretching $\nu_{\text{as}}(\text{S-N-S})$
1194		asymmetric stretching $\nu_{\text{as}}(\text{C-F})$ of group $\text{CF}_3$
1227		stretching $\nu(\text{S-O}) \otimes \nu(\text{C-S})$
	1242	symmetric stretching $\nu_{\text{s}}(\text{C-F})$
1334	1335	stretching $\nu_{\text{s}}(\text{O-S-O})$
1354		stretching $\nu_{\text{s}}(\text{O-S-O})$

#### 4.1.2 Raman and IR spectra of [EMIM] [TFSI] solutions

The IR and Raman spectra of the [EMIM] [TFSI] solutions of AgTFSI salt are displayed in Figures 4.6 and 4.7. For the sake of clarity, only the spectra of 0.10 and 0.20 mole fraction solutions of AgTFSI salt in [EMIM] [TFSI] are presented.

The Raman spectra were normalised using the band at  $960 \text{ cm}^{-1}$ , associated with the C-C stretching of the ethyl in the cations, as this band was not affected by the addition of the AgTFSI in solution. In the same manner, the IR spectra were normalised to the band at  $1574 \text{ cm}^{-1}$ , associated with the R1 and R2 modes of the imidazolium ring ( $\nu_{\text{C}(2)}\text{N}$ ,  $\nu_{\text{CC}}(\text{ring})$ ,  $\delta_{\text{C}(2,4,5)}\text{H}$ ).

In general, both spectra were not significantly modified by the addition of AgTFSI salt. In particular, no changes were observed in the C-H stretching region  $2700\text{-}3250 \text{ cm}^{-1}$  (as shown in the insert of Figure 4.6).

The Raman spectrum was only modified in the  $700\text{-}850 \text{ cm}^{-1}$  region. A new band appeared at  $753 \text{ cm}^{-1}$  with conspicuous intensity. On the other hand, a significant decrease of the intensity occurred for the band associated with the 'breathing' mode of the anion at  $742 \text{ cm}^{-1}$ . A second new band having a weak intensity appeared at  $804 \text{ cm}^{-1}$ .



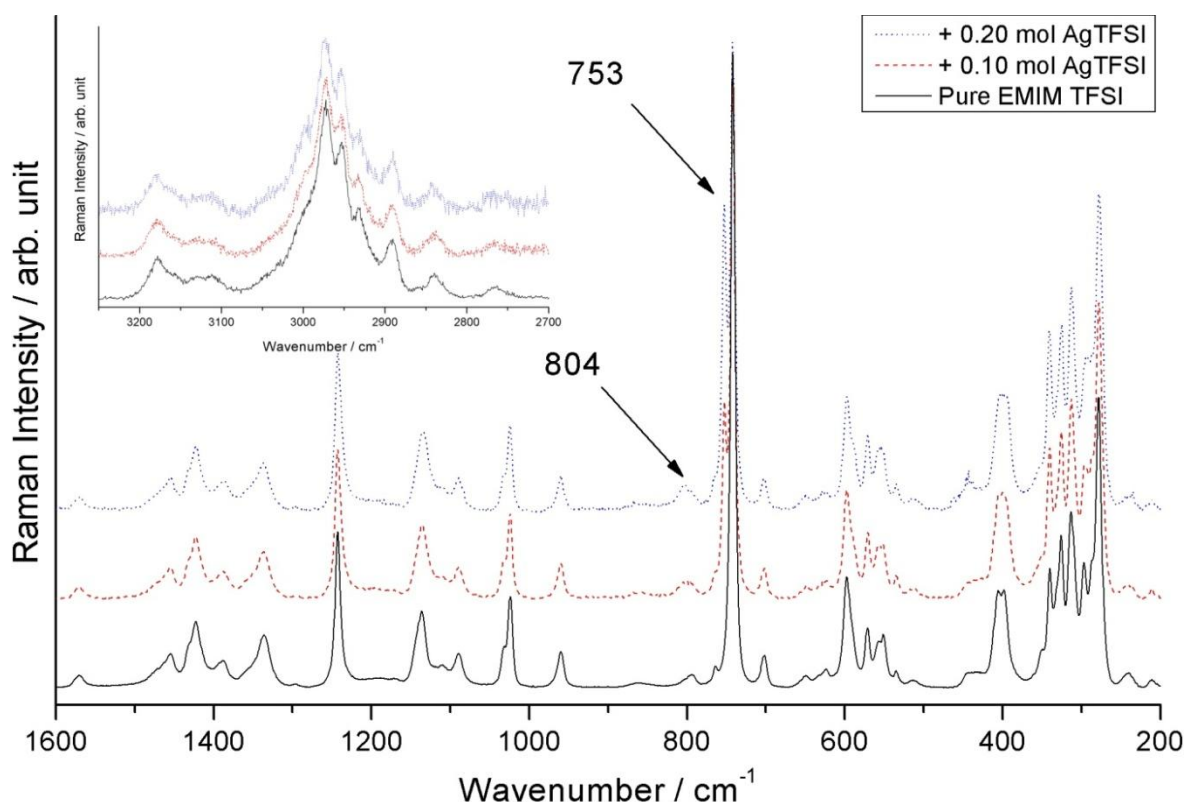


Figure 4.6: Evolution with the AgTFSI concentration of the Raman spectra of the AgTFSI/[EMIM][TFSI] solutions measured in the region 200-3250  $\text{cm}^{-1}$ . The spectra of the solutions have been shifted upward for clarity.

The IR spectra exhibited more significant changes as a result of the dissolution of AgTFSI. From Figure 4.7, we can see that as the AgTFSI concentration increases:

- A well-defined shoulder is observed around 1371  $\text{cm}^{-1}$ , associated with asymmetric stretching of  $\text{SO}_2$ . This shoulder also becomes more pronounced.
- The band at 1135  $\text{cm}^{-1}$  associated with the symmetric S-O stretching of  $\text{SO}_2$ , increases.
- A new band appears at 1015  $\text{cm}^{-1}$ . Its intensity increases whilst the intensity of the band at 1059  $\text{cm}^{-1}$ , associated with asymmetric stretching of SNS groups, decreases.
- A new weak band appears at 747  $\text{cm}^{-1}$ . This spectral component is related to the band associated with the 'breathing' mode at 753  $\text{cm}^{-1}$  which is better defined in Raman.

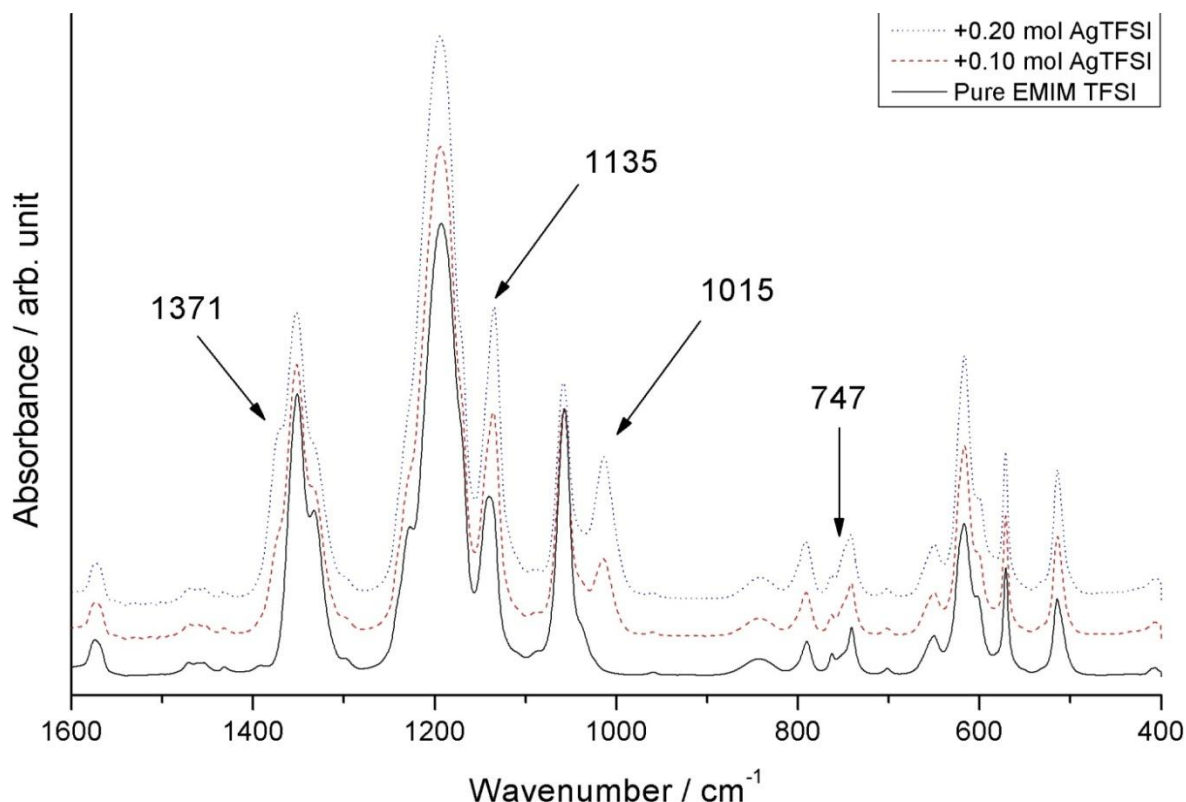


Figure 4.7: Evolution with AgTFSI concentration of the Raman spectra of the AgTFSI/[EMIM] [TFSI] solutions measured in the region 400-1600  $\text{cm}^{-1}$ . The spectra of the solutions have been shifted upwards for clarity.

## 4.2 [EMIM] [EtSO<sub>4</sub>] ionic liquid system

### 4.2.1 Infrared and Raman spectra of pure [EMIM] [EtSO<sub>4</sub>]

The experimental Raman and IR spectra of pure 1-ethyl-3-methyl-imidazolium ethyl-sulphate [EMIM] [EtSO<sub>4</sub>] ionic liquid are shown in Figures 4.8 and 4.9. Both spectra are in good agreement with those reported in the literature [234,183,208]. Similar to [EMIM] [TFSI], the spectra of [EMIM] [EtSO<sub>4</sub>] exhibit bands in two distinct spectral regions: the C-H stretching region, at 2700-3250  $\text{cm}^{-1}$ , and the region below 1650  $\text{cm}^{-1}$ .

In the C-H stretching region (2700-3250  $\text{cm}^{-1}$ ), the vibrational transitions mainly involve the cation modes and those due to the ethyl-group of the anions (see Figures 4.8, 4.9 and 4.10). In the region below 1650  $\text{cm}^{-1}$ , the IR and Raman spectra are dominated by the vibrational modes of the anions. In the IR absorption spectrum, the most intense bands are associated with the symmetric and asymmetric stretching of the SO<sub>3</sub> groups, while in the Raman spectrum, the most intense bands are associated with S-O stretching modes of the SO<sub>3</sub> group and the O-C-C stretching mode of the anions. The differences between the Raman and IR spectra are due to the difference in the selection rules, showing the complementarity of the two spectroscopic techniques.

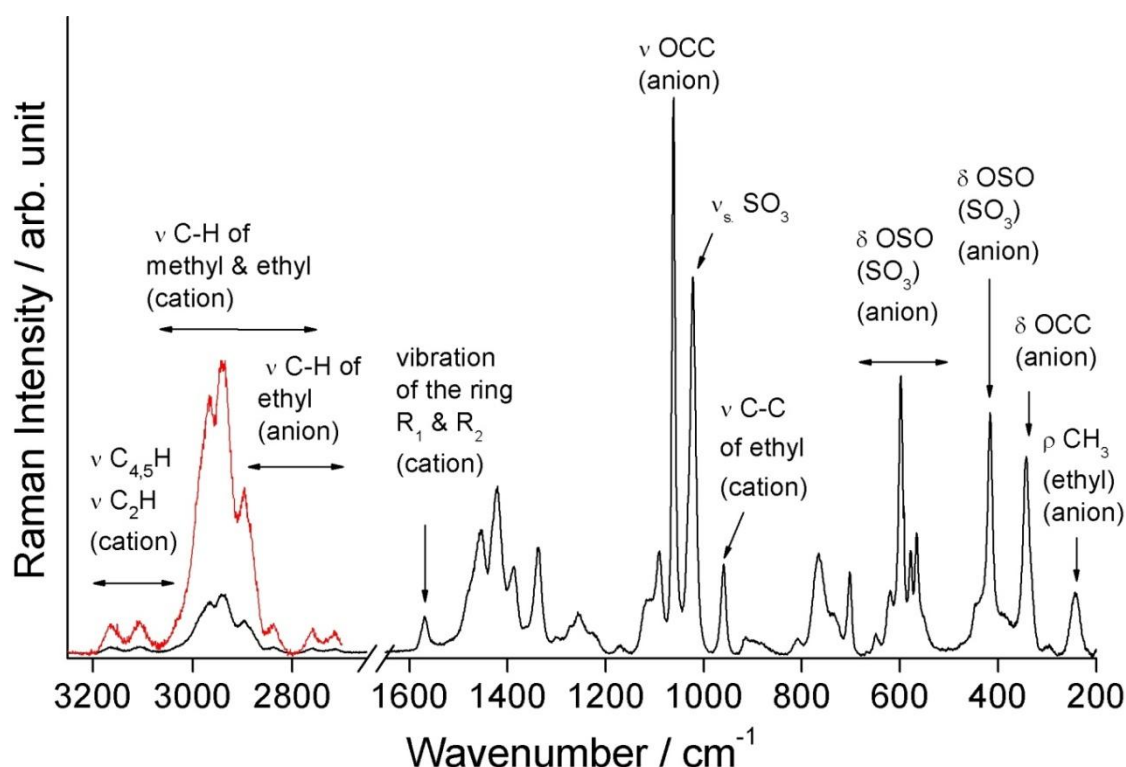


Figure 4.8: Raman spectrum of the pure [EMIM][EtSO<sub>4</sub>] in the spectral region 200-3300 cm<sup>-1</sup>. The spectrum in the region 2700-3250 cm<sup>-1</sup> is magnified for clarity. Vibrational modes are indicated with symbols:  $\nu$  = stretching;  $\delta$  = bending;  $\rho$  = rocking;  $s$  = symmetric;  $as$  = asymmetric.

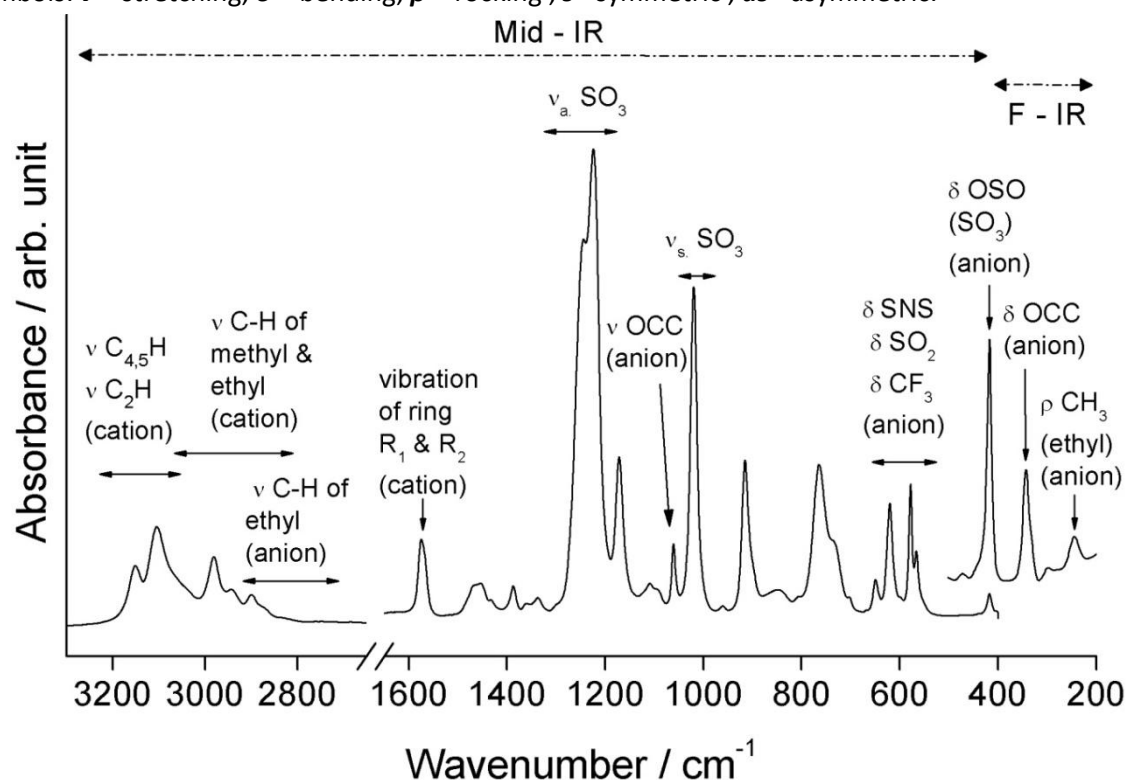


Figure 4.9: Mid-infrared (400-3300 cm<sup>-1</sup>) and far-infrared (200-500 cm<sup>-1</sup>) spectra of pure [EMIM][EtSO<sub>4</sub>]. The intensity in the far-IR region has been magnified. Vibrational modes are indicated by the same symbols as in Figure 4.8.

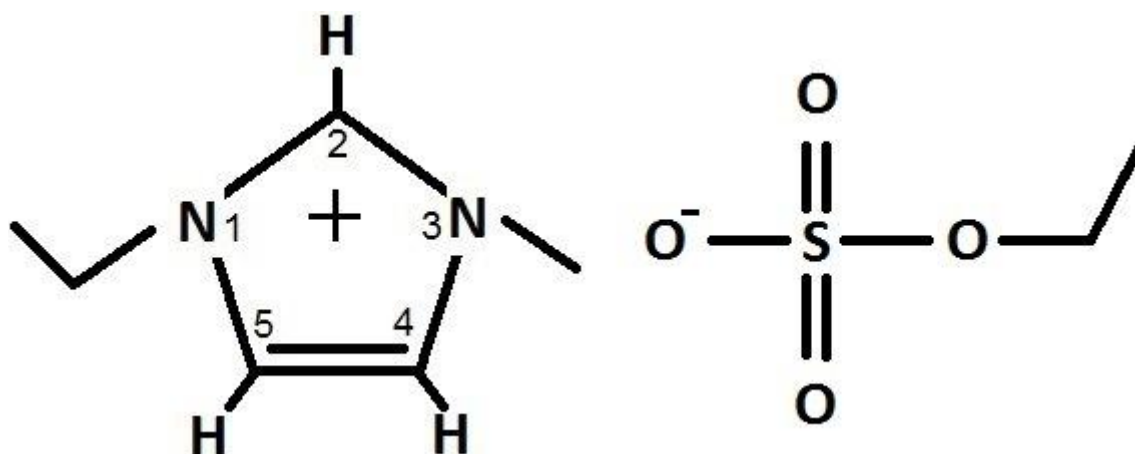


Figure 4.10: Chemical structure of cation and anion species in [EMIM] [EtSO<sub>4</sub>].

Vibrational studies of pure [EMIM] [EtSO<sub>4</sub>] were previously reported by Kiefer and Dhumal et al. [183,184]. Their interpretations of the experimental spectra were based on DFT calculations using a single-ion pair model. Calculations based on a double-ion pair model were carried out on other ionic liquids, which take into account the cooperative effect of the ions [236]. A possible new interpretation of imidazolium based ionic liquids has also been recently reported [191]. Comparing our results with these studies, as well as vibrational analysis based on DFT calculations from a representative double-ion pair of the local order in pure [EMIM] [EtSO<sub>4</sub>] (presented in Annex), the assignment of the IR and Raman spectra of pure [EMIM] [EtSO<sub>4</sub>] have been revisited in our study. More precisely, we assigned:

- the band at 621 cm<sup>-1</sup> to the symmetric  $\delta(\text{SO}_3)$  coupled with the bending of (CH<sub>2</sub>)C-O-S(SO<sub>3</sub>).
- the band at 734 cm<sup>-1</sup> to the out-of-plane bending mode  $\gamma_{\text{C}_{(4,5)}\text{H}}$  coupled with  $\gamma_{\text{C}_{(2)}\text{H}}$  of the cation.
- the band at 766 cm<sup>-1</sup> to the stretching of the O-S bond in SO<sub>3</sub> coupled with the bending of O-C-C bond in CH<sub>3</sub> of the anion.
- the band at 1175 cm<sup>-1</sup> to the rocking of methyl coupled with  $\delta_{\text{C}_{(4,5)}\text{H}}$  and  $\delta_{\text{C}_{(2)}\text{H}}$  of the cation and a small contribution from the rocking of CH<sub>2</sub> group of the ethyl in the anion.

A complete assignment of the bands of pure [EMIM] [EtSO<sub>4</sub>] is provided in Annex 1 (Tables A1.1 and A1.2) and the assignment corresponding to the anion modes is shown in Table 4.2. In the far-IR region, a band located at 243 cm<sup>-1</sup> was observed which was assigned to the rocking modes of the CH<sub>3</sub> group of the ethyl (anion).

Table 4.2: Assignments of the vibrational bands in the 200 to 1600  $\text{cm}^{-1}$  region of the IR and Raman [EMIM] [EtSO<sub>4</sub>] ionic liquid spectra.

Experimental Bands ( $\text{cm}^{-1}$ )		Assignment (Anion bands)
IR	Raman	
245	245	rocking $\rho(\text{CH}_3)$ (ethyl)
337	342	bending $\delta(\text{CH}_2, \text{CH}_3)$
418	416	bending $\delta(\text{O-S-O}(\text{SO}_3))$
579	578	bending $\delta(\text{OSO}(\text{SO}_3)) \otimes$ twisting $(\tau)(\text{SO}_3)$
621		symmetric bending $\delta_s(\text{SO}_3) \otimes$ bending $\delta((\text{CH}_2)\text{C-O-S}(\text{SO}_3))$
766	766	stretching $\nu(\text{O-S}(\text{SO}_3)) \otimes$ bending $\delta(\text{O-C-C}(\text{CH}_3))$
916		bending $\delta(\text{C}(\text{CH}_2)\text{CH}(\text{CH}_3))$
1020	1020	symmetric stretching $\nu_s(\text{O-S}(\text{SO}_3))$
1061	1061	stretching $\nu(\text{O-C}(\text{CH}_2)\text{-C}(\text{CH}_3))$
1225	1224	asymmetric stretching $\nu_{as}(\text{S-O}(\text{SO}_3)) \otimes$ rocking $\rho(\text{CH}_2)$ (ethyl)
1246	1252	asymmetric stretching $\nu_{as}(\text{S-O}(\text{SO}_3)) \otimes \text{C}_{(4,5)}\text{H} \otimes \delta\text{C}_{(2)}\text{H}$

#### 4.2.2 IR and Raman spectra of [EMIM] [EtSO<sub>4</sub>] solution

The IR and Raman spectra of CuCl<sub>2</sub> solution in [EMIM] [EtSO<sub>4</sub>] are displayed in Figures 4.11 and 4.12. For the sake of clarity, only the spectra for solutions containing 0.10 and 0.20 mole fractions of CuCl<sub>2</sub> are displayed. The spectrum of [EMIM] [EtSO<sub>4</sub>] is included for comparison.

The Raman spectra were normalised using the band at 960  $\text{cm}^{-1}$  associated with the stretching of the C-C bond of the ethyl group in the cation and the IR spectra were normalised to the band associated with the R1 and R2 modes of the imidazolium ring ( $\nu_{\text{C}(2)}\text{N}$ ,  $\nu_{\text{CC}}(\text{ring})$ ,  $\delta\text{C}_{(2,4,5)}\text{H}$ ). No spectral changes were observed in the C-H stretching region (2700-3250  $\text{cm}^{-1}$ ) of the spectra.

The Raman spectra of the CuCl<sub>2</sub> solutions are almost similar to the spectrum of pure [EMIM] [EtSO<sub>4</sub>], except for a new band that appears at 313  $\text{cm}^{-1}$ , with an amplitude that increases with the salt concentration.

Greater changes could be observed from the IR absorption spectra. Two well-defined bands could be seen at 312  $\text{cm}^{-1}$  and 1045  $\text{cm}^{-1}$ , respectively and a shoulder appeared at 1298  $\text{cm}^{-1}$ , as a result of the salt dissolution.

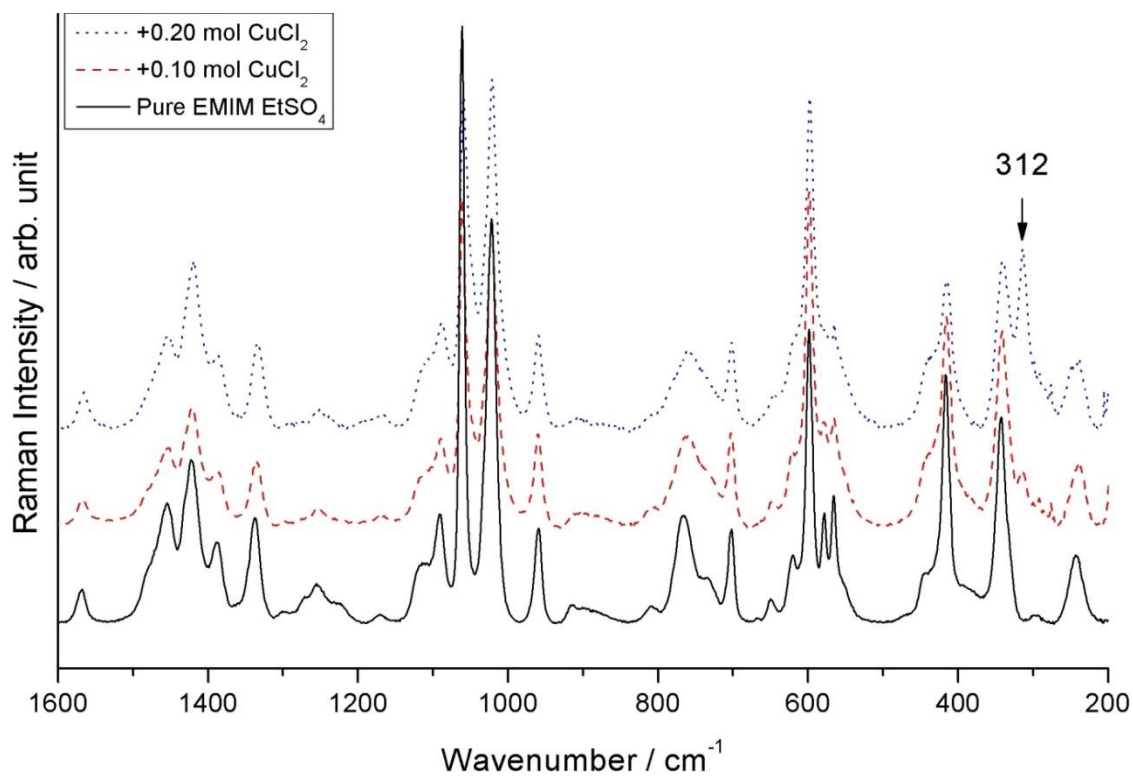


Figure 4.11: Evolution of the Raman spectra of  $\text{CuCl}_2/[\text{EMIM}][\text{EtSO}_4]$  solutions in the region 200-1600  $\text{cm}^{-1}$  with the salt concentration.

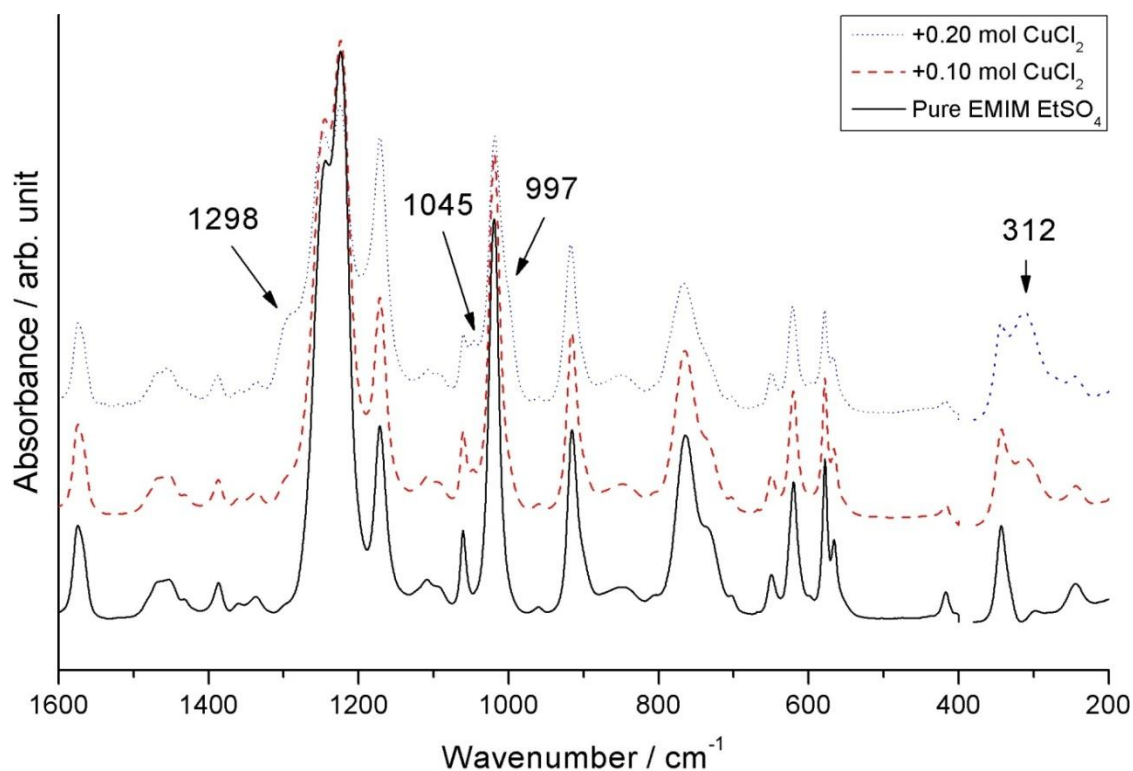


Figure 4.12: Evolution of the IR spectra of  $\text{CuCl}_2/[\text{EMIM}][\text{EtSO}_4]$  solutions in the region 200-1600  $\text{cm}^{-1}$  with the salt concentration.

### 4.3 Discussion of the results

In this section, we further analyse the new bands and other spectral changes induced by the dissolution of AgTFSI in [EMIM][TFSI] and CuCl<sub>2</sub> in [EMIM][EtSO<sub>4</sub>]. For this reason, the evolution of the vibrational profiles over the full range of concentrations is presented in the following sections. The interpretation of our experimental results is aided by calculations obtained from the modelling of the vibrational spectra (IR absorption and Raman scattering) using the DFT procedure (cf. methodology and details of the calculations in Annex 1).

#### 4.3.1 Modelling the Vibrational Spectra of the metal complexes

All calculations were performed by using the DFT method and the hybrid functional B3LYP. The systems investigated were the pure [EMIM][TFSI] and [EMIM][EtSO<sub>4</sub>] ionic liquids as well as the AgTFSI/[EMIM][TFSI] and CuCl<sub>2</sub>/[EMIM][EtSO<sub>4</sub>] solutions. The basis set 6-31+G(d,p) was used for all the atoms. An exception was the sulphur atoms in both the TFSI and EtSO<sub>4</sub> anions, which used the basis set B3LYP/6-31+G(d,p):MQZVP(S) (cf. Annex 1 for details). For the copper and silver cations (Cu<sup>2+</sup> and Ag<sup>+</sup>) involved in the metal complexes, we used the MQZVP (Modified QZVP) basis set [193] and the DGDZVP (DGauss Double-Zeta Valence Polarized) basis set [237], respectively.

The DFT calculations were performed with the assumption that the experimental spectral signatures would result mainly from interactions taking place within a representative entity involving at minimal, a double cation-anion pairs (IP2).

Firstly, we determined a local energy minimum for the IP2 structure of the pure ionic systems [EMIM][EtSO<sub>4</sub>] and [EMIM][TFSI] (Figures A1.1 and A1.2 in Annex 1). The vibrational analysis carried out from these predicted IP2 structures is briefly discussed in Annex 1. The full assignment of the predicted spectra (calculated vibrational transitions, IR and Raman intensities) is provided in the Annex 1 (Tables A1.1-A1.3). The assignment of the vibrational spectra for the system [EMIM][EtSO<sub>4</sub>], has been revisited for some internal modes (c.f. &4.1.1) in light of our DFT calculation results and also importantly, from conclusions developed in a recent spectroscopic investigation for a series of imidazolium based ionic liquids including the pure [EMIM][TFSI] [191].

In the second step, we determined possible local energy minimum structures associated with the metal-complexes formed by adding AgTFSI and CuCl<sub>2</sub> compounds in the [EMIM][TFSI] and [EMIM][EtSO<sub>4</sub>] ionic systems (double cation-anion pairs). From these structures, the vibrational analysis allowed us to determine a full assignment of the main vibrational transitions of the predicted IR and Raman spectra of these complexes (Tables A1.4-A1.6 in the Annex). In the following section, we shall mainly focus on the interaction-induced spectral features due to the complex formation with the Ag<sup>+</sup> and Cu<sup>2+</sup> cations.

#### 4.3.2 Vibrational Analysis of the Spectra (AgTFSI/[EMIM][TFSI] solution)

The calculated structure of the Ag-complex formed with TFSI and EMIM ionic species is displayed in Figure 4.13. In this structure, the cation Ag<sup>+</sup> is surrounded by three TFSI anions (which are nearly found with a cisoid conformation). It is coordinated with one of the O atoms of the SO<sub>3</sub> groups of two distinct anions and coordinated with the N-atom of a third TFSI neighbours.



The full assignment of the predicted vibrational IR and Raman spectra is provided in Annex 1 (Table A1.6). As expected, the main spectral modifications induced by the complex formation between  $\text{Ag}^+$  and TFSI anions involve the vibrational transitions due to the TFSI anions. We have compiled the predicted specific spectral features due to the Ag-complex formation with their assignment, which are shown in Table 4.3. Comparing the calculated values for the pure [EMIM] [TFSI] and the double ion pairs (with silver salt), the main specific spectral features exhibit a slight intensity variation which become noticeable for the vibrational transitions associated with the S-N-S stretching modes of the anions (in the spectral region  $1000\text{--}1060\text{ cm}^{-1}$ , cf. values in Table 4.3) and with the S-O stretching modes of the  $\text{SO}_2$  groups (in the spectral region  $1280\text{--}1400\text{ cm}^{-1}$ , Table 4.3) as well as the ‘breathing’ mode of the anion located at  $740\text{ cm}^{-1}$  (calculated at  $732\text{ cm}^{-1}$ ). For both S-N-S and S-O stretching modes, the fundamental transitions located at  $1059$  and  $1354\text{ cm}^{-1}$  respectively undergo a significant decrease of the IR intensity due to the Ag-complex formation. Similarly, the main spectral modification associated with the ‘breathing’ mode of the anion undergoes a noticeable decrease of its Raman intensity. However, the most specific spectral features due to the Ag-complex appears as new interaction-induced IR bands which are predicted at  $1015\text{ cm}^{-1}$  and  $1371\text{ cm}^{-1}$  respectively, corresponding to the S-N-S and S-O stretching modes perturbed by the interactions with the  $\text{Ag}^+$  cation. In contrast, we notice that for the ‘breathing’ mode of the anion TFSI, no interaction-induced Raman band is found whereas a new band situated at  $753\text{ cm}^{-1}$  is clearly observed and assigned to this mode engaged in a complex with the cation  $\text{Ag}^+$ . In the following paragraph, we will discuss these results by comparing them with the spectral signatures observed experimentally. A particular emphasis is placed on the spectral regions associated with the ‘breathing’ mode as well as the S-N-S and S-O stretching modes.

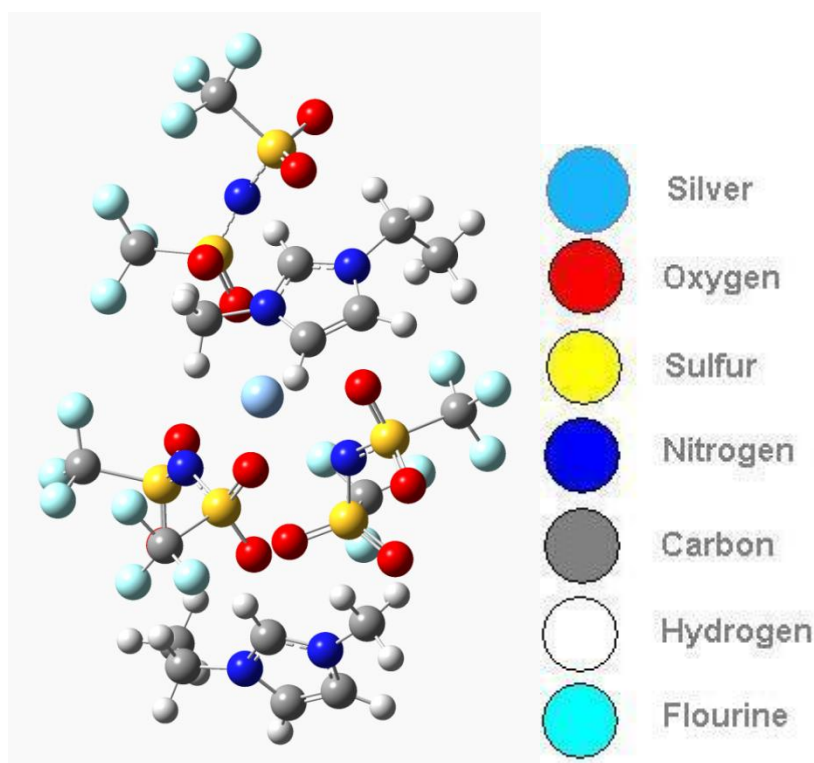


Figure 4.13: Structure of the Ag-complex formed with  $\text{TFSI}^-$  anions calculated at the [B3LYP/6-31+G(d,p):MQZVP(S):DGDZVP(Ag)] level. Two cations have been considered in the calculation of this structure.



Table 4.3: Main vibrational transitions involved in the Ag complex formation with TFSI anions evaluated from the structure AgTFSI+(TFSI<sup>-</sup>EMI)<sub>2</sub> calculated at the [B3LYP/6-31+G(d,p):MQZVP(S):DGDVZP(Ag)] level.

Exptl bands transitions (cm <sup>-1</sup> )	ion pair dimer structure			Ag-Complex Structure			Assignment
	Calc. transition (cm <sup>-1</sup> )	I(IR) Km/mol	I(Ram) Å <sup>4</sup> /amu	Calc. transition (cm <sup>-1</sup> )	I(IR) Km/mol	I(Ram) Å <sup>4</sup> /amu	
573	573.8-574.0	119.2	2.0	565.2-568.0	139.0	5.8	bending δ(SO <sub>2</sub> ) ⊗ δas.(CF <sub>3</sub> )
587*				572.0-580.2	159.8	3.4	bending δ(SO <sub>2</sub> ) ⊗ bending δ N-S(SO <sub>2</sub> )-O
589	594.3-595.2	258.6	3.8	592.4-595.2	354.0	4.9	bending δ(SO <sub>2</sub> ) ⊗ bending δ(CF <sub>3</sub> )C-S(SO <sub>2</sub> )-N
742	729.1-732.4	115.2	59.9				'breathing' mode (anion)
753*				732.3-734.3	145.1	100.5	'breathing' mode (anion)
1015*				1019.9	312.1	0.7	asymmetric stretching vas S-N-S(SO <sub>2</sub> ) ⊗ δs(CF <sub>3</sub> )
1036	1038.4-1047.7	17.0	20.6	1035.3-1050.5	18.3	26.0	(ν <sub>CN</sub> ring, δ <sub>CN</sub> ring)
1059	1052.2-1060.1	412.1	2.1	1056.2-1059.2	223.9	1.5	asymmetric stretching vas S-N-S(SO <sub>2</sub> ) ⊗ δs(SO <sub>2</sub> )
1296	1278.4-1327.1	144.4	21.2	1277.3-1321.2	72.3	10.5	in plane δC <sub>(2)</sub> H ⊗ δC <sub>(4,5)</sub> H
1334	1334.4-1341.7	402.5	16.7	1303.8-1327.9	962.6	28.3	stretching S-O(SO <sub>2</sub> ) ⊗ δC <sub>(4,5)</sub> H
1354	1352.5	651.5	4.4	1348.2	85.3	5.2	stretching S-O(SO <sub>2</sub> )
	1357.5-1359.4	45.9	30.6 P	1353.2-1354.8	20.7	47.2P	stretching ν <sub>ip</sub> CN(ring), ν <sub>ip</sub> CN(CH <sub>2(3)</sub> )
1371*				1374.1	379.4	8.4	stretching S-O(SO <sub>2</sub> )
1574	1602.7-1616.8	130.9	16.3	1602.4-1619.2	143.2	20.5	(νC <sub>(2)</sub> N ⊗ νCC(ring) ⊗ δC <sub>(2,4,5)</sub> H)

\*indicates the interaction induced vibrational transition by the complex formation

ν = stretching; δ = bending; ρ = rocking ; s= symmetric ; as= asymmetric.

### Spectral range 720-780 $\text{cm}^{-1}$ ('breathing' mode)

The evolution of the experimentally observed Raman spectra in the 730-765  $\text{cm}^{-1}$  region is displayed in Figure 4.14. The intensity of the band observed at 753  $\text{cm}^{-1}$  increases with the silver salt concentration whereas the intensity of the band associated with the breathing mode of the anion at 742  $\text{cm}^{-1}$  decreases (cf. insert in Figure 4.14). Moreover, the evolution of these profiles exhibits an isosbestic point, which clearly indicates that both bands are related to each other. Hence, the new band can be assigned to the 'breathing' mode of the anion species that was perturbed by interaction with silver cations.

This suggests that the TFSI anions experience two well-defined types of environment. The first is related to the TFSI anions in an environment similar to the one that exists in pure [EMIM][TFSI], known as the 'free' breathing mode in the literature. The second is related to the interaction between the 'breathing' mode of anion species and the silver cation to form a complex (the 'complex' breathing mode), which leads to the band observed at 753  $\text{cm}^{-1}$ .

The Raman bands associated with the 'complex' (753  $\text{cm}^{-1}$ ) and 'free' (742  $\text{cm}^{-1}$ ) 'breathing' modes of the TFSI anion were fitted by using Lorentzian profiles. For each concentration of the AgTFSI, the integrated intensity was estimated. We found that the integrated intensity of the new band linearly increased whilst the integrated intensity of the free 'anion' band decreased with increasing concentration of AgTFSI, as shown in the insert of Figure 4.14.

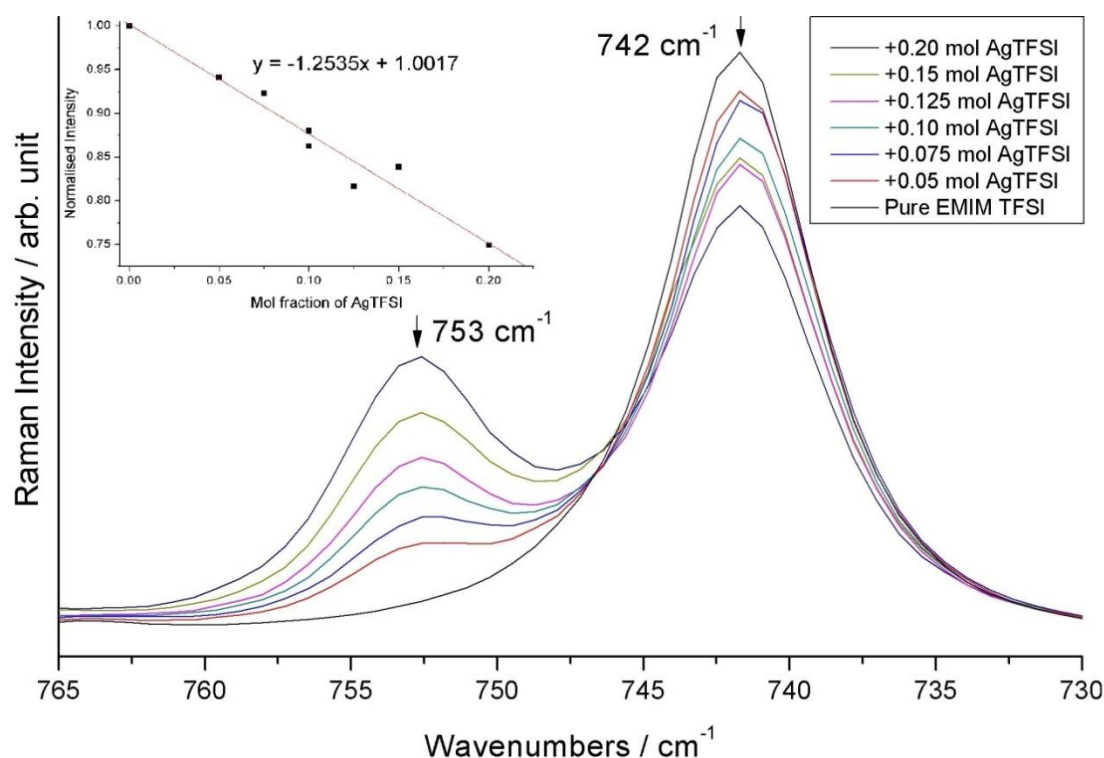


Figure 4.14: Evolution with the AgTFSI concentration of the Raman spectra of the AgTFSI/[EMIM][TFSI] solutions measured in the region of the 'breathing' modes of TFSI. The evolution of the normalised intensity with the concentration [AgTFSI] is displayed in the inset of this figure.

It should be emphasised that from the results obtained by DFT calculations, we were able to predict the enhancement in Raman intensity of the ‘breathing’ mode which was perturbed by interactions with the cation  $\text{Ag}^+$  cation (cf. &4.3.2). Nevertheless, the corresponding vibrational transition is found to shift only slightly towards higher wavenumbers by about  $2\text{--}3\text{ cm}^{-1}$  instead of  $10\text{ cm}^{-1}$  observed in the experimental profile (Figure 4.14). Such a discrepancy could arise from methodological difficulties to adequately assess the conformation of the TFSI anion involved in complex formation with  $\text{Ag}^+$ , since a large number of possible conformations existed in solution. This is especially true from a typical structure used in DFT, which is minimally reduced to include only a few partner species.

### Spectral range $980\text{--}1100\text{ cm}^{-1}$ (asymmetric S-N-S stretching mode)

The evolution with the concentration in Ag(TFSI) salt of the new IR band at  $1015\text{ cm}^{-1}$  is shown in Figure 4.15. The intensity of this new band increases linearly with the concentration at the expense of the fundamental transition at  $1059\text{ cm}^{-1}$  due to the asymmetric S-N-S stretch. The inversely proportional relationship between the intensity of these two bands suggests that they are the same mode. The vibrational transition ( $1015\text{ cm}^{-1}$ ) is associated with this mode of the anion species engaged in the complex formation with a silver cation. In contrast, the band located at  $1036\text{ cm}^{-1}$  corresponding to the C-N stretching and CNC bending modes of the imidazolium cation rings is not perturbed by the complex formation. The spectral features predicted by DFT calculations are in agreement with these experimental findings (cf. calculated values in Table 4.3).

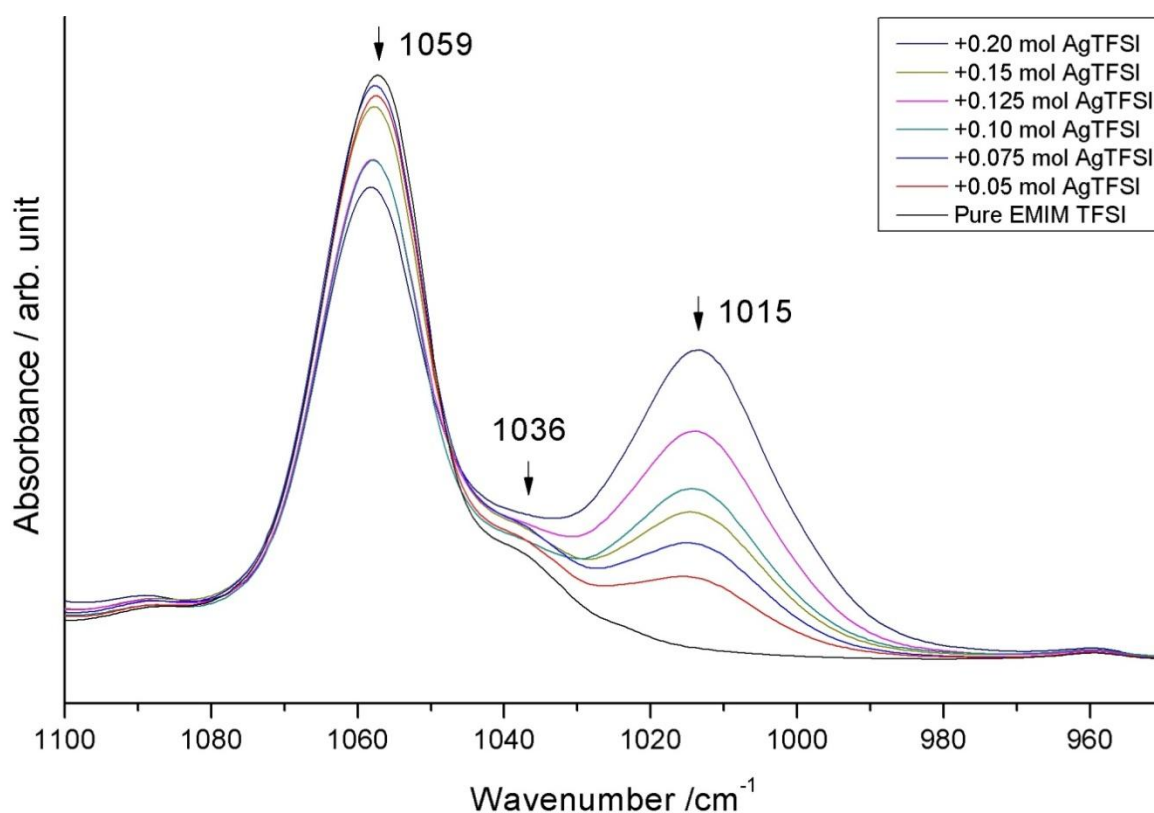


Figure 4.15: Evolution with the AgTFSI concentration of the IR spectra of the AgTFS/[EMIM] [TFSI] solutions measured in the region of the asymmetric S-N-S stretching mode.

### Spectral range 1280-1400 $\text{cm}^{-1}$ (S-O stretching mode)

The evolution of the new IR band at  $1371\text{ cm}^{-1}$  with the concentration of AgTFSI is shown in Figure 4.16. As the concentration of AgTFSI increases, this profile (initially a shoulder at very low concentration) becomes more and more defined (cf. the profile measured at concentration 0.20 mole fraction, Figure 4.15). The intensity of this new band increases with the concentration whilst the IR intensity of the fundamental transitions situated at  $1354\text{ cm}^{-1}$  and  $1334\text{ cm}^{-1}$  due to the S-O stretching modes also increases. According to the DFT results, the appearance of the new band at  $1371\text{ cm}^{-1}$  could be associated with the S-O stretching mode which was perturbed by the complex formation with the silver cation. Once again, the in-plane bending  $\delta\text{C}_{(2,4,5)}\text{H}$  modes of the cation situated at about  $1296\text{ cm}^{-1}$  are not affected by this phenomenon.

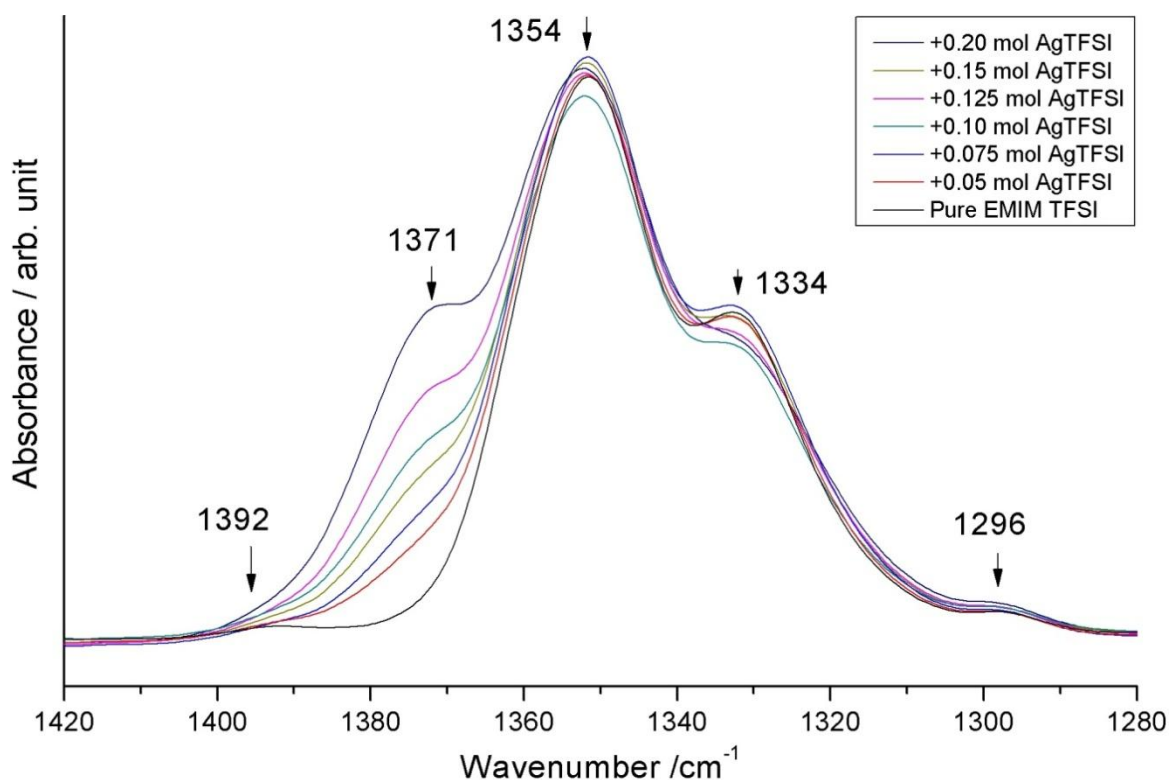


Figure 4.16: Evolution with the AgTFSI concentration of the IR spectra of the AgTFSI/[EMIM] [TFSI] solutions measured in the region of the asymmetric S-O stretching mode.).

#### 4.3.4 Vibrational Analysis of the Spectra of the solutions $\text{CuCl}_2/[\text{EMIM}][\text{EtSO}_4]$

The calculated structure of the Cu-complex formed with chlorine and  $\text{EtSO}_4^-$  anions is displayed in Figure 4.17. In this structure, the cation  $\text{Cu}^{2+}$  is coordinated with two  $\text{Cl}^-$  anions and one of the O atoms of the  $\text{SO}_3$  groups belonging to the two distinct  $\text{EtSO}_4^-$  anions.

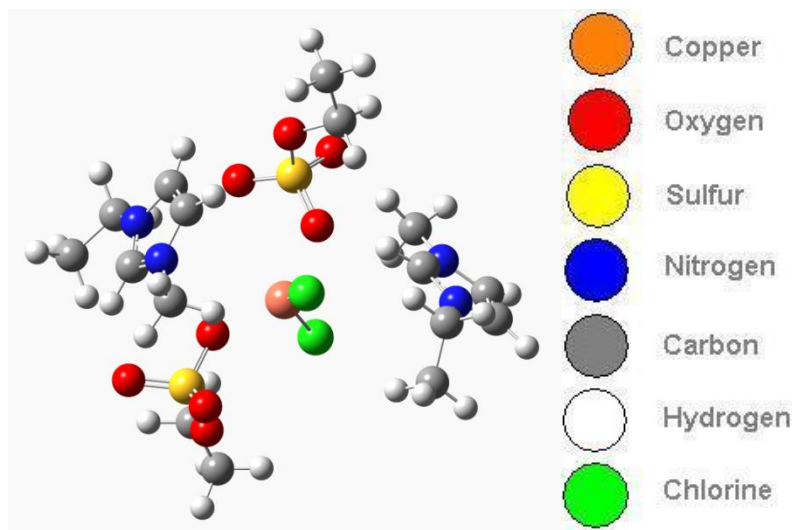


Figure 4.17: Structure of the Cu-complex formed with  $\text{Cl}^-$  and  $\text{EtSO}_4^-$  anions calculated at the [B3LYP/6-31+G(d,p):MQZVP(S,Cu)] level. Two EMIM cations have been considered in the geometry optimization of this structure.

The full assignment of the predicted vibrational spectra is provided in Annex 1 (Tables A1.4 and A1.5). As expected, the spectral modifications induced by interactions with  $\text{Cu}^{2+}$  and  $\text{Cl}^-$  anions involve the internal modes of the  $\text{EtSO}_4^-$  anions. We have compiled the predicted vibrational transitions which are shown in Table 4.4. The assignment of the theoretical IR and Raman activities mentioned above are based on the calculated structure of the Cu-complex as shown in Figure 4.17. The main specific spectral features induced by the complex formation are mainly perceived from the shifts and variation in intensity of the spectral properties related to the symmetric and asymmetric S-O stretching modes of the  $\text{SO}_3$  groups (in the spectral regions  $980\text{--}1100\text{ cm}^{-1}$  and  $1150\text{--}1350\text{ cm}^{-1}$ , respectively, in Table 4.4). In the following section, we shall discuss these predicted spectral signatures in more details, complementing the information of the measured experimental spectra. The vibrational analysis obtained from the calculated structure of the Cu-complex predicts the appearance of a new interaction-induced band at about  $313\text{ cm}^{-1}$ . This band is due to the inter-atomic Cl-Cu-Cl asymmetric stretching mode which occurs as the spectral signature of the coordination of  $\text{Cu}^{2+}$  with two  $\text{Cl}^-$  anions.

##### 4.3.4.1 Spectral range $975\text{--}1350\text{ cm}^{-1}$ (symmetric and asymmetric S-O stretching modes)

The IR profiles containing the symmetric and asymmetric S-O stretching modes are displayed in Figures 4.18 and 4.19, respectively.

In the region of the asymmetric S-O stretching modes ( $1150\text{--}1350\text{ cm}^{-1}$ ), we observe the appearance of a shoulder at  $1298\text{ cm}^{-1}$  whilst the intensity of the bands at  $1225$  and  $1246\text{ cm}^{-1}$  associated with the S-O stretching vibrations decreases as the concentration of  $\text{CuCl}_2$  is increased (Figure 4.18).

From the vibrational analysis obtained from the calculated structure of the Cu-complex (Table 4.4), we found that the fundamental transitions of the asymmetric S-O stretching modes of EtSO<sub>4</sub> located at 1225 and 1246 cm<sup>-1</sup> (calculated values at 1222 and 1243 cm<sup>-1</sup> respectively) split into two spectral components under the complex formation. The first component was shifted towards lower wavenumbers located at 1172 cm<sup>-1</sup> (calculated value at 1177 cm<sup>-1</sup>) whereas the second component was shifted towards higher wavenumbers at 1298 cm<sup>-1</sup> (calculated value at 1316-1320 cm<sup>-1</sup>). This splitting accompanied a significant intensity enhancement in both IR and Raman spectra. On a side note, the spectral component that shifted towards lower wavenumbers at 1172 cm<sup>-1</sup> merged with the fundamental vibrational transitions corresponding to the rocking modes  $\rho(\text{CH}_2)$  and  $\rho(\text{CH}_3)$  of the methyl and ethyl groups located on the imidazolium cations. These rocking modes were not affected by the interactions with copper cations. Therefore, the vibrational analysis obtained from the calculated structure of the Cu-complex displayed in Figure 4.17 would allow us to predict an IR intensity enhancement of the band situated at 1172 cm<sup>-1</sup> upon the dilution of the CuCl<sub>2</sub> salt in [EMIM] [EtSO<sub>4</sub>]. Even if the IR band at 1172 cm<sup>-1</sup> remained unchanged, the appearance of the interaction-induced band that corresponded to the asymmetric S-O stretching mode involved in the complex formation in this region would contribute to an increase in intensity of this IR profile. In contrast, the spectral component shifted at higher wavenumbers (1298 cm<sup>-1</sup>) did not overlap with any fundamental vibrational transitions of the cation modes or anion modes. From these findings, we can conclude that the intensities of the interaction-induced IR profiles situated at 1172 cm<sup>-1</sup> (symmetric S-O stretch) and 1298 cm<sup>-1</sup> (symmetric S-O stretch) increase with the concentration of CuCl<sub>2</sub> salt dissolved in [EMIM] [EtSO<sub>4</sub>] at the expense of the fundamental bands at 1246 and 1225 cm<sup>-1</sup>.

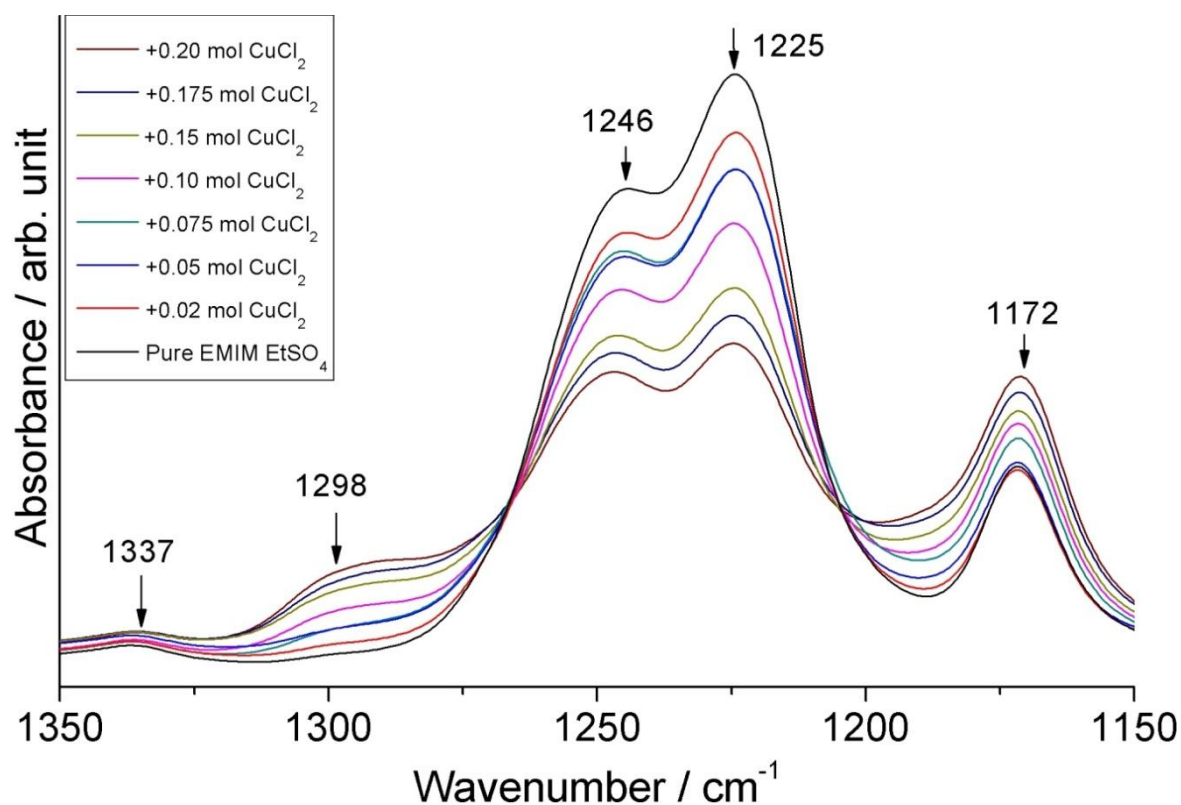


Figure 4.18: Evolution with the concentration of the CuCl<sub>2</sub> salt of the IR spectra of the CuCl<sub>2</sub>/[EMIM] [EtSO<sub>4</sub>] solutions measured in the region of the asymmetric O-S-O stretches (1150-1350 cm<sup>-1</sup>).

In the region of the symmetric S-O stretching modes ( $975\text{--}1080\text{ cm}^{-1}$ ), a well-defined new band and a shoulder were observed at  $1045\text{ cm}^{-1}$  and around  $997\text{ cm}^{-1}$  respectively (Figure 4.19). We noticed that the intensity of this new band ( $1045\text{ cm}^{-1}$ ) exhibits a linear relationship with the concentration of  $\text{CuCl}_2$ .

The vibrational analysis obtained from DFT calculations (Table 4.4) shows that the symmetric S-O stretching modes of  $\text{EtSO}_4$  in the absence of copper ion is located at  $1020\text{ cm}^{-1}$  (calculated at  $1030\text{ cm}^{-1}$ ). This mode is found to shift slightly towards lower wavenumbers by about  $10\text{--}15\text{ cm}^{-1}$  when it is engaged in a Cu-complex formation. At the same time, a new vibrational transition with a significant intensity enhancement in IR and Raman is located at  $998\text{ cm}^{-1}$ , induced by the interactions with copper. These findings are also observed experimentally, as can be clearly seen from the IR profile in Figure 4.19. From this figure, we can see that the band intensity of the symmetric S-O stretch at  $1020\text{ cm}^{-1}$  decreases as the intensity of the new band increases with the copper concentration. Moreover, the position of this band is found to shift slightly towards lower wavenumbers as the concentration of the copper salt is increased. Experimentally, a very broad shoulder is observed at about  $997\text{ cm}^{-1}$ . A reason for this is that the  $\text{SO}_3$  groups experience a large distribution of environments when interacting with copper in IL. The structure of these environments occurs at slightly different energies, leading to the observed broadening.

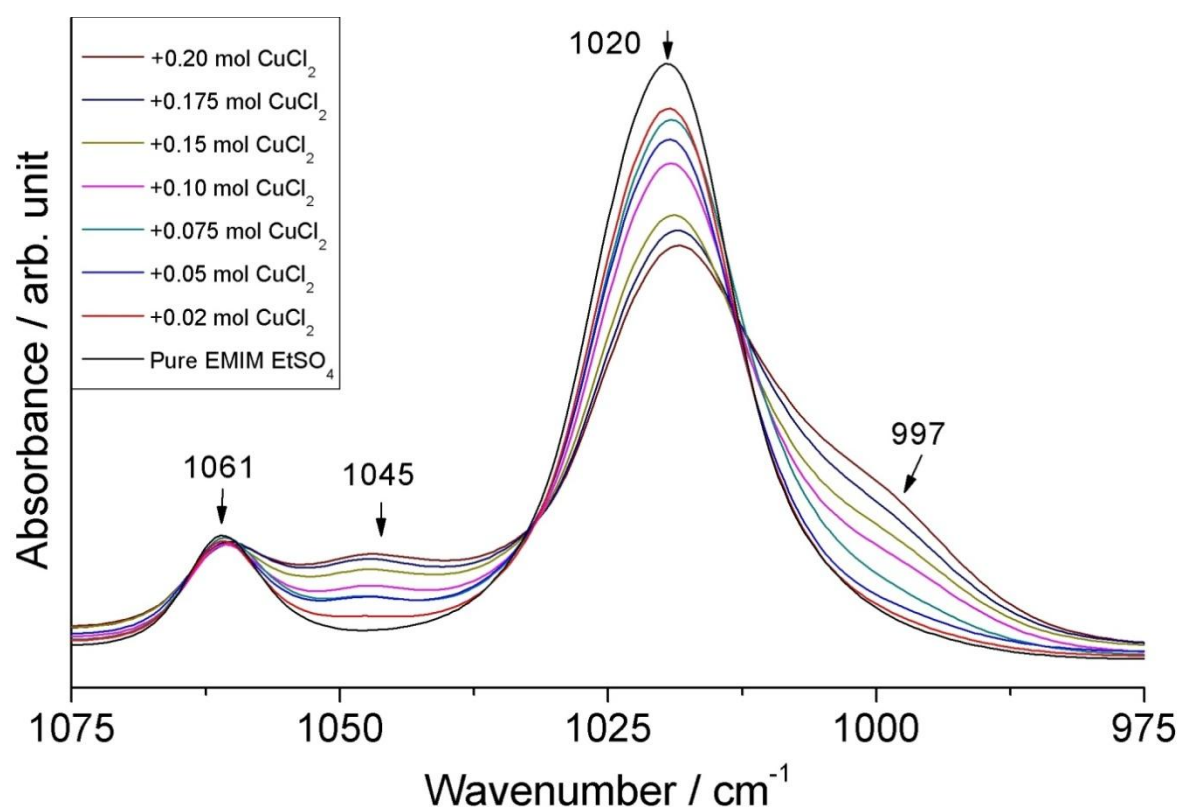


Figure 4.19: Evolution with the concentration of the  $\text{CuCl}_2$  salt of the IR spectra of the  $\text{CuCl}_2/[\text{EMIM}][\text{EtSO}_4]$  solutions measured in the region of the symmetric O-S-O stretches. The new bands are located at  $997$  and  $1045\text{ cm}^{-1}$ .



The vibrational transition located at  $1061\text{ cm}^{-1}$  (calculated at  $1068\text{ cm}^{-1}$  without copper salt) is assigned to the O-C-C stretching mode of the  $\text{EtSO}_4$  anions. This IR band is not affected by the increased dissolution of the  $\text{CuCl}_2$  salt whereas a new band clearly appears at  $1045\text{ cm}^{-1}$ . This new vibrational transition band can be assigned to the O-C-C stretching mode perturbed by the interaction of  $\text{SO}_3$  groups of the anions with copper. Indeed, the vibrational analysis obtained from DFT calculations suggests that under the complex formation this mode is shifted towards lower wavenumbers by about  $10\text{-}14\text{ cm}^{-1}$  (calculated values ranging from  $1053$  to  $1060\text{ cm}^{-1}$ , Table 4.4). Moreover, this spectral shift is accompanied by a significant increase in IR intensity induced by the interactions with copper.

In summary, the specific spectral signatures due to Cu-complex formation in [EMIM]  $[\text{EtSO}_4]$  are perceived through two interaction-induced broad IR bands located at  $997$  and  $1045\text{ cm}^{-1}$  and two interaction-induced well-defined IR bands situated at  $1171\text{ cm}^{-1}$  and  $1298\text{ cm}^{-1}$ . The broad IR bands are assigned to the symmetric S-O and OCC stretching modes respectively, when the  $\text{EtSO}_4$  anions are engaged with the copper cation during complex formation. Two other well-defined IR bands are assigned to asymmetric S-O stretching mode perturbed by the complex formation.

#### **4.3.4.2 Spectral features in the far IR region $200\text{-}500\text{ cm}^{-1}$**

The evolution of the Raman and IR profiles in the region of  $200\text{-}500\text{ cm}^{-1}$  of the solutions  $\text{CuCl}_2$ /[EMIM]  $[\text{EtSO}_4]$  are displayed in Figures 4.20 and 4.21, respectively. In both spectroscopies, we have retrieved the three fundamental bands located at:

- $416\text{ cm}^{-1}$  due to the O-S-O bending mode of the  $\text{SO}_3$  groups.
- $342\text{ cm}^{-1}$  due to the O-C-C bending mode of the anions  $\text{EtSO}_4$ .
- $245\text{ cm}^{-1}$  assigned to the rocking  $\rho(\text{CH}_3)$  mode of the ethyl group of the anions.

With the increasing concentration of the  $\text{CuCl}_2$  salt, the intensities of the bands at  $416\text{ cm}^{-1}$  and  $342\text{ cm}^{-1}$  decrease. At the same time, the shoulder observed in the IR and Raman profiles at  $430\text{-}435\text{ cm}^{-1}$  becomes better defined, and it can be assigned to the  $\delta\text{CNC}(\text{CH}_3)$  and  $\delta\text{CNC}(\text{CH}_2)$  bending modes of the cations.

The new band is located at  $313\text{ cm}^{-1}$ , which is clearly induced by the complex formation. The intensity of this band increases linearly with increasing concentration of  $\text{CuCl}_2$  as shown in the insert of Figure 4.21. From the vibrational analysis carried out from DFT calculations, we can assign this new band with the asymmetric Cl-Cu-Cl inter-atomic stretching motion within the Cu-complex formed with surrounding the  $\text{EtSO}_4$  anions.



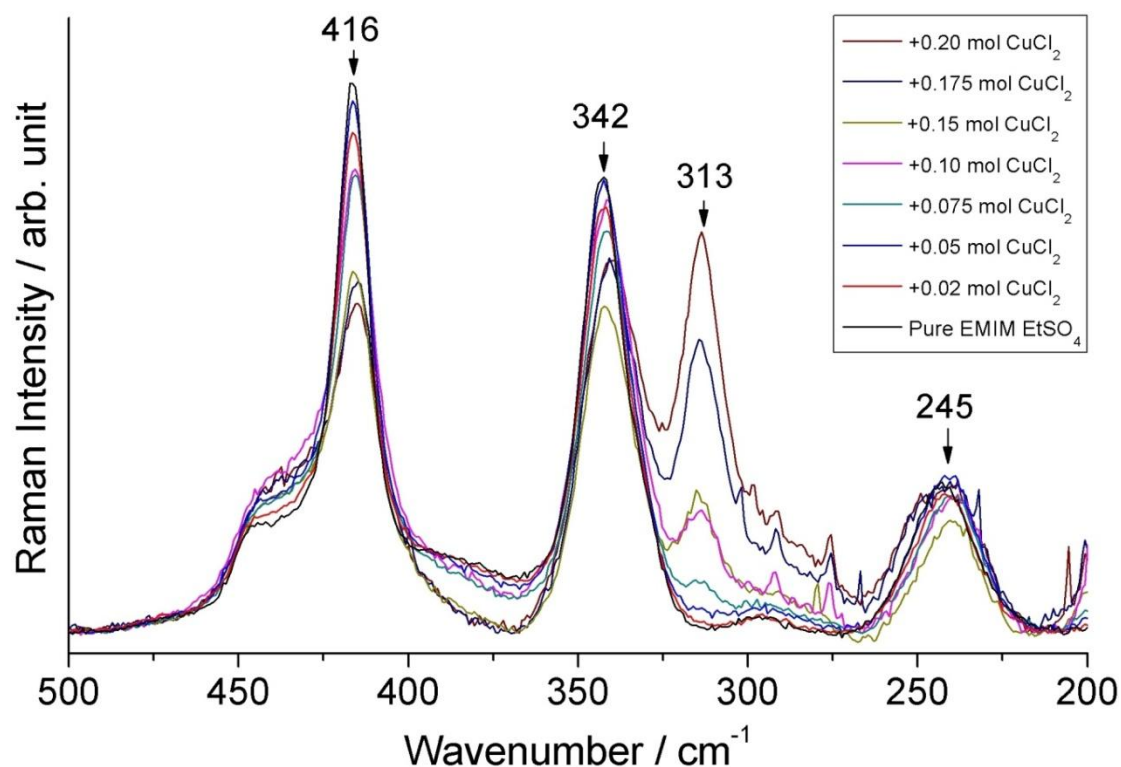


Figure 4.20: Evolution with the concentration of the  $\text{CuCl}_2$  salt of the Raman spectra of the  $\text{CuCl}_2/[\text{EMIM}][\text{EtSO}_4]$  solutions measured in the far IR spectral region  $200\text{--}500\text{ cm}^{-1}$ . The new band obtained upon the dissolution of the  $\text{CuCl}_2$  salt is located at  $313\text{ cm}^{-1}$ .

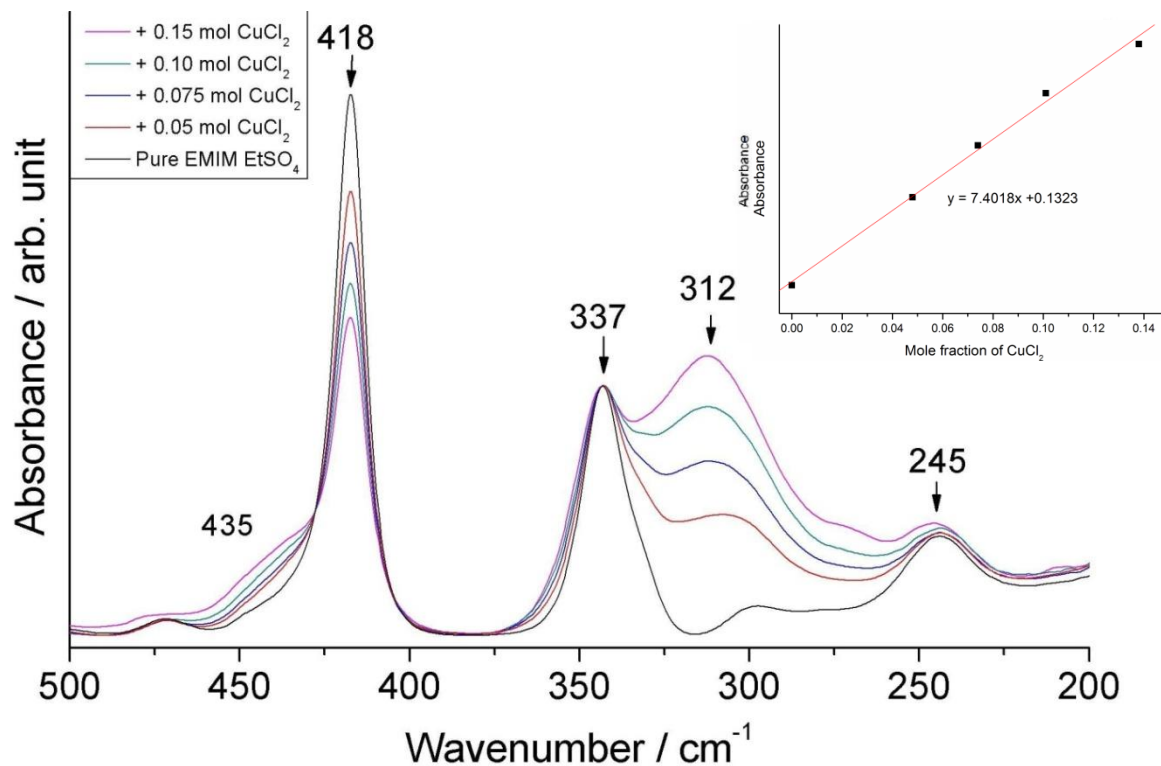


Figure 4.21: Evolution with the  $\text{CuCl}_2$  concentration the far-IR spectra ( $200\text{--}500\text{ cm}^{-1}$ ) showing the new band at  $312\text{ cm}^{-1}$ . The relationship between the intensity of the band at  $312\text{ cm}^{-1}$  and concentration of the  $\text{CuCl}_2$  salt is given in the inset.

Table 4.4: Main vibrational transitions of the complex  $\text{Cu}(\text{Cl}_2)\text{-(EthOSO}_3^-\text{EMI)}_2$  calculated at the [B3LYP/ 6-31+G(d,p):MQZVP(S,Cu)] level.

Exptl bands transitions ( $\text{cm}^{-1}$ )	ion pair dimer structure			Ag-Complex Structure			Assignment
	Calc. transition ( $\text{cm}^{-1}$ )	I(IR) Km/mol	I(Ram) $\text{\AA}^4/\text{amu}$	Calc. transition ( $\text{cm}^{-1}$ )	I(IR) Km/mol	I(Ram) $\text{\AA}^4/\text{amu}$	
245	250.0	1.8	0.5	247-257	53.	29	rocking $\rho$ ( $\text{CH}_3$ ) ethyl (anion)
313*				313	69	1.6	asym. external stretching vas Cl-Cu-Cl (complex signature)
337-342	337.5	18.7	7.9	340	20.8	6.1	bending $\delta$ O-C-C( $\text{CH}_3$ ) (anion)
416-418	404.0-414.7	26.6	0.5	399-423	15.8	5.5	bending $\delta$ O-S-O( $\text{SO}_3$ )
430 (shoulder)	429-433	10.1	1.0	436.4-451.2	2.4	3.8	bending $\delta$ ( $\text{CNCH}_3$ , $\text{CNCH}_2$ )
997*				998.2	749	6.2	sym stretching vs S-O( $\text{SO}_3$ ) $\otimes$ str. $\nu\text{C}(\text{CH}_2)\text{-O-S}(\text{SO}_3)$
	1029.6	764.8	0.				sym stretching vs S-O( $\text{SO}_3$ ) $\otimes$ str. $\nu\text{C}(\text{CH}_2)\text{-O-S}(\text{SO}_3)$
1020	1032.1	0.2	61.4 P	1014.6	44.3	21.5 P	sym stretching vs S-O( $\text{SO}_3$ )
	1032.8-1048	18.0	18.4	1037-1050	43.1	18.7	( $\nu$ CNring, $\delta$ CNCring)
1045*				1053-1060	138.0	16.0	stretching $\nu$ O-C( $\text{CH}_2$ )-C( $\text{CH}_3$ )
1061	1068.2	51.4	28.0				stretching $\nu$ O-C( $\text{CH}_2$ )-C( $\text{CH}_3$ )
1172	1163.8-1173.9	35.5	4.8	1145-1184	30.0	40.0	rocking $\rho$ $\text{CH}_2$ , $\text{CH}_3$ (ethyl), rock. $\text{CH}_3$ (methyl)
1172*				1177.1	181.8	34.4	asym stretching vas S-O( $\text{SO}_3$ )
1225	1221.9-1223.3	853.7	13.2				asym stretching vas S-O( $\text{SO}_3$ ) $\otimes$ rocking $\rho$ $\text{CH}_2$ (ethyl) anion)
1246-1252	1239.3-1247.1	606.0	8.7				asym stretching vas S-O( $\text{SO}_3$ ) $\otimes$ $\delta\text{C}_{(4,5)}\text{H} \otimes \delta\text{C}_{(2)}\text{H}$
1298*				1316.2-1320.0	504.6	49.5	asym stretching vas S-O( $\text{SO}_3$ ) $\otimes$ rocking $\rho$ $\text{CH}_2$ (ethyl) anion)
1337	1358.2-1361.0	29.8	51.9 P	1352.4-1374.2.	23.8	29.4 P	stretching $\nu_{\text{ip}}\text{CN}(\text{ring})$ , $\nu_{\text{ip}}\text{CN}(\text{CH}_2(3))$
1568-1574	1597.0-1615.5	124.3	12.8	1607.0-1618.9	127.3	16.2	( $\nu\text{C}(2)\text{N} \otimes \nu\text{CC}(\text{ring}) \otimes \delta\text{C}(2,4,5)\text{H}$ )

\*indicates the interaction induced vibrational transition by the complex formation

$\nu$  = stretching;  $\delta$  = bending;  $\rho$  = rocking ; s= symmetric ; as= asymmetric.

## 4.4 Summary

From our vibrational spectroscopic results of the silver and copper salt solutions in the two imidazolium based ionic liquid, we can see that the interactions induced by the dissolution of the metal cation lead to very specific spectral features.

In the AgTFSI-[EMIM] [TFSI] system, the vibrational analysis carried out from our experimental measurements and DFT calculations allow us to assess the structural organisation in the first shell of solvation around the silver cation. In this case, the silver salt involves the same anion as the ionic liquid (TFSI). Our results show that the silver cation is solvated by three first neighbouring TFSI anions which interact with one of the O atoms of each SO<sub>2</sub> groups.

In the CuCl<sub>2</sub>-[EMIM] [TFSI] system, our results reveal very specific spectral features induced by the complex formation of copper cation with EtSO<sub>4</sub> (mainly perceived through the bands associated with the S-O stretches). As the salt and the ionic liquid involve two distinct anions, the first solvation shell of the Cu-complex involves two chlorine anions and two EtSO<sub>4</sub> anions, located at two distinct separation distances. The presence of the two chlorine anions interacting with the copper cation induced a well-defined band at 313 cm<sup>-1</sup> in both the IR and Raman spectra. This band is associated with the asymmetric stretching motion of Cl-Cu-Cl.

## 5 Electrochemical Results of EMIM EtSO<sub>4</sub>-based Electrolytes

The results of Cu electrodeposition from the [EMIM] [EtSO<sub>4</sub>] system are presented in this chapter. In the first section, the electrochemical characteristics of the pure [EMIM] [EtSO<sub>4</sub>] are presented. This is followed by the electrochemical characterisation results of the three different copper-containing electrolytes. Lastly, we present the electrodeposition results, describing the structure and properties of the film deposited from these electrolytes.

The three electrolyte solutions were prepared, using three mono and divalent copper salts: CuCl, CuCl<sub>2</sub> and CuSO<sub>4</sub>. These salts were chosen in order to investigate the influence of the oxidation state of the metal, as well as the anions, on the electrolyte behaviour and on the film properties. The influence of the oxidation state of the metals can be investigated by comparing the results between copper(I) and copper(II) electrolytes. Similarly, the influence of the anion can be studied by comparing the results obtained from the chloride and sulphate solutions.

### 5.1 Electrochemical stability window of the [EMIM] [EtSO<sub>4</sub>] ionic liquid

The electrochemical window of an electrolyte is the range of potential in which the electrolyte is electrochemically stable. As discussed in Chapter 2, a large electrochemical window is advantageous for solvents used in electrodeposition, and it is one of the main reasons for the interest in ionic liquids as electrodeposition media [10].

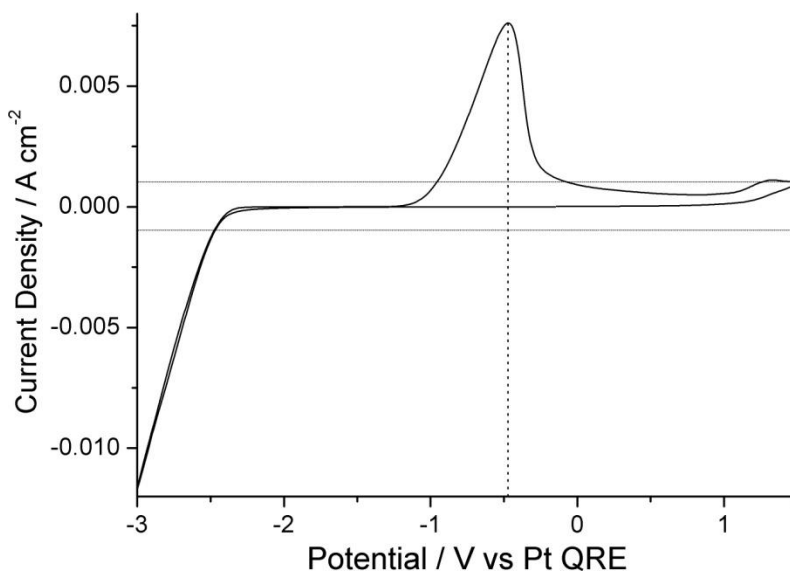


Figure 5.1: Cyclic voltammogram showing the electrochemical window of the pure [EMIM] [EtSO<sub>4</sub>] between -2.5 to 1.5 V. The working electrode was a GC disc. The experimental temperature was 35 °C and the scan rate was 50 mV s<sup>-1</sup>.

The electrochemical window of a solvent can be measured from its cyclic voltammogram. The electrochemical stability window is defined by convention as the potential range where the current density does not exceed 0.001 A cm<sup>-2</sup> [192]. Using the above definition, an electrochemical window of 4 V (between -2.5 and 1.5 V) was found for [EMIM] [EtSO<sub>4</sub>], as shown in Figure 5.1. The increase in the cathodic current at around -2.3 V during the forward scan can be attributed to the reduction of the [EMIM] cation when the potential exceeds the upper boundary of the electrochemical window

[238]. In the reverse scan an anodic peak is observed at -0.5 V, corresponding to the oxidation of the species formed in the forward scan [238].

A direct quantitative comparison of this electrochemical window with results found in the literature is difficult because the anodic and cathodic potential limits depend on many factors, such as the electrode material and geometry, potential scan rate, temperature, atmosphere, nature and concentration of impurities in the ionic liquid, as well as the electrochemical cell setup [11,10]. That said, the measured electrochemical window value obtained in this study was in agreement with those found in the literature [238,239].

## 5.2 Electrochemical characterisation of the electrolyte solutions

The cyclic voltammograms of 0.1 M CuCl, 0.1 M CuCl<sub>2</sub> and 0.1 M CuSO<sub>4</sub> solutions in [EMIM] [EtSO<sub>4</sub>] are presented in this section. The reduction and oxidation peaks observed in the cyclic voltammograms are assigned and the evolution of these peaks as a function of the potential, current density and temperature analysed. Using the cyclic voltammograms data, the reduction activation energies were calculated.

### 5.2.1 Cyclic voltammograms of the [EMIM] [EtSO<sub>4</sub>] solutions

#### 5.2.1.1 0.1 M CuCl solution in [EMIM] [EtSO<sub>4</sub>]

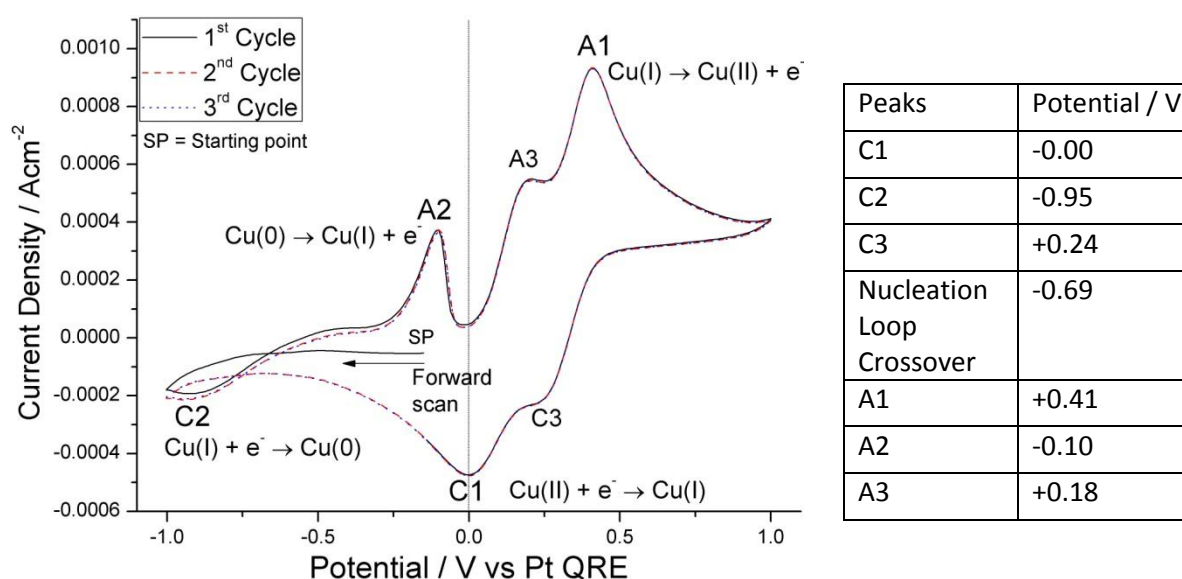


Figure 5.2: Cyclic voltammogram (3 cycles) of 0.1 M CuCl solution in [EMIM] [EtSO<sub>4</sub>] at 35 °C. The working electrode was a GC disc and the scan rate was 50 mV s<sup>-1</sup>. The potential of the cathodic and anodic peaks are shown in the accompanying table.

The voltammogram of the 0.1 M CuCl solution is shown in Figure 5.2. In the forward scan, the cathodic current density increases gradually at -0.75 V until the reversal potential at -1.00 V. In the reverse scan, a cathodic peak is observed at -0.95 V (C2), which can be attributed to the reduction of Cu(I) to metallic copper (Cu(0)), in agreement with our electrodeposition results and the literature [240-242]. This assignment is further confirmed by the appearance of a nucleation loop with a crossover at -0.69 V, an indication for metallic nucleation [243]. In the reverse scan, three oxidation

peaks are observed. The A2 peak at -0.10 V corresponds to the oxidation of the metallic copper (Cu(0)) formed during the forward scan to Cu(I). This can be seen from the cyclic voltammograms obtained using different cathodic reversal potentials as shown in Figure 5.3, where the A2 peak only appears when the potential range includes the C2 reduction peak. The A3 and A1 oxidation peaks at +0.18 and +0.41 V correspond to the oxidation of Cu(I) to Cu(II). The appearance of two oxidation peaks for the same reaction may be due to the presence of two different types of complexes, a more detailed discussion of this will be given in Chapter 7.

After the potential is reversed once again at +1.00 V, two cathodic peaks appear at +0.24 V (C3) and -0.00 V (C1). The potential of peaks C1 and C3 are characteristic of the reduction of Cu(II) to Cu(I) [240-242], suggesting that Cu(II) was present in the electrolyte. The presence of Cu(II) in a CuCl solution can be explained by the presence of the divalent cation in the original salt as an impurity. This is supported by the fact that the electrolyte presents a pale green colour, when Cu(II) impurities are present in Cu(I) solutions, as observed by previous authors [241]. Similar evolutions are observed in the second and third cycles of the voltammograms.

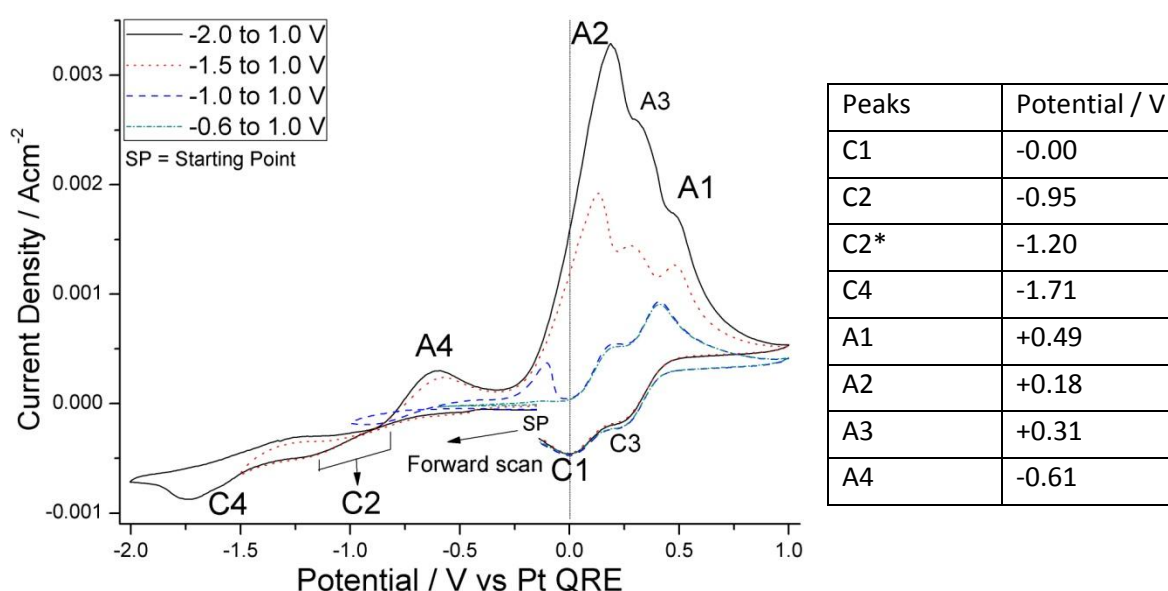


Figure 5.3: Cyclic voltammograms of 0.1 M CuCl solution in [EMIM][EtSO<sub>4</sub>] at 35 °C using different reversal potentials. The working electrode was a GC disc and the scan rate was 50 mV s<sup>-1</sup>. The potential of the cathodic and anodic peaks are shown in the accompanying table.

When the reversal potential is set to a more negative value than -1.00 V, two additional cathodic reduction peaks are observed in the forward scan, at -1.20 V (C2) and -1.71 V (C4), as shown in Figure 5.3. In this voltammogram (Figure 5.2), the peak C2 appears over a range of potentials, due to the different voltammograms being reversed at different reversal potentials. Hence this peak also corresponds to the reduction of Cu(I) to metallic copper (Cu(0)). The C4 peak is likely to be due to the further formation of metallic copper (Cu(0)). In the reverse scan, a new oxidation peak is observed at -0.60 V (A4), which is at a potential almost similar to the oxidation peak observed in Figure 5.1, and it may correspond to the breakdown of the ionic liquid. Significant increases in the current density of the anodic peaks at A3, A2 and A1 are also observed. The potential of these peaks shift to more positive values when the reversal potential is more negative than -1.00 V, as shown by

comparing Figures 5.2 and 5.3. A possible explanation for these variations is that a larger amount of metallic copper is formed during the reduction steps, resulting in an increase in the current density of these anodic peaks.

### 5.2.1.2 0.1 M CuCl<sub>2</sub> solution in [EMIM] [EtSO<sub>4</sub>]

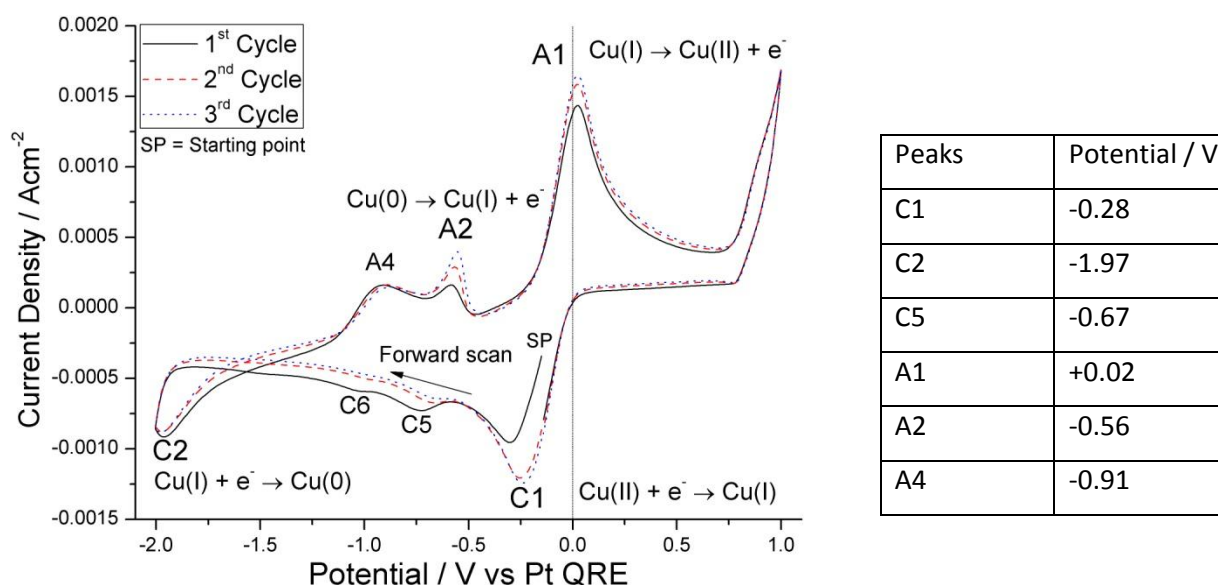
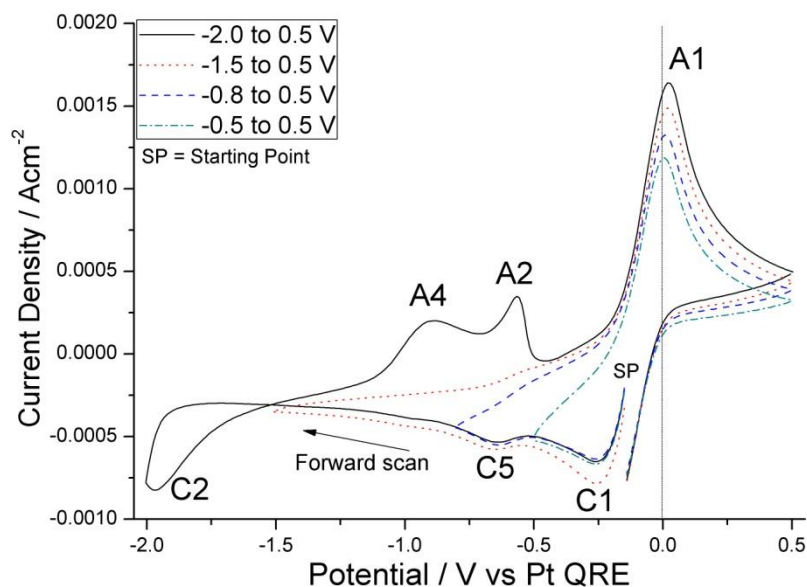


Figure 5.4: Cyclic voltammograms of 0.1 M CuCl<sub>2</sub> solution in [EMIM] [EtSO<sub>4</sub>] at 35 °C. The working electrode was a GC disc and the scan rate was 50 mV s<sup>-1</sup>. The potential of the cathodic and anodic peaks are shown in the accompanying table.

The voltammogram of the 0.1 M CuCl<sub>2</sub> solution is presented in Figure 5.4. In the forward scan, the cathodic current density increases sharply at around 0.00 V, forming a cathodic peak at -0.30 V (C1), attributed to the reduction of Cu(II) to Cu(I). Pursuing the scan reveals two additional cathodic peaks at -0.73 (C5) and -1.06 V (C6). Peak C5 may be associated with the underpotential deposition of Cu(I) to metallic copper. The current density of the peak C5 was greatly reduced in the second and third cycles of the cyclic voltammogram, an indication that the reaction is stopped when the original substrate surface is covered by the copper deposition [173]. Peak C6 is probably due to the reduction of the ionic liquid product formed at +0.75 V, as this peak does not exist when the reversal potential was at 0.5 V (Figure 5.5). As the scan progresses, the cathodic current continues to decrease up to the potential of -1.85 V, where a sharp increase in current is observed until the reversal potential at -2.0 V. In the reverse scan, a cathodic peak at -1.97 V (C2) is observed and it could be attributed to the reduction of Cu(I) to metallic copper (Cu(0)). Similar to what was observed for the CuCl solution, the reverse scan presents a nucleation loop with a crossover at -1.59 V, corresponding to the nucleation of metallic copper on the substrate [243]. As the scan progresses, two anodic peaks at -0.92 (A4) and -0.55 V (A2) can be observed. From Figure 5.5 showing the voltammograms at different reversal potentials, the A2 and A4 peaks are present only when the reversal potential includes the nucleation loop and the C2 peak. The A2 peak can be attributed to the oxidation of the metallic copper to Cu(I). Similar to the CuCl solution, the A4 peak is most likely

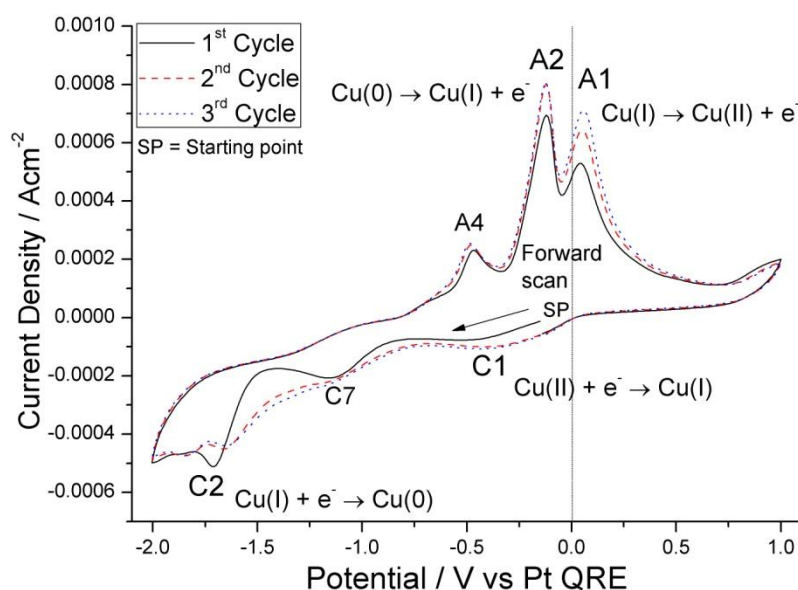
to be due to the oxidation of the ionic liquid products. Finally, the anodic peak at +0.02 V (A1) can be attributed to the oxidation of Cu(I) to Cu(II).



Peaks	Potential / V
C1	-0.28
C2	-1.97
C5	-0.67
A1	+0.02
A2	-0.56
A4	-0.91

Figure 5.5: Cyclic voltammograms of 0.1 M CuCl<sub>2</sub> solution in [EMIM][EtSO<sub>4</sub>] at 35 °C using different cathodic reversible potentials. The working electrode was a GC disc and the scan rate was 50 mV s<sup>-1</sup>. The potential of the cathodic and anodic peaks are shown in the accompanying table.

### 5.2.1.3 0.1 M CuSO<sub>4</sub> solution in [EMIM][EtSO<sub>4</sub>]



Peaks	Potential / V
C1	-0.67
C2	-1.68
C7	-1.25
A1	+0.05
A2	-0.12
A4	-0.47

Figure 5.6: Cyclic voltammogram (3 cycles) of 0.1 M CuSO<sub>4</sub> solution in [EMIM][EtSO<sub>4</sub>] at 35 °C. The working electrode was a GC disc and the scan rate was 50 mV s<sup>-1</sup>. The potential of the cathodic and anodic peaks are shown in the accompanying table.



The voltammogram of the 0.1 M  $\text{CuSO}_4$  solution is presented in Figure 5.6. In the forward scan a cathodic wave is observed at -0.67 V (C1) which is due to the reduction of  $\text{Cu(II)}$  to  $\text{Cu(I)}$ . A second cathodic peak is observed at -1.25 V (C7), probably associated with the presence of impurities in the electrolyte, such as water [242]. A steep increase in the cathodic current occurs at -1.45 V, leading to a cathodic peak at -1.68 V (C2), which can be attributed to the reduction of  $\text{Cu(I)}$  to metallic copper ( $\text{Cu(0)}$ ). In the reverse scan, the anodic peaks at -0.47 V (A4) and -0.12 V (A2) are related to the C2 reduction peak. This can be seen in Figure 5.7 where the peaks A4 and A2 are not present until the reversal potential includes the C3 peak. The A2 peak is due to the oxidation of metallic copper to  $\text{Cu(I)}$ . A possible explanation for the A4 peak is that it corresponds to the oxidation of small amounts of ionic liquid products, similar to the results found in the other two solutions. Lastly, the anodic peak at 0.05 V (A1) is related to the oxidation of  $\text{Cu(I)}$  to  $\text{Cu(II)}$ .

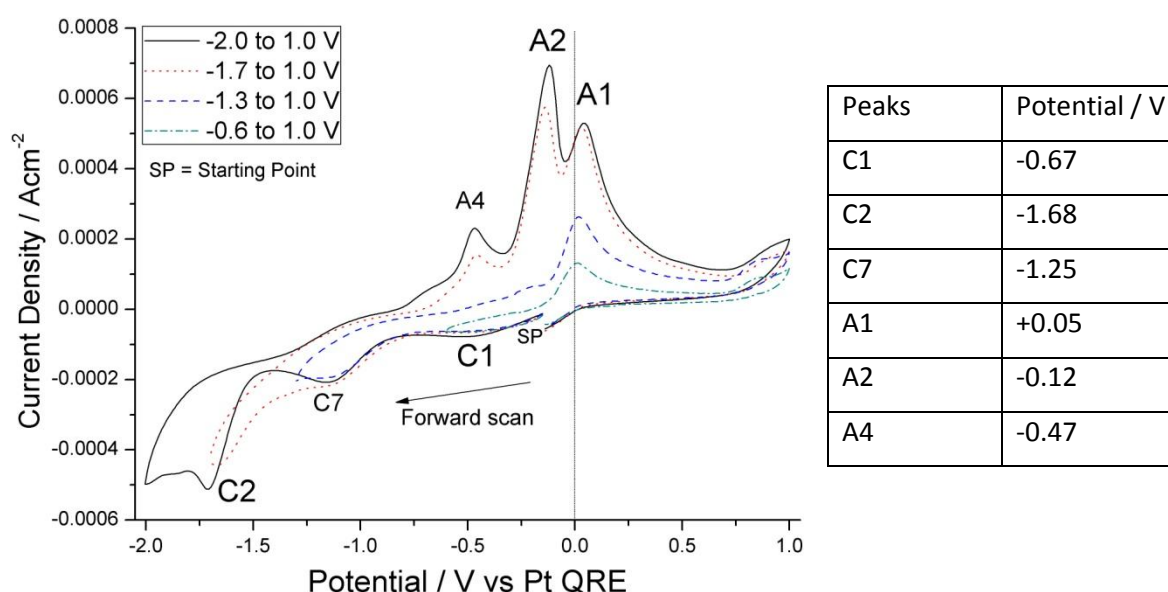


Figure 5.7: Cyclic voltammograms of 0.1 M  $\text{CuSO}_4$  solution in  $[\text{EMIM}][\text{EtSO}_4]$  at 35 °C using different cathodic reversible potentials. The working electrode was a GC disc and the scan rate was  $50 \text{ mV s}^{-1}$ . The potential of the cathodic and anodic peaks are shown in the accompanying table.

#### 5.2.1.4 Summary of the cyclic voltammograms

These cyclic voltammetry results show that the reduction of  $\text{Cu(II)}$  solutions in  $[\text{EMIM}][\text{EtSO}_4]$  occurs in two steps for all three Cu salts, in agreement with the results reported for  $\text{Cu(II)}$  solutions in  $[\text{EMIM}][\text{DCA}]$  [242],  $[\text{EMIM}][\text{BF}_4]$  [240] and  $[\text{TMHA}][\text{TFSI}]$  [241]. The results also show that the potential range for copper deposition for both the  $\text{Cu(II)}$  solutions lies between -1.5 and -2.0 V and for the  $\text{CuCl}$  solution, between -0.7 and -2.0 V. The difference in potentials between the peaks corresponding to the  $\text{Cu(II)}/\text{Cu(I)}$  and  $\text{Cu(I)}/\text{Cu(0)}$  redox reactions for the three solutions is large, but comparable to the values reported in the literature when glassy carbon is used as the working electrode material [240,242].

## 5.2.2 Mechanism of the electrochemical reaction

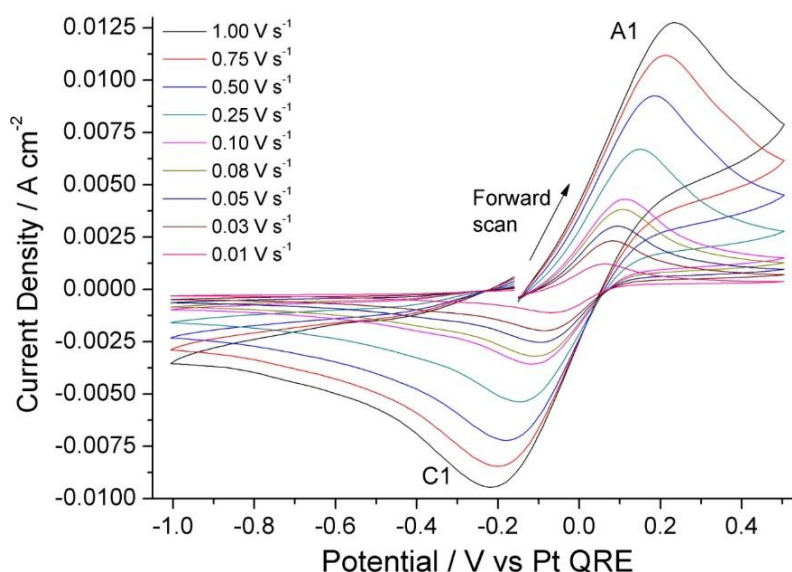


Figure 5.8: Cyclic voltammograms of 0.1 M  $\text{CuCl}_2$  solution in [EMIM] [EtSO<sub>4</sub>] at 85 °C using different potential scan rates between 0.01 and 1.00  $\text{V s}^{-1}$ . The working electrode was a GC disc.

Cyclic voltammograms of the solutions were also carried out using different potential scan rates. An example of our results is shown in Figure 5.8, for the 0.1 M  $\text{CuCl}_2$  solution in [EMIM] [EtSO<sub>4</sub>] at 85 °C. The potential range was chosen to cover the peak due to the reduction of Cu(II) to Cu(I) and also the corresponding oxidation peak of Cu(I) to Cu(II). To determine the reversibility of the reaction, the data obtained from the cyclic voltammograms was tested against the conditions for a reversible process described by Equations 3.4, 3.5, 3.6 and 3.7 listed in Section 3.4.1, reproduced below for convenience.

- $I_p = v^{1/2}$  Eq. 3.4

- $E_p$  is independent of  $v$
- $|E_p - E_{p/2}| = 2.2RT/nF$  Eq. 3.5

- $E_{p,a} - E_{p,c} = 2.3RT/nF$  ( $E_a \leq E_{p,c}$  or  $E_a \geq E_{p,o}$ ) Eq. 3.6

- $|I_{p,a}/I_{p,c}| = 1$  Eq. 3.7

$I_p$  is the peak current density,  $E_p$  is the peak potential,  $E_{p/2}$  is the potential when the current density is half of the peak current density,  $E_{p,a}$  is the oxidation peak potential,  $E_{p,c}$  is the reduction peak potential,  $I_{p,a}$  is the oxidation peak current density and  $I_{p,c}$  is the reduction peak current density.

The current density of the anodic (A1) and cathodic (C1) peaks for the 0.1 M  $\text{CuCl}_2$  solution in [EMIM] [EtSO<sub>4</sub>] at 85 °C was found to vary linearly with the square root of the scan rate ( $v^{1/2}$ ) as shown in Figure 5.9. This satisfies Equation 3.4, indicating that the process is diffusion controlled [29,8]. However, the oxidation and reduction peak positions were found to depend on the scan rate, and this does not satisfy the condition for a reversible process for which the peak potential must be

independent of the scan rate. The oxidation peak (A1) shifts to a more positive potential and the reduction peak (C1) shifts to a more negative potential as the scan rate is increased, as clearly seen in Figure 5.8. The calculated values for  $|E_p - E_{p/2}|$  and  $E_{p,a} - E_{p,c}$  are larger than the values provided by Equations 3.5 and 3.6 for a reversible process. This is an indication of the high resistance of the solution, as often found for ionic liquid based electrolytes [129]. Besides that, the anodic peak current densities are slightly larger than the cathodic peak current densities; hence they do not satisfy Equation 3.7 for a reversible process. Based on the above considerations as well as the large separation between the anodic and cathodic peaks observed in Figures 5.2, 5.4 and 5.6, the reduction of Cu(II) to Cu(I) in [EMIM] [EtSO<sub>4</sub>], on a glassy carbon electrode, at 85 °C, can be described as a quasi-reversible process.

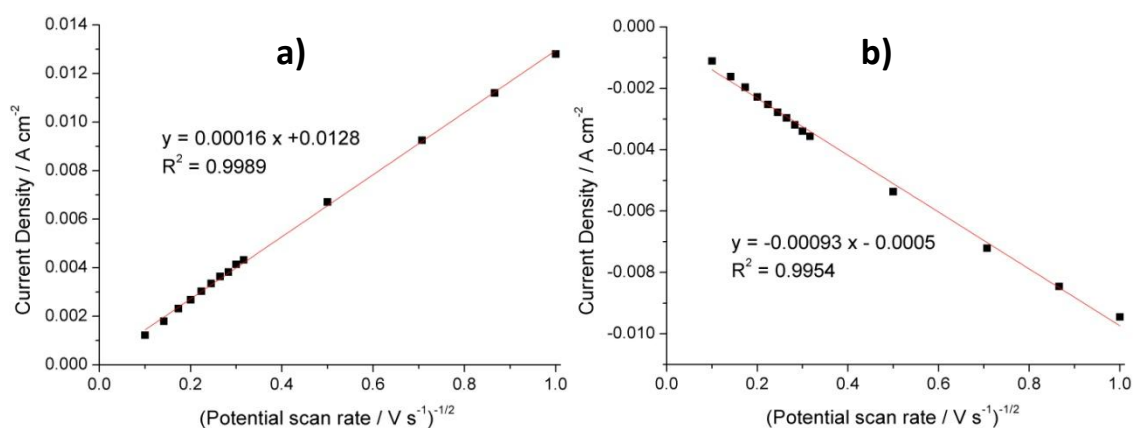


Figure 5.9: **a)** The anodic peak current (A1) and **b)** cathodic peak current (C1) as a function of scan rate for the 0.1 M CuCl<sub>2</sub> solution in [EMIM] [EtSO<sub>4</sub>] at 85 °C shown in Figure 5.8.

### 5.2.3 Stability of the solutions

Our results show that the potential of the cathodic and anodic peak positions and their relative current density values for the CuCl<sub>2</sub> and CuSO<sub>4</sub> solutions change with temperature (Figures 5.10 and 5.11).

In the CuCl<sub>2</sub> solution (Figure 5.10), the C1 and C2 reduction peaks shift to less negative potential from -0.30 and -1.97 V at 35 °C, to -0.21 and -1.89 V at 50 °C, and finally to -0.08 and -1.59 V at 85 °C. Similarly, the A4 anodic peak shifts from -0.55 V at 35 °C, to -0.46 V at 50 °C, and finally -0.21 V at 85 °C. The potential of A1 experiences a slight shift towards the positive potential with an increase in temperature, from +0.02 V at 35 °C, to +0.03 V at 50 °C and +0.09 V at 85 °C. On the contrary, A2 peak shifts slightly towards more negative potentials with the increase in temperature, from -0.97 V at 35 °C, to -1.02 V at 50 °C and -1.04 V at 85 °C. At 50 °C, a new oxidation peak appears at -0.3 V. This peak shifts to -0.1 V and grows larger as the temperature is increased to 50 °C. This peak is probably due to the formation of a less stable oxidation product resultant from the increase in thermal energy.

Besides the shift in peak potential, there is also an increase of the current density of all the peaks with increasing temperature. At 35 °C (Figure 5.10 a), the oxidation peak A1 has a much higher current density than peak A2. However at 50 and 85 °C (Figures 5.10 b and c), the difference in the relative current densities of peak A1 and A2 is smaller than at 35 °C (Figure 5.10 a). On the contrary,

the current density of peaks C5 and C6 do not depend on the temperature, and both peaks disappear from the voltammogram at 85 °C. This supports the hypothesis that C5 and C6 peaks are due to impurities, with water as a likely candidate.

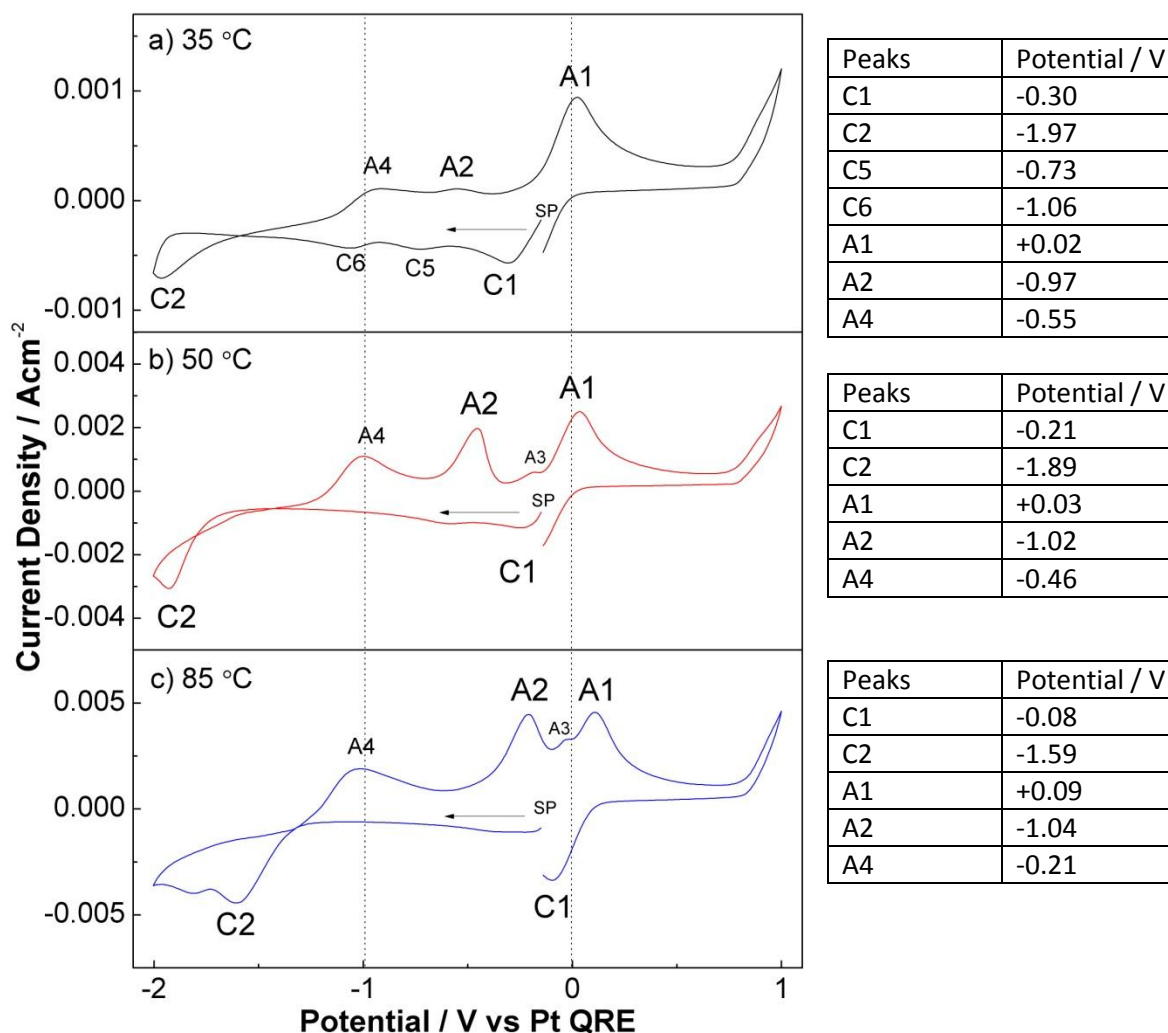


Figure 5.10: Cyclic voltammograms of 0.1 M  $\text{CuCl}_2$  solution in  $[\text{EMIM}][\text{EtSO}_4]$  at a) 35, b) 50 and c) 85 °C. The working electrode was a GC disc and the scan rate was  $50 \text{ mV s}^{-1}$ . The potential of the cathodic and anodic peaks are shown in the accompanying tables.

In the  $\text{CuSO}_4$  solution (Figure 5.11), we can see that C1 peak shifts slightly towards more positive potential with increasing temperature, from -0.56 V at 35 °C, to -0.36 V at 50 °C and -0.37 V at 85 °C. On the contrary, C2 shifts to more negative potentials, from -1.68 V at 35 °C, to -1.80 V at 50 °C and to -1.98 V at 85 °C. The potential of C7 does not depend significantly on the temperature, being -1.23 V at 35 °C, -1.26 V at 50 °C and -1.15 V at 85 °C. A new reduction peak at -0.61 V (C8) and a nucleation loop at -1.82 V are observed at 85 °C (Figure 5.11 c), which are not present in the cyclic voltammograms obtained at lower temperatures (Figure 5.11 a and b). Similarly, there is no significant change in the potential of peaks A1 and A2 with temperature. They are at +0.05 and -0.12 V at 35 °C, +0.06 and 0.15 V at 50 °C and +0.05 and -0.16 V at 85 °C, respectively. The peak A4 shifts

towards a slightly less negative potential, from -0.47 V at 35 °C, to -0.51 V at 50 °C and to -0.57 V at 85°C.

Our results also show that the overall current density increases with increasing temperature. At 35 °C (Figure 5.11 a), A2 peak has the highest current density compared to A1 and A4. Increasing the electrolyte temperature to 50 and 85 °C (Figures 5.11 a and b) does not affect the current density of A2 and A4 peaks significantly but it increases in the relative current density of A1.

The colour of the solutions changes as the temperature was increased. CuCl<sub>2</sub> and CuSO<sub>4</sub> solutions were dark green and green, respectively, at 35 °C and they change to light green and greenish blue, at 85 °C. This change in colour suggests that there is a change in the ionic complexes existing in the solution or a breakdown of the solvent has occurred. The colour of the CuCl solution is not affected by the electrolyte temperature and remains light green, suggesting that no change has occurred in the ionic complexes.

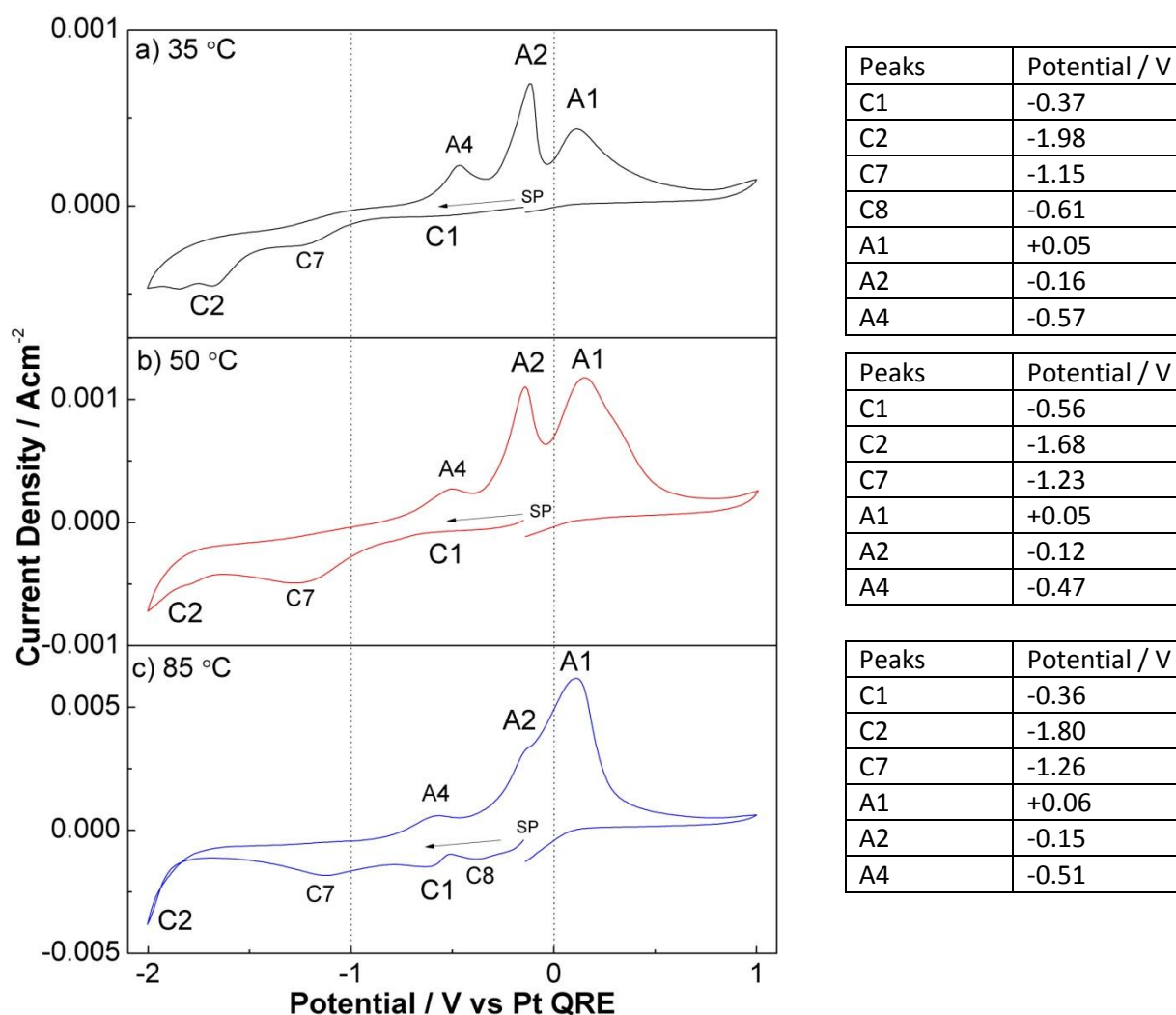


Figure 5.11: Cyclic voltammograms of 0.1 M CuSO<sub>4</sub> solution in [EMIM][EtSO<sub>4</sub>] at a) 35, b) 50 and c) 85 °C. The working electrode was a GC disc and the scan rate was 50 mV s<sup>-1</sup>. The potential of the cathodic and anodic peaks are shown in the accompanying tables.

### 5.2.4 Activation Energy of Cu(II) to Cu(I)

The variation in current density of peak C1 due to the reduction of Cu(II) to Cu(I) with the electrolyte temperature is presented in Figure 5.12. The observed increase of current density with temperature can be explained by the decrease of viscosity of the ionic liquid solution [10,244]. This leads to a higher mobility of the charge carrying species in solution, thereby increasing the electrical conductivity and, ultimately, the overall reaction rate at the electrode-electrolyte interface [10].

Since Cu(II) to Cu(I) reduction reaction is thermally activated, it behaves in accordance with the Arrhenius equation, given by:

$$i_{pc} = ke^{-\frac{E_a}{RT}} \quad \text{Eq. 5.1}$$

$i_{pc}$  is the peak current density,  $T$  is temperature in Kelvin,  $R$  is the ideal gas constant and  $k$  is a constant.

The activation energy  $E_a$  of the reaction can be calculated from the slope of a plot of the natural logarithm of ( $i_{pc}$ ) versus the inverse of the temperature, according to the equation:

$$\ln(i_{pc}) = -\frac{E_a}{RT} + \ln(k) \quad \text{Eq. 5.2}$$

This graph is shown in Figure 5.13. The calculated activation energy values of the Cu(II) to Cu(I) reduction reaction for the three different solutions are shown in Table 5.1 below.

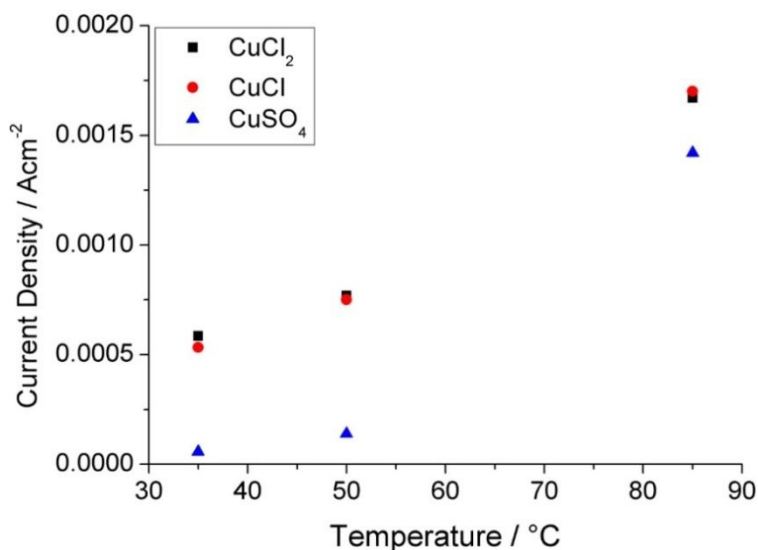


Figure 5.12: Change in the current density of peak C1 with temperature for 0.1 M CuCl, CuCl<sub>2</sub> and CuSO<sub>4</sub> solutions in [EMIM] [EtSO<sub>4</sub>]. The working electrode was a GC disc and the scan rate was 50 mV s<sup>-1</sup>.

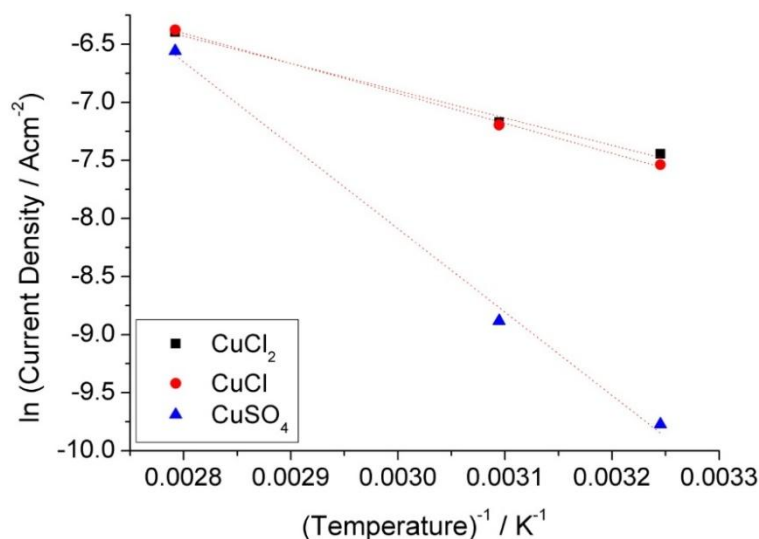


Figure 5.13: A plot of the current density of peak C1 versus the electrolyte temperature. A linear relationship shows that Equation 5.2 is satisfied.

Table 5.1: Calculated activation energy of the Cu(II) to Cu(I) reduction reaction for the three solutions.

Ionic liquid solution	Activation energy / kJ mol <sup>-1</sup>
0.1 M CuCl	19.5
0.1 M CuCl <sub>2</sub>	21.5
0.1 M CuSO <sub>4</sub>	59.7

The activation energy for the Cu(II) to Cu(I) reduction is similar for both CuCl and CuCl<sub>2</sub> solutions, which suggests that the species involved in the reaction for both electrolytes is the same. The activation energy of the CuSO<sub>4</sub> solution is much higher compared to the other two chloride-based solutions. From this, we can deduce that the copper complexation of the two chloride based solutions are probably the same, involving the chloride ions. For the CuSO<sub>4</sub> solution, the complexation will involve the sulphate ions.

### 5.2.5 Diffusion Coefficient

The chronoamperograms acquired with potential steps in the range corresponding to the reduction of Cu(II) (in CuCl<sub>2</sub> and CuSO<sub>4</sub> solutions) and Cu(I) (in CuCl solutions) are presented in Figure 5.14 a. After an initial current oscillation due to double-layer charging, the current density,  $i$  varies linearly with  $t^{-1/2}$  (Figure 5.14 b), according to Cottrell equation [8]:

$$i(t) = \frac{nFAD^{1/2}C_{\infty}}{\pi t^{1/2}} \quad \text{Eq. 5.3}$$

According to this equation, the diffusion coefficient can be calculated from the gradient of the  $i$  versus  $t^{-1/2}$  plot. The values obtained are presented in Table 5.2. The diffusion coefficient increases with temperature as expected, but the values are about an order of magnitude smaller than those found for Cu(I) and Cu(II) salt solutions in [EMIM] [DCA] ( $2.13 \times 10^{-6}$  and  $2.06 \times 10^{-6} \text{ cm}^2 \text{ s}^{-1}$ , respectively [242]) and about half the values found for Cu(I) and Cu(II) salt solutions in [EMIM] [Cl] [BF<sub>4</sub>] ( $2.3 \times 10^{-7}$  and  $1.5 \times 10^{-7} \text{ cm}^2 \text{ s}^{-1}$ , respectively [240]) reported in the literature. This difference can be explained by the higher viscosity of [EMIM] [EtSO<sub>4</sub>] [62] as compared to [EMIM] [DCA] and [EMIM] [Cl] [BF<sub>4</sub>] [242] and this suggests that these ionic liquids may allow higher deposition rate under similar deposition conditions.

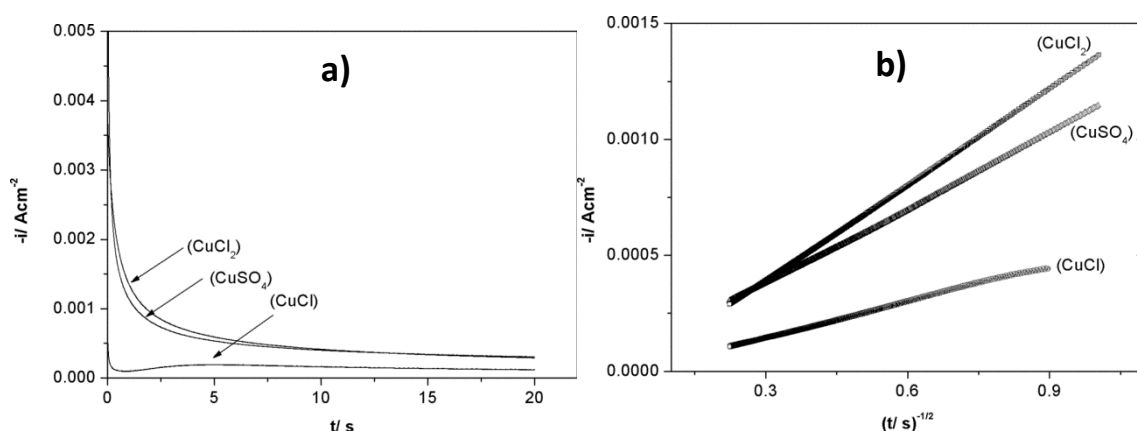


Figure 5.14: **a)** Chronoamperograms of 0.1 M CuCl, CuSO<sub>4</sub> and CuCl<sub>2</sub> solutions obtained at 35 °C with a GC disc electrode, using potential steps of -1.0, -0.7 and -0.3 V, respectively; **b)** respective variation of the current density with  $t^{-1/2}$ .

Table 5.2: Diffusion coefficient of the copper species in the three EMIM-EtSO<sub>4</sub> solutions calculated from chronoamperometry data.

Solution	Diffusion Coefficient, $D \text{ (cm}^2 \text{ s}^{-1}\text{)}$		
	35 °C	50 °C	85 °C
0.1 M Cu(I)Cl – EMIM EtSO <sub>4</sub>	$1.8 \times 10^{-07}$	$2.3 \times 10^{-07}$	$2.1 \times 10^{-06}$
0.1 M Cu(II)Cl <sub>2</sub> – EMIM EtSO <sub>4</sub>	$5.7 \times 10^{-08}$	$1.5 \times 10^{-07}$	$2.9 \times 10^{-06}$
0.1 M Cu(II)SO <sub>4</sub> – EMIM EtSO <sub>4</sub>	$3.0 \times 10^{-09}$	$8.4 \times 10^{-09}$	$9.1 \times 10^{-07}$

Comparing the diffusion coefficients of the active species in the three solutions, the CuCl and CuCl<sub>2</sub> solutions have values of the same magnitude, whereas the diffusion coefficient for the CuSO<sub>4</sub> solution is always about one order of magnitude lower. A possible explanation for this is that the copper complexes involving sulphate anions are much larger, because this anion is bigger than the chloride anion. A larger complex diffuses more slowly due to interactions with other compounds and molecules in the solution. This observation is also consistent with the activation energy values calculated for the Cu(II) to Cu(I) reduction in the previous section, where the rate determining step of the Cu(II) to Cu(I) reduction is the mass transport from the bulk solution to the electrode



interface. Hence the low diffusion coefficient in the  $\text{CuSO}_4$  solution, compared to the  $\text{CuCl}$  and  $\text{CuCl}_2$  solutions, results in the higher activation energy.

### 5.3 Electrodeposition

Copper films were obtained for 0.1 M  $\text{CuCl}$ , 0.1 M  $\text{CuCl}_2$  and 0.1 M  $\text{CuSO}_4$  solutions in [EMIM]  $[\text{EtSO}_4]$  by varying the applied potentials, deposition temperatures and times. For the  $\text{CuCl}_2$  and  $\text{CuSO}_4$  solutions, visible deposits were only obtained for the applied potential of -1.6 V or lower, except for the  $\text{CuSO}_4$  solution at high deposition temperature (85 °C), where a metallic film was obtained at -1.2 V. For the  $\text{CuCl}$  solution, very faint brownish deposits were observed at -0.8 V. Other deposition conditions failed to produce visible deposits. A summary of the electrodeposition results is shown in Table 5.3.

All deposited films have the metallic brown colour typical of copper, although those deposited at -1.6 V or higher have a metallic sheen while those deposited at -1.8 V have a darker brown colour with no lustre.

Table 5.3: Summary of the electrodeposition results obtained under different experimental conditions.

Electrolyte solutions	Temp/ °C	Deposition Potential/ V			
		-0.6/-0.8	-1.0/-1.2	-1.6	-1.8
0.1 M CuCl	35	Partial Deposit	Partial Deposit	Metallic Brown Deposit	Dark Brown Deposit
	50				
	85				
0.1 M CuCl <sub>2</sub>	35	No Deposit	No Deposit	Metallic Brown Deposit	Dark Brown Deposit
	50				
	85				
0.1 M CuSO <sub>4</sub>	35	No Deposit	no Deposit	Metallic Brown Deposit	Dark Brown Deposit
	50		Metallic Deposit		
	85				

#### 5.3.1 Microstructure of the films

##### 5.3.1.1 0.1 M $\text{CuCl}$ solutions

Visible films were obtained from the  $\text{CuCl}$  solution when the applied potential was more negative than -0.8 V. Between -0.8 to -1.2 V, the deposits were discontinuous and consisted of irregular clusters of roughly polyhedral particles as shown in Figure 5.15 a. The particles had diameters varying from 100 to 500 nm, with most particles in the 150-300 nm range (Figure 5.15 b). In this potential range, increasing the deposition temperature and time did not significantly improve the film coverage. An explanation is that at these potentials the particles only nucleate at the most conspicuous surface defects such as edges, steps, and surface protrusions, where the nucleation potential and current density is higher compared to most of the surface for geometric reasons. As

a result, the nucleation density is low and insufficient for the particles to grow and cover the substrate surface.

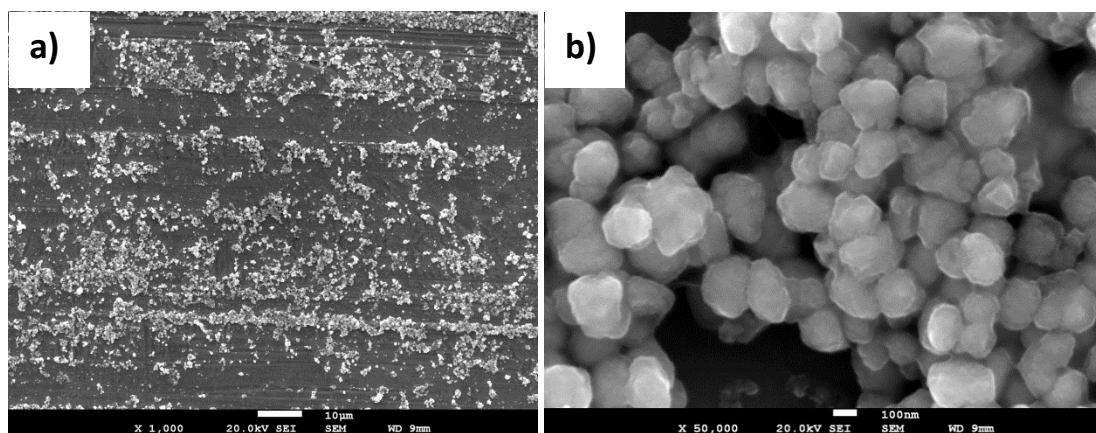


Figure 5.15: SEM micrographs at **a)** lower magnification and **b)** higher magnification of films electrodeposited from 0.1 M CuCl solution at -0.8 V. Deposition temperature: 35 °C. Deposition time: 900 s.

Increasing the potential to -1.6 V improves the continuity of the films, although the structures are widely dependent on the experimental parameters. The structure of films deposited at different temperatures and times is shown in the SEM micrographs of Figures 5.16 and 5.17. Similar to the films deposited at -0.8 V, the films are made up of roughly polyhedral particles but the size of these particles is much smaller, with diameter around 100 nm or lower. The size and shape of the particles are not significantly affected by the deposition temperature and time.

The continuity of the films is significantly improved when the deposition temperature is increased. The films are discontinuous at 35 °C (Figures 5.16 **a** and **b**), almost continuous at 50 °C (Figure 5.16 **c** and **d**) and fully continuous at 85 °C (Figures 5.16 **e** and **f**). Increasing the deposition time does not significantly affect the continuity of the films, but increases the film roughness. For deposition time of 1800 s (Figures 5.17 **b**, **d** and **f**), an overgrowth of the films is observed. This overgrowth is made up of particles that form clumps of large irregular aggregates on the surface. These occur Independently of the electrolyte temperature.

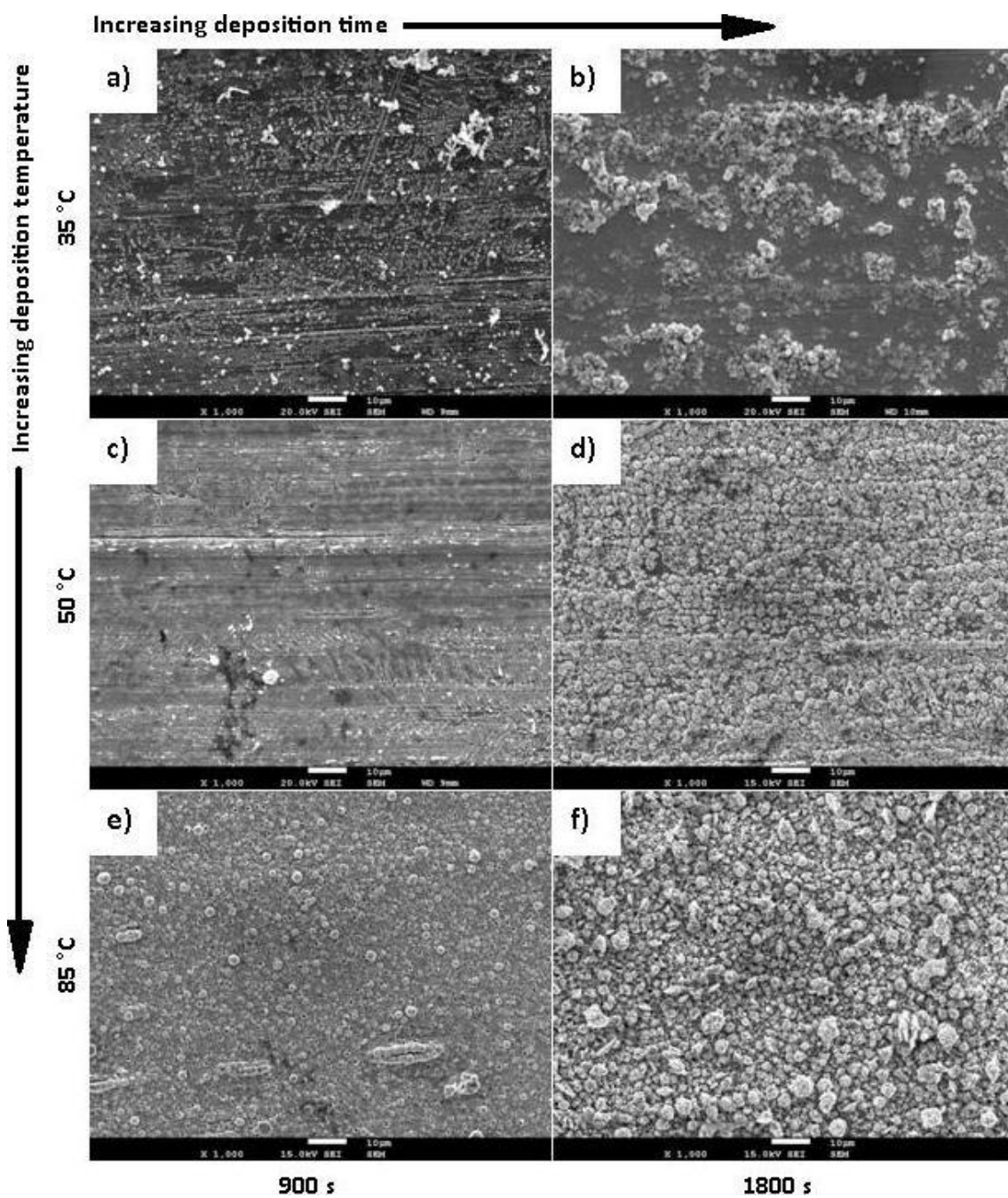


Figure 5.16: SEM micrographs (lower magnification) of films electrodeposited from 0.1 M CuCl solution at -1.6 V. Deposition temperatures: 35, 50 and 85 °C. Deposition times: 900 and 1800 s.

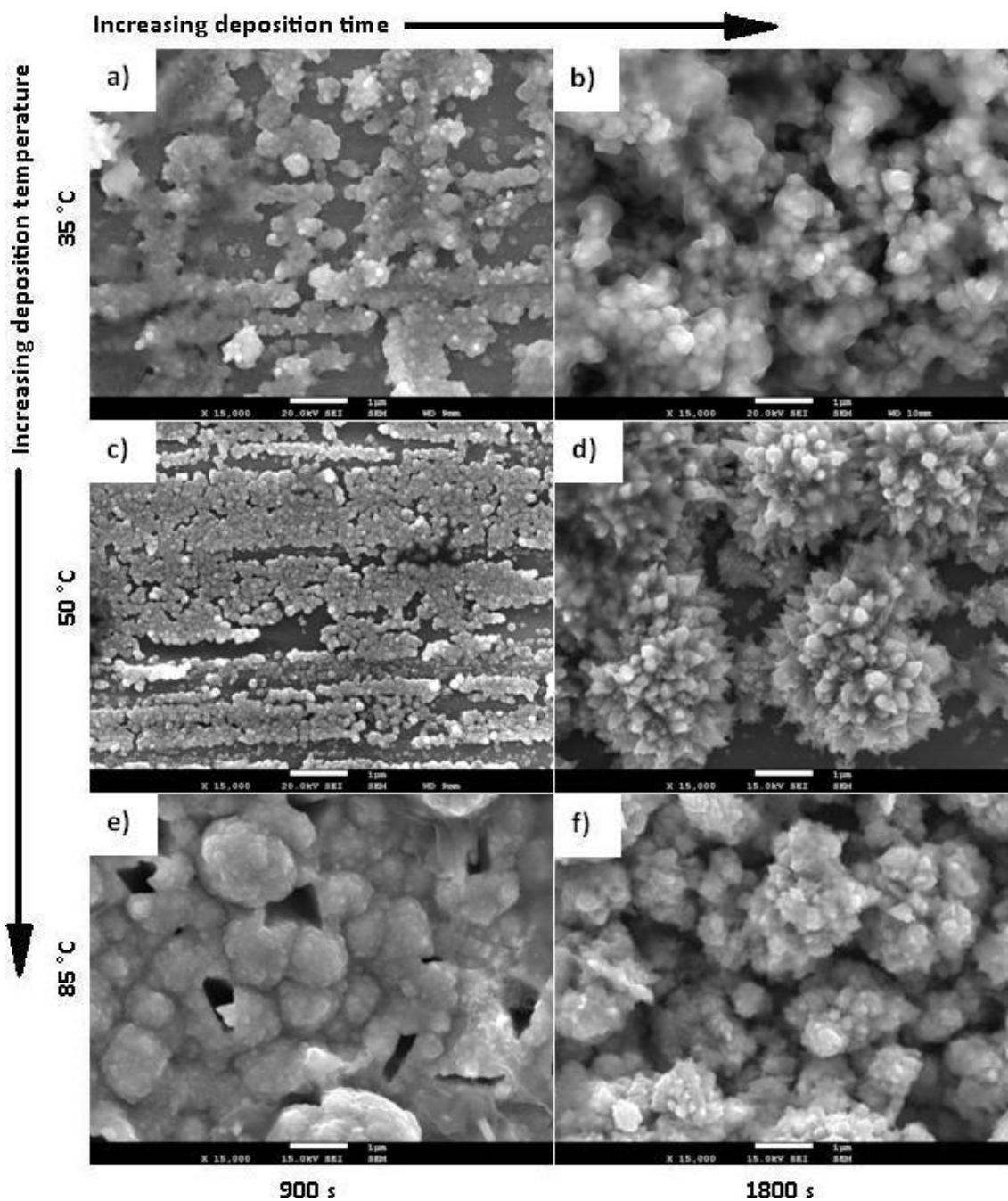


Figure 5.17: SEM micrographs (higher magnification) of films electrodeposited from 0.1 M CuCl solution at -1.6 V. Deposition temperatures: 35, 50 and 85 °C. Deposition times: 900 and 1800 s.

For -1.8 V, continuous films were obtained for all deposition temperatures (Figures 5.18 a, c and e). The film roughness increases with temperature, as shown by the SEM micrographs of the films deposited at -1.8 V for 900 s (Figures 5.18 b, d, and f). The best films were those deposited at 35 °C. They were continuous and regular, consisting of globular particles with an average particle size of 100 nm (Figure 5.18 b). For a deposition temperature of 50 °C, the film consists of globular clusters with a diameter of around 1 μm (Figure 5.18 d). When deposition is carried out at 85 °C

(Figure 5.18 f), large irregular aggregates of particles were formed. Independently of the deposition temperature, the average particle size remained at around 100 nm.

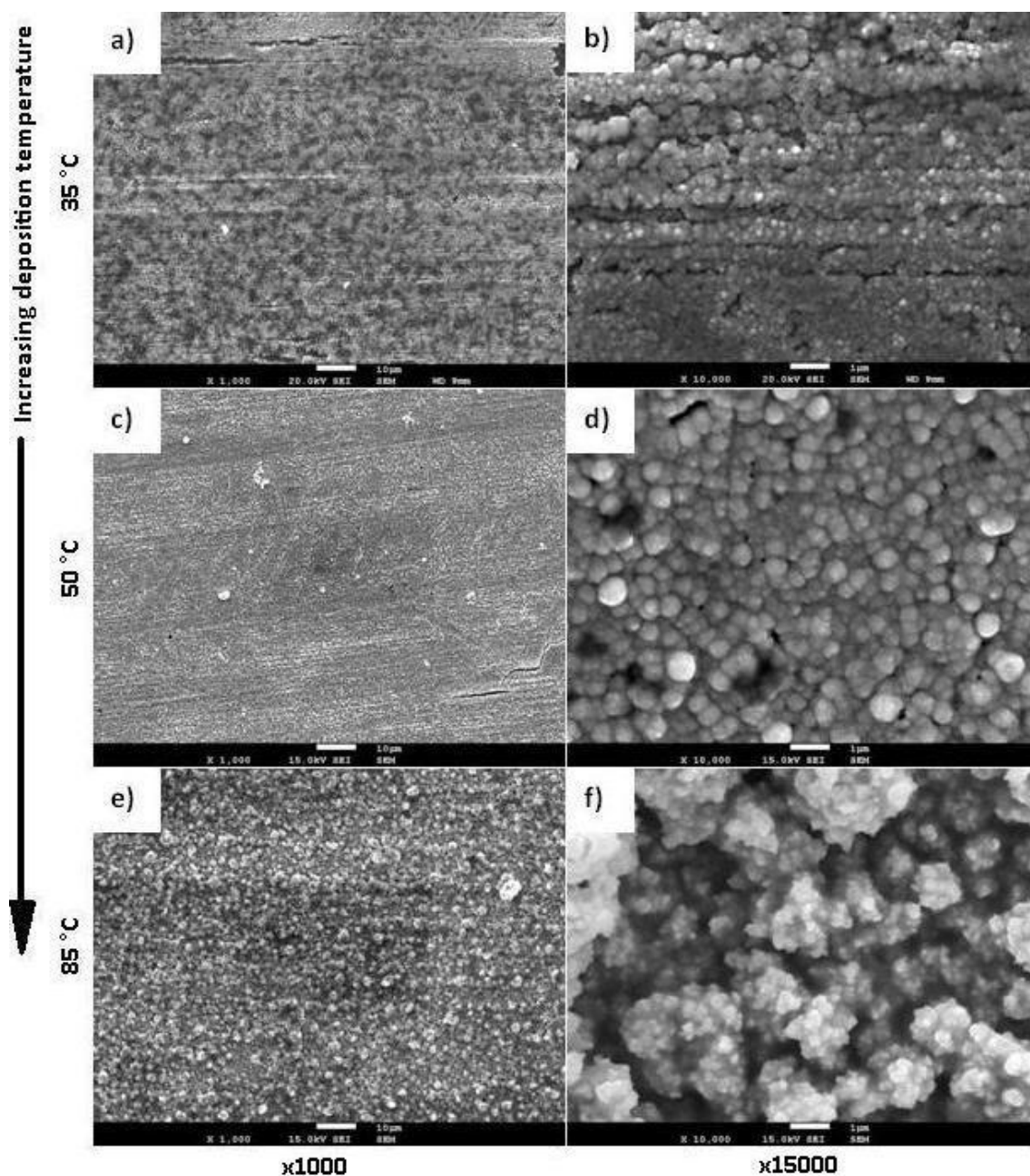


Figure 5.18: SEM micrographs of films electrodeposited from 0.1 M CuCl solution at -1.8 V for 900 s. Deposition temperatures: 35, 50 and 85°C.

### 5.3.1.2 0.1 M CuCl<sub>2</sub> solutions

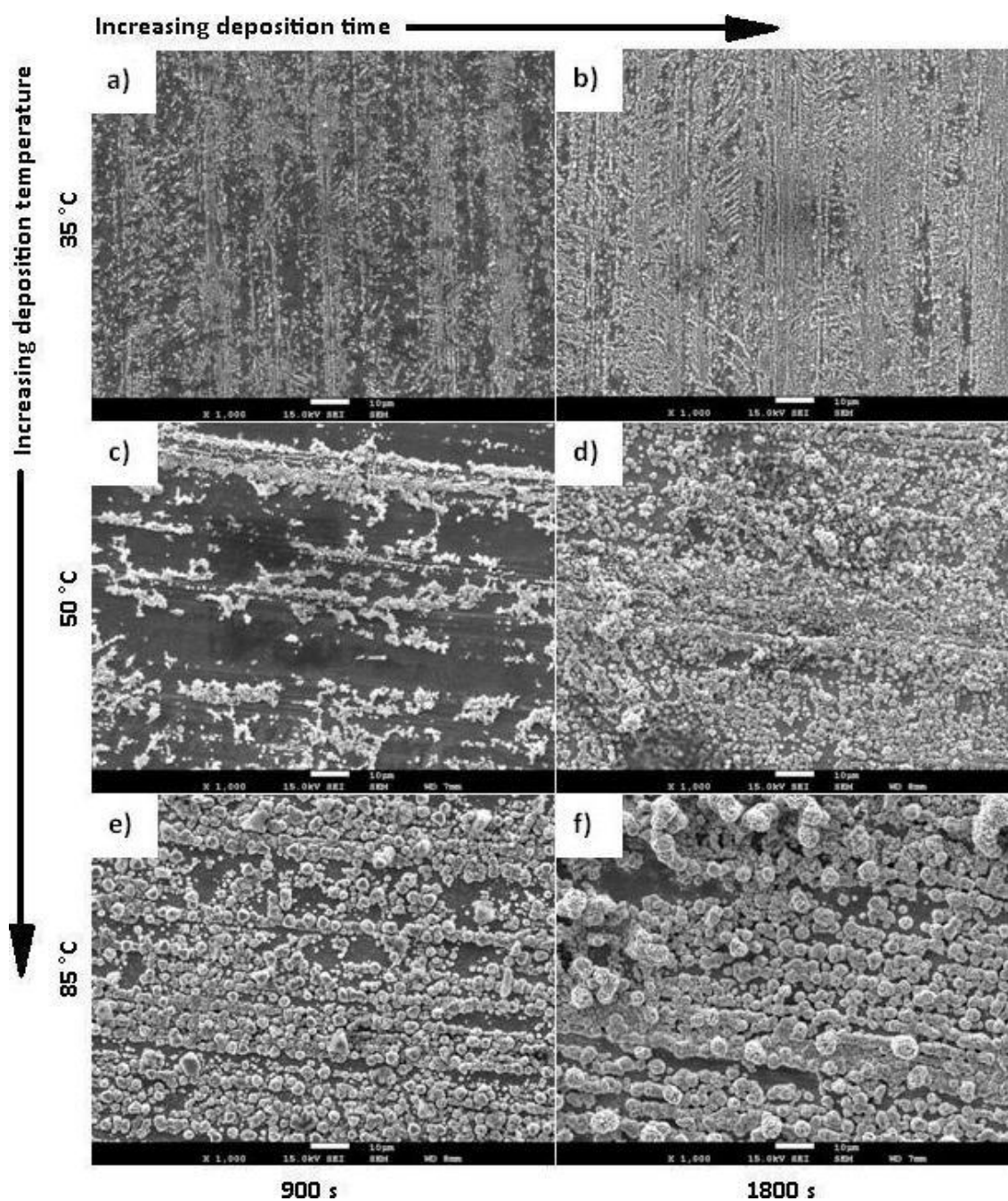


Figure 5.19: SEM micrographs of films electrodeposited from 0.1 M CuCl<sub>2</sub> solution at -1.6 V. Deposition temperatures: 35, 50 and 85 °C. Deposition times: 900 and 1800 s.

Visible films were obtained from the CuCl<sub>2</sub> solution when the applied potential was more negative than -1.6 V, as shown in Figures 5.19 and 5.20. The surface coverage and the average particle size increased with increasing deposition time and temperature. The films deposited at 35 and 50 °C for 900 s were discontinuous (Figures 5.19 a and c), but increasing the deposition time to 1800 s



led to almost continuous films (Figures 5.19 **b** and **d**). At low deposition temperature and time (35 °C, 900 s), the films consisted of globular sub-micron particles between 200 to 500 nm (Figures 5.20 **a** and **b**). The particle size increased with increasing deposition temperature and time and at 50 °C (Figures 5.20 **c** and **d**), the particles were typically 1 µm in diameter. At 85 °C (Figures 5.20 **e** and **f**), the particles were 1 to 5 µm in diameter and had a polyhedral shape with distinct triangular and rectangular facets. Large globular particles were observed as well, in particular for the film deposited at 1800 s deposition time (Figure 5.20 **f**).

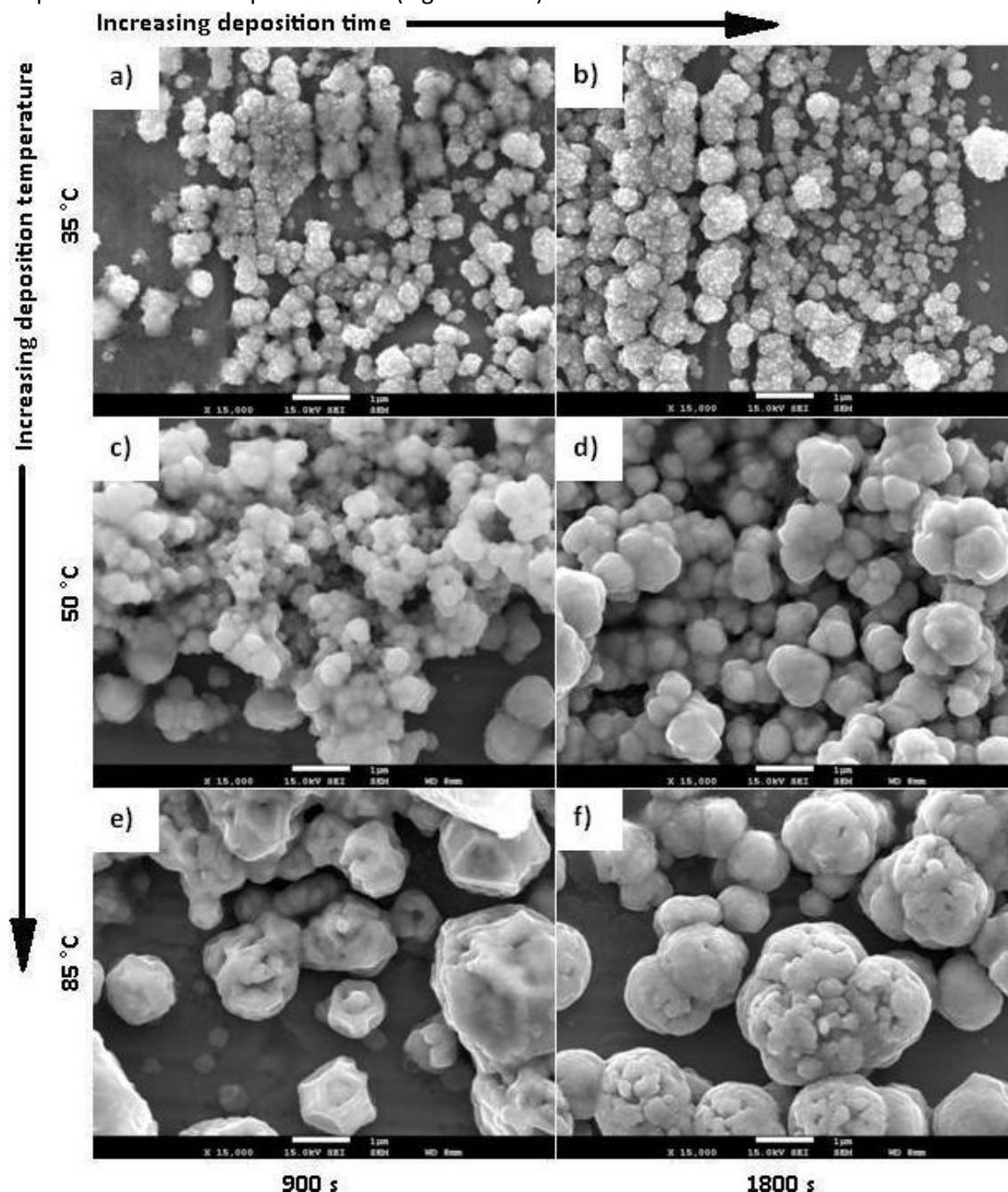


Figure 5.20: SEM micrographs of films electrodeposited from 0.1 M  $\text{CuCl}_2$  solution at -1.6 V. Deposition temperatures: 35, 50 and 85 °C. Deposition times: 900 and 1800 s.

Increasing the deposition potential to -1.8 V improved the continuity of the films without significantly altering their microstructure. Similar to the deposition carried out at -1.6 V, the deposition temperature had a strong effect on the microstructure of the films, as shown by the SEM micrographs of films prepared with a deposition time of 900 s (Figure 5.21). The films deposited at 35 °C (Figures 5.21 **a** and **b**) consisted of globular particles with an average diameter of approximately 100 nm, however for a deposition temperature of 85 °C, the particles were polyhedral, with visible crystallographic facets and their size varied between 0.5 and 5 μm (Figures 5.21 **c** and **d**). This indicates that the nucleation rate is low and the growth rate high at high temperatures, while the opposite occurs at lower temperatures.

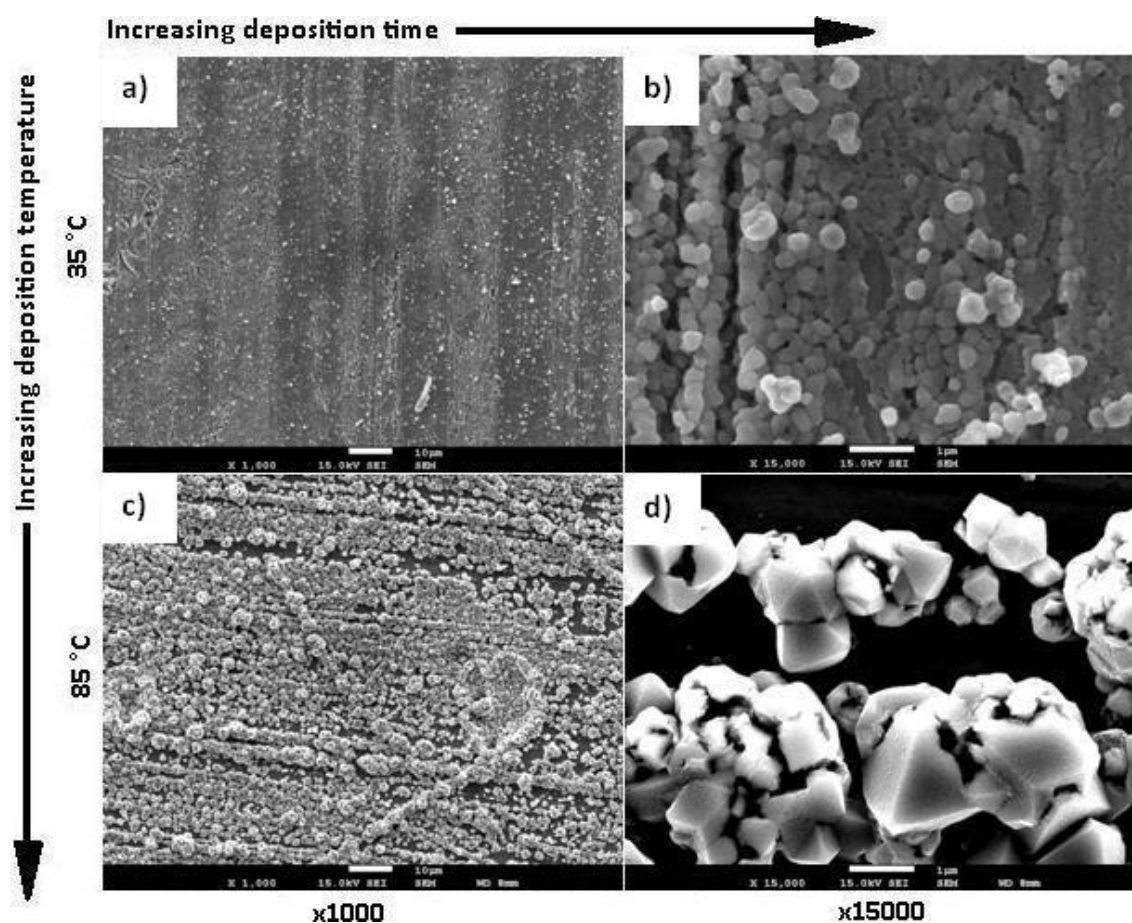


Figure 5.21: SEM micrographs of films electrodeposited from 0.1 M  $\text{CuCl}_2$  solution at -1.8 V for 900 s. Deposition temperatures: 35 and 85 °C.



### 5.3.1.3 0.1 M CuSO<sub>4</sub> solutions

Visible films were obtained from the CuSO<sub>4</sub> solution at an applied potential of -1.2 V and deposition temperature of 85 °C. No visible deposits were observed for this potential at 35 and 50 °C. The films were almost continuous and consisted of globular particles with sizes ranging from 100 to 500 nm (Figure 5.22). The films had some roughly circular pores (Figure 5.22 **b**), probably due to the detachment of the larger particles on the surface during the cleaning or evolution of hydrogen resulting from the decomposition of H<sub>2</sub>O present in the electrolyte as an impurity.

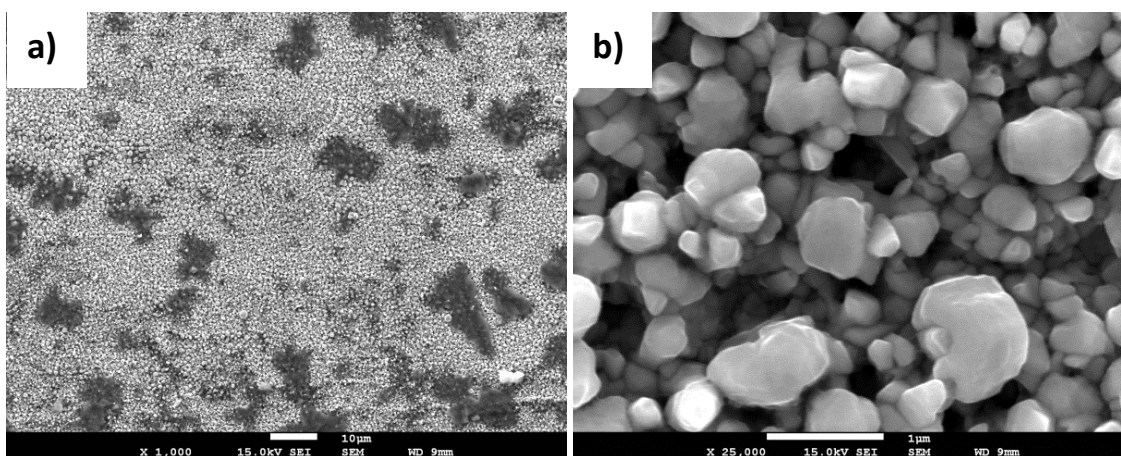


Figure 5.22: SEM micrographs at **a)** lower magnification and **b)** higher magnification of films electrodeposited from 0.1 M CuSO<sub>4</sub> solution at -1.2 V. Deposition temperature: 85 °C. Deposition time: 900 s.

As the deposition potential became more negative (from -1.2 to -1.6 V), the particle size decreased and the continuity of the films was improved. The evolution of the film structure with increasing deposition temperature and time is illustrated by the SEM micrographs of Figures 5.23 and 5.24. The particles diameter varied from 20 to 50 nm, and was significantly influenced by the deposition temperature and time. Continuous films were obtained at all deposition temperatures and times (Figure 5.23). At 35 °C, the particles were globular and aggregated into interconnected clusters around 100 nm in size, unevenly distributed across the surface (Figure 5.24 **a**). Increasing the deposition time from 900 to 1800 s increased the homogeneity of the films as shown in Figure 5.24 **b**. For the deposition temperature of 50 °C (Figure 5.24 **c**), the size of the particle clusters increased to around 200-300 nm, but the morphology of the film remained similar. At 85 °C (Figure 5.24 **e**), the clusters were evenly distributed across the surface.

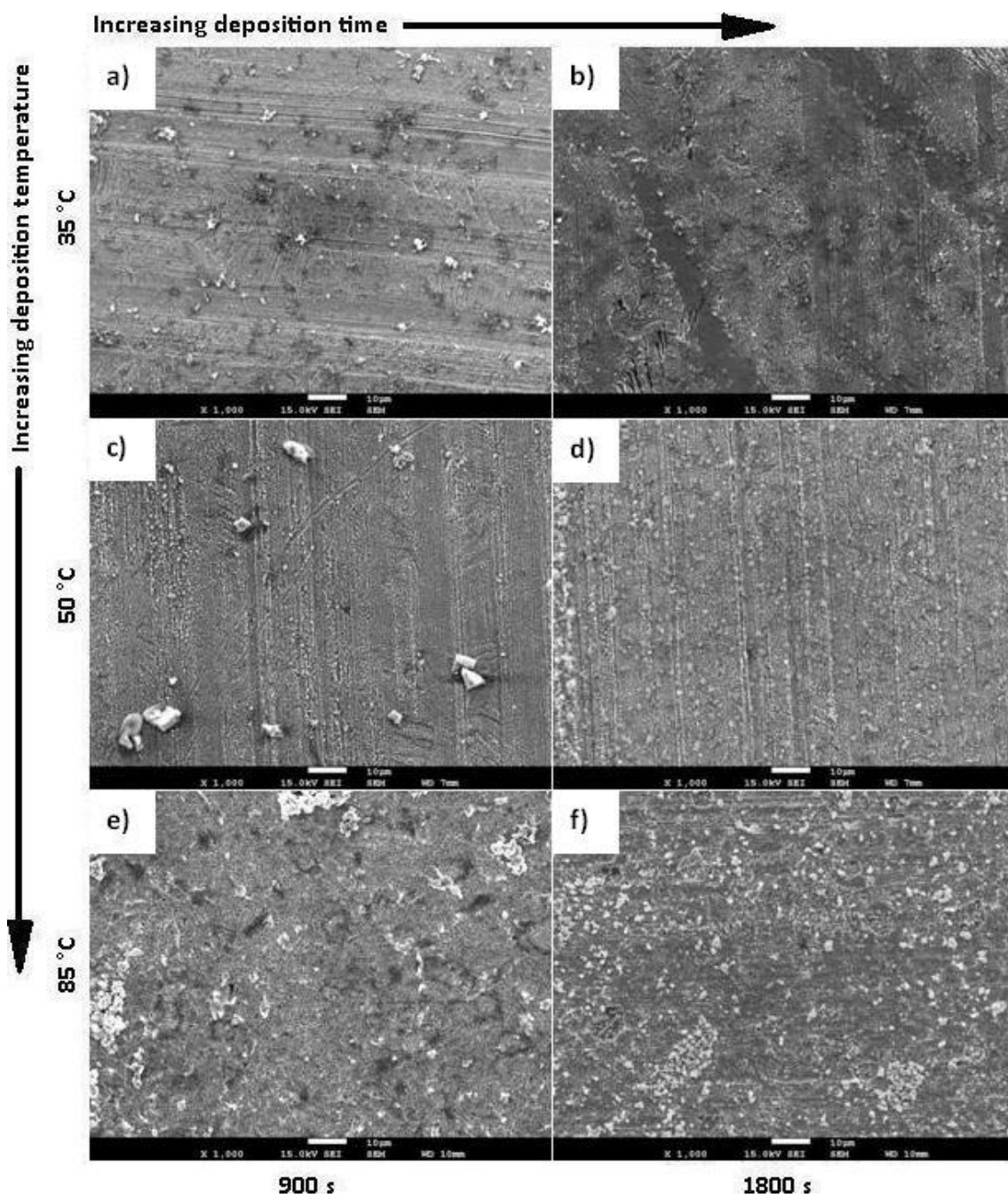


Figure 5.23: SEM micrographs (lower magnification) of films electrodeposited from 0.1 M  $\text{CuSO}_4$  solution at -1.6 V. Deposition temperatures: 35, 50 and 85 °C. Deposition times: 900 and 1800 s.

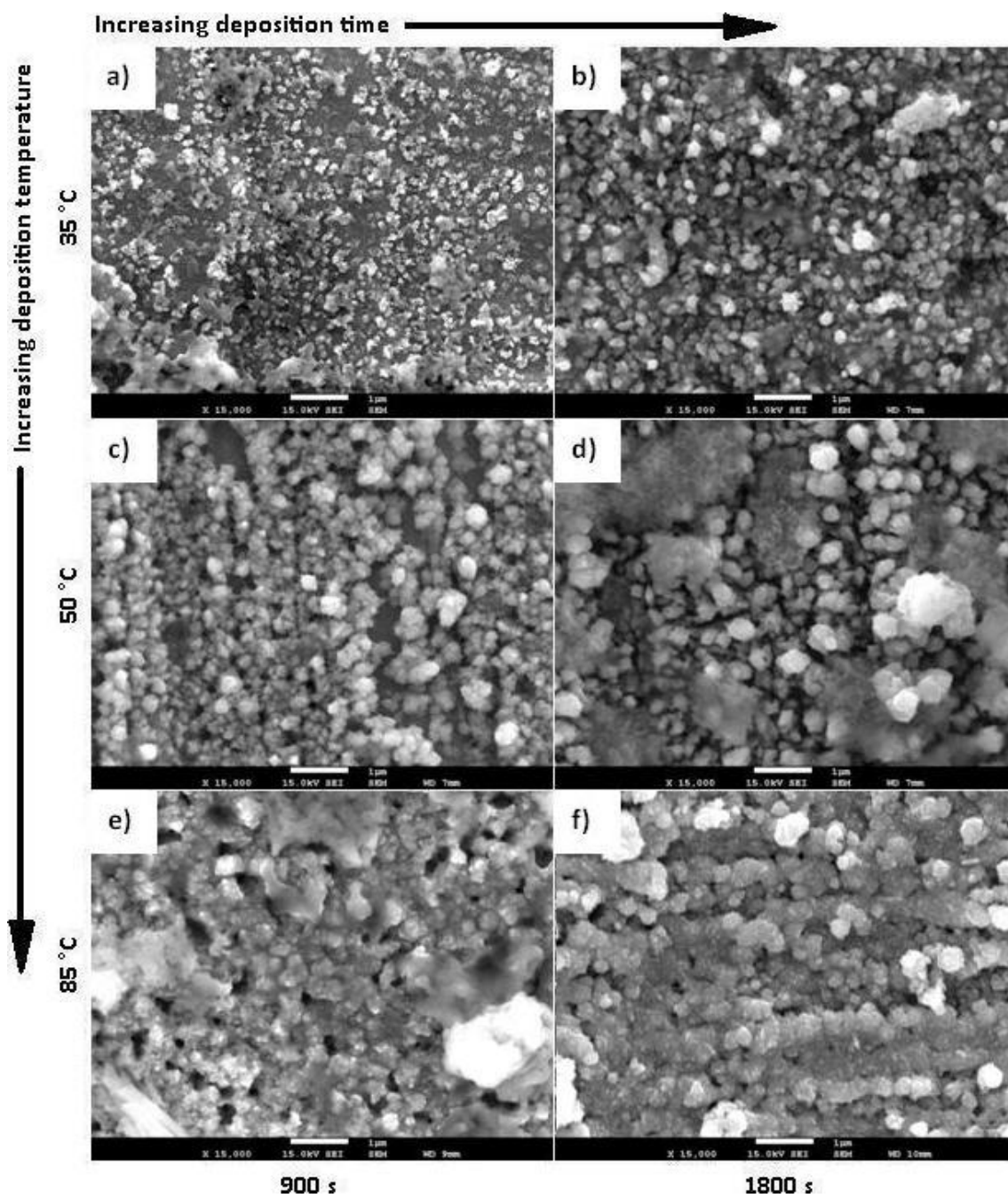


Figure 5.24: SEM micrographs (higher magnification) of films electrodeposited from 0.1 M  $\text{CuSO}_4$  solution at -1.6 V. Deposition temperatures: 35, 50 and 85 °C. Deposition times: 900 and 1800 s.

The microstructure of films deposited at -1.8 V and different deposition temperatures are shown in Figure 5.25. Continuous films consisting of submicrometric globular particles were obtained at 35 and 50 °C (Figures 5.25 **b** and **d** respectively). The average particle size increased from about 100 nm for 35 °C to 200 nm for 50 °C. For an electrolyte temperature of 85 °C (Figure 5.25 **f**) overgrowth occurred, similarly to what was observed for the CuCl electrolyte under the same conditions.

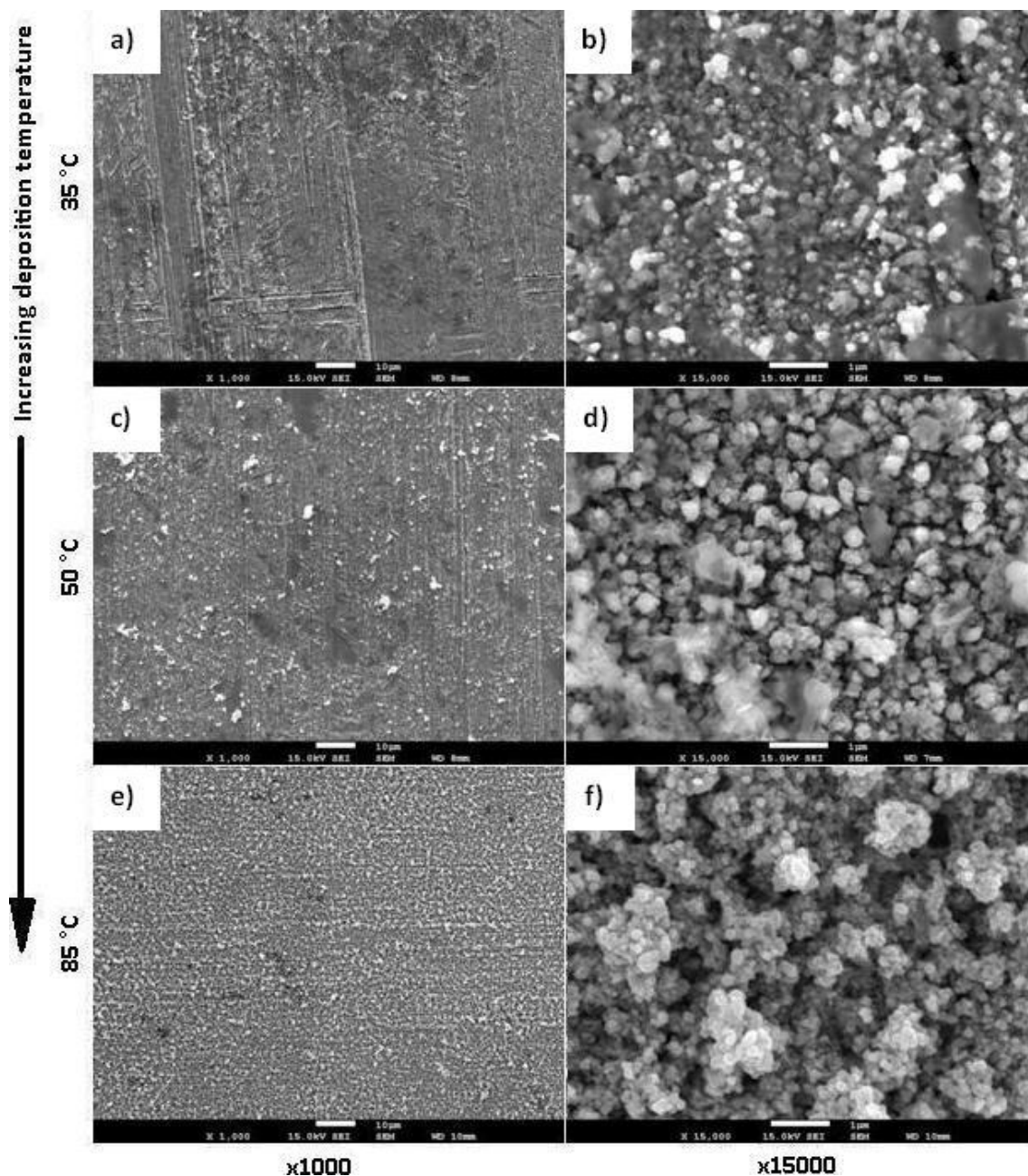


Figure 5.25: SEM micrographs of films electrodeposited from 0.1 M CuSO<sub>4</sub> solution at -1.8 V for 900 s. Deposition temperatures: 35, 50 and 85 °C.

### 5.3.2 Synthesis of the film microstructure observations

Comparing the films prepared from the different electrolytes, it is clear that the films deposited from the  $\text{CuCl}_2$  solution (Figures 5.20 and 5.21) produce larger particle size and have lower continuity compared with those obtained with similar deposition parameters from  $\text{CuCl}$  (Figures 5.17 and 5.18) and  $\text{CuSO}_4$  (Figures 5.24 and 5.25) solutions. A possible explanation is that the nucleation of copper in the  $\text{CuCl}_2$  solution occurs at a much more negative potential compared to the  $\text{CuCl}$  solution. From the cyclic voltammograms we can see that the nucleation loop for the nucleation of metallic copper occurs at -0.69 V for  $\text{CuCl}$  (Figure 5.2) and at -1.59 V for the  $\text{CuCl}_2$  (Figure 5.4), indicating that the potential required for copper nucleation is much lower for the  $\text{CuCl}$  solution compared to the  $\text{CuCl}_2$  solution. Hence at -1.6 and -1.8 V for the  $\text{CuCl}_2$  solution, the number of nuclei is low and nucleation is restricted to the few most active sites. Consequently, the grain size will be much larger as there is more room for them to grow. For the  $\text{CuCl}$  solution, there is a massive overpotential for copper deposition at -1.6 and -1.8 V. As a result, nucleation may occur on weaker sites and the number of nuclei will be much higher than for the  $\text{CuCl}_2$  solution. The higher nucleation density limits the size of the grains as there are less room for them to grow. Comparing the films deposited from the  $\text{CuCl}_2$  and  $\text{CuSO}_4$  solutions, the difference in film morphology is probably due to the influence of the anion of the salt. The anion affects the copper complexes in solution, as well as the double-layer structure formed near the substrate surface. It is well known that the double-layer structure has a huge impact on film nucleation and growth in ionic liquid electrolytes and small changes in the double-layer structure can change the size, shape and morphology of the particles that are formed in the film [10]. A more detailed study of the molecular interactions between cations and anions in the bulk solution and near the substrate-solution interface is needed in order to get a better understanding of the structure and morphology of the films. A small step in this direction was taken in this study with the vibrational analysis of the bulk ionic liquid solution described in Chapter 4.

The best films are those prepared from  $\text{CuCl}$  and  $\text{CuSO}_4$  electrolytes with -1.8 V applied potential and at 35 °C deposition temperature (Figures 5.18 a, 5.21 a). Films deposited at 35 °C have small particle size, leading to lower surface roughness, while for 50 °C, the particle size increases leading to rougher surfaces and for 85 °C the films are still rougher and irregular due to overgrowth. Increasing the applied potential from -1.6 to -1.8 V does not significantly change the morphology of the films deposited from the same electrolyte, but improves the surface coverage for similar deposition parameters.

The characteristics of our films were compared to those deposited from ionic based electrolytes as described in the literature. Chen et al. [240] deposited copper films on tungsten substrate from 0.02 M of  $\text{Cu(I)}$  in  $[\text{EMIM}]\text{--Cl--}[\text{BF}_4]$  solution at room temperature. Their films were rougher and the particle size larger (500 nm - 1  $\mu\text{m}$ ) when compared to our film deposited under similar conditions (average particle size of 100 nm). Their films structure was very sensitive to the deposition potential, a small difference of 0.1 V changes the film microstructure [240]. On the contrary, the microstructure of our films is less dependent on the deposition potential. In another study, Leong et al. [242] deposited copper on nickel substrates from 0.05 M  $\text{CuCl}$  in  $[\text{EMIM}][\text{DCA}]$

at room temperature. Their films were dense and compact, with particle size about 100 nm, but these particles aggregated to form large hemispherical clusters with a typical diameter of 5  $\mu\text{m}$ . The films obtained in our study were smoother as no clusters were observed for the films deposited at 35  $^{\circ}\text{C}$  (Figures 5.18 **a** and **b**), and clusters with diameters of 1  $\mu\text{m}$  were only observable for the films deposited at 50  $^{\circ}\text{C}$  (Figures 5.18 **c** and **d**). At a deposition potential of -1.8 V, their films exhibited a cauliflower-like structure which reduced the uniformity and compactness of the films [242]. Similar structures were only observed in our study for a deposition temperature of 85  $^{\circ}\text{C}$  and long deposition times.

### 5.3.3 Current Efficiency

The current efficiencies of the CuCl and CuCl<sub>2</sub> electrolytes were estimated using Faraday's laws of electrolysis (see Section 2.2.1). The electrodeposition experiments were carried out on a nickel substrate at a deposition potential of -1.5 V versus a Pt quasi-reference electrode (QRE). For the CuCl solution the total charges that flowed during electrodeposition for a period of 1 h was 0.8335 C. The equivalent mass corresponding to this charge was calculated by using Faradays law. Assuming that the electrodeposition corresponded to the reaction  $\text{Cu}^{+} + \text{e}^{-} \rightarrow \text{Cu}$ , a current efficiency was calculated to be 55 %. For the CuCl<sub>2</sub> solution, the total charge that flowed during electrodeposition for a period of 6 h was 6.0539 C. The current efficiency was calculated to be 43 % for the reaction  $\text{Cu}^{+} + \text{e}^{-} \rightarrow \text{Cu}$ . These results indicate that for both solutions the current efficiencies of the reactions are low.

### 5.3.4 Composition of the film

EDX analysis showed that the films consisted essentially of copper, with small proportions of oxygen and sulphur, due to traces of the electrolyte retained in the film. The chemical composition of the films did not depend on the electrodeposition parameters or the electrolyte. X-ray diffractograms of films deposited from CuSO<sub>4</sub> and CuCl solutions are shown in Figures 5.26 **a** and **b**, respectively. The diffractograms present three peaks at 43.4, 50.5 and 74.2  $^{\circ}$ , which can be indexed as the (111), (200) and (220) peaks of copper. Peaks from the nickel substrate were also observed at 44.5, 56.8 and 76.4  $^{\circ}$  because the X-ray penetration depth exceeded the film thickness. The average particle size, calculated from the Cu (111) peak full-width at half-maximum using Scherrer's equation (see Section 3.6.3) was 24 nm for the films obtained from CuSO<sub>4</sub> solutions and 22 nm for the films obtained from CuCl solution. XRD analysis revealed that the films electrodeposited from CuSO<sub>4</sub> and CuCl ionic liquid solutions were polycrystalline with a nanometric grain size.

TEM analysis was performed on films deposited from 0.1 M CuCl<sub>2</sub> and CuSO<sub>4</sub> solution in [EMIM][EtSO<sub>4</sub>] at 85  $^{\circ}\text{C}$  (Figure 5.28 **a**). Angular particles with diameters of 200 nm aggregated in large clusters were observed, consistent with the results obtained from the SEM micrographs. Electron diffraction patterns of the film (Figure 5.28 **b**) consisted of rings, typical of a polycrystalline material, which can be indexed as copper (111), (200) and (220) diffractions, in agreement with the XRD results.

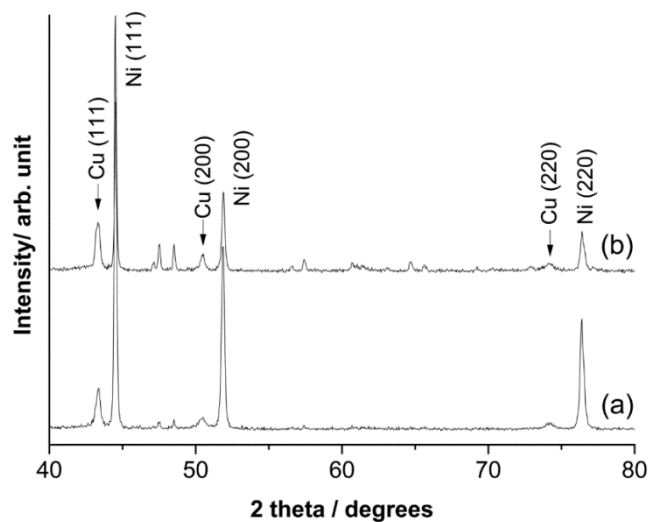


Figure 5.26 XRD patterns of copper films electrodeposited at -1.8 V for 900 s from **a)** 0.1 M  $\text{CuSO}_4$  and **b)** 0.1 M  $\text{CuCl}$  solutions in [EMIM]  $[\text{EtSO}_4]$  at 85 °C.

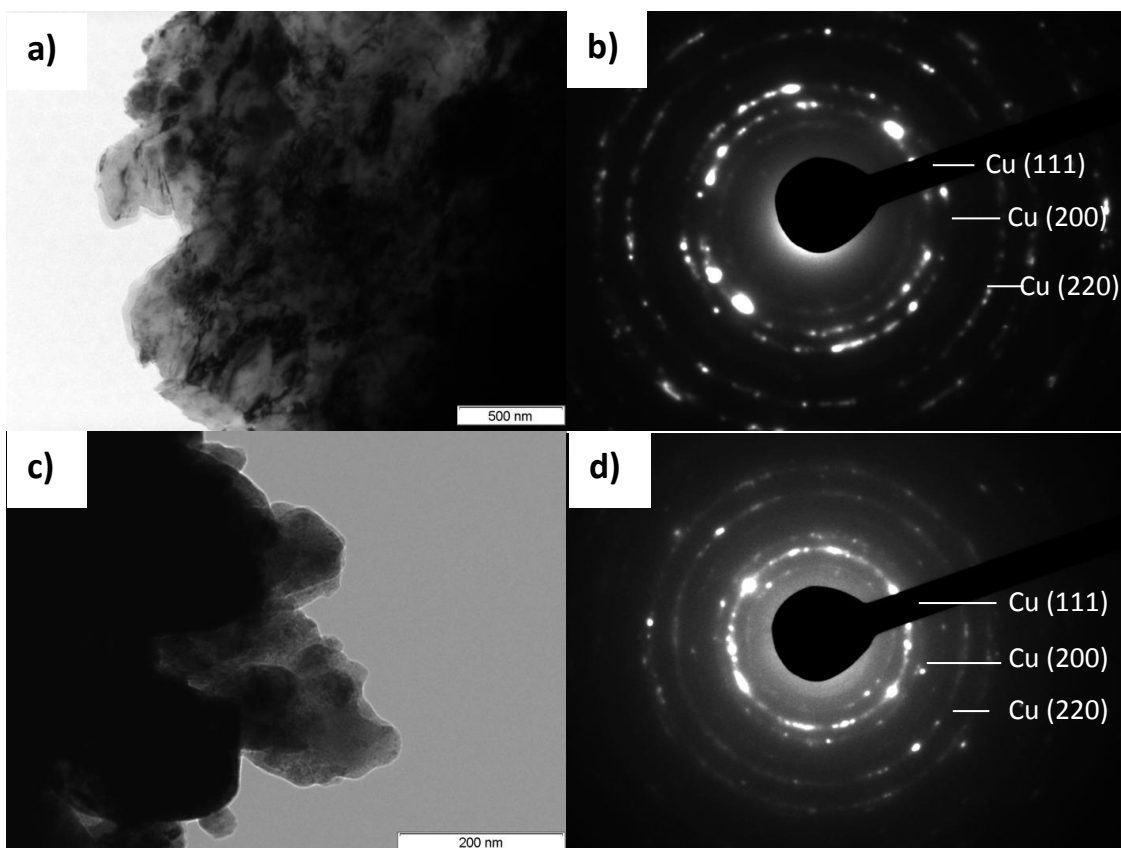


Figure 5.27 TEM micrographs of films electrodeposited with -1.8 V for 900 s from **a)** 0.1 M  $\text{CuCl}_2$  solution with **b)** the corresponding selected area diffraction pattern and **c)** 0.1 M  $\text{CuSO}_4$  solution with **d)** the corresponding selected area diffraction pattern.



## 5.4 Summary

Electrochemical characterisation was carried out on 0.1 M CuCl, CuCl<sub>2</sub> and CuSO<sub>4</sub> solutions in [EMIM] [EtSO<sub>4</sub>]. The cyclic voltammograms for the three solutions show that the reduction of copper in ionic liquid solutions is a one-electron transfer-step process, from Cu(II) to Cu(I) and Cu(I) to Cu(0). The copper oxidation state in solution and the anion group of the salts affect the electrochemical results. For the solutions of salts with the same anion group but at different oxidation state (CuCl and CuCl<sub>2</sub>), there is a shift in the potentials of the peaks corresponding to the same reaction in the voltammogram. The peaks for the CuCl<sub>2</sub> solution are at a more negative potential than those for the CuCl solution. For solutions of salts with the same copper oxidation state but with a different anion group (CuCl<sub>2</sub> and CuSO<sub>4</sub>), there is a huge difference between the cation diffusion coefficient values. The diffusion coefficients of the copper species are an order of magnitude larger for the chloride solutions compared with the sulphate solution. This is consistent with the higher activation energy of the Cu(II) to Cu(I) reduction in the copper sulphate solution compared to the copper(II) chloride solution. The influence of the copper oxidation state or the anion of the salts may be explained by the complexes that are formed in each solution.

Copper thin films can be electrodeposited from CuCl<sub>2</sub>, CuCl and CuSO<sub>4</sub> solutions in [EMIM] [EtSO<sub>4</sub>]. The analysis of the films by EDX and XRD shows that they are crystalline and consist mainly of copper, with trace amount of oxygen and sulphur. The morphology of the films changes with the electrolyte temperature, deposition potential and deposition time. In general, the films continuity and particle size increase when the electrolyte temperature increases from 35 to 85 °C. Increasing the deposition time from 900 to 1,800 s marginally improves the continuity of the films for the three electrolytes at -1.6 V, although film overgrowth occurs for the CuCl solution. While the general trends are similar, there are also some differences in the morphology of the films deposited from the three electrolytes under similar deposition parameters:

- The films deposited from the CuCl<sub>2</sub> solutions present have larger particles and are discontinuous. The best films have been obtained for electrolyte temperature of 35 and 50 °C, deposition potential of 1.8 V and deposition time of 900 s.
- The films deposited from CuCl solutions are continuous even when a deposition time of 900 s is used and they consist of extremely small globular particles aggregated in clusters. Increasing the deposition time to 1,800 s leads to an overgrowth of the films, due to the formation of a cauliflower-like structure, increasing their roughness.
- Continuous films could be prepared from CuSO<sub>4</sub> solutions at -1.6 and -1.8 V for all temperatures and at a potential of -1.2 V for deposition temperature of 85 °C. The structure of the films consists of clusters of nanometre size irregular shaped particles.





## 6 Electrochemical Results of EMIM TFSI-based Electrolytes

The results from the [EMIM] [TFSI] electrolytes are presented in this chapter. Electrolytes were prepared by dissolving the three salts of AgTFSI, Cu(TFSI)<sub>2</sub> and Al(TFSI)<sub>3</sub> in [EMIM] [TFSI]. All the materials were provided by Solvionic (The industrial partner of this study). These salts were specially prepared to have the same anion as the ionic liquid, so as to eliminate the influence of other competing anions and to simplify the possible reaction in solution. Ag(I), Cu(II) and Al(III) ions were selected in order to investigate the influence of their oxidation state on the electrolyte's behaviour and on the film's properties.

In the first section, the electrochemical window of the pure [EMIM] [TFSI] is presented. This is followed by the electrochemical characterisation results of the three different electrolyte solutions. Lastly, the electrodeposition results are presented together with descriptions of the structure and properties of the deposited films.

### 6.1 Electrochemical window of [EMIM] [TFSI] ionic liquid

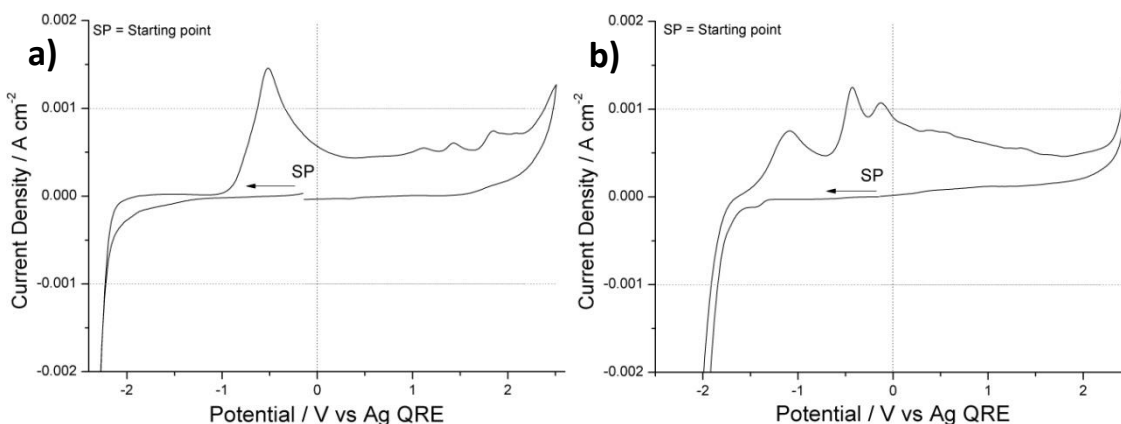


Figure 6.1: Cyclic voltammograms of pure [EMIM] [TFSI] between -2.5 to 2.5 V using **(a)** a GC disc and **(b)** a Pt disc. The electrolyte temperature was 35 °C and the scan rate was 0.05 V s<sup>-1</sup>.

Cyclic voltammograms were obtained for pure [EMIM] [TFSI] using two different working electrodes, namely, glassy carbon (GC) and platinum (Pt) discs (Figures 6.1 **a** and **b**, respectively). A silver wire was used as a quasi-reference electrode (QRE). The electrochemical windows were measured from these voltammograms. For the voltammogram obtained by using the GC disc (Figure 6.1 **a**), an electrochemical window of 4.6 V was recorded, which lay between -2.2 and 2.4 V. Similarly, a value of 4.4 V was recorded for the voltammogram obtained with the (Pt) disc (Figure 6.1 **b**), which lay between -1.9 and 2.5 V. The boundary of the electrochemical window lay at potentials where the maximum current density values do not exceed 0.001 A cm<sup>-2</sup>, as defined by convention [192]. Similar to the [EMIM] [EtSO<sub>4</sub>] results, an anodic peak was observed at -0.5 V in the voltammogram obtained by using the GC electrode (Figure 6.1 **a**), corresponding to the oxidation of the products that were formed during the [EMIM] reduction [238,10]. This behaviour

was more complicated on the Pt electrode (Figure 6.1 **b**), where three anodic peaks were observed at -1.1, -0.5 and -0.1 V. The measured electrochemical windows had similar values to those found in the literature [238,239].

## 6.2 Electrochemical characterisation of the electrolyte solutions

Cyclic voltammograms of 0.05 M AgTFSI, 0.05 M CuTFSI<sub>2</sub> and 0.50 M AlTFSI<sub>3</sub> solutions in [EMIM] [TFSI] are presented in this section. The oxidation and reduction peaks are identified and their evolution as a function of scan rates and electrolyte temperatures are investigated. Using this information, the stability of the electrolyte solutions and nucleation and growth mechanisms are discussed. Chronoamperograms of the electrolyte solutions are also presented, from which the diffusion coefficients are calculated.

### 6.2.1 Cyclic Voltammogram of AgTFSI in [EMIM] [TFSI] solution

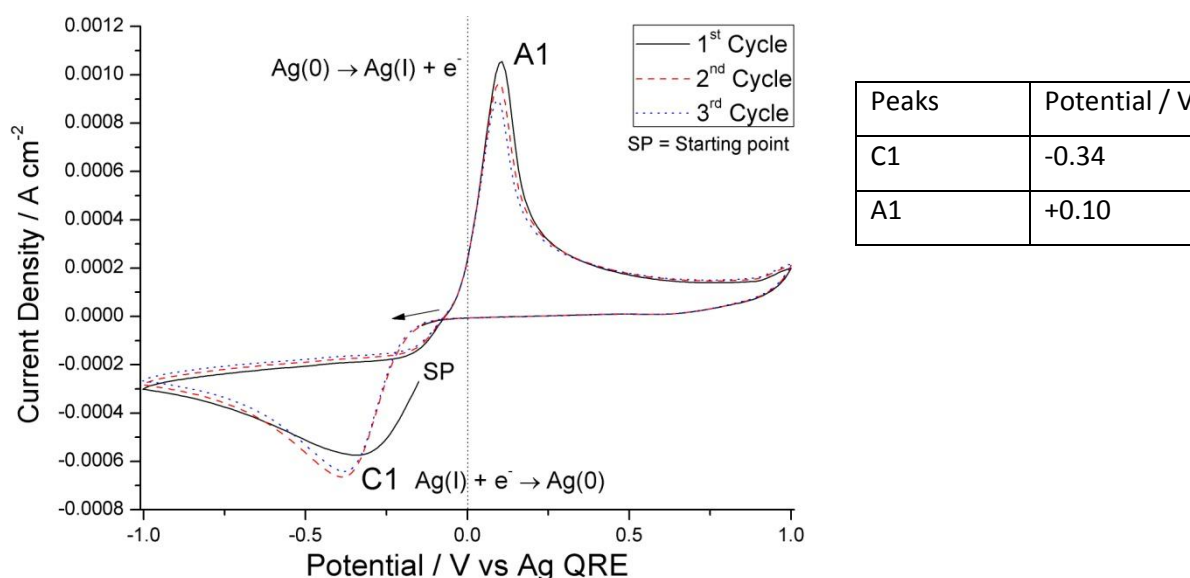


Figure 6.2: Cyclic voltammogram (3 cycles) of 0.05 M AgTFSI solution in [EMIM] [TFSI] at 35 °C. The working electrode was a GC disc and the scan rate was 50 mV s<sup>-1</sup>. The potential of the cathodic and anodic peaks are shown in the accompanying table.

The voltammogram of the 0.05 M AgTFSI solution obtained by using a glassy carbon (GC) working electrode is shown in Figure 6.2. In the forward scan, the cathodic current density increased sharply at -0.18 V, leading to the cathodic peak C1 at -0.34 V, which could be attributed to the reduction of Ag(I) to metallic silver (Ag(0)). A slight shift in this peak from -0.34 to -0.38 V was observed in the second and third cycles. An oxidation peak (A1) was observed at +0.10 V in the reverse scan, which could be attributed to the oxidation of metallic silver (Ag(0)) to Ag(I). The peak height A1 was more than double that of C1, and this was also observed for the silver containing [BMPyr] [TFSI] solution under similar conditions [132]. Additionally, a nucleation loop was observed with a crossover at -0.08 V in the second and third cycles, indicating that an

overpotential was required to initiate the nucleation process [124]. This behaviour is typical of GC working electrodes [124,106,142,128,121,245,136].

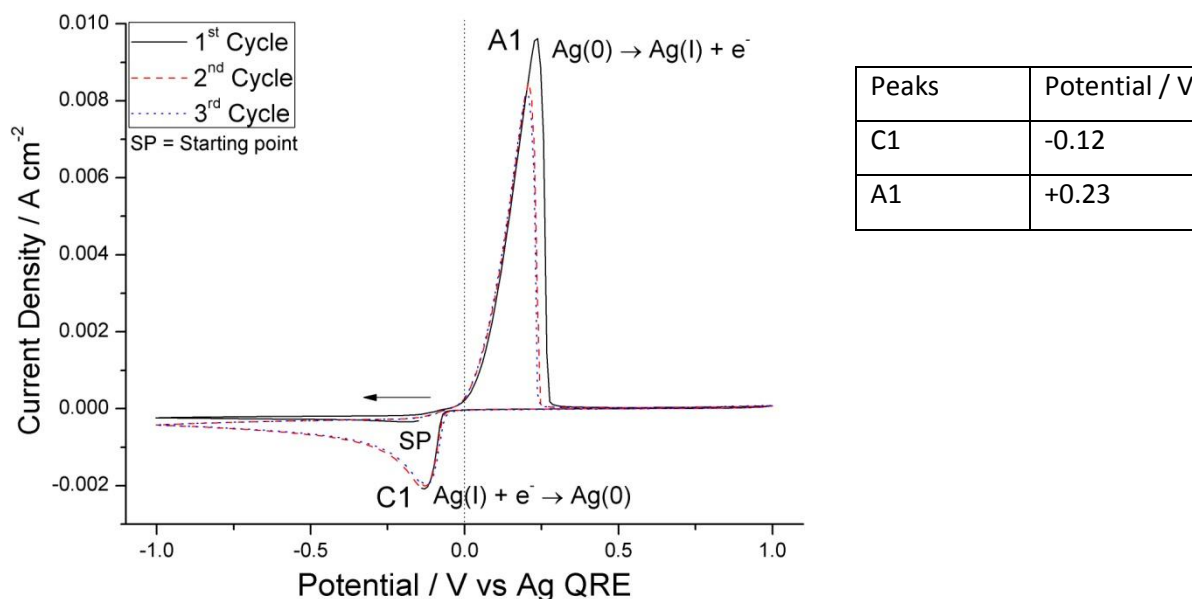


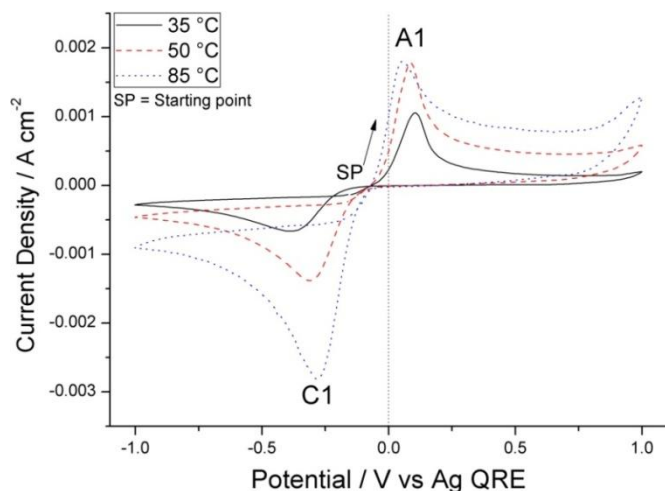
Figure 6.3: Cyclic voltammogram (3 cycles) of 0.05 M AgTFSI solution in [EMIM][TFSI] at 35 °C. The working electrode was a Pt disc and the scan rate was 50 mV s<sup>-1</sup>. The potential of the cathodic and anodic peaks are shown in the accompanying table.

A reduction (C1) and oxidation (A1) peaks were also observed in the cyclic voltammogram obtained by using a platinum working electrode, as shown in Figure 6.3. These peaks were located at -0.12 and +0.23 V, respectively. C1 was located at a less negative potential when a Pt electrode was used as compared to a GC electrode. This potential difference was due to the higher energy required to overcome the activation barrier for nucleation on the GC electrode [124]. The A1 peak height was five times larger than the C1 peak height, and there was an even larger difference when Pt was used as compared to the GC working electrode.

The change in the cyclic voltammogram with temperature when using a GC electrode is shown in Figure 6.4. As seen in this figure, the C1 peak shifts to more positive potentials with increasing temperature; from -0.35 V at 35 °C, to -0.31 V at 50 °C and -0.29 V at 85 °C. This shift is accompanied by an increase in the cathodic current density: from  $-6.6 \times 10^{-4}$  A cm<sup>-2</sup> at 35 °C, to  $-1.38 \times 10^{-3}$  A cm<sup>-2</sup> at 50 °C, and  $-2.81 \times 10^{-3}$  A cm<sup>-2</sup> at 85 °C. This is expected as increasing the temperature decreases the viscosity of the electrolyte, consequently increasing the mobility of the charge carrying species and the electrical conductivity of the solution [10].

On the other hand, the A1 peak shifts to more negative potentials with increasing temperature; from +0.10 V at 35 °C, to +0.09 V at 50 °C, and +0.06 V at 85 °C. The current density of A1 increases from  $1.05 \times 10^{-4}$  to  $1.79 \times 10^{-4}$  A cm<sup>-2</sup> for 35 to 50 °C, but remains similar when the temperature is increased to 85 °C. This indicates that the oxidation of metallic silver (Ag(0)) to Ag(I) is limited at 85

°C. The shape of the voltammogram curve is similar at all temperatures. No colour changes are observed for the 0.05 M AgTFSI solution, indicating that it is stable up to 85 °C.



Peaks	Potential / V
C1 (35 °C)	-0.35
C1 (50 °C)	-0.23
C1 (85 °C)	-0.29
A1 (35 °C)	+0.10
A1 (50 °C)	+0.09
A1 (85 °C)	+0.06

Figure 6.4: Cyclic voltammograms of 0.05 M AgTFSI solution in [EMIM] [TFSI] at 35, 50 and 85 °C. The working electrode was a GC disc and the scan rate was 50 mV s<sup>-1</sup>. The potential of the cathodic and anodic peaks are shown in the accompanying table.

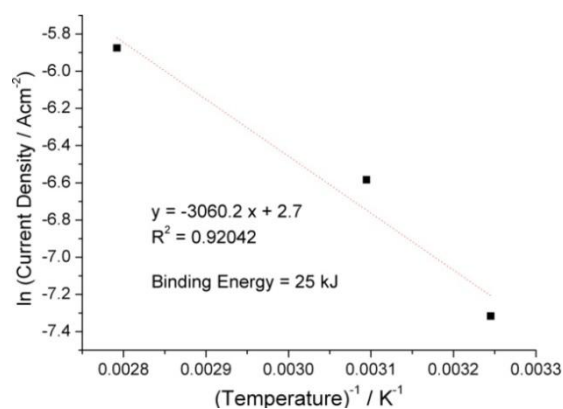


Figure 6.5: Relationship between current density of C1 with temperature. The working electrode was a GC disc and the scan rate was 50 mV s<sup>-1</sup>.

Since the Ag(I) to Ag(0) reduction reaction is thermally activated, its kinetics could be represented by the Arrhenius equation:

$$i_{pc} = k e^{-\frac{E_a}{RT}} \quad \text{Eq. 6.1}$$

$E_a$  is the activation energy,  $i_{pc}$  the peak current density,  $T$  the absolute temperature,  $R$  the ideal gas constant and  $k$  is a constant.

$E_a$  can be calculated from the slope of a plot of the natural logarithm of ( $i_{pc}$ ) versus the inverse of the temperature according to the equation:

$$\ln(i_{pc}) = -\frac{E_a}{RT} + \ln(k) \quad \text{Eq. 6.2}$$

This graph is shown in Figure 6.5. The calculated activation energy values of the Ag(I) to Ag(0) reduction reaction for is 25 kJ mol<sup>-1</sup>.

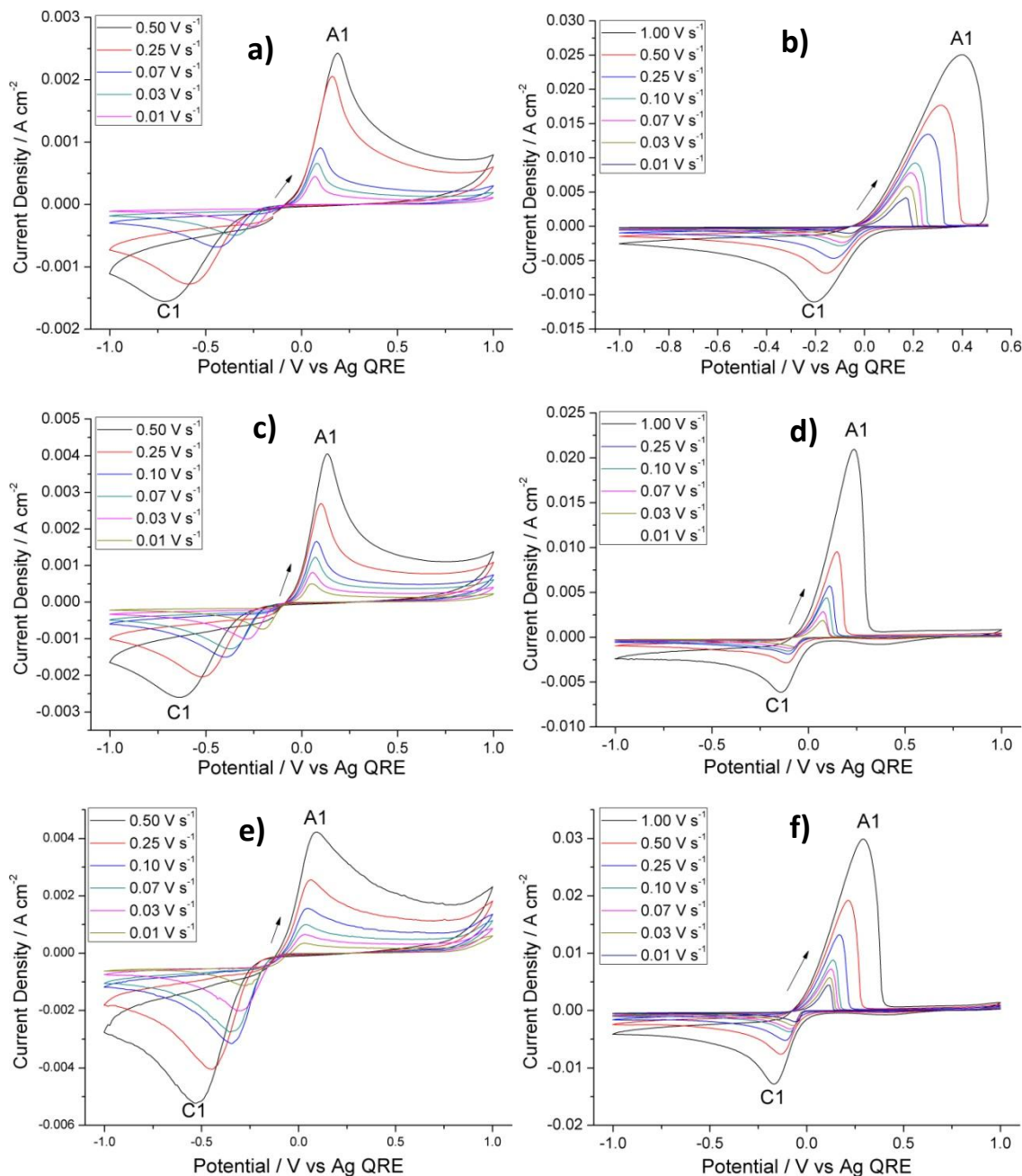


Figure 6.6: Cyclic voltammograms of 0.05 M AgTFSI solution in [EMIM] [TFSI] using different potential scan rates between 0.01 and 1.00 V s<sup>-1</sup> at **a)** 35 °C on GC, **b)** 35 °C on Pt, **c)** 50 °C on GC, **d)** 50 °C on Pt, **e)** 85 °C on GC and **f)** 85 °C on Pt.

Cyclic voltammetry was also carried out at different scan rates using both GC and Pt working electrodes and different electrolyte temperatures. The resulting voltammograms are shown in Figure 6.6. Using these voltammograms, the reversibility of the reactions were tested against the conditions for a reversible reaction described by Equations 3.4, 3.5, 3.6 and 3.7 listed in Section 3.4.1, reproduced below for easy reference:

$$I_p = v^{1/2} \quad \text{Eq. 3.4}$$

$E_p$  is independent of  $v$

$$|E_p - E_{p/2}| = 2.2RT/nF \quad \text{Eq. 3.5}$$

$$E_{p,a} - E_{p,c} = 2.3RT/nF \quad (E_\lambda \leq E_{p,c} \text{ or } E_\lambda \geq E_{p,a}) \quad \text{Eq. 3.6}$$

$$|I_{p,a}/I_{p,c}| = 1 \quad \text{Eq. 3.7}$$

The current densities for the anodic (A1) and cathodic (C1) peaks varied linearly with the square root of the scan rate ( $v^{1/2}$ ), as seen in Figures 6.7 and 6.8. The linear fit was better for the results obtained at 35 and 50 °C, as compared to those obtained at 85 °C. The fact that Equation 3.4 was satisfied indicates that the process was likely to be diffusion controlled [29,8].

The peak potentials ( $E_p$ ) were found to depend on the scan rate for all experimental conditions, and as such, they did not satisfy the conditions for a reversible reaction. The oxidation peak (A1) shifted to a more positive potential while the reduction peak (C1) shifted to a more negative potential as the scan rate was increased, as shown in Figure 6.6.

At a scan rate of 0.01 V s<sup>-1</sup> and at 50 and 85 °C, the calculated  $|E_p - E_{p/2}|$  values were larger than the values provided by Equation 3.5 for the voltammograms obtained with a GC electrode, except for the peak A1 (Figures 6.7 **a** and **c**). This is expected since overpotential is usually observed on a GC working electrodes, due to the higher energy required to drive the reaction [124]. The calculated  $|E_p - E_{p/2}|$  values satisfied Equation 3.5 when a low scan rate of 0.01 V s<sup>-1</sup> was used at 35 °C (Figure 6.6 **b**) and when scan rates of 0.03 V s<sup>-1</sup> and below were used at 50 and 85 °C (Figures 6.6 **d** and **f**) for the voltammograms obtained on a Pt working electrode. An explanation is that increasing the temperature decreases the viscosity of the solution, thereby increasing the mass transport and maintaining the reversibility of the process at higher scan rates [10].

The A1 and C1 peaks were far apart and the  $E_{p,a} - E_{p,c}$  values did not satisfy Equation 3.6. This indicates that the solution resistance is high, typical behaviour for ionic liquid based electrolytes [129].

The current densities corresponding to peak A1 ( $I_{p,a}$ ) were larger than those corresponding to C1 ( $I_{p,c}$ ) for most cases, although the reverse was observed for voltammograms obtained at 85 °C on a GC working electrode (Figure 6.6 **e**). Regardless, they did not satisfy Equation 3.7 for a reversible

reaction. An exception was when the scan rate was lower than  $0.07 \text{ V s}^{-1}$  for the voltammograms obtained at  $50^\circ\text{C}$  on a GC electrode (Figure 6.6 c), which did satisfy Equation 3.7.

These results show that for the experimental conditions used, the reduction of  $\text{Ag(I)}$  to  $\text{Ag(0)}$  in [EMIM] [TFSI] is a quasi-reversible process. However, lowering the scan rate and increasing the electrolyte temperature help improve the reversibility of the reaction as shown from the analysis of Figure 6.6 described in the previous five paragraphs. For the reduction carried out on a GC electrode, the conditions for a reversible reaction were almost satisfied where the electrolyte temperature was  $50^\circ\text{C}$  and scan rates were lower than  $0.03 \text{ V s}^{-1}$ . The same was not true at  $85^\circ\text{C}$  because the anodic current density was limited at this temperature, as shown in Figure 6.4.

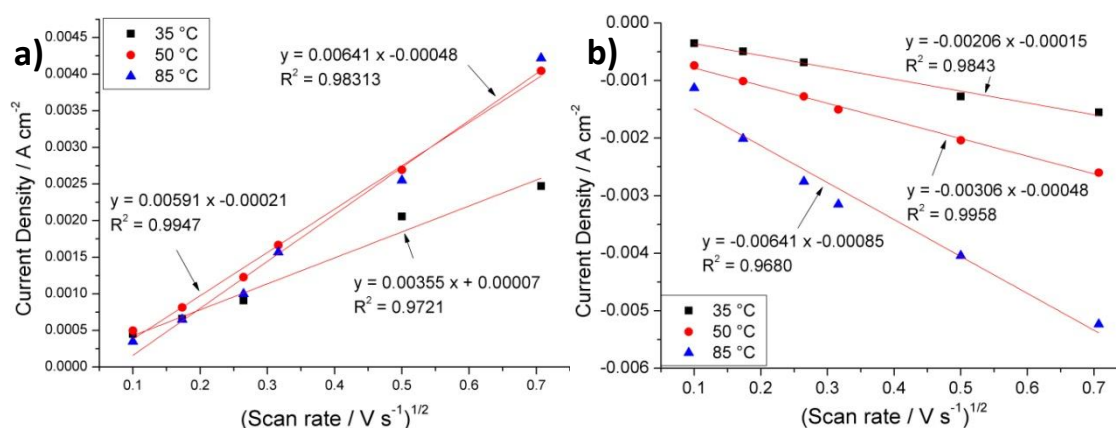


Figure 6.7: **a)** The anodic peak current (A1) and **b)** cathodic peak current (C1) as a function of scan rate for the 0.05 M AgTFSI solution in [EMIM] [TFSI] using a GC working electrode.

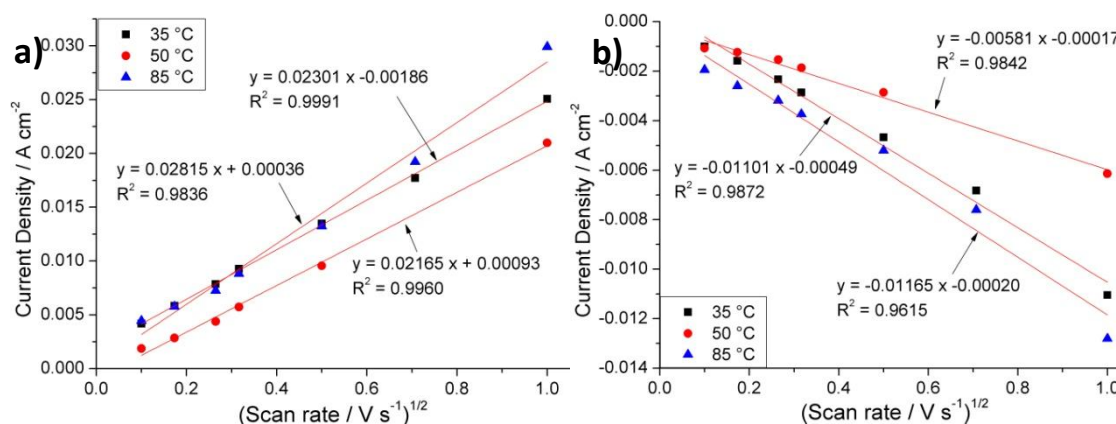


Figure 6.8: **a)** The anodic peak current (A1) and **b)** cathodic peak current (C1) as a function of scan rate for the 0.05 M AgTFSI solution in [EMIM] [TFSI] using a Pt working electrode.

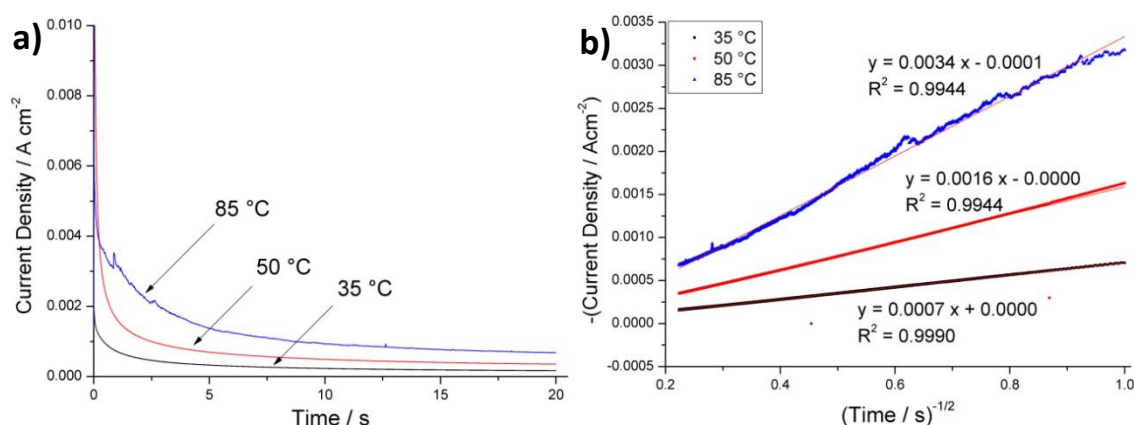


Chronoamperograms acquired with potential steps corresponding to the reduction of Ag(I) on GC and Pt working electrodes are presented in Figures 6.9 **a** and 6.10 **a**. After an initial current oscillation due to double-layer charging, the current density ( $i$ ) varies linearly with  $(t^{-1/2})$ , in agreement with Cottrell equation, as follows [8]:

$$I(t) = \frac{nFAD^{\frac{1}{2}}C_{\infty}}{\pi t^{\frac{1}{2}}} \quad \text{Eq. 6.3}$$

The diffusion coefficient can be estimated from the slope of an ( $i$ ) versus  $(t^{-1/2})$  plot (Figures 6.9 **b** and 6.10 **b**). The calculated values are presented in Table 6.1 below. The diffusion coefficients obtained on the GC and Pt working electrodes were in agreement with each other. The diffusion coefficient values also increased with temperature, in agreement with the increase in current density as shown in Figure 6.4, since both process were thermally activated and behaved in accordance with the Arrhenius equation.

The estimated diffusion coefficient values are similar to those found for Ag(I) salt solutions in [BMIM] [BF<sub>4</sub>] ( $4.2 \times 10^{-7}$  and  $9.9 \times 10^{-7} \text{ cm}^2 \text{ s}^{-1}$ , [106]) and [EMIM] [BF<sub>4</sub>] ( $6.0 \times 10^{-7} \text{ cm}^2 \text{ s}^{-1}$ , [66]) at 25 °C, but they are one order of magnitude larger than those found for the Ag(I) solution in [BMIM] [PF<sub>6</sub>] ( $1 \times 10^{-8}$  and  $3 \times 10^{-8} \text{ cm}^2 \text{ s}^{-1}$ , [106]). This difference can be explained from the viscosity of the ionic liquids, since [EMIM] [TFSI] (34 cP [50]) has a similar viscosity value to [EMIM] [BF<sub>4</sub>] (43 cP [47]) whereas [BMIM] [PF<sub>6</sub>] has a higher viscosity (450 cP, [58]). The diffusion coefficient of Ag(I) salt solutions in ethylammonium nitrate ( $2.0 \times 10^{-6} \text{ cm}^2 \text{ s}^{-1}$ , [136]) is an order of magnitude larger than our diffusion coefficient values. This discrepancy can be explained by the fact that the purity of the ethylammonium nitrate was around 97% [136] and the solution might contain water as an impurity, which will significantly affect the results.



Figures 6.9: **a**) Chronoamperograms of 0.05 M AgTFSI solution obtained at 35, 50 and 85 °C on a GC disc electrode with potential steps of -0.39, -0.31 and -0.28 V, respectively; and **b**) respective variation of the current density with  $t^{-1/2}$ .

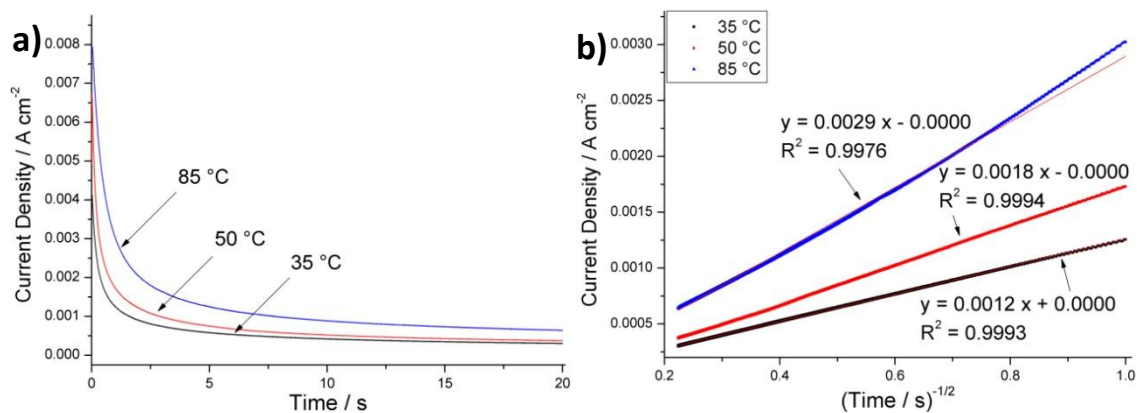


Figure 6.10: **a)** Chronoamperograms of 0.05 M AgTFSI solution obtained at 35, 50 and 85 °C on a Pt disc electrode with potential steps of -0.34, -0.22 and -0.24 V, respectively; and **b)** respective variation of the current density with  $t^{-1/2}$ .

Table 6.1: Diffusion coefficient of the silver species in [EMIM] [TFSI] solutions calculated from chronoamperometry data.

0.05 M AgTFSI solution	Diffusion Coefficient, D (cm <sup>2</sup> s <sup>-1</sup> )		
	35 °C	50 °C	85 °C
GC electrode	$6.6 \times 10^{-08}$	$3.5 \times 10^{-07}$	$1.6 \times 10^{-06}$
Pt electrode	$1.9 \times 10^{-07}$	$4.4 \times 10^{-07}$	$1.2 \times 10^{-06}$

## 6.2.2 Cyclic Voltammogram of CuTFSI<sub>2</sub> in [EMIM] [TFSI] solution

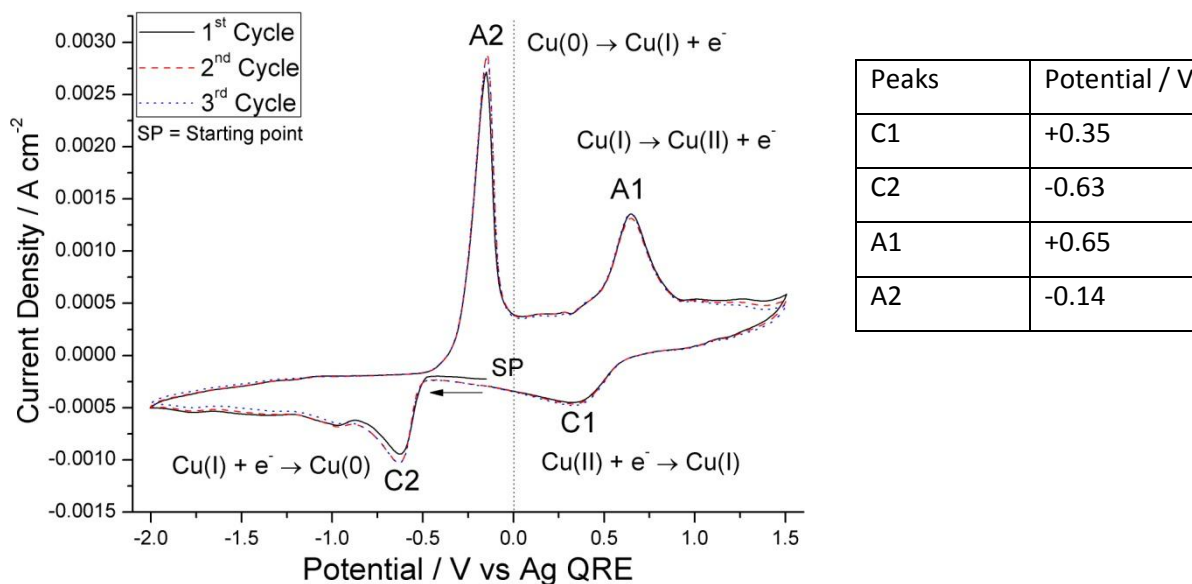


Figure 6.11: Cyclic voltammogram (3 cycles) of 0.05 M CuTFSI<sub>2</sub> solution in [EMIM] [TFSI] at 35 °C. The working electrode was a GC disc and the scan rate was 50 mV s<sup>-1</sup>. The potential of the cathodic and anodic peaks are shown in the accompanying table.

The voltammogram of the 0.05 M CuTFSI<sub>2</sub> solution obtained on a GC working electrode is presented in Figure 6.11. In the forward scan, the cathodic current density increases sharply around -0.47 V and presents a cathodic peak at -0.63 V (C2). This is caused by the reduction of Cu(I) to metallic copper (Cu(0)). A small reduction wave is also observed at -0.96 V, possibly due to impurities. The cathodic current decreases slowly down to the reversal potential at -2.0 V. In the reverse scan, the anodic current increases gradually until -0.48 V, where a sharp increase is observed. This leads to an anodic peak at -0.14 V (A2), corresponding to the oxidation of metallic copper to Cu(I). This is evident from voltammograms with different reversal potentials (Figure 6.13), where the A2 peak is only present when the reversal potential includes the peak C2. The A2 peak has a larger current density than the C2 peak. Another anodic peak is located at +0.65 V (A1), which is attributed to the oxidation of Cu(I) to Cu(II). A cathodic peak corresponding to the reduction of Cu(II) to Cu(I) is observed at +0.35 V (C1) as the scan is reversed once again at 1.5 V.

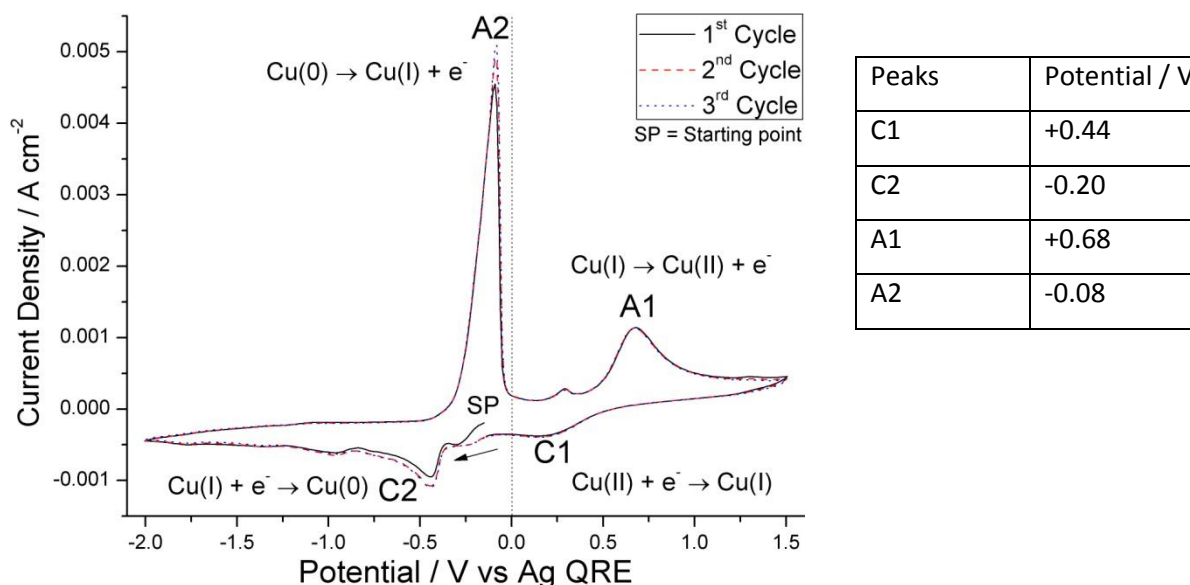


Figure 6.12: Cyclic voltammogram (3 cycles) of 0.05 M CuTFSI<sub>2</sub> solution in [EMIM][TFSI] at 35 °C. The working electrode was a Pt disc and the scan rate was 50 mV s<sup>-1</sup>. The potential of the cathodic and anodic peaks are shown in the accompanying table.

A similar evolution is observed in the voltammogram of the 0.05 M CuTFSI<sub>2</sub> solution obtained on a Pt working electrode (Figure 6.12). The cathodic peaks C1 and C2 are respectively located at +0.44 and -0.20 V, and the anodic peaks A1 and A2 at +0.68 and -0.08 V, in agreement with the results obtained using a GC electrode. An exception is C2, which is located at a less negative potential for the Pt electrode. This may be explained by the fact that an overpotential is required to start the nucleation process on GC substrate [124], as shown by the presence of a nucleation loop with a crossover at -0.40 in Figure 6.13.

The reduction of Cu(II) solutions in [EMIM] [TFSI] occurs in two steps, in agreement with the results reported for Cu(II) solutions in [EMIM] [DCA] [242], [EMIM] [BF<sub>4</sub>] [240] and [TMHA] [TFSI] [241].

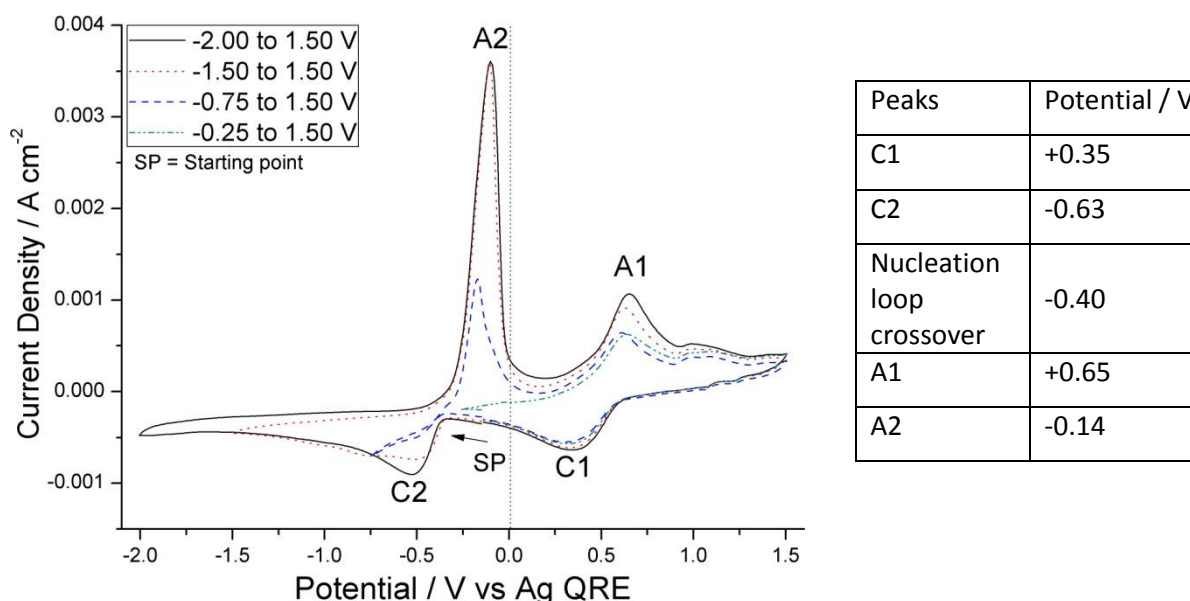
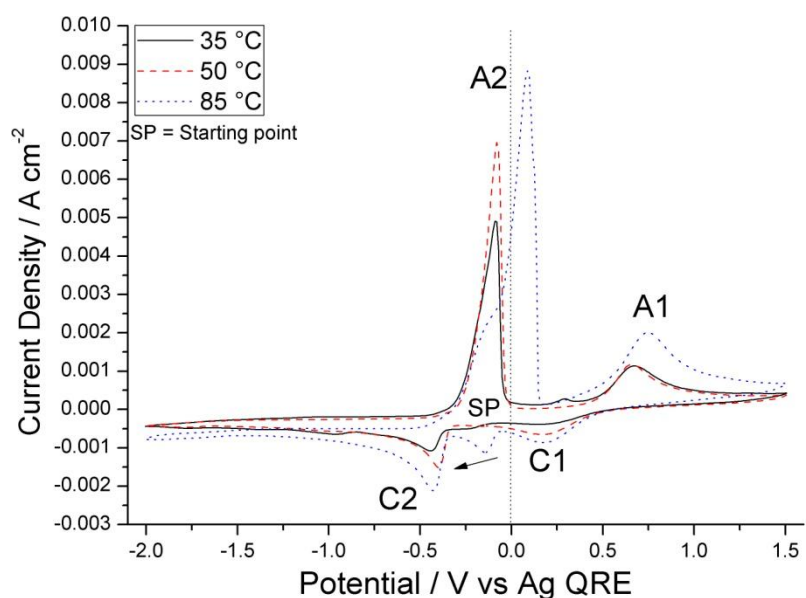


Figure 6.13: Cyclic voltammograms of 0.05 M CuTFSI<sub>2</sub> solution in [EMIM] [TFSI] at 50 °C using different cathodic reversible potentials. The working electrode was a GC disc and the scan rate was 50 mV s<sup>-1</sup>. The potential of the cathodic and anodic peaks are shown in the accompanying table.

The change in the cyclic voltammogram with temperature is shown in Figure 6.14. The current density for all the peaks increased with temperature, as previously observed for the AgTFSI solution. The viscosity of the ionic liquid solution decreased with increasing temperature, leading to an increase of the mass transport and electrical conductivity [10]. No changes were observed in the potential of C1 and C2, which remained close to +0.44 and -0.44 V respectively at different electrolyte temperatures. A1 and A2 peaks also remained at the same potential when the temperature was increased to 50 °C, but they shifted to a more positive potential of +0.12 V at 85 °C. The solution appeared to be less stable at 85 °C as a new reduction peak was observed at -0.14 V and a large change in the shape and position of the A2 peak was detected. There was also a slight change in the colour of the 0.05 M CuTFSI<sub>2</sub> solution to a darker shade of green.

The increase in current density of peak C1 due to the reduction of Cu(II) to Cu(I) with the electrolyte temperature is presented in Figure 6.15. As Cu(II) to Cu(I) reduction reaction is thermally activated, it behaves in accordance with the Arrhenius equation (Equations 6.1 and 6.2). From Equation 6.2, the activation energy for the Cu(II) to Cu(I) reduction was calculated as 12 kJ mol<sup>-1</sup>.



Peaks	Potential / V
C1 (35 °C)	+0.19
C1 (50 °C)	+0.19
C1 (85 °C)	+0.19
C2 (35 °C)	-0.44
C2 (50 °C)	-0.40
C2 (85 °C)	-0.43
A1 (35 °C)	+0.67
A1 (50 °C)	+0.66
A1 (85 °C)	+0.73
A2 (35 °C)	-0.09
A2 (50 °C)	-0.08
A2 (85 °C)	+0.08

Figure 6.14: The variation in current density with temperature for the 0.05 M CuTFSI<sub>2</sub> solution in [EMIM][TFSI] obtained on a Pt working electrode. The potential of the cathodic and anodic peaks are shown in the accompanying table.

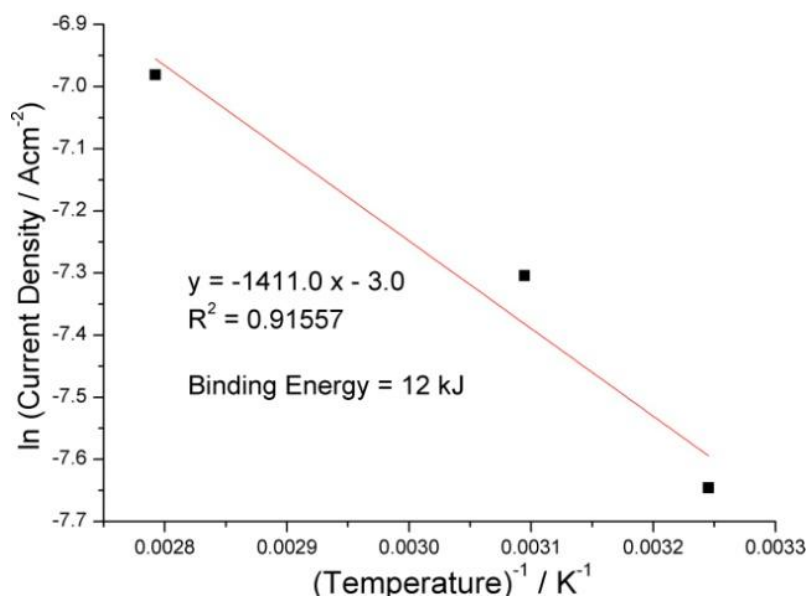


Figure 6.15: Relationship between current density of C1 with temperature. The working electrode was a GC disc and the scan rate was 50 mV s<sup>-1</sup>.

Cyclic voltammetry carried out at different potential scan rates was also performed for the 0.05 M CuTFSI<sub>2</sub> solution. GC and Pt working electrodes were used and the results are shown in Figure 6.16. The reversibility of the Cu(II) to Cu(I) reaction is tested against the conditions for a reversible reaction described by Equations 3.4, 3.5, 3.6 and 3.7 listed in Sections 3.4.1 and 6.1.1 above.

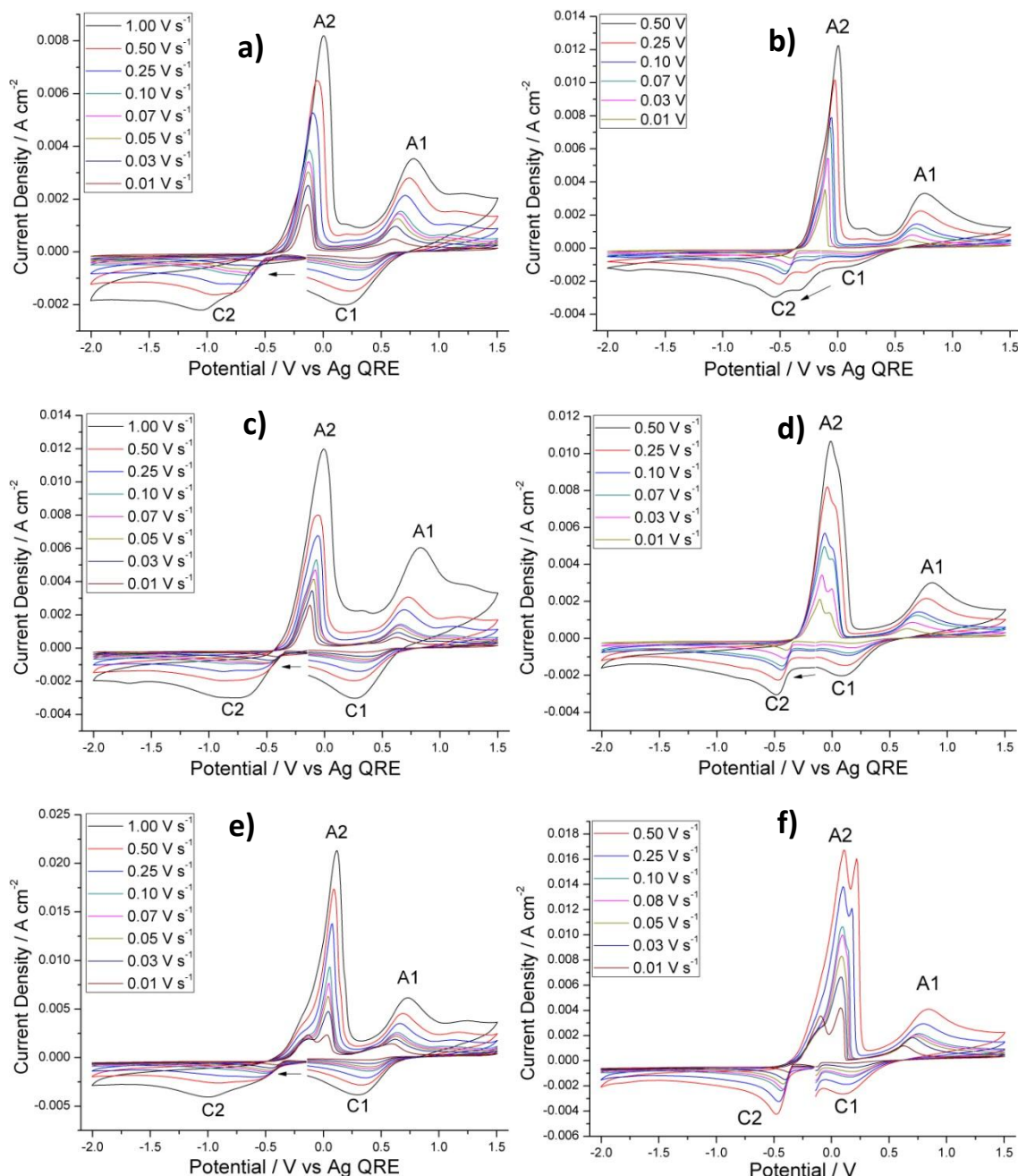


Figure 6.16: Cyclic voltammograms of 0.05 M CuTFSI<sub>2</sub> solution in [EMIM] [TFSI] using different potential scan rates between 0.01 and 1.00 V s<sup>-1</sup> at **a)** 35 °C on GC, **b)** 35 °C on Pt, **c)** 50 °C on GC, **d)** 50 °C on Pt, **e)** 85 °C on GC and **f)** 85 °C on Pt.



The current density of the anodic (A1) and cathodic (C1) peaks varied linearly with the square root of the scan rate ( $v^{1/2}$ ), as seen in Figures 6.17 and 6.18. This relationship satisfies Equation 3.4 indicating that the process is likely diffusion controlled [29,8].

However, A1 shifted to a more positive potential and C1 shifted to a more negative potential as the scan rate was increased as shown in Figure 6.16. This shows that the peak potentials ( $E_p$ ) are not independent of the scan rate, hence they do not satisfy the condition for a reversible reaction.

The  $|E_p - E_{p/2}|$  values calculated are also larger than those provided by Equation 3.5.

In addition, A1 and C1 are too far apart and the calculated  $E_{p,a} - E_{p,c}$  does not satisfy Equation 3.6.

The current densities of A1 ( $I_{p,a}$ ) are larger than C1 ( $I_{p,c}$ ) and they do not satisfy Equation 3.7.

Based on these considerations, the reduction of Cu(II) to Cu(I) in [EMIM] [TFSI] is deemed to be a quasi-reversible process.

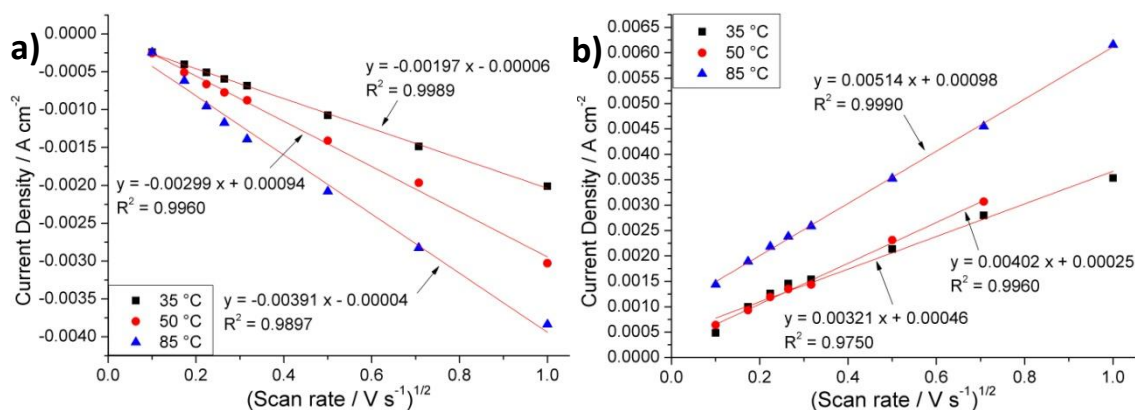


Figure 6.17: **a)** The anodic peak current (A1) and **b)** cathodic peak current (C1) as a function of scan rate for the 0.05 M CuTFSI<sub>2</sub> solution in [EMIM] [TFSI] using a GC working electrode.

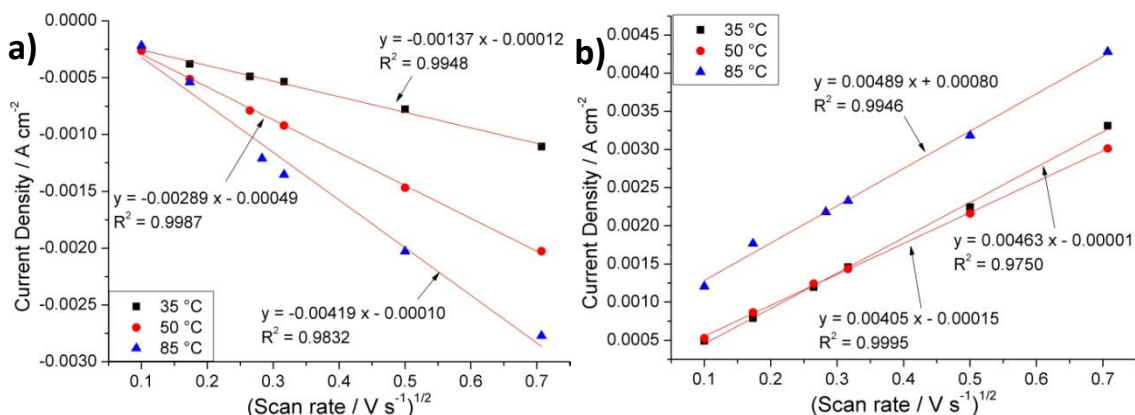


Figure 6.18: **a)** The anodic peak current (A1) and **b)** cathodic peak current (C1) as a function of scan rate for the 0.05 M CuTFSI<sub>2</sub> solution in [EMIM] [TFSI] using a Pt working electrode.

Chronoamperograms obtained by using GC and Pt working electrodes are presented in Figures 6.19 **a** and 6.20 **a**. These chronoamperograms were acquired with potential steps corresponding to the reduction of Cu(II) to Cu(I). The diffusion coefficient can be estimated from the slope of an (*i*) versus ( $t^{-1/2}$ ) plot (Figures 6.19 **b** and 6.20 **b**). The calculated values are presented in Table 6.2. The diffusion coefficients obtained with GC and Pt working electrodes are similar. The diffusion coefficient increases with temperature, due to a corresponding decrease in viscosity of the electrolyte.

The calculated diffusion coefficients are an order of magnitude smaller than the Cu(II) solutions in [EMIM] [DCA] ( $2.06 \times 10^{-6} \text{ cm}^2 \text{ s}^{-1}$ , [242]) and slightly larger than those of Cu(II) solutions in [EMIM]–Cl–[BF<sub>4</sub>] ( $1.5 \times 10^{-7} \text{ cm}^2 \text{ s}^{-1}$ , [240]). This difference may be explained by the viscosity of the solutions, the viscosity of [EMIM] [DCA] (21 cP) being much lower than those of [EMIM] [TFSI] (34 cP [50]) and [EMIM] [BF<sub>4</sub>] (43 cP [47]).

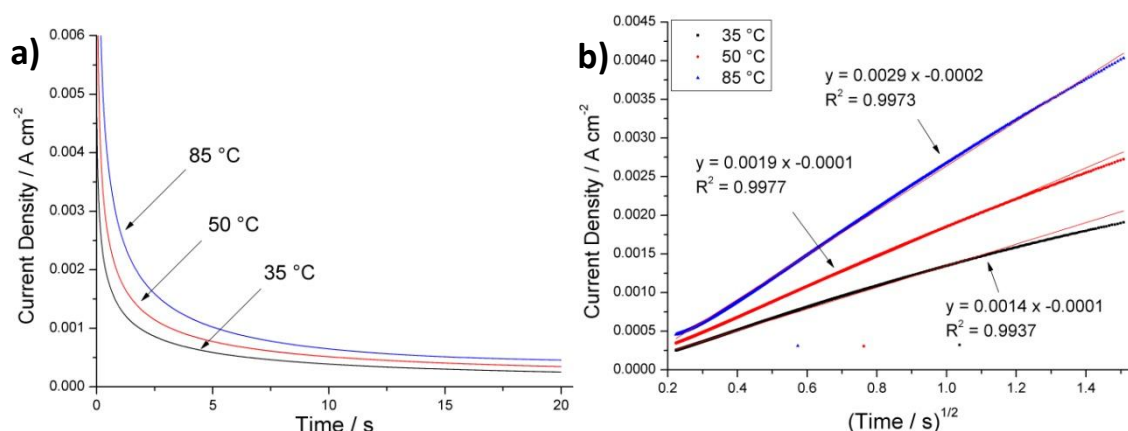


Figure 6.19: **a**) Chronoamperograms of 0.05 M CuTFSI<sub>2</sub> solutions obtained on a GC disc electrode with potential steps of -0.30, -0.30 and -0.24 V, respectively; and **b**) respective variation of the current density with  $t^{-1/2}$ .

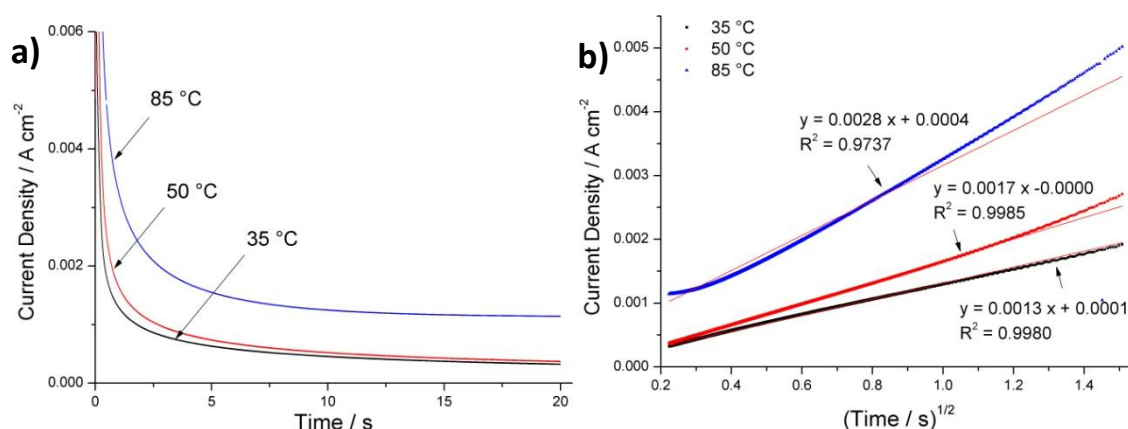


Figure 6.20: **a**) Chronoamperograms of 0.05 M CuTFSI<sub>2</sub> solutions obtained on a Pt disc electrode with potential steps of -0.1 V; and **b**) respective variation of the current density with  $t^{-1/2}$ .



Table 6.2: Diffusion coefficient of the copper species in [EMIM] [TFSI] solutions calculated from chronoamperometry data.

0.05 M CuTFSI <sub>2</sub> solution	Diffusion Coefficient, D (cm <sup>2</sup> s <sup>-1</sup> )		
	35 °C	50 °C	85 °C
GC electrode	2.7 x 10 <sup>-07</sup>	4.9 x 10 <sup>-07</sup>	1.1 x 10 <sup>-06</sup>
Pt electrode	2.3 x 10 <sup>-07</sup>	3.9 x 10 <sup>-07</sup>	1.1 x 10 <sup>-06</sup>

### 6.2.3 Cyclic Voltammogram of AlTFSI<sub>3</sub> in [EMIM] [TFSI] solution

The voltammogram of the 0.50 M AlTFSI<sub>3</sub> solution obtained on a GC working electrode is presented in Figure 6.21. In the forward scan, the current density increased gradually until -1.1 V, where a sharp increase in current density occurred. This led to a cathodic peak at -1.55 V (C1), which was probably due to the bulk reduction of aluminium, as previously observed in [EMIM] [TFSI] and [BMPyr] [TFSI] solutions of AlCl<sub>3</sub> [171,213,173,174]. The current density continued to increase until the reversal potential at -2.0 V. In the reverse scan, an anodic peak was found at -0.12 V, possibly associated with the oxidation of the aluminium. A decrease in the current density of C1 was observed in the second and third cycles.

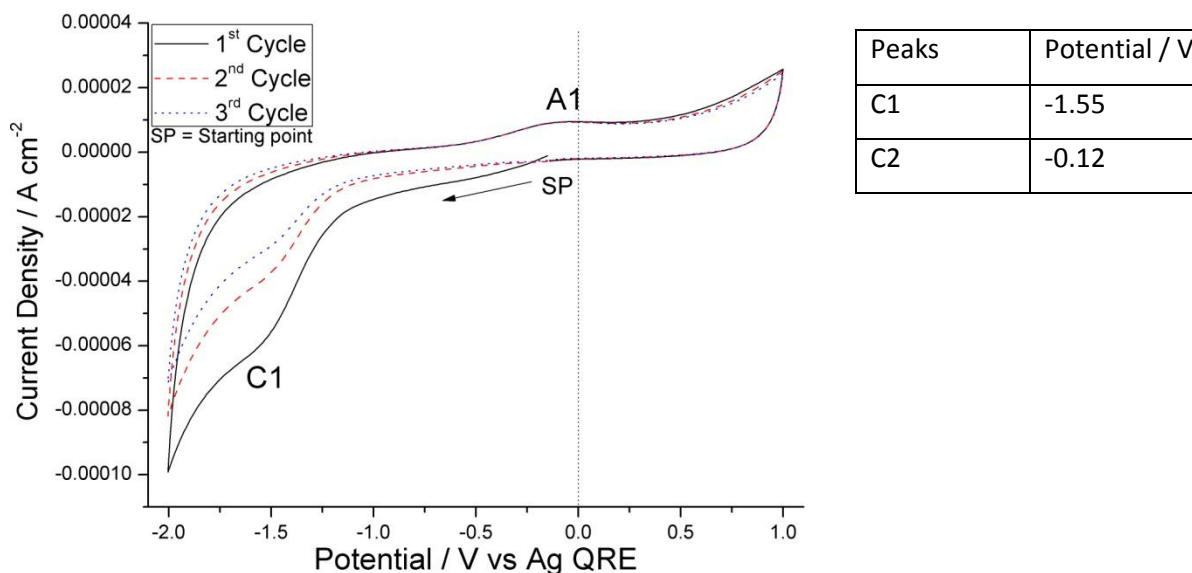


Figure 6.21: Cyclic voltammogram (3 cycles) of 0.50 M AlTFSI<sub>3</sub> solution in [EMIM] [TFSI] at 35 °C. The working electrode was a GC disc. The scan rate was 50 mV s<sup>-1</sup>.

The voltammogram obtained with a Pt working electrode is shown in Figure 6.22. Similar to Figure 6.21, the cathodic and anodic peaks were observed at -1.06 V (C1) and +0.86 V (A1) in the first cycle. In the second cycle, a new reduction peak was observed at -2.42 V (C2), while a new

oxidation peak appeared at -2.00 V. Additionally, C1 shifted to a more positive potential in subsequent cycles, and eventually settled at a potential of -0.25 V.

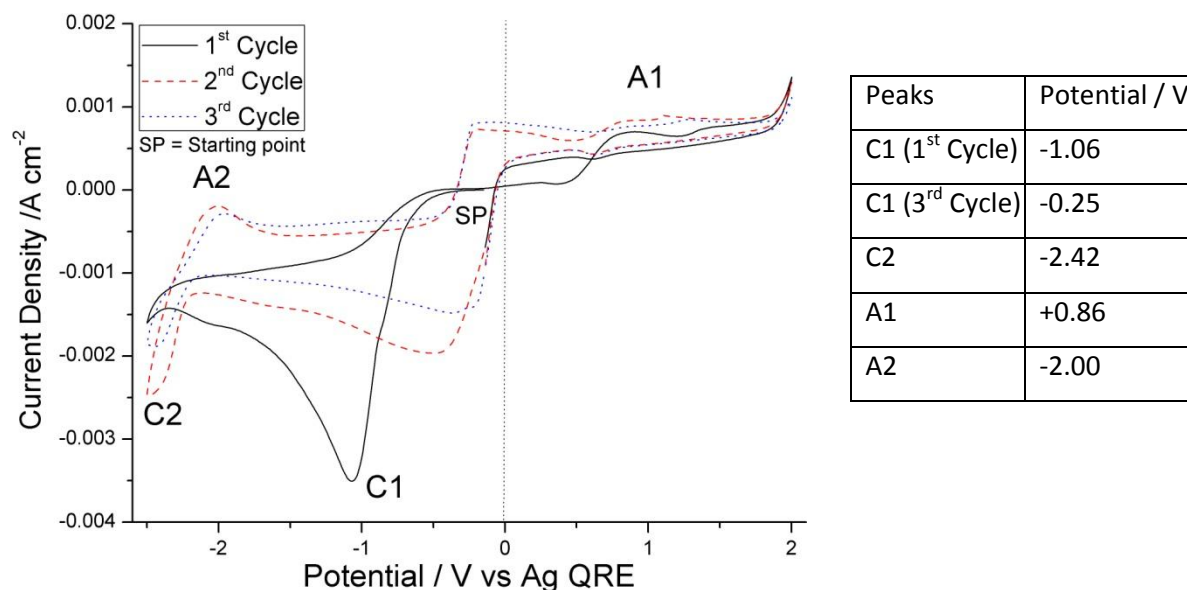


Figure 6.22: Cyclic voltammogram (3 cycles) of 0.50 M AlTFSI<sub>3</sub> solution in [EMIM] [TFSI] at 35 °C. The working electrode was a Pt disc. The scan rate was 50 mV s<sup>-1</sup>. The potential of the cathodic and anodic peaks are shown in the accompanying table.

Evolution of the cyclic voltammogram with temperature is shown in Figure 6.23 a. The potential of C1 did not change with temperature, but a large increase in the current density of this peak was observed when the temperature increased from 35 to 50 °C, however, a decrease of C1 current density occurred when the temperature increased from 50 to 85 °C. The solution became unstable when exposed at 85 °C. After a few experiments, the solution changed from colourless to a brownish colour (Figure 6.23 b).

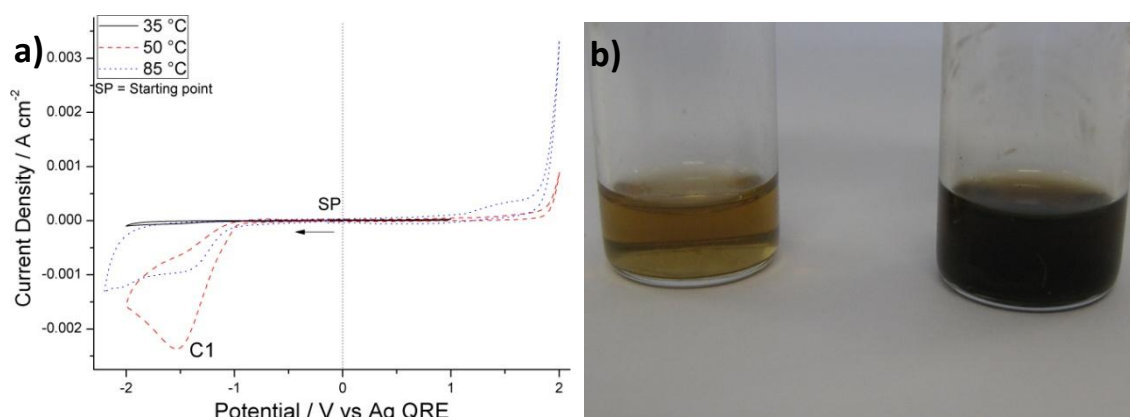


Figure 6.23: **a)** Variation in current density with temperature for the 0.50 M AlTFSI<sub>3</sub> solution in [EMIM] [TFSI] using a GC working electrode. **b)** Colour change after electrochemical characterisation experiments for the 0.50 M and 1.00 M AlTFSI<sub>3</sub> solution.

Cyclic voltammograms of the 0.50 M AlTFSI<sub>3</sub> solution obtained at different potential scan rates are shown in Figure 6.24. Due to the instability of the solutions at high temperatures with a Pt working electrode, only the voltammograms obtained with the GC working electrode at 50 °C were usable. The reversibility of the C1 reduction was tested against the conditions for a reversible reaction described by Equations 3.4, 3.5, 3.6 and 3.7 listed in Section 6.1.1. The current density of C1 varies linearly with the square root of the scan rate ( $v^{1/2}$ ) as shown in Figure 6.24 **b**, thus satisfying Equation 3.4. However, the other conditions were not met. Based on this, the electrochemical process is deemed to be irreversible for the 0.50 M AlTFSI<sub>3</sub> solution at 50 °C and with a GC working electrode.

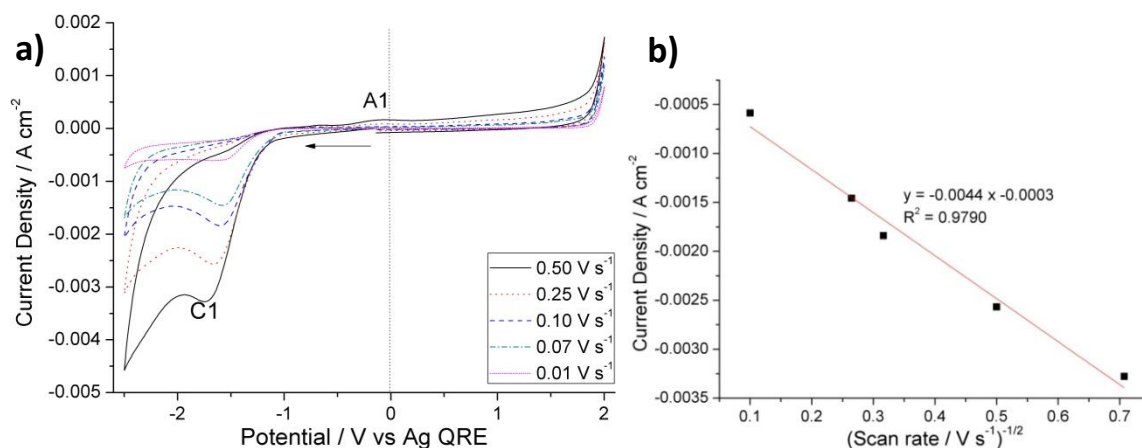


Figure 6.24: a) Cyclic voltammograms of 0.50 M AlTFSI<sub>3</sub> solution in [EMIM][TFSI] at 50 °C using different potential scan rates between 0.01 and 0.50 V s<sup>-1</sup>. The working electrode was a GC disc. b) Corresponding cathodic peak current of C1 as a function of scan rate.

Chronoamperograms were obtained at -1.49, -1.50 and -1.50 V corresponding to the C1 peak at 35, 50 and 85 °C on a GC electrode (Figure 6.25 **a**). The diffusion coefficient was calculated from the slope of the ( $i$ ) versus ( $t^{-1/2}$ ) plot presented in Figure 6.25 **b**. The calculated values were  $1.2 \times 10^{-12}$ ,  $6.0 \times 10^{-11}$  and  $1.8 \times 10^{-9}$  cm<sup>2</sup> s<sup>-1</sup> for 35, 50 and 85 °C, respectively.

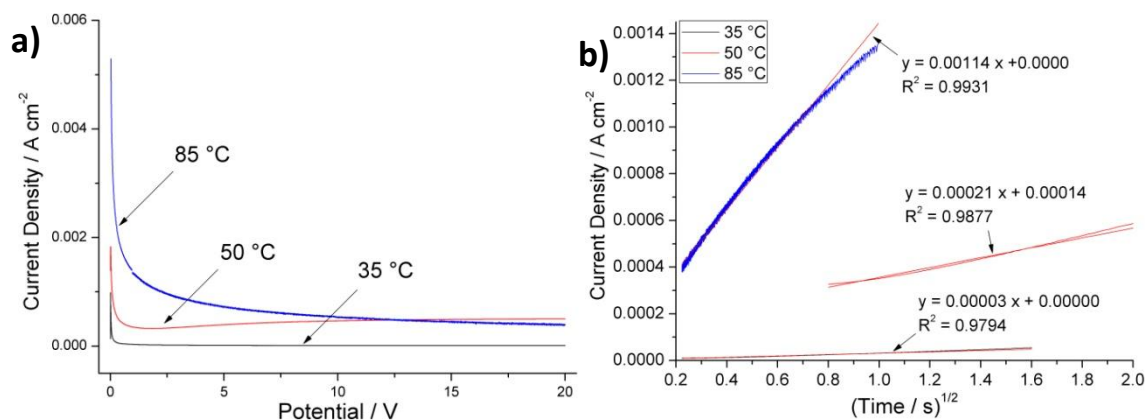


Figure 6.25: **a**) Chronoamperograms of 0.50 M AlTFSI<sub>3</sub> solutions obtained with a GC disc electrode and potential steps of -0.1 V; **b**) respective variation of the current density with  $t^{-1/2}$ .

### 6.3 Electrodeposition

Electrodeposition was carried out from 0.05 M AgTFSI and CuTFSI<sub>2</sub> solutions in [EMIM] [TFSI] and visible films of copper and silver were obtained. However, electrodeposition experiments carried out from 1.00 M AlTFSI<sub>3</sub> solutions in [EMIM] [TFSI] failed to yield any aluminium films. SEM micrographs showing the microstructures of the films deposited at different temperatures, times and potentials are presented below.

#### 6.3.1 Microstructure of the films

##### 6.3.1.1 0.05 M AgTFSI solutions

Visible silver films were obtained from the AgTFSI solution when the applied potential was more negative than -0.2 V. The microstructure of the films deposited at 35 °C is shown in Figures 6.26 and 6.27. The films deposited at -0.2 V for 900 s were discontinuous (Figure 6.26 a). Increasing the deposition potential to -0.5 V significantly improved the film continuity (Figure 6.26 b). A slight improvement in the surface coverage could also be achieved by increasing the deposition time from 900 s to 1800 and 3600 s, as shown in Figures 6.26 c and e. At -0.5 V and 3600 s, a continuous film was obtained (Figure 6.26 f). The films consisted of particles that nucleated preferentially at the scratches on the nickel substrate made during the manufacturing process by rolling. This occurred because the current density was higher at these edges, so the nucleation and growth would occur preferentially at these points. The particles of the film appeared to have an angular shape, aggregated into cauliflower-like clusters with a cluster size of 100-200 nm (Figures 6.27 a). The particle and cluster size increased with an increase in deposition time and potential. This is because the thickness of the film increased with the deposition time, and the particle size increased with the growth of each successive layer of the film. The mechanism for this process may be explained by the depletion of metal ions near the electrode-electrolyte interface during electrodeposition. This, in turns, leads to the decrease in the rate of nucleation of the particles, giving more room for each particle to grow, thereby leading to a larger particle size at the surface of the film.

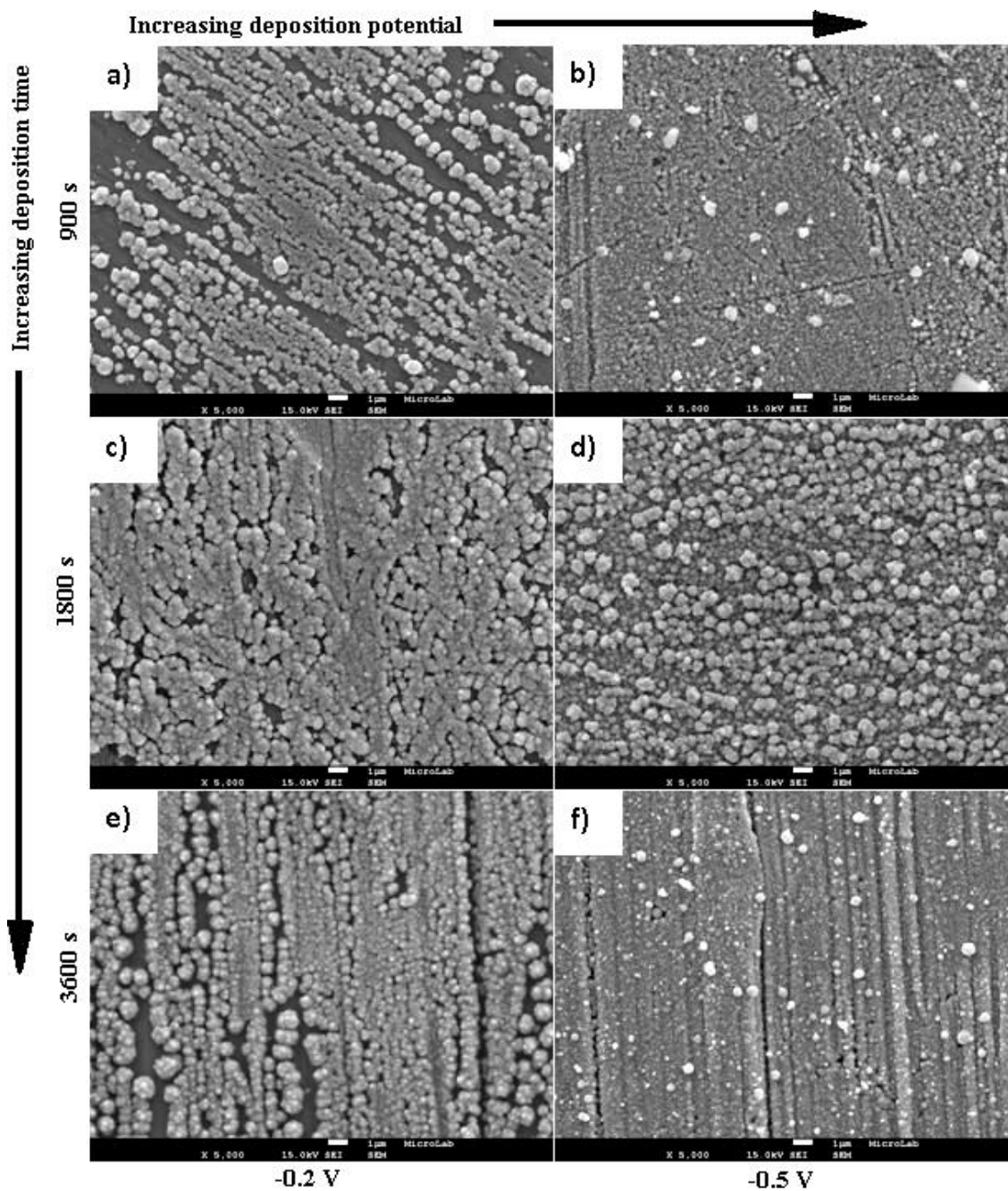


Figure 6.26: SEM micrographs (low magnification) of films electrodeposited from 0.05 M AgTFSI solution at 35 °C. Deposition potential: -0.2 and -0.5 V. Deposition time: 900, 1800 and 3600 s.

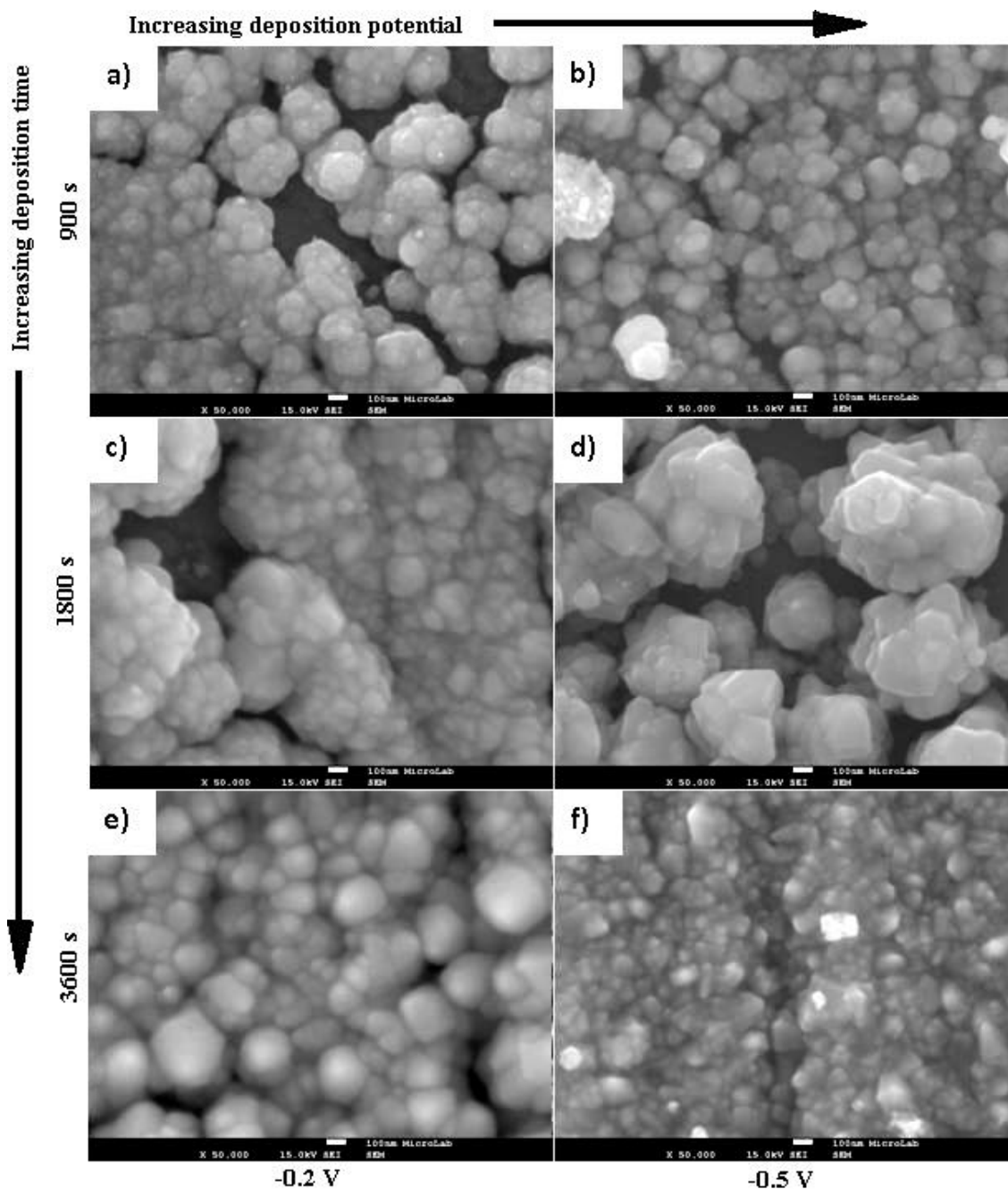


Figure 6.27: SEM micrographs (high magnification) of films electrodeposited from 0.05 M AgTFSI solution at 35 °C. Deposition potential: -0.2 and -0.5 V. Deposition time: 900, 1800 and 3600 s.

The microstructure of the films deposited at 50 °C is shown in Figures 6.28 and 6.29. At this temperature, the continuity of the film was better than those deposited at 35 °C, as can be seen by comparing Figures 6.26 a and 6.28 a. The particle shape of the films deposited at 50 °C was similar to the films deposited at 35 °C, although the size of the particles and particle clusters were larger. For deposition at -0.2 V, the average particle size increased when the deposition time



increased from 900 s (Figure 6.28 a) to 1800 s (Figure 6.28 c). Large silver particles were observed on the films prepared with a deposition time of 3600 s (Figure 6.28 e). These particles were probably formed by secondary nucleation, and their sizes varied between 0.5 to 1  $\mu\text{m}$ . Similar changes were also observed when the deposition was carried out at -0.4 V, but on average, the particle and cluster size were smaller compared to those obtained at -0.2 V (Figures 6.29 e and f).

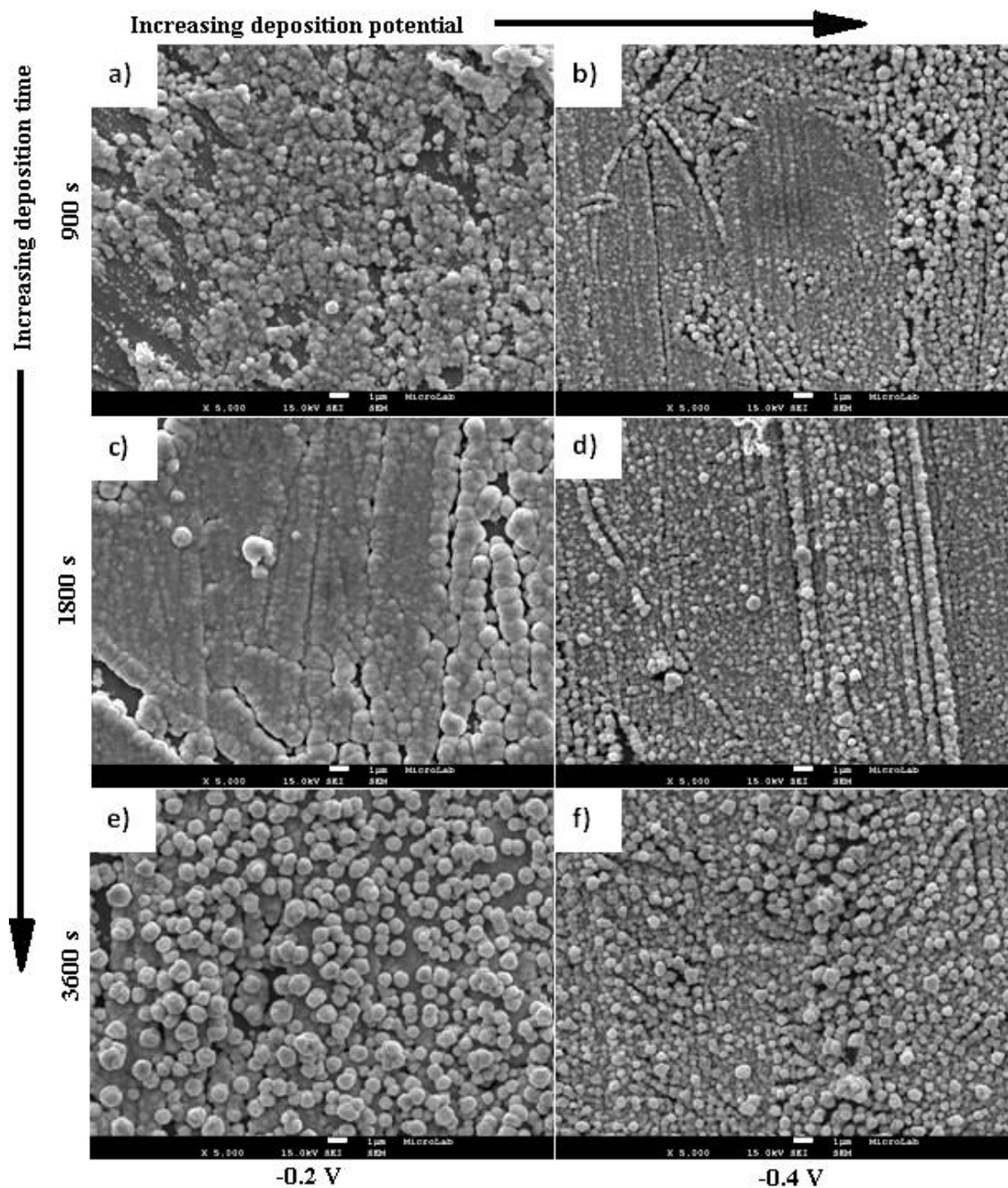


Figure 6.28: SEM micrographs (low magnification) of films electrodeposited from 0.05 M AgTFSI solution at 50 °C. Deposition potential: -0.2 and -0.4 V. Deposition time: 900, 1800 and 3600 s.

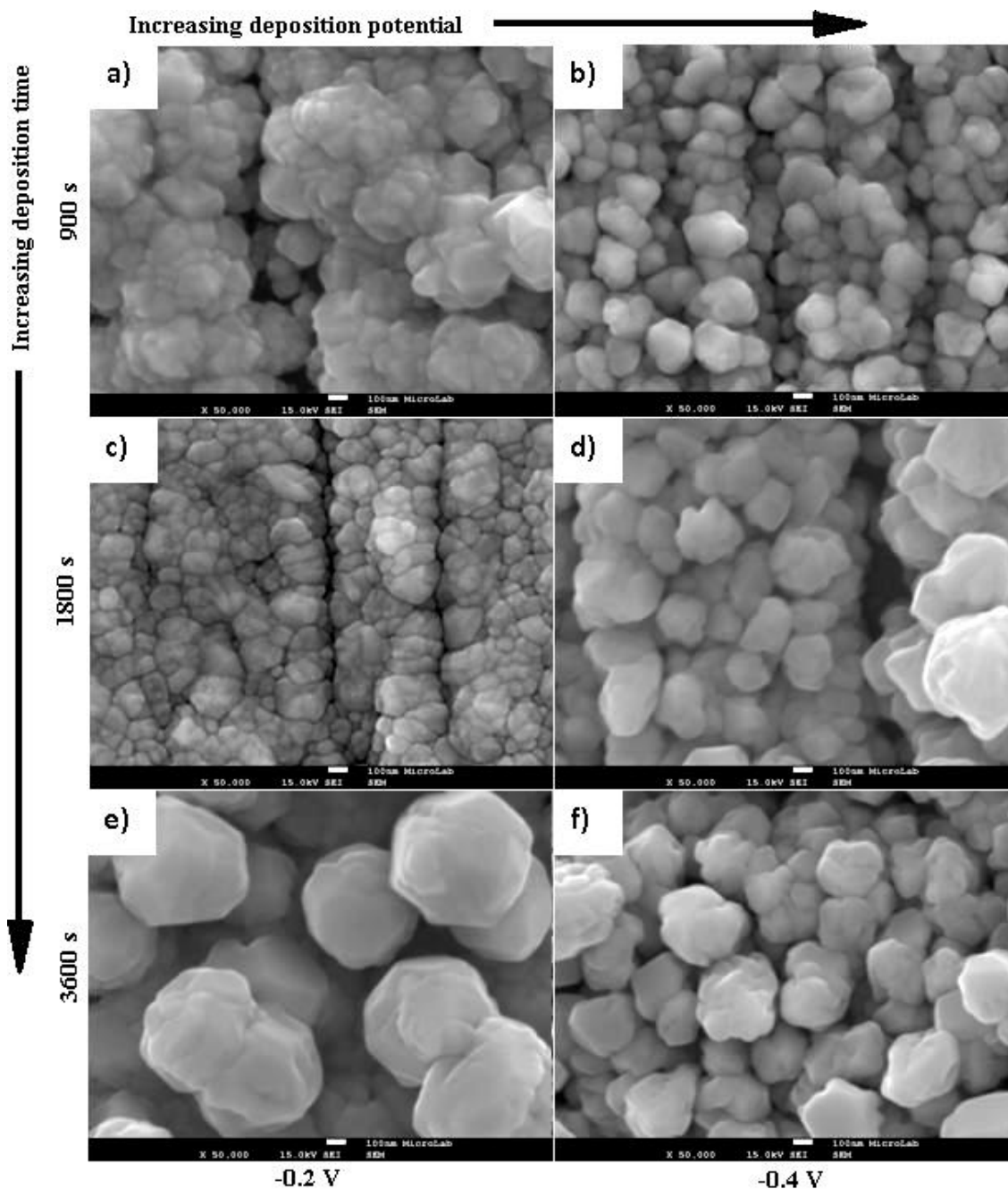


Figure 6.29: SEM micrographs (high magnification) of films electrodeposited from 0.05 M AgTFSI solution at 50 °C. Deposition potential: -0.2 and -0.4 V. Deposition time: 900, 1800 and 3600 s.

The roughness of the films increased when the deposition temperature was increased to 85 °C (Figures 6.30 a and c). At 900 s, the particles formed large globular clusters with a size around 1  $\mu\text{m}$  growing outwards from the surface (Figure 6.30 b). For a deposition time of 1800 s, the clusters acquired a more angular shape, due to the coalescence of larger particles formed at the top of the film compared with the smaller particles within the film (Figure 6.30 d). This shows that



the particle size increases with each addition of new film layer. For a deposition time of 3600 s, a continuous film was formed (Figure 6.30 e). The film consisted of large angular particles. The longer deposition time probably allowed the gaps between 1  $\mu\text{m}$  size angular particles to be filled, forming the continuous film (Figure 6.30 f).

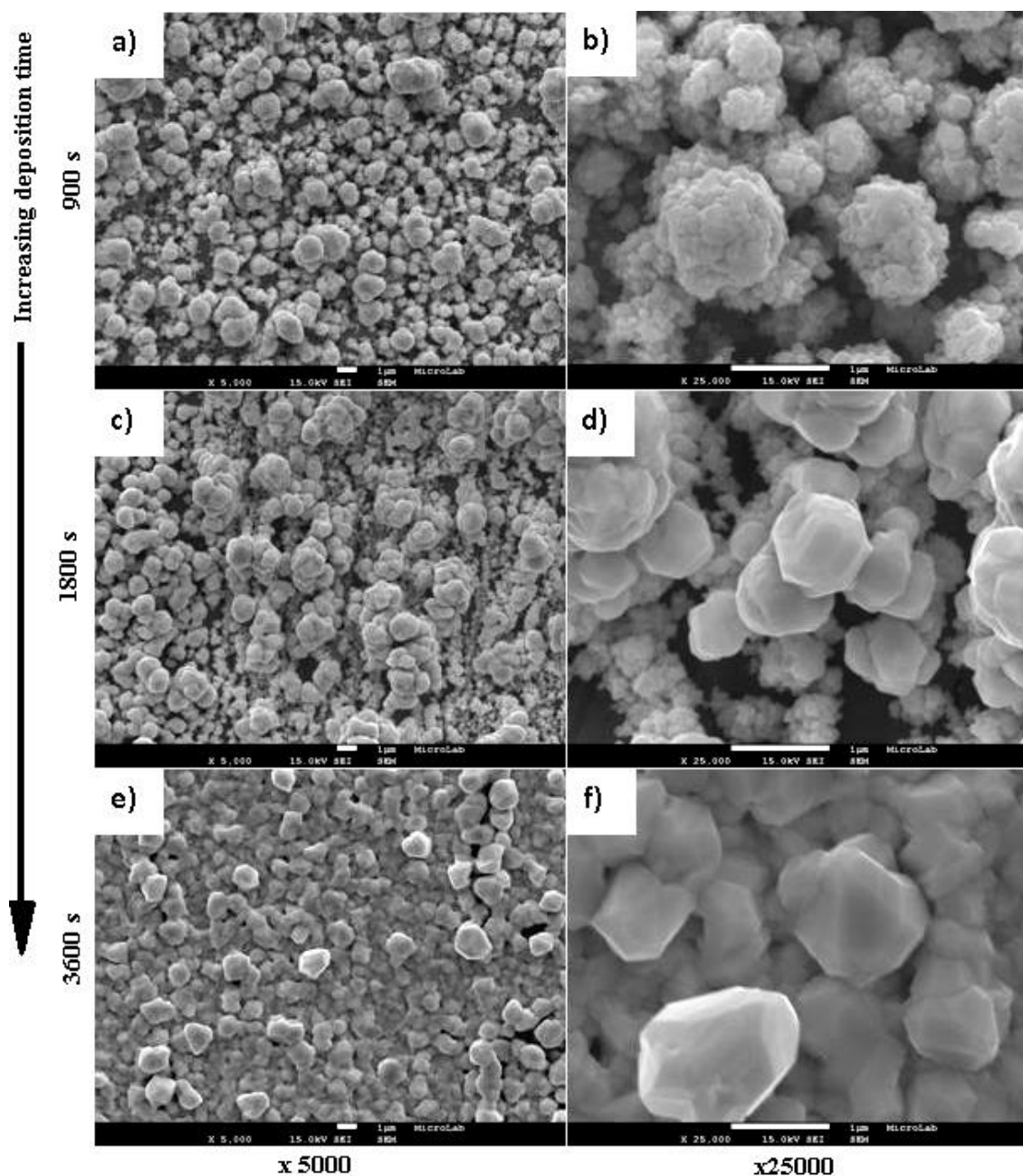


Figure 6.30: SEM micrographs of films electrodeposited from 0.05 M AgTFSI solution at 85 °C and -0.2 V.

### **6.3.1.2 0.05 M CuTFSI<sub>2</sub> solutions**

Visible copper films were obtained from the CuTFSI<sub>2</sub> solution when the applied potential was more negative than -0.5 V. The microstructure of the films deposited at 35 °C is shown in Figures 6.31 and 6.32. The films were continuous for all deposition parameters tested, as seen in Figure 6.31. They consisted of particles which were less than 50 nm in diameter, aggregated into globular clusters. The size of these clusters increased with the deposition time. The cluster size of the films deposited at -0.7 V for 900 s was between 100 and 120 nm (Figure 6.32 **a**). The average size of the clusters increased to about 200 nm when a deposition time of 1800 s was used (Figure 6.32 **c**). For 3600 s, the cluster size increased further to between 200 and 300 nm (Figure 6.32 **e**). The larger particle clusters appeared to have formed from secondary nucleation at the surface of the copper film, since the clusters at the top of the films were much larger than those forming the film below (Figure 6.32 **e**). However, increasing the deposition potential from -0.7 to -1.7 V had the opposite effect: the average cluster size decreased slightly (Figures 6.32 **b**, **d** and **f**). Aside from the changes in the cluster size, the morphology of the films was independent of the deposition parameters.

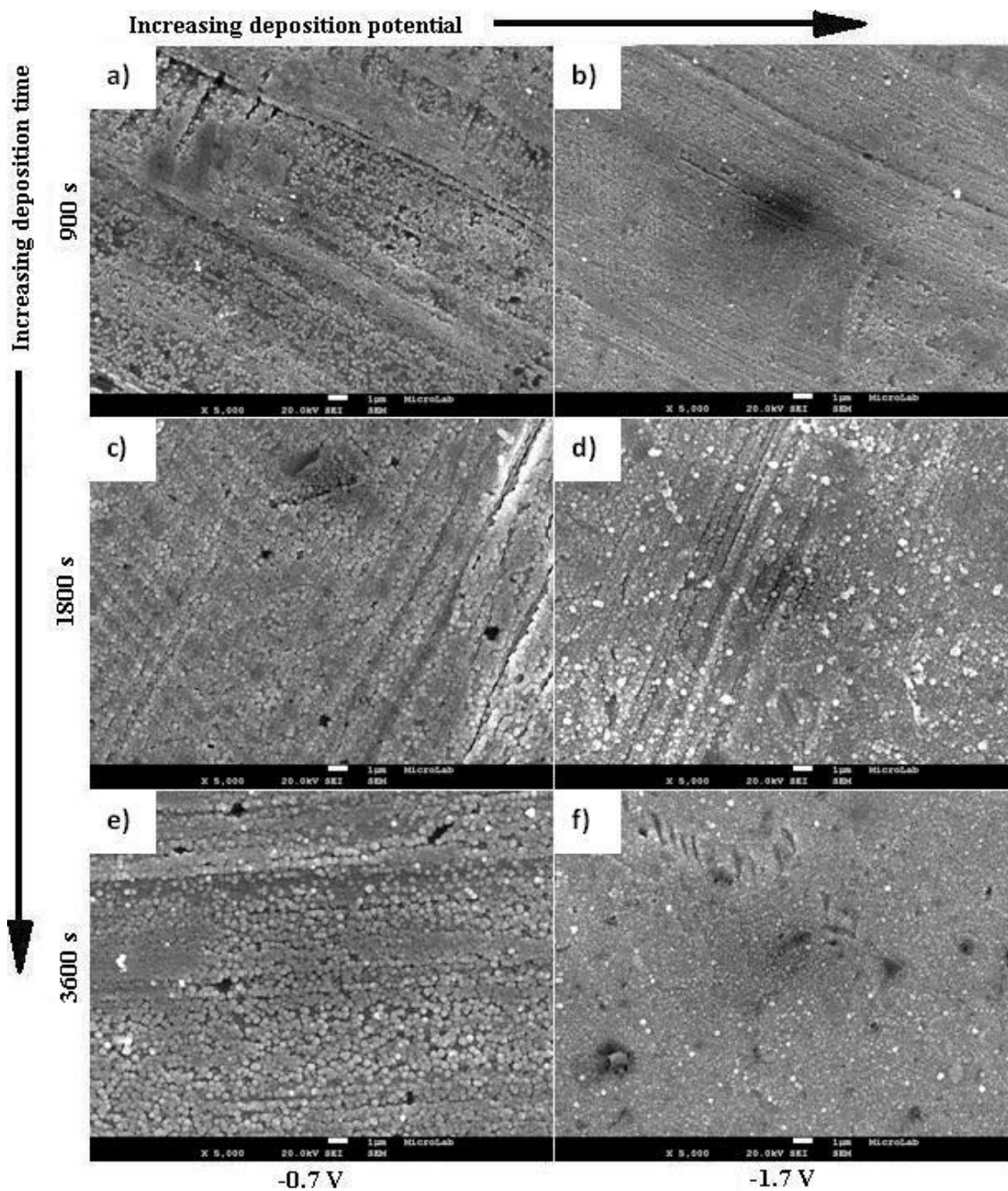


Figure 6.31: SEM micrographs (low magnification) of films electrodeposited from 0.05 M  $\text{CuTFSI}_2$  solution at 35 °C. Deposition potentials: -0.7 and -1.7 V. Deposition times: 900, 1800 and 3600 s.

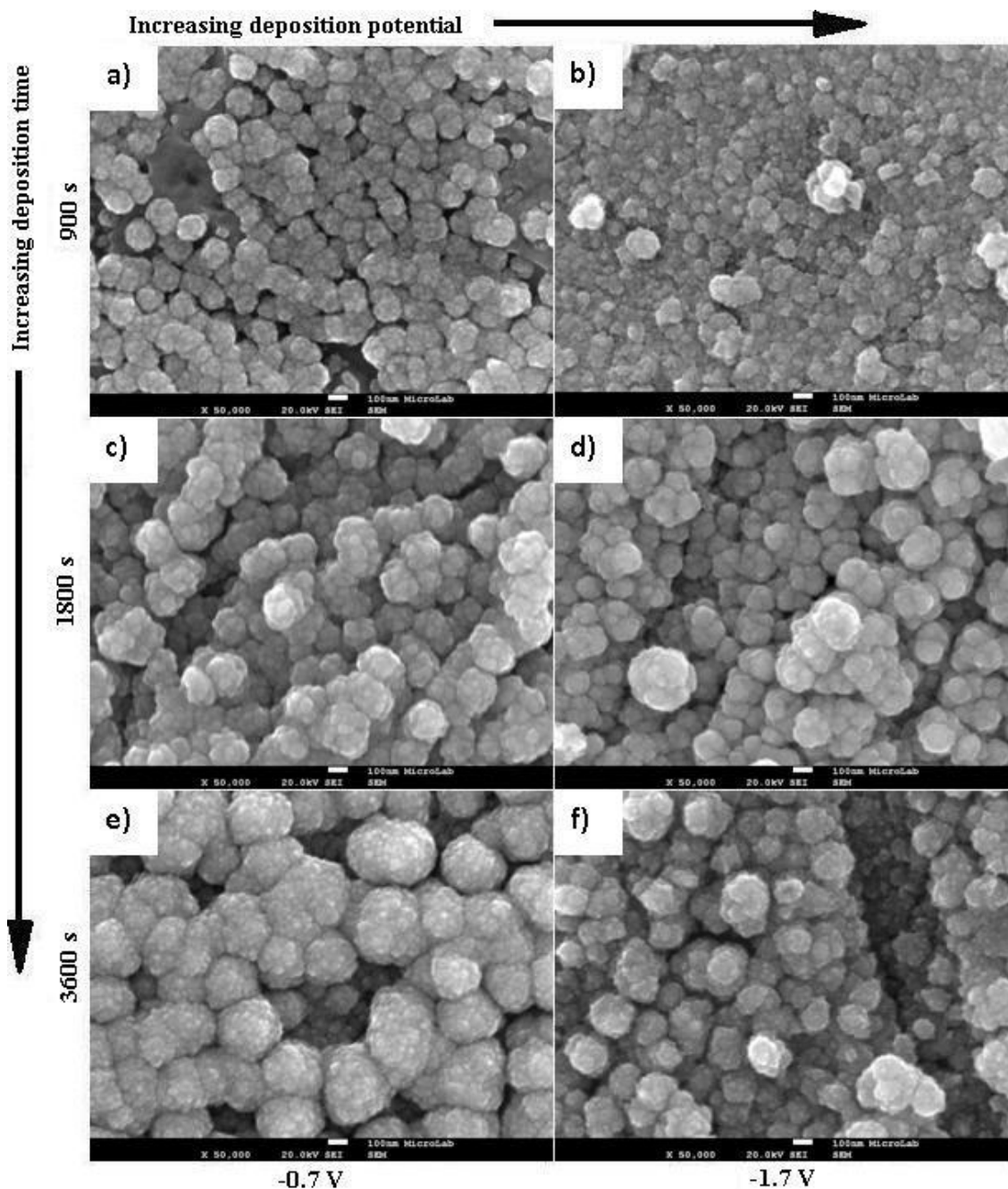


Figure 6.32: SEM micrographs (high magnification) of films electrodeposited from 0.05 M  $\text{CuTFSI}_2$  solution at 35 °C. Deposition potentials: -0.7 and -1.7 V. Deposition times: 900, 1800 and 3600 s.

The microstructure of the films deposited at 50 °C is shown in Figures 6.33 and 6.34. Continuous films were formed for all the parameter values tested (Figure 6.33). For a deposition potential of -0.7 V, the particle and cluster sizes increased with increasing temperature, but the morphology of the films remained relatively unchanged. For example, at a deposition time of 900 s (Figures 6.32 a and 6.34 a), the cluster size increased from around 100 nm at 35 °C to 150 nm at 50 °C. The size of the clusters in the films deposited at -0.7 V also increased with the deposition time. The cluster

size increased to around 200 nm for 1800 s (Figure 6.34 c) and 300 nm for 3600 s (Figure 6.34 e). At 50 °C, increasing the potential from -0.7 to -1.7 V led to a decrease of the average cluster size, as seen in Figures 6.34 b, d and f. The average size of the clusters in the films deposited at -1.7 V was independent of the deposition time, although some larger clusters around 200 nm could be seen on the surface of the film (Figure 6.34 f).

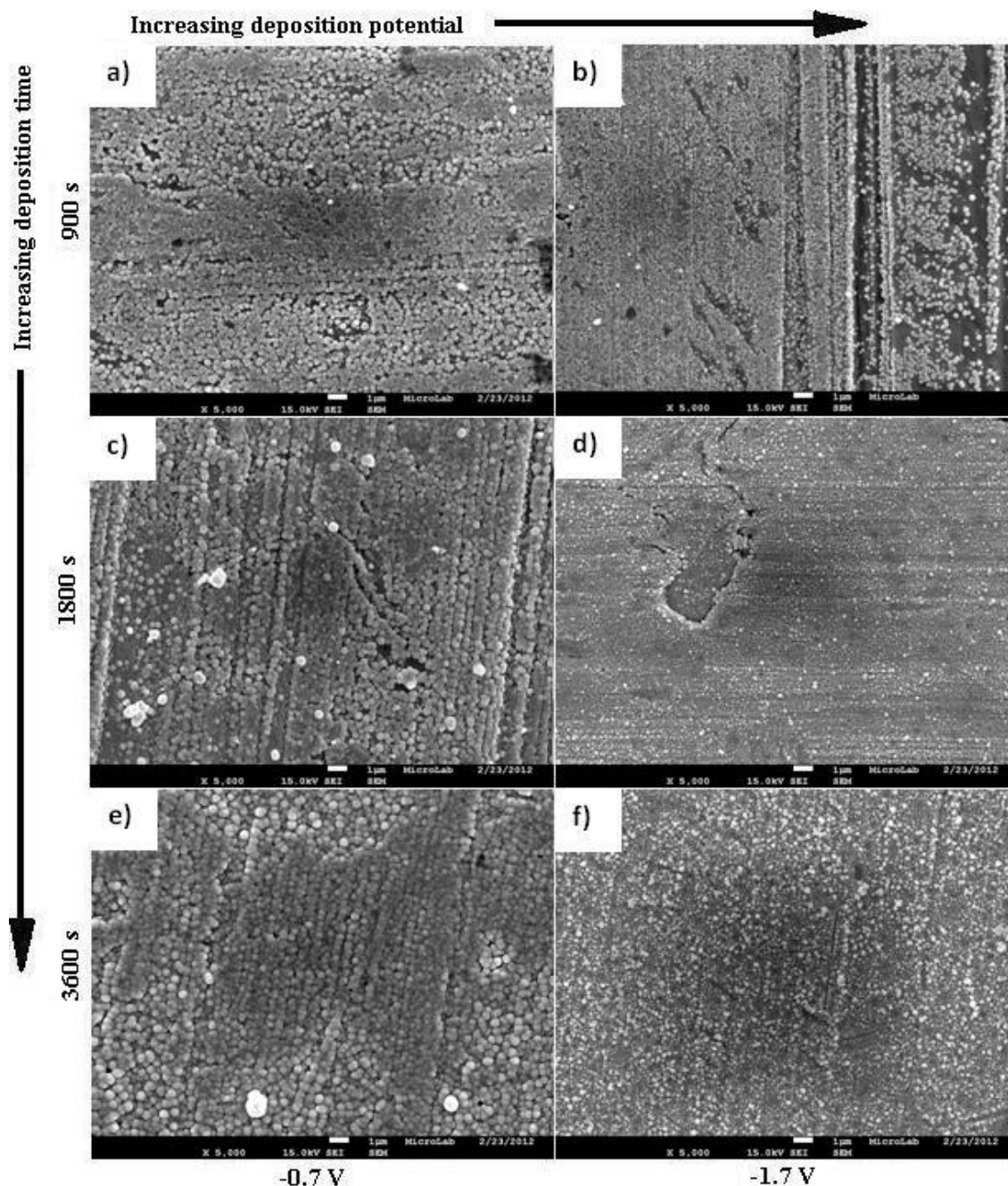


Figure 6.33: SEM micrographs (low magnification) of films electrodeposited from 0.05 M CuTFSI<sub>2</sub> solution at 50 °C. Deposition potentials: -0.7 and -1.7 V. Deposition times: 900, 1800 and 3600 s.

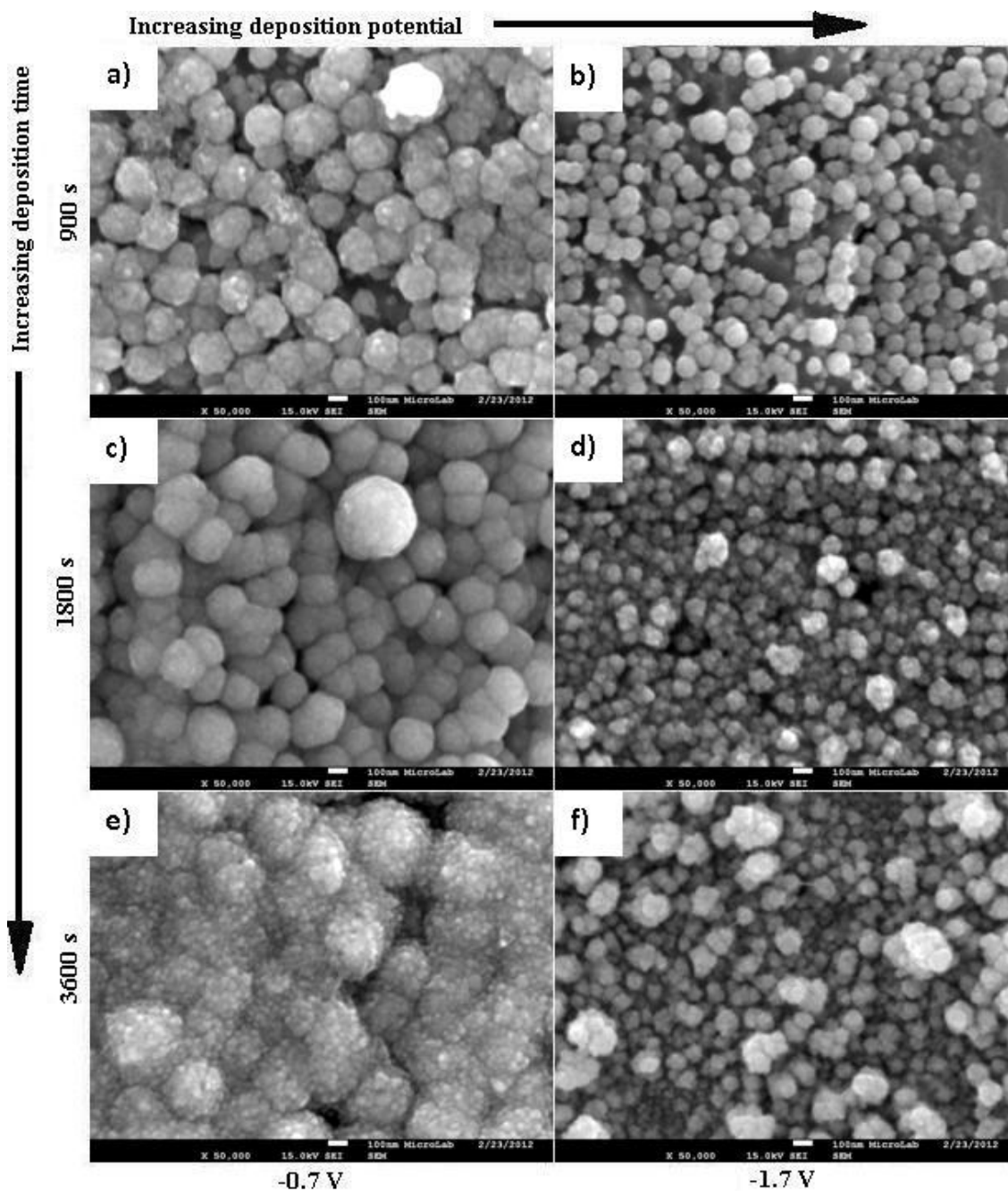


Figure 6.34: SEM micrographs (high magnification) of films electrodeposited from 0.05 M CuTFSI<sub>2</sub> solution at 50 °C. Deposition potentials: -0.7 and -1.7 V. Deposition times: 900, 1800 and 3600 s.

The microstructure of the films deposited at 85 °C is shown in Figures 6.35 and 6.36. The morphology of the films was different from those deposited at 35 and 50 °C, as the particle clusters were not compact, rather, they congregated irregularly across the film surface (Figure 6.36). This increased the roughness of the film. The film morphology was different because a copper-silver alloy film was deposited as detected by EDX analysis, instead of a pure copper film obtained at lower temperatures. This probably occurred as the increase in temperature provided a high enough thermal energy for the silver ions from the electrode to dissolve into the electrolyte solution. On the other hand, the films deposited at -0.7 V for 900 and 1800 s were very similar, consisting of small aggregates of particles growing outwards from the film surface (Figures 6.36 **a** and **c**). The particle size was around 100 nm and the cluster size was around 200-300 nm. The clusters were more globular in shape as the deposition was increased to 3600 s and their average size increased to around 400 nm, with some of them growing up to 1  $\mu\text{m}$  (Figures 6.30 **e** and 5.36 **e**). Increasing the potential to -1.7 V, led to a decrease of the particle size to less than 50 nm (Figure 6.36 **b**), while increasing the deposition time to 1800 and 3600 s increased the particle and cluster sizes and the roughness of the film (Figures 6.36 **d** and **f**).



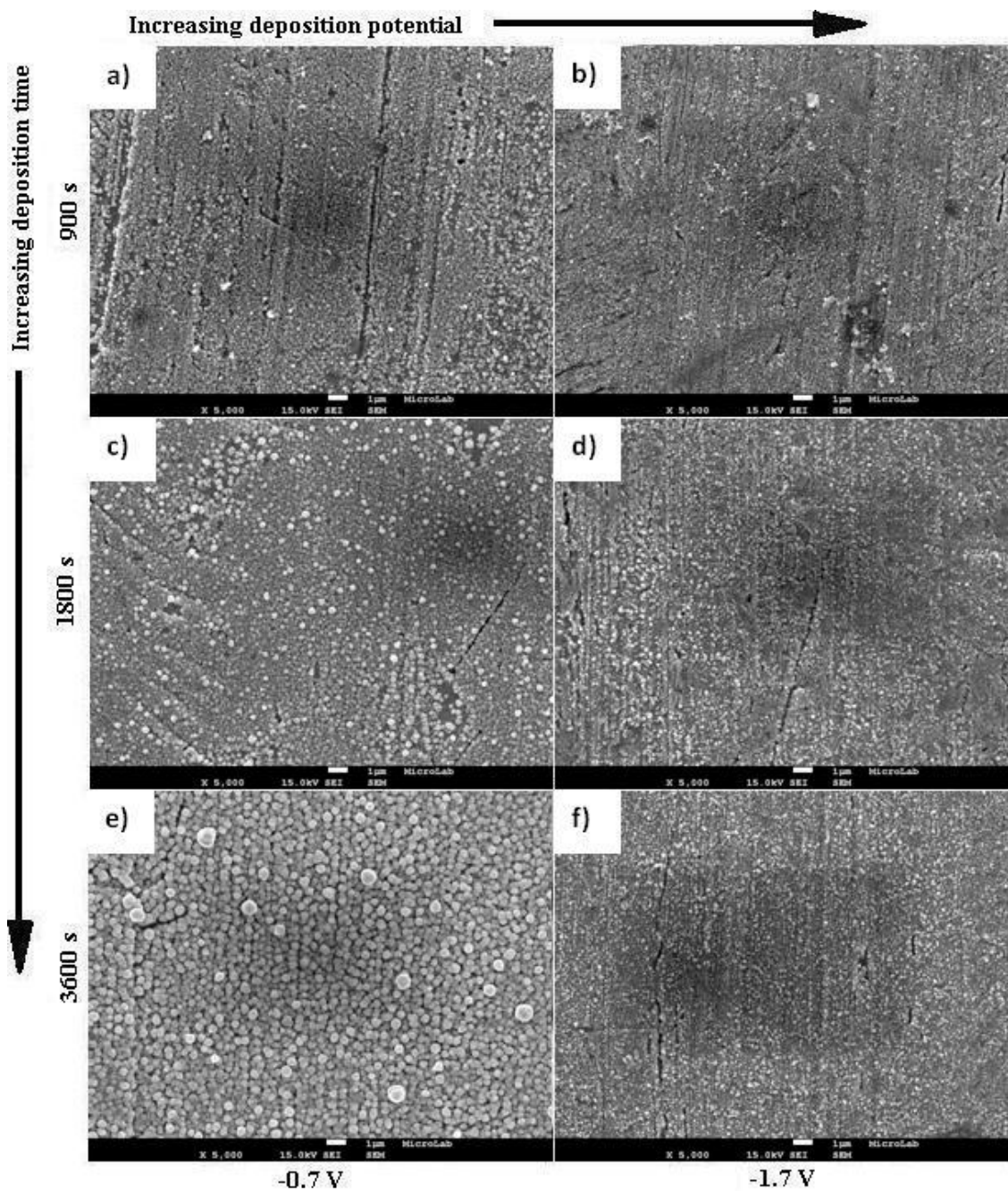


Figure 6.35: SEM micrographs (low magnification) of films electrodeposited from 0.05 M  $\text{CuTFSI}_2$  solution at 85 °C. Deposition potentials: -0.7 and -1.7 V. Deposition times: 900, 1800 and 3600 s.



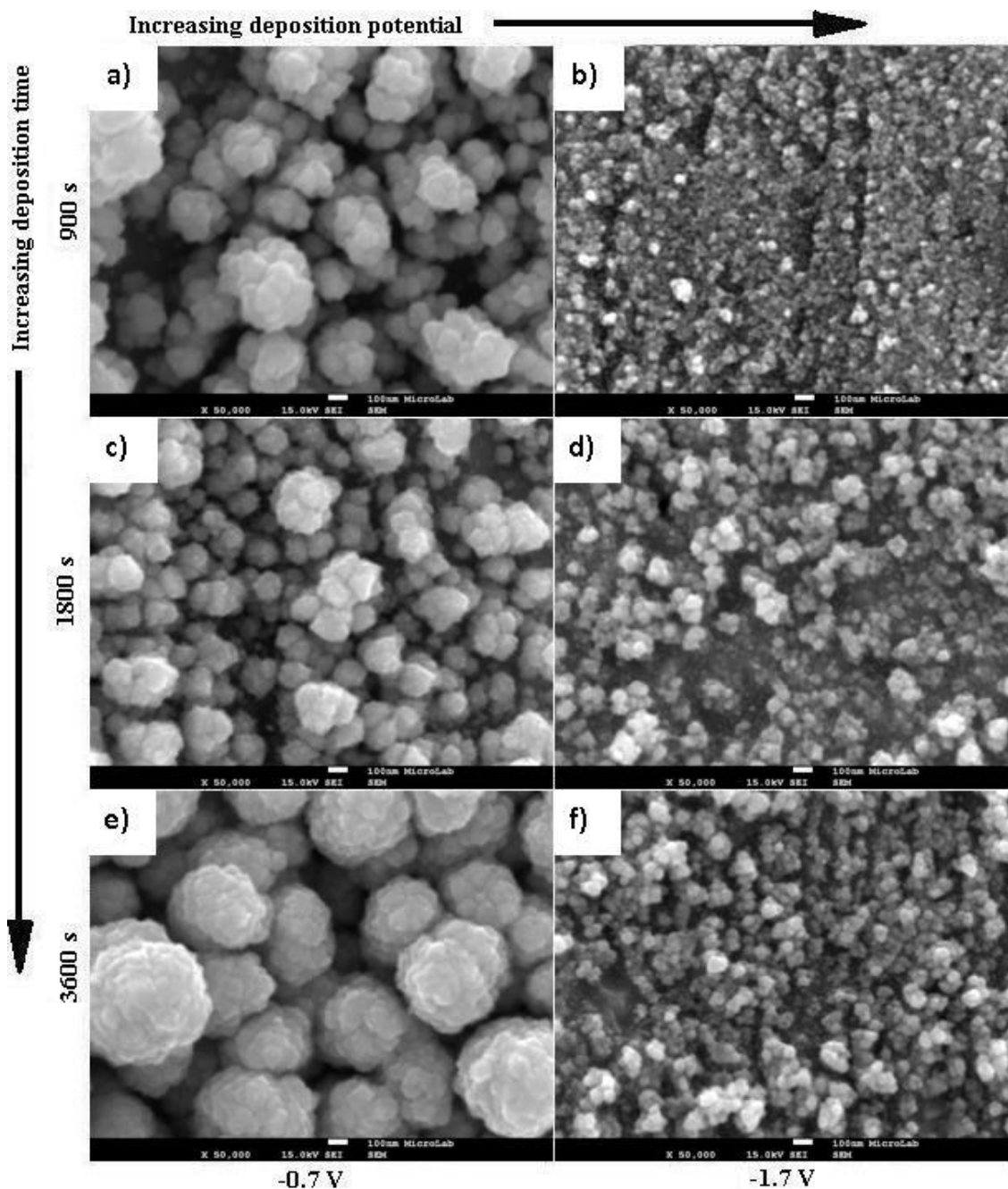


Figure 6.36: SEM micrographs (high magnification) of films electrodeposited from 0.05 M  $\text{CuTFSI}_2$  solution at 85 °C. Deposition potentials: -0.7 and -1.7 V. Deposition times: 900, 1800 and 3600 s.

## 6.4 Chemical analysis of the films

The films were analysed by EDX analysis in the TEM and SEM. The films deposited from 0.05 M AgTFSI solution consisted essentially of silver with a trace amount of oxygen, as shown, for example in Figure 6.37. Nickel was also detected because the substrate was nickel. The chemical composition of the films was found to be independent of the electrodeposition parameters used.

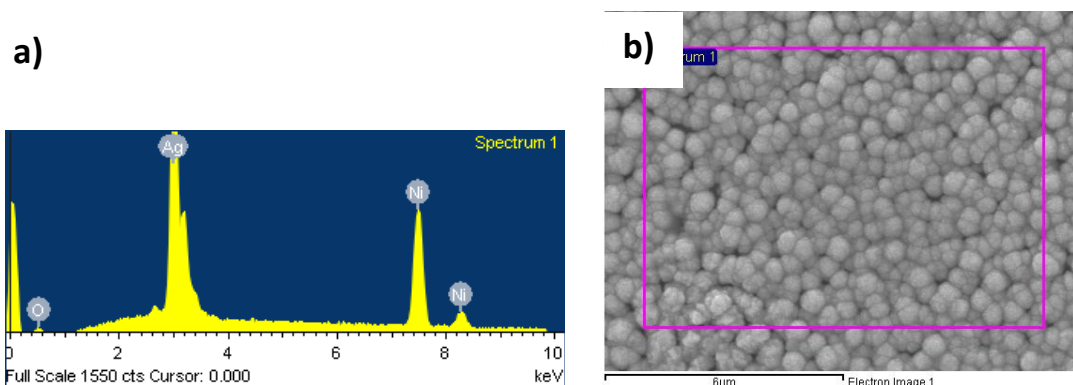


Figure 6.37: **a)** EDX analysis of silver film deposited from 0.05 M AgTFSI solution at 50 °C, -0.4 V and 3600 s. **b)** SEM image of the site where the spectrum was collected.

The films deposited from 0.05 M CuTFSI<sub>2</sub> solutions consisted essentially of copper when the deposition temperature was 50 °C or below, shown by the spectrum detected in Figure 6.38 whereas the films deposited at 85 °C were found to contain silver, as shown in Figure 6.39.

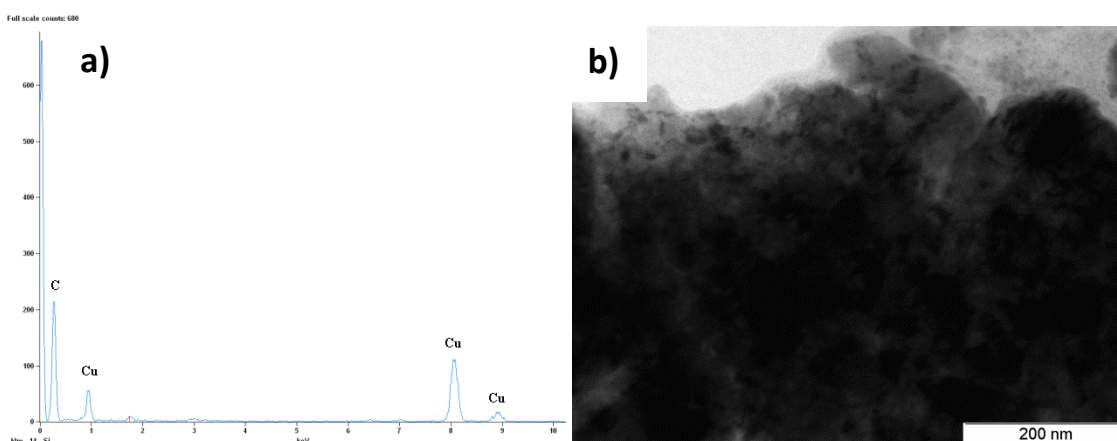


Figure 6.38: **a)** EDX analysis of a copper film deposited from 0.05 M CuTFSI<sub>2</sub> solution at 35 °C, -0.7 V for 3600 s. **b)** TEM image of the site where the spectrum was collected.

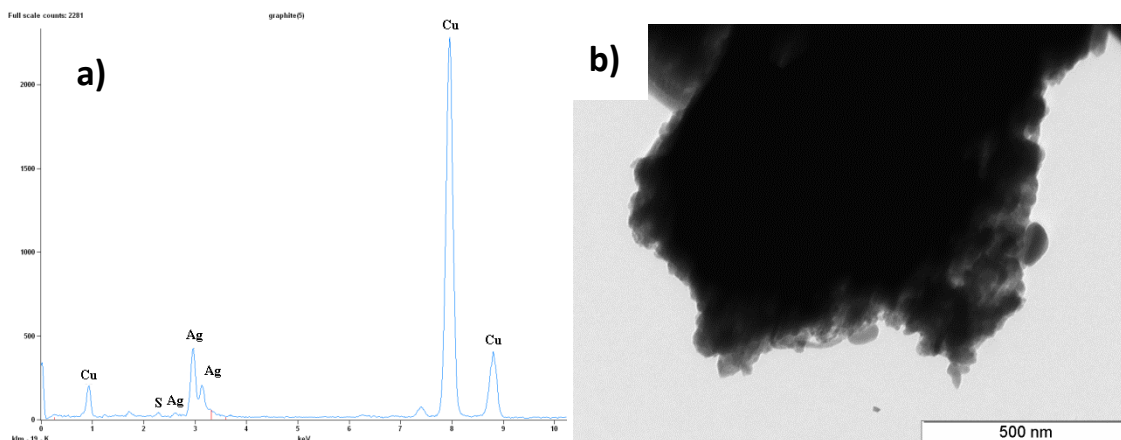


Figure 6.39: **a)** EDX analysis of a copper-silver film deposited from 0.05 M CuTFSI<sub>2</sub> solution at 85 °C, -0.7 V for 3600 s. **b)** TEM image of the site where the spectrum was collected.

TEM analysis was also performed on films deposited from 0.05 M AgTFSI and CuTFSI<sub>2</sub> solutions. The TEM images for the silver films are shown in Figure 6.40. The films consisted of silver particles of two different size ranges (Figure 6.41 a). The larger particle type had an ellipsoidal shape and an average size diameter between 50-60 nm. They corresponded to the particles observed at the surface of the films as seen in the SEM images. The smaller particle type had a much smaller diameter of below 20 nm, and they formed the bulk of the film. The electron diffraction pattern of the films deposited at -0.2 V and 50 °C for 900 s as well as at -0.4 V and 85 °C for 3600 s (Figures 6.40 b and 6.41 b respectively) showed several diffuse rings, compatible with the extremely small particle size. The width of these diffusion rings were typically observed for randomly-oriented nano-polycrystalline material [228]. The rings could be indexed as silver (111), (200), (220) and (311) diffraction.

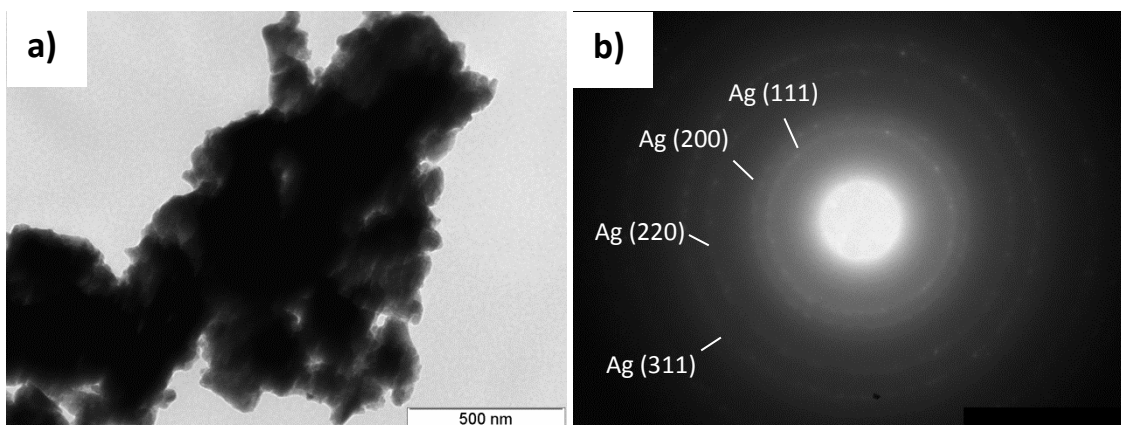


Figure 6.40: TEM micrographs of films electrodeposited from 0.05 M AgTFSI solution at **a)** -0.2 V for 900 s at 50 °C with **b)** the corresponding selected area diffraction pattern.

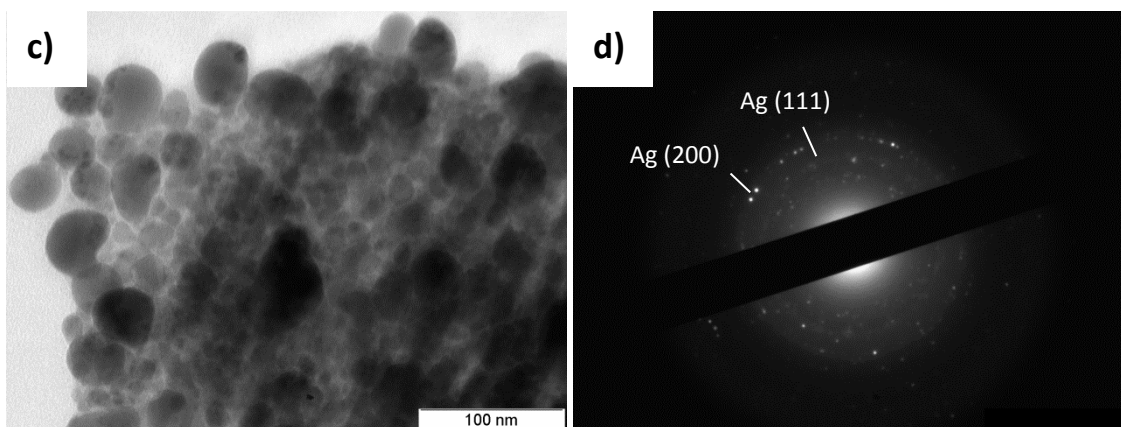


Figure 6.41: TEM micrographs of films electrodeposited from 0.05 M AgTFSI solution **a)** at -0.4 V for 3600 s at 85 °C **b)** the corresponding selected area diffraction pattern.

The TEM images of the copper films are shown in Figure 6.42. In the films deposited at 35 °C, the copper particles had diameters below 20 nm (Figure 6.42 **a**). The electron diffraction pattern of these films (Figure 6.42 **b**) showed several rings, which corresponded to copper (111), (200), (220) and (311) diffractions as well as diffraction from copper oxide. In the films deposited at 85 °C, larger particles with diameter about 50 nm were also observed (Figure 6.43 **a**). We believe that these were silver particles.

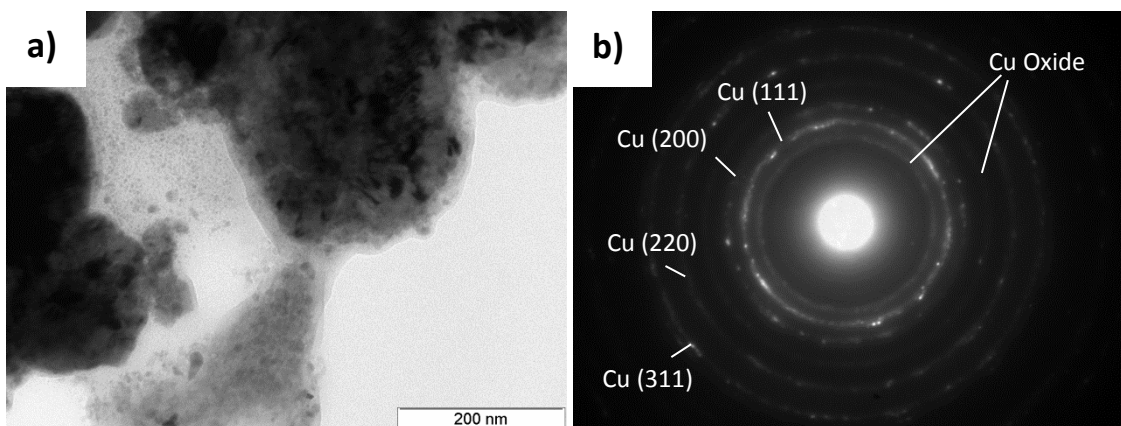


Figure 6.42: **a)** TEM micrographs of films electrodeposited from 0.05 M CuTFSI<sub>2</sub> solution at -0.7 V for 3600 s at 35 °C and **b)** the selected diffraction patterns.

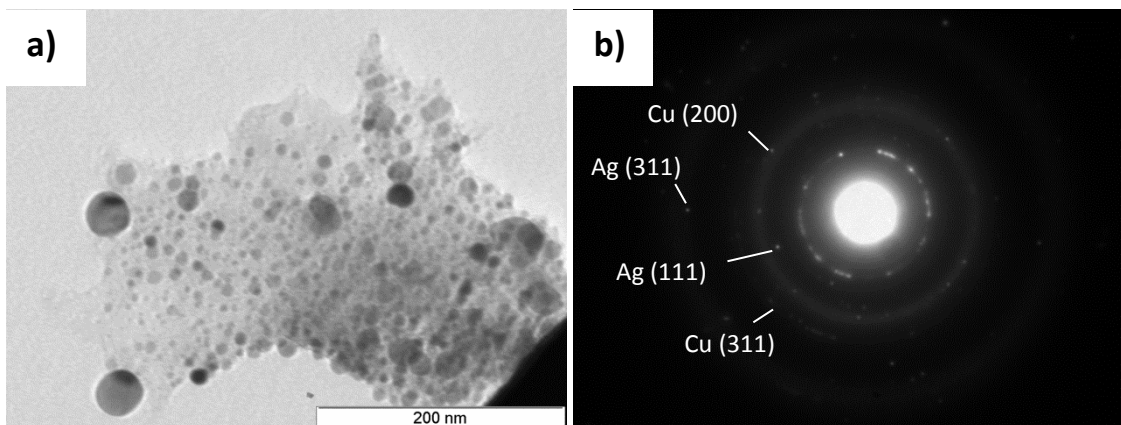


Figure 6.43: **a)** TEM micrographs of films electrodeposited from 0.05 M CuTFSI<sub>2</sub> solution at -0.7 V for 3600 s at 85 °C and **b)** the selected diffraction patterns.

## 6.5 Mechanical properties of the films

The hardness and reduced Young's Modulus ( $E_r$ ) of the deposited films were measured by nano-indentation. The nickel substrate was tested first, yielding the hardness and reduced Young's modulus values of  $2.46 \pm 0.22$  GPa and  $201 \pm 14$  GPa, respectively. The load-displacement curves for the silver films are shown in Figure 6.44. The silver films deposited at 35 °C had a hardness of  $2.0 \pm 0.40$  GPa and a Young's modulus of  $176 \pm 23$  GPa, while for the films deposited at 50 °C, the hardness and reduced Young's Modulus were  $1.8 \pm 0.32$  GPa and  $178 \pm 24$  GPa. The lower hardness value could be explained by the larger particle size. The Young's moduli of both films were similar, within the limits of the experimental error. This was expected, since it is an intrinsic property that is independent of the structure.

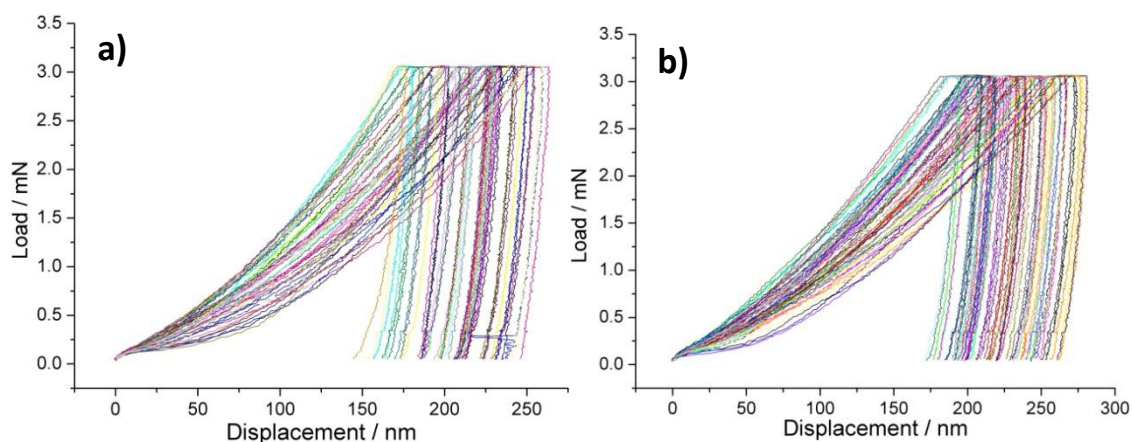


Figure 6.44: The load-displacement curves for nano-indentation tests carried out on silver films deposited at **a)** 35 °C, -0.2 V for 1800 s and **b)** 50 °C, -0.2 V for 900 s.



## 6.6 Summary

Electrochemical characterisation and electrodeposition were carried out on 0.05 M AgTFSI, 0.05M CuTFSI<sub>2</sub> and 0.50 M AlTFSI<sub>3</sub> solutions in [EMIM] [TFSI]. The main findings are as follows:

- The reduction of silver from the AgTFSI solution was a quasi-reversible process on both the GC and Pt working electrode. The activation energy for this reduction was 25 kJ mol<sup>-1</sup>. An overpotential was required to initiate nucleation and growth on GC electrode.
- The reduction of copper from the CuTFSI<sub>2</sub> solution occurred in a two-step one-electron transfer process, from Cu(II) to Cu(I) and Cu(I) to Cu(0). The Cu(II) to Cu(I) reaction was quasi-reversible, with an activation energy of 12 kJ mol<sup>-1</sup>.
- The reduction of aluminium from the AlTFSI<sub>3</sub> solution occurred in a one-step process, leading to the deposition of aluminium. This reduction was an irreversible process. The solution was electrochemically unstable at 85 °C.
- The diffusion coefficients of silver and copper species in [EMIM] [TFSI] increased with temperature, as expected, and their values were quite similar and typical of ionic liquid electrolyte with similar viscosity. However, the diffusion coefficient of the aluminium species in [EMIM] [TFSI] was six orders of magnitude lower than those of silver and copper.
- Dense nano-crystalline silver and copper films were easily obtained from AgTFSI and CuTFSI<sub>2</sub> solutions in [EMIM] [TFSI]. However, no aluminium film was deposited from AlTFSI<sub>3</sub> solution. This result was consistent with the very low diffusion coefficient of aluminium species when compared with silver and copper.
- The continuity of the silver films improved as the deposition potential, time and temperature increased. However, the films obtained at 85 °C were very rough, with large particles growing outwards from the film surface. The roughness was reduced with the increase of deposition time. The best films were obtained at 35 and 50 °C, and at -0.4 V. The silver films hardness was 2.0 ± 0.40 GPa and their reduced Young's modulus was 176 ± 23 GPa.
- The morphology of the copper films deposited at 35 °C was independent of the deposition potential and time. The particle size only increased slightly with increasing deposition time and decreasing potential. EDX analysis showed that pure copper films were obtained at 35 and 50 °C, but at 85 °C, the films were contaminated with silver, most likely from the silver wire used as the reference electrode.
- The silver and copper particles were very small, ranging from 10 to 50 nm. The silver particles were slightly larger than those of copper.



## 7 Discussion

### 7.1 Suitability of the electrodeposition solvents

In this study we investigated the electrodeposition of pure metals from salt solutions in two different ionic liquids: [EMIM] [TFSI] and [EMIM] [EtSO<sub>4</sub>]. In this section, we will discuss the suitability of these ionic liquids as solvent of the electrolyte used in electrodeposition, by analysing the electrochemical and deposition results.

#### 7.1.1 Electrochemical window

As expected, both ionic liquids have large electrochemical windows, which allow them to be used for the electrodeposition of a wide range of metals and alloys. [EMIM] [EtSO<sub>4</sub>] has an electrochemical window of 4.0 V when a GC working electrode and a platinum reference electrode are used, while [EMIM] [TFSI] has a slightly larger value of 4.6 V when a GC working electrode and a silver reference electrode are used. These electrochemical windows are much larger than that of water (~1.2 V) and they are in agreement with the values reported in the literature for other ionic liquids [47,50].

#### 7.1.2 Solubility of the metal salts

In electrodeposition, a high concentration of the metal salts is usually required to provide a sufficient current density during the electrodeposition process to yield uniform and continuous films. The solubility of a salt in a solvent depends on the ability of the solvent molecules to separate the cations and anions in the salt. In general, the solubility of metallic salts in ionic liquids is much lower than the solubility of similar salts in water [10]. The solvation ability of the ions of the ionic liquids is too weak to break the electrostatic bonds between the metal cations and the anions in the salt. This is an unintended consequence arising from the design of ionic liquids, whereby the cations and anions of the ionic liquids are large and weakly coordinating to one another, in order to keep their melting point low (at around room temperature). While metal salts with low solubility in ionic liquids appears to be the norm, metal salts with high solubility have also been reported in the literature. In some studies, concentrations of up to 1.6 and 2.5 M were achieved for AlCl<sub>3</sub> in [BMPyr] [TFSI] and [EMIM] [TFSI] respectively, although both solutions split into two different liquid phases [173,171]. Similarly, the solubility of CuCl and CuCl<sub>2</sub> in [EMIM] [DCA] have been reported to be 1.1M and 0.9M respectively [242]. This is due to the more symmetric nature of the [DCA] anion, as this characteristic would allow a better coordination between this anion and copper cations, compared to other less symmetrical anions.

In this study, we have found that the solubility of the metallic salts is dependent on three factors, namely, the metallic cation, the oxidation states of the metal and the anions present in solution. The difference in solubility of salts containing different metallic cations in the same ionic liquids



can be observed from our Ag(TFSI), Cu(TFSI)<sub>2</sub> and Al(TFSI)<sub>3</sub> solutions in [EMIM] [TFSI]. The solubility of Cu(TFSI)<sub>2</sub> in [EMIM] [TFSI] was lower than the solubility of the other two salts and visible precipitates were observed when the concentration of Cu(TFSI)<sub>2</sub> was 0.05 mole fraction. On the contrary, the solubility of Ag(TFSI) and Al(TFSI)<sub>3</sub> in the same ionic liquid was much higher. A colourless solution was obtained when up to 0.20 mole fraction of Ag(TFSI) was dissolved in [EMIM] [TFSI]. Similarly, an extremely viscous colourless solution containing 1.6 M AlTFSI<sub>3</sub> in [EMIM] [TFSI] could be prepared, consistent with the high solubility of aluminium in ionic liquids reported in the literature [173,171]. The effects of the oxidation states of the metal and the difference in anions present in solution on the salt solubility can be seen from the CuCl, CuCl<sub>2</sub> and CuSO<sub>4</sub> solutions in [EMIM] [EtSO<sub>4</sub>]. The solubility of CuCl<sub>2</sub> in [EMIM] [EtSO<sub>4</sub>] is found to be high (up to 0.20 mole fraction of CuCl<sub>2</sub>). The solubility is lower when the oxidation state of copper is Cu(I) instead of Cu(II), as can be seen from the lower solubility of CuCl in [EMIM] [EtSO<sub>4</sub>] (less than 0.1 M). Given the same oxidation state, it is found that the solubility is lower when the anion of the salt is the sulphate instead of the chloride anion, as seen from the low solubility of CuSO<sub>4</sub> in [EMIM] [EtSO<sub>4</sub>] (less than 0.1 M).

Since the salts used in the [EMIM] [TFSI] electrolytes have the same anions as the ionic liquid, we can evaluate the effect of having a common anion on the solubility. This phenomenon has been investigated by Chiappe et al. [246] and they found that the presence of a common ion led to a higher solubility of the metal salts in the ionic liquids. This conclusion was confirmed in our study, with the slight exception of the CuTFSI<sub>2</sub> solution. The reason for this phenomenon is that the metal complexes with a single type of ligand have higher energy of formations and they are more stable than metal complexes with several types of ligands, which are formed when different anions exist in solution [247]. Besides that, typical anions in an ionic liquid (such as the TFSI-) are large and they contain electron withdrawing groups, which inevitably lower the overall electronegativity of the anion. Hence a metal salt composed of these anions will have weaker ionic interactions and lower coordination as compared to a typical inorganic salt (for example, CuCl). As a result, the solvation energy required to separate the ions in the salt is much lower. In aqueous solutions, the solubility of a salt will usually decrease if a common ion is already present, as the system will oppose the dissolution of excess ions, in line with Le Chatelier's principle. However, this behaviour has not been observed in ionic liquids [246], possibly because of the differences between a solvent containing mainly neutral molecules like water and a solvent containing only ions. Besides that, transition metals can also form complexes that are soluble in ionic liquids.

In all cases, the dissolution of the salt is accompanied by the formation of different metal complexes in solution, governed by the coordination of the anions of both the ionic liquid and the salt around the metallic cations. The formation of these complexes affects the kinetics and thermodynamics of the dissolution [247]. The copper salt solutions in [EMIM] [EtSO<sub>4</sub>] contain multi-type ligand complexes involving the copper cation with EtSO<sub>4</sub><sup>-</sup> and either Cl<sup>-</sup> or SO<sub>4</sub><sup>-</sup> anions, while the silver, copper and aluminium salt solutions in [EMIM] [TFSI] only contain mono-type

ligand complexes involving the metal cations with TFSI<sup>-</sup>. A more detailed discussion of these complexes will be presented in Section 7.2.

### 7.1.3 Mobility of the ionic species

The conductivity of the electrolyte depends on two factors. Aside from the concentration of the metal cations in solution, another factor that affects the conductivity of the electrolyte is the mobility of the charge carriers in solution. In an ionic liquid, the mobility is controlled by the diffusion of the metal cations, usually in the form of metal complexes. The ionic conductivity in an ionic liquid is related to the diffusion coefficient, given by the Nernst-Einstein equation:

$$\sigma = \frac{Dnq^2F^2}{RT} \quad \text{Eq. 7.1}$$

$\sigma$  is the ionic conductivity,  $D$  is the diffusion coefficient of the metal cations,  $n$  is the number of charge carrier per mole,  $q$  is the electric charge,  $F$  is the Faraday constant,  $R$  is the ideal gas constant and  $T$  is the absolute temperature.

The mobility of the metal complexes in ionic liquids is generally quite low, due to the high viscosities of ionic liquids as compared to aqueous solutions. The high viscosities are due to the strong ionic interactions between cations and anions in the ionic liquids, whereas the low viscosities in aqueous solution are due to the much weaker hydrogen bonding and Van Der Waals bonding. Since these ionic interactions are thermally activated, the viscosity of an ionic liquid behaves in accordance with the Arrhenius equation (Equation 2.29). At higher temperatures, the viscosity will decrease exponentially with temperature. As a consequence, the diffusion of metallic species in solution will increase with temperature, as observed from the results of this study.

Comparing the diffusion coefficients for the copper species in both [EMIM] [TFSI] and [EMIM] [EtSO<sub>4</sub>] obtained in this study, we can see that the diffusion coefficient values at 35 °C for [EMIM] [TFSI] ( $2.7 \times 10^{-7} \text{ cm}^2 \text{ s}^{-1}$ ) is much larger than those for [EMIM] [EtSO<sub>4</sub>] (Table 5.2). This is expected because the viscosity at around room temperature for [EMIM] [TFSI] (34 cP, [50]) is lower than [EMIM] [EtSO<sub>4</sub>] (78 cP, [62]). Our diffusion coefficient values are one order of magnitude smaller than the Cu(II) solutions in [EMIM] [DCA] ( $2.06 \times 10^{-6} \text{ cm}^2 \text{ s}^{-1}$ , [242]) because this liquid has a viscosity of 21 cP, which is slightly larger than those of Cu(II) solutions in [EMIM]-Cl-[BF<sub>4</sub>] ( $1.5 \times 10^{-7} \text{ cm}^2 \text{ s}^{-1}$ , [240]), which has a viscosity of 43 cP [47]. A similar trend has also been found for the silver species in [EMIM] [TFSI], where the diffusion coefficient obtained in this study at 35 °C ( $1.9 \times 10^{-7} \text{ cm}^2 \text{ s}^{-1}$ ) is similar to those found at 25 °C for Ag(I) salt solutions in [BMIM] [BF<sub>4</sub>] ( $4.2 \times 10^{-7}$  and  $9.9 \times 10^{-7} \text{ cm}^2 \text{ s}^{-1}$ , [106]) and [EMIM] [BF<sub>4</sub>] ( $6.0 \times 10^{-7} \text{ cm}^2 \text{ s}^{-1}$ , [66]), but one order of magnitude larger than those found for [BMIM] [PF<sub>6</sub>] ( $1 \times 10^{-8}$  and  $3 \times 10^{-8} \text{ cm}^2 \text{ s}^{-1}$ , [106]). As expected, these differences diffusion coefficient values are explained by the differences in viscosity of the ionic liquids; [EMIM] [BF<sub>4</sub>] (43 cP [47]) has a similar value to [EMIM] [TFSI], whereas [BMIM] [PF<sub>6</sub>] has a larger value (450 cP, [58]).

For the different cations in solution containing the same ionic liquid, the diffusion coefficients may reflect the different sizes of the metal complexes that exist in solution. This can be seen from the Stokes-Einstein equation (Equation 2.5), which describes the motion of a spherical particle through a solution at low Reynolds number. According to the Stoke-Einstein equation, the diffusion coefficient is inversely proportional to the particle size. By comparing the diffusion coefficient values of the different copper species in [EMIM] [EtSO<sub>4</sub>] (shown in Table 5.2), we can predict that the copper complexes in the CuCl solution will have the smallest size, followed, in ascending order, by the complexes in the CuCl<sub>2</sub> solution and lastly the complexes in the CuSO<sub>4</sub> solution. This prediction is also supported by the values obtained for the activation energy for reduction of all three solutions. A similar comparison can be made for the silver, copper and aluminium species in [EMIM] [TFSI]. In this study, the diffusion coefficient of the silver, copper and aluminium species at 35 °C are  $6.6 \times 10^{-8}$ ,  $2.7 \times 10^{-7}$  and  $1.2 \times 10^{-12} \text{ cm}^2 \text{ s}^{-1}$ , respectively. This means that the complexes for copper will have the smallest size, followed by the complexes involving silver and finally aluminium. The diffusion coefficient of the aluminium species in this study might be less accurate since the reduction mechanism of aluminium does not follow the one-electron transfer step reaction seen in both copper and silver and no deposition of aluminium was obtained. The strong bonds in the aluminium complex also increase the activation energy for aluminium reduction, hindering the charge transfer reaction.

#### 7.1.4 Stability of the solution

An important requirement for an electrodeposition solvent is that the electrochemical properties of the electrolytes must be consistent and reproducible. We have discussed the electrochemical properties of solutions in [EMIM] [EtSO<sub>4</sub>] and [EMIM] [TFSI] in Chapters 5 and 6, and the comparison of all the different results are discussed in this section.

The cyclic voltammograms of the AgTFSI solution in [EMIM] [TFSI] (Figures 6.2 and 6.3) presented an oxidation peak corresponding to  $\text{Ag}(0) \rightarrow \text{Ag}(\text{I})$  and a reduction peak corresponding to  $\text{Ag}(\text{I}) \rightarrow \text{Ag}(0)$ , in agreement with the literature [124,106,142,128,121,245,136]. These peaks were reproducible over a large number of cycles, showing that this solution is electrochemically stable.

Similarly, we expected the cyclic voltammograms of the copper solutions in both the [EMIM] [EtSO<sub>4</sub>] and [EMIM] [TFSI] electrolytes to present two oxidation peaks corresponding to  $\text{Cu}(0) \rightarrow \text{Cu}(\text{I})$  and  $\text{Cu}(\text{I}) \rightarrow \text{Cu}(\text{II})$  and two reduction peaks corresponding to the inverse reactions, which are typically observed for copper solutions in ionic liquids [240,248,241,242]. This is confirmed, in our case for [EMIM] [TFSI]-based electrolytes, although several additional peaks were observed for the [EMIM] [EtSO<sub>4</sub>]-based electrolytes (Figures 5.2 to 5.6). We believe that several factors contributed to the appearance of these peaks. Firstly, the copper salts that were used in this study were initially hydrous. Although the salts were heated in an oven at 120 °C for several days, some water may still be present in the salts. Hence, some of these peaks may also be due to the water left over as impurities. Secondly, some of the peaks may correspond to the products formed from the partial breakdown of the ionic liquid. As seen in the cyclic

voltammogram in Figure 5.1, the oxidation of the [EMIM] products occurs at around -0.5 V, which we believe corresponds to the A4 peak in Figures 5.3 to 5.6. This may be an indication that the addition of the solutes decreases the electrochemical window of [EMIM] [EtSO<sub>4</sub>], potentially making it less suitable as electrodeposition solvents, compared to other available ionic liquids. Thirdly, we believe that many of the additional peaks observed for the CuCl solution in [EMIM] [EtSO<sub>4</sub>] are probably due to the existence of two different sets of copper complexes in solution. Cu(I) is not stable in the ionic liquid solution and it will transform into Cu(II) [240,241]. As a consequence, the CuCl solution will contain variable amounts of Cu(II) cations. One set of oxidation and reduction peaks corresponds to the complexes formed from CuCl while the other set corresponds to the complexes formed from CuCl<sub>2</sub>. The relevant cyclic voltammogram is shown in Figure 5.3 on page 89:

In Figure 5.3, C1 and C3 are the reduction of Cu(II) to Cu(I); C2 and C4 are the reduction of Cu(I) to Cu(0); A2 is the oxidation of Cu(0) to Cu(I); and A1 and A3 are the oxidation of Cu(I) to Cu(II). We speculate that C3, C2, A2 and A1 correspond to the oxidation and reduction peaks of the complexes formed from CuCl, while C1, C4 and A3 correspond to those of CuCl<sub>2</sub>. The justifications for these assignments are discussed here. As seen in Table 5.1, the activation energy for the Cu(II) + e<sup>-</sup> → Cu(I) reduction from the CuCl solution (19.5 kJmol<sup>-1</sup>) is similar to the values calculated for the CuCl<sub>2</sub> solution (21.5 kJmol<sup>-1</sup>). This suggests that they correspond to the same reactions, namely those involving the complexes formed from CuCl<sub>2</sub>. This is further supported by the similarity in the diffusion coefficients of the active species, which indicates that the complexes are likely to be the same, since the sizes are similar according to Stokes-Einstein equation. Besides that, the potential of the C4 peak is similar to the potential for the reduction of Cu(I) to Cu(0) in the CuCl<sub>2</sub> solution and is most likely due to the complexes formed from CuCl<sub>2</sub>. The A1 peak is only present in the voltammogram when the C3 peak is present. Hence by a process of elimination, the A3 oxidation peak corresponds to the C1 reduction peak, and it is associated with the complexes formed from CuCl<sub>2</sub>. Vainikka et al. [249] found a similar behaviour for both the copper(I) chloride and copper(II) chloride solutions in [BMPyr] [TFSI], and they also concluded that the appearance of two sets of reduction peaks was due to the presence of two different copper complexes in solution.

After discussing the electrochemical behaviour of silver and copper in ionic liquid electrolytes, it is natural to assume that aluminium would present three oxidation peaks and three reduction peaks corresponding to the oxidation and reduction of the three oxidation states of aluminium. However, this behaviour has not been reported in the literature for aluminium salts in both the first- and second-generation ionic liquids. Only one oxidation and one reduction peaks were observed in the deposition of aluminium from solutions containing AlCl<sub>3</sub> salts [197,250,77-79,173,171,172]. Hence, the reduction peak was assigned to the bulk deposition of aluminium and the oxidation peak corresponds to the partial stripping of aluminium [171]. In our AlTFSI<sub>3</sub> solutions in [EMIM] [TFSI], we found similar results when using a glassy carbon and platinum working electrode (Figures 6.21 and 6.22). However, the voltammogram observed with the platinum working electrode was unstable as the potential of the reduction peak shifted to more positive values with each consecutive cycles, eventually settling at -0.25 V. This shift was observed when

tested with both the silver and platinum reference electrodes. This suggests that deposition of aluminium is easier with each consecutive cycle, but no aluminium deposits were found on the substrate. We also found that the solutions changed from colourless to a light brownish colour, slightly lighter than those in Figure 6.23 **b**. This suggests that the reduction of aluminium may have occurred, but instead of depositing aluminium on the substrate, the aluminium may have formed new complexes in solution.

The changes in the voltammograms at different temperatures were also investigated for both the [EMIM] [EtSO<sub>4</sub>] and [EMIM] [TFSI] electrolytes. We found that the current density in both solutions increased as expected due to the decrease in the viscosity of the solutions with temperature. This led to an increase in the mobility of the charge carriers in the solutions, as confirmed by the values of diffusion coefficient in Tables 5.3, 6.1 and 6.2. The electrochemical properties for the AgTFSI and CuTFSI<sub>2</sub> solutions in [EMIM] [TFSI] were stable when tested up to a temperature of 85 °C. This was confirmed by the fact that the cyclic voltammograms presented a similar evolution with temperature in Figures 6.4 and 6.14 and that the colour for both solutions did not change. However, the AlTFSI<sub>3</sub> solutions became unstable at 50 °C when using a Pt working electrode and at 85 °C when using a GC working electrode. This was demonstrated by the evolution of the voltammograms with temperature (Figure 6.23 **a**), where the current density of the reduction peak when using a GC electrode at 85 °C was much lower than that at 50 °C. This shows that the solution suffered some degradation during the reduction of aluminium. The solution was also unstable when using a Pt electrode. Its colour changed from colourless to dark brown and very fine dark precipitates were formed. In general, the copper solutions in [EMIM] [EtSO<sub>4</sub>] were electrochemically stable up to 50 °C and the evolution of the cyclic voltammograms remained unchanged (Figures 5.10 and 5.11). However at 85 °C, additional oxidation and reduction peaks appeared. This could be due to impurities such as water present from the copper salts, leading to changes in the complexes or perhaps a breakdown of the ionic liquid. The electrochemical instability of the solutions was also confirmed by their colour change. Initially, CuCl<sub>2</sub> and CuSO<sub>4</sub> solutions were dark green and green, respectively, but the colour changed to light green and greenish blue at 85 °C.

Apart from the AlTFSI<sub>3</sub> solution in [EMIM] [TFSI], the electrolyte based on [EMIM] [TFSI] seemed to provide a more consistent and reproducible electrochemical properties compared to the electrolyte based on [EMIM] [EtSO<sub>4</sub>], as shown by the consistency of their voltammograms over multiple cycles and at several different temperatures. A possible reason for this is that the purity of the salts used in the [EMIM] [EtSO<sub>4</sub>] solutions might be lower than those used for the [EMIM] [TFSI] solutions, that is, they may contain other impurities such as water. These impurities may cause the appearance of additional peaks, or interact with and destabilise the metal complexes in solution. Besides that, using salts with the same anion as the ionic liquid increases the energy of formation and stability of the metal complexes [247]. This means that the complexes in solution are more stable at higher temperatures and are less likely to transform into different complexes.

### 7.1.5 Morphology of the films

Except for  $\text{AlTFSI}_3$  solutions in [EMIM] [TFSI], metallic thin films were deposited from all other electrolytes of both [EMIM]  $[\text{EtSO}_4]$  and [EMIM] [TFSI]. We studied the changes in the film morphology with the deposition parameters (electrolyte temperature, deposition time and deposition temperature), anions present in the solutions and oxidation states of the metal cation.

We have found that for both solutions of [EMIM]  $[\text{EtSO}_4]$  and [EMIM] [TFSI], the films morphologies change with the deposition parameters in a predictable way. In general, increasing the electrolyte temperature and deposition time will increase the particle size and surface coverage of the films, while increasing the cathodic deposition potential will decrease the particle size of the films. The deposition current density increases with temperature due to the higher mobility of the charge carrying species in solution, as a result of the lower viscosity of the solution. This increase in current density increases the rate of deposition, resulting in the formation of particles with larger size and better surface coverage of the films. A longer deposition time allows more time for the film to grow, leading to a better surface coverage and yielding particles with larger size. When the cathodic potential increases, the nucleation overpotential on the system is increased. A large nucleation overpotential has the effect of reducing the energy required to form nuclei, and this allows the nucleation on less active nucleation sites. This, in turns, increases the nucleation density on the substrate, leading to smaller particle sizes, as less space is available for each individual particle to grow.

In solutions containing the same metallic cation, the film morphology can also be influenced by the oxidation state of the metal and the anions in solution, because both cases would lead to the formation of different metal complexes in solution. These complexes have different electrochemical behaviour, which affects the film morphology. An example can be seen in the case of the  $\text{CuCl}$  and  $\text{CuCl}_2$  solutions in [EMIM]  $[\text{EtSO}_4]$ , where the cyclic voltammograms of both solutions and the morphology of their deposited films are different (Figures 5.2 and 5.5). The reduction of metallic copper for the  $\text{CuCl}$  solution occurs at a less negative potential than that for the  $\text{CuCl}_2$  solution. This means that under similar deposition parameters, the  $\text{CuCl}$  solution experiences a larger nucleation overpotential than the  $\text{CuCl}_2$  solution. This implies that the nucleation density for the films deposited from the  $\text{CuCl}$  solution will be higher than that for the  $\text{CuCl}_2$  solution, which will lead to the formation of smaller particles. In our study, this is indeed the case: the films deposited from the  $\text{CuCl}_2$  solution are less continuous and they contain particles with larger size compared to those obtained from the  $\text{CuCl}$  solution. Besides influencing the electrochemical properties, the anions in solution also influence the double-layer structure near the electrolyte-electrode interface. The double-layer structure has a huge impact on film nucleation and growth, and small changes in this structure can affect the size and morphology of the particles that are formed in the film [10]. This can be seen in the films deposited from the  $\text{CuCl}_2$  and  $\text{CuSO}_4$  solutions in [EMIM]  $[\text{EtSO}_4]$ , in which the films present completely different morphologies. A more detailed study of the double-layer region is required to truly understand the

mechanism controlling the film morphology. In a latter section on the future work, we shall suggest ways of probing this double-layer structure.

A comparison of the morphologies of the copper and silver films deposited from the AgTFSI and CuTFSI<sub>2</sub> solutions in [EMIM] [TFSI] is interesting, because in this case, only one type of anion exists in solution and any differences are due to the oxidation state, the intrinsic properties of silver and copper and the interplay of these properties with the deposition parameters. Structural analyses of the copper and silver films show that they are crystalline and consist mainly of pure metal, with trace amounts of oxygen. Both copper and silver films present the face-centred cubic (FCC) crystal structure which is typical of these metals, as detected by their (111), (200), (220) and (311) planes from X-ray diffraction. The silver films consist of angular particles of about 100 nm aggregated in globular clusters. The particles can grow up to 1 µm on the films surfaces as the thickness of the films increases. On the other hand, the copper films consist of smaller spherical particles (<50 nm), also aggregated in globular clusters. No aluminium films could be deposited from the AlTFSI<sub>3</sub> solutions in [EMIM] [TFSI], and this is consistent with the extremely low diffusion coefficient values of the active species in these solutions.

The influence of the ionic liquids used as solvents on the morphologies of the films can be studied by comparing the copper films deposited from the [EMIM] [TFSI] and [EMIM] [EtSO<sub>4</sub>] electrolytes. The copper films deposited from [EMIM] [TFSI] are less sensitive to changes in the deposition parameters. We have found that the morphologies of the films were similar when the deposition temperature, time and potential were increased, with only a slight decrease in the particle size. This is not the case for the copper films deposited from [EMIM] [EtSO<sub>4</sub>]. The films deposited from the CuCl solution experienced an uneven overgrowth when the deposition time was increased, while the particles of the films deposited from the CuCl<sub>2</sub> solution increased in size and became more angular when the deposition temperature was increased. Overall, we can say that the films deposited from [EMIM] [TFSI] are of better quality than those deposited from [EMIM] [EtSO<sub>4</sub>], as they are smoother, have better coverage and their morphology can be easily controlled. Several factors may contribute to the quality of the films. Firstly, the copper salts used in the [EMIM] [EtSO<sub>4</sub>] solutions may contain more impurities than those used for the [EMIM] [TFSI] solutions. This is not surprising as the voltammograms obtained for the CuTFSI<sub>2</sub> solution in [EMIM] [TFSI] show that this solution is stable, and does not present the extra cathodic and anodic peaks seen in the copper solutions in [EMIM] [EtSO<sub>4</sub>]. Secondly, the copper complexes formed in [EMIM] [TFSI] solutions may be more stable than the complexes formed in [EMIM] [EtSO<sub>4</sub>], because in the first case there is only one type of anion in solution, whereas multiple anions exist in solution in the latter case. As discussed in Section 7.1.2, Chiappe et al. [247] found that metal complexes with only one type of ligand have a much higher energy of formation than metal complexes with mixed ligands. Hence the copper complexes in [EMIM] [TFSI] solutions may remain stable over wide ranges of deposition parameters, compared to the mixed type-ligand copper complexes in [EMIM] [EtSO<sub>4</sub>]. This may also explain why the morphology of copper films deposited from [EMIM] [TFSI] is stable over wide ranges of deposition parameters, as the reaction mechanism is the same if the copper complexes in solution remain similar. The change in the morphology of the films deposited

from the [EMIM] [EtSO<sub>4</sub>] solutions may be due to changes in their copper complexes existing in the solution with the deposition temperature, which in turns, leads to the different reaction mechanism during deposition.

#### 7.1.6 Summary

Both [EMIM] [EtSO<sub>4</sub>] and [EMIM] [TFSI] appear to be good solvents for electrodeposition. Electrolytes based on [EMIM] [TFSI] have superior properties compared to those based on [EMIM] [EtSO<sub>4</sub>], due to the larger electrochemical window, lower viscosity, higher solubility of metal salts in solution, larger diffusion coefficient, better electrochemical stability of the electrolytes and better quality of the deposited films. However, many of these properties are not purely due to the influence of the ionic liquids, as they are also influenced by the metal salts used. The metal salts used in [EMIM] [TFSI] are clearly superior to those used in [EMIM] [EtSO<sub>4</sub>]. They share the same anions with the ionic liquid, which improve the physiochemical properties of the electrolyte and stabilise the metal complexes existing in solution. In addition, they also have a higher purity. This shows that all aspects of the electrodeposition processes must be taken into account in order to design a good electrodeposition system.



## 7.2 Complex formation in the ionic liquid electrolytes

From the Raman and infrared spectroscopic work presented in Chapter 4, we were able to predict the structure of the complexes formed in the  $\text{CuCl}_2$  solutions in  $[\text{EMIM}][\text{EtSO}_4]$  and the  $\text{AgTFSI}$  solutions in  $[\text{EMIM}][\text{TFSI}]$ . However due to the high concentration of salts required to obtain observable signals in the vibrational spectra, we were not able to test the solutions in which the solubility of the salts were low. For the  $\text{AlTFSI}_3$  solutions in  $[\text{EMIM}][\text{TFSI}]$ , some information can be extracted from the studies carried out by Eiden et al. [213] and Rocher et al. [172] on the aluminium complex formation in TFSI-based ionic liquid solutions.

### 7.2.1 Effect of the complexes on the deposition mechanism

In Section 2.2.2, we described the structure of the solution and the mechanisms during an electrochemical reaction. Here we will look at the effect of the metal complexes at each stage of the deposition process.

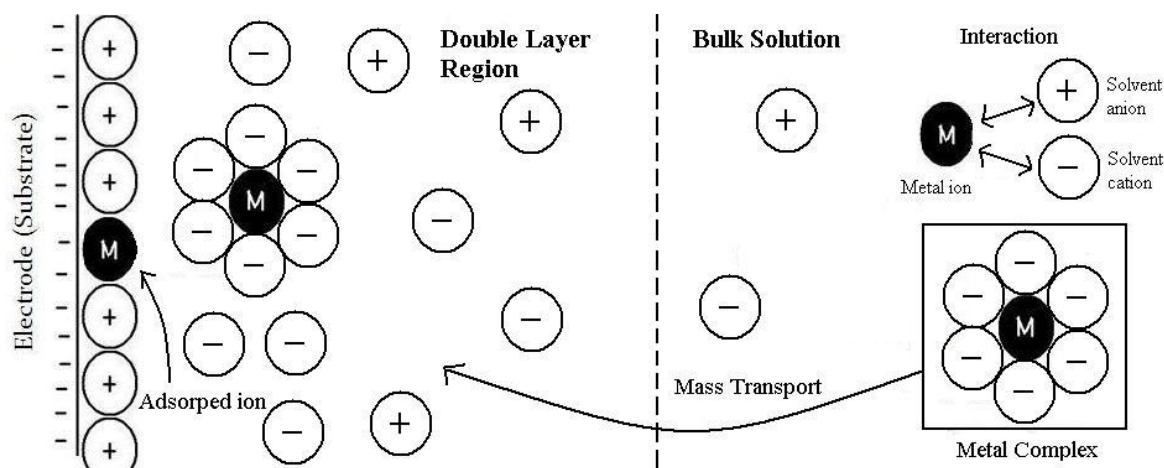


Figure 2.3 Structure of the solution in an electrochemical cell during an electrochemical reaction.

The first stage of the deposition is the diffusion of the metal species from the bulk solution to the double-layer region. As the metal species exist as a complex, the interactions between these complexes and the ions in solution have a direct effect on their transport properties. The size of the complex is inversely proportional to the diffusion coefficient, as described by the Stokes-Einstein equation (Equation 2.5). Thus, the shape and size of the complex will affect the rate of mass transport.

Before the charge transfer reaction can take place at the electrode, the metal complex must dissociate to allow for the adsorption of the metal cation on the surface of the electrode. Only after this adsorption has taken place can the reduction of the metal cation occur. Hence the total energy for the metal reduction reaction consists of three parts: The energy associated with the dissociation of the complex, the energy associated with the adsorption of the metal cation and the

energy associated with the charge transfer reaction. The energy of the charge transfer reaction is associated with the enthalpy of formation, while the energy required to dissociate the complex and the energy associated with the adsorption of the metal are mainly related to the activation energy of the reduction reaction. Hence, we are able to estimate the stability of the complexes from the activation energy of the metal reduction calculated from the cyclic voltammogram.

## 7.2.2 Structure of the metal complexes

In this study, the structure predicted for the complexes that exist in the solutions of  $\text{CuCl}_2$  in [EMIM] [EtSO<sub>4</sub>] and AgTFSI in [EMIM] [TFSI] are shown in Figure 7.1.

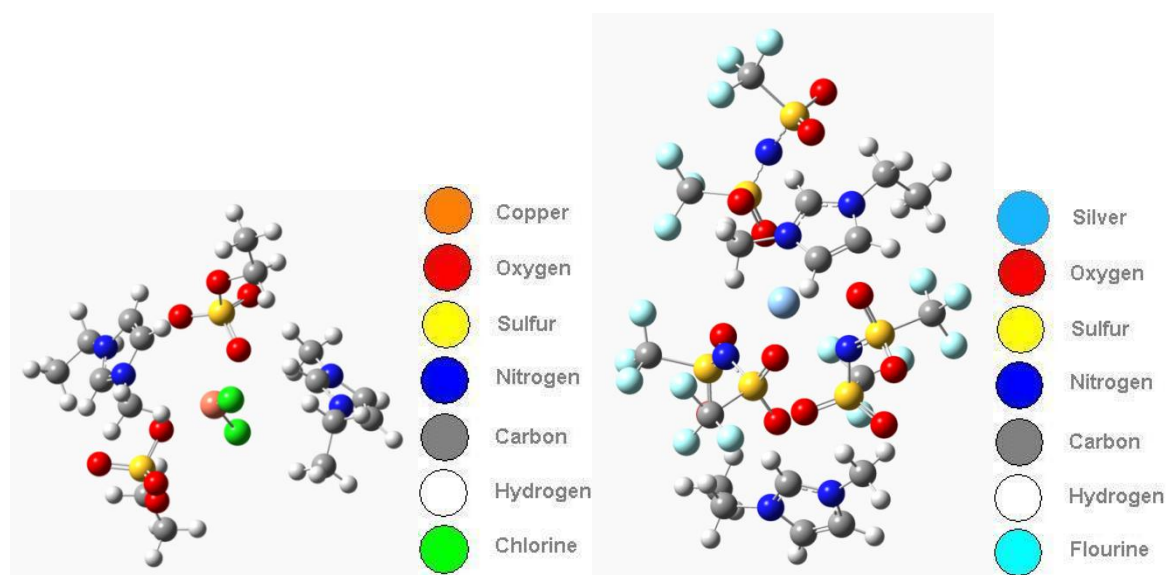


Figure 7.1: **a)** Structure of the copper complex in the  $\text{CuCl}_2$  solutions in [EMIM] [EtSO<sub>4</sub>] reproduced from Figure 4.17 and **b)** Structure of the silver complex in the AgTFSI solutions in [EMIM] [TFSI] reproduced from Figure 4.13.

For the  $\text{CuCl}_2$  solution in [EMIM] [EtSO<sub>4</sub>], the first solvation shell of the copper complex involves two chlorine anions and two EtSO<sub>4</sub><sup>-</sup> anions, located at two distinct distances (Figure 7.1 **a**). We propose that the predominant complex takes the form of  $[\text{CuCl}_2(\text{EtSO}_4)_2]^{2-}$ . Several other copper(II) complexes have also been proposed in the literature. Nanjundiah et al. [251] found that the Cu(II) complex in the first-generation [BMPyr] [Cl] [AlCl<sub>3</sub>] ionic liquid takes the form of  $[\text{CuCl}_6]^{4-}$  when the solution has excess Cl<sup>-</sup> anions. Chen et al. [240] investigated the copper(II) complex existing in a  $\text{CuCl}_2$  solution in [EMIM] [BF<sub>4</sub>] by ultraviolet-visible spectroscopy and found that the complex is  $[\text{CuCl}_4]^{2-}$ , which takes the shape of the Jahn-Teller distorted tetrahedral ( $D_{2d}$ ). Jahn-Teller theorem states that non-linear molecules in an electronic degenerate state will undergo a geometric distortion to remove this degeneracy, lowering the symmetry and the overall energy of the molecules [252]. The prediction of Chen et al. [240] of a copper complex involving only Cl<sup>-</sup> ligands

is in contrast with our results in which we predict that the copper complexes involve  $\text{Cl}^-$  and  $\text{EtSO}_4^-$  as ligands. This is slightly surprising because it means that the electronegativity of the  $\text{BF}_4^-$  anion is lower than the  $\text{EtSO}_4^-$  anion, and their electronegativity are too low to compete with the chloride anion during the complex formation. However we do not believe this to be the case, as the thermal properties of [EMIM] [EtSO<sub>4</sub>] and [EMIM] [BF<sub>4</sub>] are quite similar (Table 2.3). According to our spectroscopy results, the new vibrational bands at 997, 1045 and 1298  $\text{cm}^{-1}$  are clearly due to the interaction between the copper cation and the oxygen in the  $\text{EtSO}_4^-$ , hence the complex must involve the anions of the ionic liquid. Abbot et al. [253] found that copper(II) complexes also take the form of  $[\text{CuCl}_4]^{2-}$  in a eutectic based ionic liquid of urea–choline chloride and ethylene glycol–choline chloride. The authors found that hydrous or anhydrous  $\text{CuCl}_2$  salts led to the same complexes, in which the water molecules do not play a critical role in the first solvation shell of the complex. The large concentration of chloride (4.8 M) in their solution also explains why their complexes only contain chloride ligands instead of mixed ligands. In aqueous solutions, the copper (II) chloride complexes usually exist as  $\text{Cu}^{2+}$ ,  $[\text{CuCl}]^+$ ,  $[\text{CuCl}_2]$ ,  $[\text{CuCl}_3]^-$  and  $[\text{CuCl}_4]^{2-}$ , depending on the concentration of chloride in solution [254].

The first solvation shell of the silver complex in the AgTFSI solution in [EMIM] [TFSI] involves three TFSI<sup>-</sup> anions. The silver cation interacts with one of the O atoms of each  $\text{SO}_2$  groups (Figure 7.1 **b**). We propose that the predominant complex takes the form of  $[\text{AgTFSI}_3]^{2-}$ .

Although we were not able to study the copper complexes in the CuCl and  $\text{CuSO}_4$  solutions in [EMIM] [EtSO<sub>4</sub>] by vibrational spectroscopy, it is possible to narrow down the possible complexes by considering our electrochemical results and results of other relevant studies reported in the literature. We know that the diffusion coefficient is inversely proportional to the size of the complex (Stokes-Einstein equation). The diffusion coefficient value of the copper complex in the CuCl solution is larger than that in the  $\text{CuCl}_2$  solution while the  $\text{CuSO}_4$  solution has the smallest value. Based on this, the complex formed in the  $\text{CuSO}_4$  solution should be the largest, while the complex formed in the CuCl solution should be the smallest. As we have a prediction for the complex in the  $\text{CuCl}_2$  solution,  $[\text{CuCl}_2(\text{EtSO}_4)]^{2-}$ , we can suggest the identities of possible copper complexes in the CuCl and  $\text{CuSO}_4$  solutions based on their relative sizes.

The possible complexes in the CuCl solution with sizes smaller than  $[\text{CuCl}_2(\text{EtSO}_4)_2]^{2-}$  are the following:  $\text{Cu}^+$ ,  $\text{CuCl}$ ,  $[\text{CuCl}_2]^-$ ,  $[\text{CuCl}_3]^{2-}$ ,  $[\text{CuCl}_4]^{3-}$ ,  $\text{Cu}(\text{EtSO}_4)$ ,  $[\text{CuCl}(\text{EtSO}_4)]^-$ ,  $[\text{CuCl}_2(\text{EtSO}_4)]^{2-}$  and  $[\text{CuCl}(\text{EtSO}_4)_2]^{2-}$ . In the discussion of the voltammograms obtained from the CuCl solution in Section 7.1.4, we proposed that one set of the oxidation and reduction peaks is due to  $[\text{CuCl}_2(\text{EtSO}_4)]^{2-}$  while the other set is due to the copper(I) complexes. As the potentials of these two set of peaks vary widely, the copper(I) complex is most likely to be quite different from  $[\text{CuCl}_2(\text{EtSO}_4)]^{2-}$ , and will probably involve only the copper cation and the chloride anions, forming complexes such as  $[\text{CuCl}_2]^-$ ,  $[\text{CuCl}_3]^{2-}$  and  $[\text{CuCl}_4]^{3-}$ . This behaviour is observed in first-generation ionic liquids, which is not too surprising because they contain high concentrations of  $\text{Cl}^-$  anion. Nanjundiah et al. [251] found that the copper(I) complexes in [BMPyr]-Cl-[AlCl<sub>3</sub>] is  $[\text{CuCl}_4]^{3-}$ . However, Laher et al. [255] found that three copper(I) chloride complexes exist in equilibrium in the [EMIM] [Cl] [AlCl<sub>3</sub>] solution, namely  $[\text{CuCl}_2]^-$ ,  $[\text{CuCl}_3]^{2-}$  and  $[\text{CuCl}_4]^{3-}$ . A similar behaviour was also

found in second-generation ionic liquids. Chen et al. [240] found that the copper(I) complex in [EMIM] [BF<sub>4</sub>] is [CuCl]<sup>+</sup>. The possible complexes in the CuSO<sub>4</sub> solution with sizes large than [CuCl<sub>2</sub>(EtSO<sub>4</sub>)<sub>2</sub>]<sup>2-</sup> are the following: [CuSO<sub>4</sub>(EtSO<sub>4</sub>)<sub>2</sub>]<sup>2-</sup>, [Cu(EtSO<sub>4</sub>)<sub>4</sub>]<sup>2-</sup>, [Cu(SO<sub>4</sub>)<sub>2</sub>(EtSO<sub>4</sub>)<sub>2</sub>]<sup>4-</sup>, [Cu(SO<sub>4</sub>)<sub>3</sub>(EtSO<sub>4</sub>)]<sup>5-</sup> and [Cu(SO<sub>4</sub>)<sub>4</sub>]<sup>6-</sup>.

Although the structure of the aluminium complex in the AlTFSI<sub>3</sub> solutions in [EMIM] [TFSI] was not investigated in this study, it can be inferred from studies carried out on other aluminium solutions reported in the literature. Nuclear magnetic resonance (NMR) and vibrational spectroscopy (Raman and infrared) were used to investigate the aluminium complexes existing in the AlCl<sub>3</sub> solutions in [BMPyr] [TFSI] [213,172,256], 1-propyl-1-methylpiperidinium bis(trifluoromethylsulfonyl)imide [PMPip] [TFSI] [256] and [EMIM] [TFSI] [213]. All these mixtures formed biphasic liquids, a white cloudy phase from which aluminium may be deposited, and a denser colourless phase. The aluminium complexes found at room temperature in the white cloudy phase were predominantly the tetrahedral complex of [AlCl<sub>4</sub>]<sup>-</sup>, with small amount of the octahedral complexes [AlCl<sub>3</sub>(TFSI)]<sup>-</sup> and [AlCl<sub>2</sub>(TFSI)<sub>2</sub>]<sup>-</sup> being also present [213,256,172]. At a higher temperature (80 °C), two additional aluminium complexes were detected, [AlCl<sub>3</sub>(TFSI)]<sup>-</sup> and [AlCl<sub>2</sub>(TFSI)<sub>2</sub>]<sup>-</sup> [256]. The colourless phase contained the octahedral complex of Al(TFSI)<sub>3</sub> [213]. Our AlTFSI<sub>3</sub> solution in [EMIM] [TFSI] was colourless and did not allow the deposition of aluminium. This behaviour is similar to that of the denser colourless phase of the AlCl<sub>3</sub>-[EMIM] [TFSI] mixtures. Based on this comparison, we suggest that the aluminium complexes in our solution should be the same as the denser colourless phase of the AlCl<sub>3</sub>-[EMIM] [TFSI] mixtures, namely, the octahedral complex of [Al(TFSI)<sub>3</sub>].

From the discussions above concerning the [EMIM] [TFSI] based solutions, we predict that the silver complex in AgTFSI solution is [AgTFSI<sub>3</sub>]<sup>2-</sup> and suggest that the aluminium complex in AlTFSI<sub>3</sub> solution may be [Al(TFSI)<sub>3</sub>]. Due to the large size of the TFSI<sup>-</sup> anions, only a maximum of three TFSI<sup>-</sup> ligands can fit around the silver and aluminium cations. Lassegue et al. [204] studied the lithium complex existing in LiTFSI solution in [EMIM] [TFSI], and they found that lithium formed a complex with two TFSI<sup>-</sup> anions, [Li(TFSI)<sub>2</sub>]<sup>-</sup>. Their result is consistent with our prediction because the lithium ion has a smaller radius than both aluminium and silver cations. Since the ionic radius of copper(II) is in-between those of silver(I) and aluminium(III), it is likely that the copper complex in CuTFSI<sub>2</sub> solution will also involve three TFSI<sup>-</sup> ligands and take the form of [Cu(TFSI)<sub>3</sub>]<sup>-</sup>.

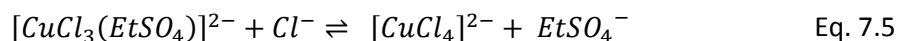
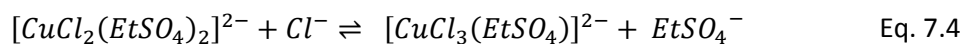
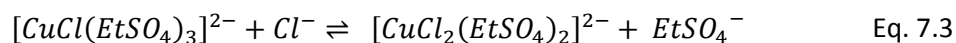
### 7.2.3 Stability of the complexes

Since metal complexes consist of a central cation coordinated by anions, their stability depends on the strength of the interaction between the metal cation and the ligands as well as on the interference of other ions in solution. As metal cations always exist as complexes in solution, changes in the anions concentration in solution and in the solution temperature may change the metal complex.

In order to study the stability of these complexes, we must first understand the nature of the bonding in the complexes. For the  $\text{CuCl}_2$  solution in [EMIM]  $[\text{EtSO}_4]$ , we predict that the first shell of the complexation takes the form of  $[\text{CuCl}_2(\text{EtSO}_4)_2]^{2-}$ . The metal cation ( $\text{Cu}^{2+}$ ) has the electronic structure  $1s^2 2s^2 2p^6 3s^2 3p^6 4s^0 3d^9 4p^0 4d^0$ . The entire  $n = 4$  orbitals are empty, so nine orbitals are free to bond with the possible ligands. However, due to the sizes of  $\text{Cl}^-$  and  $\text{EtSO}_4^-$  anions in relation to  $\text{Cu}^{2+}$  cation, only four of these anions can coordinate with  $\text{Cu}^{2+}$ . This can be confirmed by the theoretical copper complexes presented in Figure 7.1 a as well as by the fact that in aqueous solutions containing  $\text{CuCl}_2$ , the most common complex formed is  $[\text{CuCl}_4]^{2-}$  [257]. Hence the bonding of the two  $\text{Cl}^-$  and two  $\text{EtSO}_4^-$  anions will involve  $4sp^3$  hybridized orbitals. As  $\text{Cl}^-$  is more electronegative than  $\text{EtSO}_4^-$ , the Cu-Cl bond will be stronger and thus shorter than the Cu- $\text{EtSO}_4$  bond. This complex will mostly likely take the shape of a distorted tetrahedral.

In the  $\text{CuCl}_2$  solution in [EMIM]  $[\text{EtSO}_4]$ , there are two possible ligands,  $\text{Cl}^-$  and  $\text{EtSO}_4^-$ . Due to this, the changes that occur in the complex may involve the changes in the number of ligands and the changes in the type of ligands, thus a large family of complexes may be formed. This makes it quite difficult to predict the copper complex, which is further complicated by the fact that several complexes may co-exist in the solution. We believe that the large family of complexes that may be formed in solution has an influence on the electrochemical stability of the electrolyte, as seen from the voltammograms of the copper solutions in [EMIM]  $[\text{EtSO}_4]$  in Chapter 5 and the discussion of the stability of the electrolytes in Section 7.1.4. This, in turns, leads to the differences in the morphology of the deposited films.

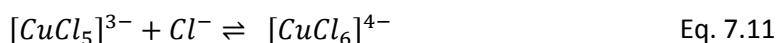
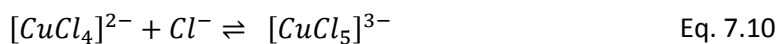
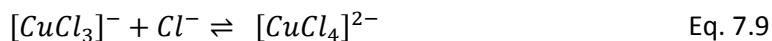
The concentration of the  $\text{CuCl}_2$  solution in [EMIM]  $[\text{EtSO}_4]$  used in our spectroscopic analysis (Chapter 4) was 0.20 mole fraction, much higher than the concentration used in our electrolytes for electrodeposition (0.1 M). As a result, it is important to know how the concentration of the copper salts affects the complexes in solution. In order to do so, we analysed the ligand changes that may occur in solution as a result of changes in the concentration of the anions. The ligands will be exchanged one at a time, as shown in Equations 7.2 to 7.5. To simplify the analysis, we assumed that no changes occur in the coordination number of the complex.



From Equations 7.2 to 7.5, we see that increasing the concentration of  $\text{Cl}^-$  anions in solution drive the reactions to the right, thereby increasing the number of  $\text{Cl}^-$  ligands in the copper complexes. Similarly, increasing the concentration of  $\text{EtSO}_4^-$  anions in solution will drive the reactions to the

left, increasing the number of  $\text{EtSO}_4^-$  ligands in the complexes. This was observed in first-generation ionic liquids which contain a high concentration of  $\text{Cl}^-$  in solution. An example is the  $[\text{BMPyr}]\text{-Cl-}[\text{AlCl}_3]$  ionic liquid, in which  $[\text{CuCl}_6]^{4-}$  is the predominant complex in solution, but when an excess of  $\text{AlCl}_3$  was added to the solution, the copper complex changed to  $[\text{Cu}(\text{AlCl}_4)_4]^{2-}$  [251].

Increasing the concentration of salts in solution can also change the coordination number of the copper complexes. In this case, we simplify the analysis by considering a complex with a single type of ligand, such as  $[\text{CuCl}_4]^{2-}$ , instead of our predicted complex of  $[\text{CuCl}_2(\text{EtSO}_4)_2]^{2-}$ .



From Equations 7.6 to 7.11, one may conclude that increasing the concentration of  $\text{Cl}^-$  anions in solution drives the reactions to the right, thereby increasing the coordination number of the complex. This behaviour was observed by Zhao et al. [254] in aqueous solutions, where the dominant complex changed from  $[\text{CuCl}]^+$ , to  $[\text{CuCl}_2]$  and finally to  $[\text{CuCl}_4]^{2-}$  when the concentration was increased from 0.01 M, to 0.10 M and finally to 1.00 M, respectively. The authors also found that the concentration of  $\text{Cu}^{2+}$  did not significantly affect the type of complex formed. A similar behaviour was observed in the  $[\text{BMPyr}][\text{TFSI}]$  ionic liquid, where the  $\text{Cu}^{2+}$  complex changed from  $[\text{CuCl}_3]^-$  to  $[\text{CuCl}_4]^{2-}$  and the  $\text{Cu}^+$  complex changed from  $[\text{CuCl}_3]^{2-}$  to  $[\text{CuCl}_4]^{3-}$  with increasing concentration of chloride in solution [249].

In our electrodeposition studies, the electrolyte temperature was varied between 35 and 85 °C. This variation in temperature could also change the complexes in solution. Laher et al. [255] studied the copper(I) and copper(II) complexes in  $[\text{EMIM}][\text{Cl}][\text{AlCl}_3]$  and found that  $[\text{CuCl}_2]$  and  $[\text{CuCl}_4]^{3-}$  were the predominant complexes at 40 °C, but  $[\text{CuCl}_3]^{2-}$  became predominant at 100 °C. A similar behaviour was also detected in the  $\text{AlCl}_3$  solutions in  $[\text{BMPyr}][\text{TFSI}]$ , where  $[\text{AlCl}_4]^-$  was the dominant complex at room temperature but at 80 °C, the concentration of  $[\text{AlCl}_3(\text{TFSI})]^-$  and  $[\text{AlCl}_2(\text{TFSI})_2]^-$  complexes increased [256].

We predict that the first shell of the silver complex in the  $\text{AgTFSI}$  solution in  $[\text{EMIM}][\text{TFSI}]$  is  $[\text{Ag}(\text{TFSI})_3]^{2-}$ . The  $\text{Ag}^+$  cation has the electronic structure of  $1s^2 2s^2 2p^6 3s^2 3p^6 4s^0 3d^9 4p^6 4d^{10} 5s^0$ . Thus, the three  $\text{TFSI}^-$  anions are thus bonded to  $\text{Ag}^+$  via the  $5s^2$  orbitals.

Since the AgTFSI salt has the same anion as [EMIM] [TFSI], the only possible modification of the silver complex is via the changes in the coordination number. From the discussion of the complex structure in Section 7.2.2, we have concluded that due to geometric reasons, the silver complex can only bond with three TFSI<sup>-</sup> ligands. This means that the only other two possible complexes in solution are [AgTFSI] and [Ag(TFSI)<sub>2</sub>]<sup>-</sup>, a much lower number of possibilities compared to the copper chloride solutions in [EMIM] [EtSO<sub>4</sub>]. This means that complexes in solution are less affected by the changes in concentration of the ionic species and solution temperature. This may explain the consistent morphology of the films deposited from AgTFSI and CuTFSI<sub>2</sub> solutions in [EMIM] [TFSI].

The stability of the complexes over time was investigated for both the CuCl<sub>2</sub> solution in [EMIM] [EtSO<sub>4</sub>] and the AgTFSI solution in [EMIM] [TFSI]. The cyclic voltammograms of both solutions remained similar when tested over a period of 3 months and the Raman and infrared spectra of both solutions were also similar when tested over a period of one year. This shows that the structures of these solutions are stable.

#### 7.2.4 Summary

Understanding the structure of the metal complex in the electrolyte is important for further improvement to the electrodeposition process, because it affects the solubility of the metal salt in solution, the transport properties of the electrolyte, the charge transfer reaction and the morphology of the deposited films. For the CuCl<sub>2</sub> solution in [EMIM] [EtSO<sub>4</sub>], the predominant complex is [CuCl<sub>2</sub>(EtSO<sub>4</sub>)<sub>2</sub>]<sup>2-</sup>. The complexes in CuCl solution must be smaller while the complex in CuSO<sub>4</sub> solution should be larger than [CuCl<sub>2</sub>(EtSO<sub>4</sub>)<sub>2</sub>]<sup>2-</sup>. For the AgTFSI solution in [EMIM] [TFSI], the predominant complex is [AgTFSI<sub>3</sub>]<sup>2-</sup>. For geometric reasons, it can be predicted that the complexes in the CuTFSI<sub>2</sub> and AlTFSI<sub>3</sub> solutions in [EMIM] [TFSI] are [CuTFSI<sub>3</sub>]<sup>-</sup> and [AlTFSI<sub>3</sub>], respectively. The composition of the electrolyte, namely the type of anions present in solution, their respective concentration and the electrolyte temperature affect the type of ligands and the coordination number in the complex. The concentration of the metal cations does not significantly affect the complex structure. Since the AgTFSI salt has the same anions as [EMIM] [TFSI], the [AgTFSI<sub>3</sub>]<sup>2-</sup> complex structure is stable over wide ranges of concentrations and temperatures.

### 7.3 Future works

In our vision, every thin film that requires complex structures and properties can be created by electrodeposition from an ionic liquid electrolyte, with considerable advantage over other techniques. Before this dream can be realised in industry, several prerequisites need to be met. Firstly, significant gaps in knowledge and technical knowhow must be filled. Secondly, any potential problems with the system must be fixed. Lastly, the cost of the system must be capped at a reasonable level.

In our study, we only investigated the metal complexes that existed at room temperature in solutions with very high concentration of the metal salts. Since electrodeposition are mostly carried out from electrolytes with much lower concentrations of the metal salts, the next logical step is to investigate how the metal complexes change with the concentrations of the metal salts and with the electrolyte temperatures. Due to the limitations of vibrational spectroscopy, other techniques will be needed to analyse the metal complexes existing in ionic liquid solutions with low concentration of the metal salt.

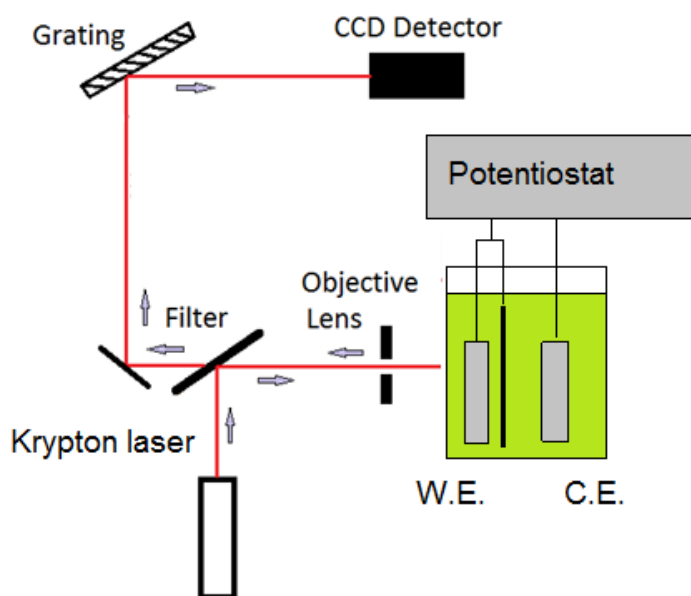


Figure 7.2: Schematic of a combined electrochemical cell and surface enhanced Raman spectroscopy experimental setup required to probe the double-layer structure near the electrode/electrolyte in ionic liquids.

One of the main limitations to the current understanding of electrodeposition from ionic liquids is that no one really knows how the double-layer structure near the electrode/electrolyte interface looks like in an ionic liquid electrolyte. Many theoretical models have been proposed based on theoretical calculations but not many experiments have been carried out to test them [218,219]. In the current state of the art, only the structure of the ions adsorbed on the substrate surface has



been probed, while the structure of the remaining double-layer remains elusive [220-225]. We propose a method to probe the double-layer based on sum frequency generation spectroscopy (SFGS) and surface enhanced Raman spectroscopy (SERS) [220,221,223,224,258]. As the double-layer structure is near the electrode/electrolyte interface, it is under the influence of an electric field. In order to probe this structure, we will need an experimental setup which incorporates the analytical technique and an electrochemical cell in which in-situ measurements can be taken. For SERS, using a working electrode that is SERS active will amplify the Raman signal from the vibrational interaction near the electrode surface by several orders of magnitude, allowing us to separate this signal from those coming from the bulk solution. By comparing these spectra with those obtained by using regular Raman spectroscopy, it is possible to get an insight on the double-layer structure. A schematic of the proposed experimental setup is shown in Figure 7.2. Recently, Liu et al. [259] from Pacific Northwest National Laboratory created a new chemical analysis method to probe the electrode-electrolyte interface by time-of-flight secondary ion mass spectrometry (ToF-SIMS), in conjunction with electrochemical analysis. A new device for this purpose might be commercialised in the near future, which will simplify the experiments to probe the double-layer structure. Currently research in this niche area is limited as all existing experimental setups are self-built.

While ionic liquid electrolytes have many major advantages, they also suffer from two drawbacks. One is the low solubility of the metal salts in solution and the other is the high viscosity of the ionic liquid. Currently, a common method used to increase the concentration of the metal cation in solution is by anodic dissolution of the metal, although this does not guarantee a high current density [253]. Another method to increase the salt solubility is to choose a metal salt with the same anion as the ionic liquid [246], as adopted in this study. A way to solve both problems is by carefully designing the ionic liquid and the metal salt. One specific method is to design an ionic liquid with a small and symmetrical anion, such as [EMIM] [DCA], which has a low viscosity and high solubility of the metal salts [260]. Another specific method has been reported in recent studies in which the metal cation was incorporated into the cationic structure of the ionic liquids that have low viscosity. The results from these studies show that the solubility of the metal cations has increased and this has significantly increased the current density during electrodeposition [147,261,262]. We believe that greater improvements can still be made in this area and better designed ionic liquids may eliminate these two problems in the future.

## 8 Conclusion

Functional thin films are important in our everyday electronics, and their applications are constantly expanding into other niches. Electrodeposition from ionic liquids has the potential to be an inexpensive and efficient method of creating these films. However, the deposition mechanisms from ionic liquid-based electrolytes are not fully understood due to the difference between high-level theory and industrial practice, especially the difficulties in probing the electrolyte structure. In this study, we aim to narrow this knowledge gap by investigating the links between the films morphology, the electrochemical properties of the electrolyte and the molecular structure and interactions in the electrolyte.

This investigation was carried out on the CuCl, CuCl<sub>2</sub> and CuSO<sub>4</sub> solutions in 1-ethyl-3-methylimidazolium ethylsulphate [EMIM][EtSO<sub>4</sub>] and the AgTFSI, CuTFSI<sub>2</sub> and AlTFSI<sub>3</sub> solutions in 1-ethyl-3-methylimidazolium bis(trifluoromethylsulfonyl)imide [EMIM][TFSI].

Understanding the complex structure is important as it affects the salt solubility in solution, ionic conductivity, the charge transfer reaction and the morphology of the deposited films. The structure of the complex formation was investigated by using Raman and infrared spectroscopies, assisted by density functional theory (DFT) calculations. Only the CuCl<sub>2</sub> solution in [EMIM][EtSO<sub>4</sub>] and the AgTFSI solution in [EMIM][TFSI] were studied, as the concentration of several other solutions were too low to induce any changes in the spectra signatures. In the AgTFSI solution in [EMIM][TFSI], the silver cation is solvated by three first neighbouring TFSI anions, interacting with one of the O atoms of each SO<sub>2</sub> groups. The first solvation shell of silver has the structure [Ag(TFSI)<sub>3</sub>]<sup>2-</sup>. In the CuCl<sub>2</sub> solution in [EMIM][TFSI], the new bands at 997, 1045 and 1298 cm<sup>-1</sup> are associated with the S-O stretches, induced by the interaction between copper cation and EtSO<sub>4</sub><sup>-</sup> anion. Similarly a new band at 312 cm<sup>-1</sup> was induced by the asymmetric stretching of Cl-Cu-Cl. The copper complex involves two chlorine and two EtSO<sub>4</sub><sup>-</sup> anions, located at two distinct separation distances. The first solvation shell of copper has the structure [CuCl<sub>2</sub>(EtSO<sub>4</sub>)<sub>2</sub>]<sup>2-</sup>.

Both [EMIM][EtSO<sub>4</sub>] and [EMIM][TFSI] appear to be good solvents for electrodeposition, although electrolyte based on [EMIM][TFSI] present better properties compared to those based on [EMIM][EtSO<sub>4</sub>]. The cyclic voltammograms show that the reductions of silver and copper in ionic liquids are quasi-reversible and involve a one-electron transfer-step process: (Ag(I)→Ag(0), (Cu(II)→Cu(I)) and (Cu(I)→Cu(0)). The reduction of aluminium from the AlTFSI<sub>3</sub> solution is irreversible and occurs in a one-step process, leading to the deposition of aluminium. The diffusion coefficients of silver and copper species in the ionic liquids increase with temperature, as expected, and their values are quite similar and typical of ionic liquid electrolyte with similar viscosity. However, the diffusion coefficient of the aluminium species in [EMIM][TFSI] is six orders of magnitude lower than those of silver and copper. For the copper solutions in [EMIM][EtSO<sub>4</sub>], the oxidation state of copper in solution and the anion group of the salts affect the electrochemical results. In the solutions containing salts with the same anion group but at different oxidation states (CuCl and CuCl<sub>2</sub>), there is a shift in the potentials of the peaks corresponding to the same reaction seen in the

voltammogram. The peaks for the  $\text{CuCl}_2$  solution are at a more negative potential than those for the  $\text{CuCl}$  solution. In solutions containing salts with the same copper oxidation state but with a different anion group ( $\text{CuCl}_2$  and  $\text{CuSO}_4$ ), there is a huge difference between the cation diffusion coefficient values. The diffusion coefficients of the copper species are an order of magnitude larger for the chloride solutions compared with the sulphate solution. This is consistent with the higher activation energy of the  $\text{Cu(II)}$  to  $\text{Cu(I)}$  reduction in the copper sulphate solution compared to the copper(II) chloride solution. The influence of the copper oxidation state or the anion of the salts may be explained by the complexes that are formed in each solution.

Silver and copper thin films can be electrodeposited from  $\text{CuCl}_2$ ,  $\text{CuCl}$  and  $\text{CuSO}_4$  solutions in [EMIM] [EtSO<sub>4</sub>] and AgTFSI and CuTFSI<sub>2</sub> solution in [EMIM] [TFSI]. However, no aluminium film was deposited from AlTFSI<sub>3</sub> solution, consistent with the very low diffusion coefficient of aluminium species when compared with silver and copper. The analysis of the films by EDX and XRD shows that they are crystalline and consist mainly of the pure silver or copper, with trace amounts of oxygen and sulphur. The morphology of the films changes with the electrolyte temperature, deposition potential and deposition time. In general, the films continuity and particle size increase when the electrolyte temperature increases from 35 to 85 °C. Increasing the deposition time from 900 to 1,800 s marginally improves the continuity of the films. While the general trends are similar, there are also some differences in the morphology of the films deposited under similar deposition parameters:

- The films deposited from the  $\text{CuCl}_2$  solutions in [EMIM] [EtSO<sub>4</sub>] had larger particles and were discontinuous. The best films were obtained for electrolyte temperatures of 35 and 50 °C, deposition potential of 1.8 V and deposition time of 900 s.
- The films deposited from  $\text{CuCl}$  solutions in [EMIM] [EtSO<sub>4</sub>] were continuous even when a deposition time of 900 s was used and they consisted of extremely small globular particles aggregated in clusters. Increasing the deposition time to 1,800 s led to an overgrowth of the films which increased their roughness, due to the formation of a cauliflower-like structure.
- Continuous films could be prepared from  $\text{CuSO}_4$  solutions in [EMIM] [EtSO<sub>4</sub>] at -1.6 and -1.8 V for all temperatures and at a potential of -1.2 V for deposition temperature of 85 °C. The structure of the films consisted of clusters of nanometre size irregularly shaped particles.
- Dense and continuous silver films were obtained from the AgTFSI solution in [EMIM] [TFSI]. However, the films obtained at 85 °C were very rough, with large particles growing outwards from the film surface. The roughness was reduced with the increase of deposition time. The best films were obtained at 35 and 50 °C, and at -0.4 V. The silver films hardness was  $2.0 \pm 0.40$  GPa and their reduced Young's modulus was  $176 \pm 23$  GPa.
- At 35 °C, the morphology of the copper films deposited from CuTFSI<sub>2</sub> solution in [EMIM] [TFSI] was independent of the deposition potential and time. The particle size only increased slightly with increasing deposition time and decreasing potential. EDX analysis showed that at 85 °C, the films were contaminated with silver, most likely from the silver

wire used as the reference electrode. The silver and copper particles were very small, ranging from 10-50 nm. The silver particles were slightly larger than those of copper.

The stability of the metal complexes with respect to the ion concentration in solution and electrolyte temperature was not fully investigated. Cursory analysis showed that electrolytes where the ionic liquid and metal salt shared the same anion ( $\text{AgTFSI}$  and  $\text{CuTFSI}_2$  solutions in  $[\text{EMIM}][\text{TFSI}]$ ) were more stable. This can be seen from their cyclic voltammograms which are stable over a wide range of temperature and did not contain extra peaks. The morphologies of the films deposited from these solutions were also quite similar over a wide range of deposition potentials, times and temperatures.



## 9 References

1. Al-Salman R, El Abedin SZ, Endres F (2008) Electrodeposition of Ge, Si and Si(x)Ge(1-x) from an air- and water-stable ionic liquid. *Physical Chemistry Chemical Physics* 10 (31):4650-4657. doi:10.1039/b806996b
2. Pradhan D, Reddy RG (2007) Production of A-Ti alloys using ionic liquid electrolytes at low temperatures. *Innovations in Titanium Technology*.
3. Hsieh Y-T, Sun IW (2011) Electrochemical growth of hierarchical CuSn nanobrushes from an ionic liquid. *Electrochemistry Communications* 13 (12):1510-1513. doi:10.1016/j.elecom.2011.10.006
4. El Abedin SZ, Endres F (2012) Free-Standing Aluminium Nanowire Architectures Made in an Ionic Liquid. *Chemphyschem* 13 (1):250-255. doi:10.1002/cphc.201100639
5. Meng X, Al-Salman R, Zhao J, Borissenko N, Li Y, Endres F (2009) Electrodeposition of 3D Ordered Macroporous Germanium from Ionic Liquids: A Feasible Method to Make Photonic Crystals with a High Dielectric Constant. *Angewandte Chemie-International Edition* 48 (15):2703-2707. doi:10.1002/anie.200805252
6. Popov KI, Djokić SS, Grgur BN (2002) *Fundamental Aspects of Electrometallurgy*. Kluwer Academic/Plenum Publishers,
7. Bard AJ, Faulkner LR (2001) *ELECTROCHEMICAL METHODS: Fundamentals and Applications*. 2nd edn. John Wiley & Sons, Inc, New York
8. Brett C, Brett A (2005) *Electrochemistry principles, methods and applications*. Oxford University Press, New York
9. Tosaka (2008) Electric double-layer (BMD model) NT. [http://en.wikipedia.org/wiki/File:Electric\\_double-layer\\_\(BMD\\_model\)\\_NT.PNG](http://en.wikipedia.org/wiki/File:Electric_double-layer_(BMD_model)_NT.PNG).
10. Endres F, Abbott A, MacFarlane D (2008) *Electrodeposition from Ionic Liquids*. Weinheim
11. Eugénio SCdCdM (2012) *Electrodeposition of black chromium thin films from ionic liquid-based electrolyte*. PhD, INSTITUTO SUPERIOR TÉCNICO, Lisbon
12. Stuart BH (2004) *Infrared Spectroscopy: Fundamentals and Applications*. Analytical Techniques in the Sciences. Wiley,
13. EM Spectrum Properties. (2007) Wikimedia Commons. [http://en.wikipedia.org/wiki/File:EM\\_Spectrum\\_Properties\\_edit.svg](http://en.wikipedia.org/wiki/File:EM_Spectrum_Properties_edit.svg).
14. .
15. Karonen I (2006) Spontaneous emission.png. Wikimedia commons. <http://en.wikipedia.org/wiki/Image:Spontaneous emission.png>.
16. Moxfyre (2009) Raman energy levels. Wikimedia Commons. [http://en.wikipedia.org/wiki/File:Raman\\_energy\\_levels.svg](http://en.wikipedia.org/wiki/File:Raman_energy_levels.svg).
17. Steff (2010) Schema\_MEB\_(it).svg. Wikimedia Commons. [http://en.wikipedia.org/wiki/File:Schema\\_MEB\\_\(en\).svg](http://en.wikipedia.org/wiki/File:Schema_MEB_(en).svg).
18. Vaughan D, Corporation K (1989) *Energy-dispersive X-ray Microanalysis: An Introduction*. Kevex Instruments, Incorporated,
19. Gringer (2009) Scheme TEM en.png. Wikimedia Commons. [http://en.wikipedia.org/wiki/File:Scheme\\_TEM\\_en.svg](http://en.wikipedia.org/wiki/File:Scheme_TEM_en.svg).
20. Peter J. Goodhew JH, Richard Beanland (2001) *Electron Microscopy and Analysis*. Third edn. Taylor and Francis, London and New York
21. Jputhoff (2006) Load v disp.JPG. Wikipedia Commons. [http://en.wikipedia.org/wiki/File:Load\\_v\\_disp.JPG](http://en.wikipedia.org/wiki/File:Load_v_disp.JPG).

22. Oliver WC, Pharr GM (2004) Measurement of hardness and elastic modulus by instrumented indentation: Advances in understanding and refinements to methodology. *Journal of Materials Research* 19 (01):3-20. doi:doi:10.1557/jmr.2004.19.1.3
23. Herstedt M, Smirnov M, Johansson P, Chami M, Grondin J, Servant L, Lassègues JC (2005) Spectroscopic characterization of the conformational state of the bis(trifluoromethanesulfonyl)amide anion (TFSI<sup>-</sup>). *Journal of Raman Spectroscopy* 36:762-770
24. Hayes R, Warr GG, Atkin R (2010) At the interface: solvation and designing ionic liquids. *Physical Chemistry Chemical Physics* 12 (8):1709-1723. doi:10.1039/b920393a
25. Bockris JOM, Razumney GA (1967) *Fundamental aspects of electrocrystallization*. Plenum Press,
26. Hunt LB (1973) The early history of gold plating. *Gold Bull* 6 (1):16-27. doi:10.1007/BF03215178
27. McNaught AD, Wilkinson A (1997) *Compendium of Chemical Terminology (the "Gold Book")*. doi:10.1351/goldbook.
28. Housecroft CE, Sharpe AG (2005) *Inorganic Chemistry*. 2nd edn. Pearson Education Limited, Essex
29. Jeon Y, Sung J, Seo C, Lim H, Cheong H, Kang M, Moon B, Ouchi Y, Kim D (2008) Structures of Ionic Liquids with Different Anions Studied by Infrared Vibration Spectroscopy. *The Journal of Physical Chemistry B* 112 (15):4735-4740. doi:10.1021/jp7120752
30. Hurley FH, Wier TP (1951). *J Electrochem Soc* 98:203
31. Gale RJ, Gilbert B, Osteryoung RA (1978) Raman spectra of molten aluminum chloride: 1-butylpyridinium chloride systems at ambient temperatures. *Inorganic Chemistry* 17 (10):2728-2729. doi:10.1021/ic50188a008
32. Robinson J, Osteryoung RA (1979) An electrochemical and spectroscopic study of some aromatic hydrocarbons in the room temperature molten salt system aluminum chloride-n-butylpyridinium chloride. *Journal of the American Chemical Society* 101 (2):323-327. doi:10.1021/ja00496a008
33. Wilkes JS, Levisky JA, Wilson RA, Hussey CL (1982) Dialkylimidazolium chloroaluminate melts: a new class of room-temperature ionic liquids for electrochemistry, spectroscopy and synthesis. *Inorganic Chemistry* 21 (3):1263-1264. doi:10.1021/ic00133a078
34. Fannin AA, Floreani DA, King LA, Landers JS, Piersma BJ, Stech DJ, Vaughn RL, Wilkes JS, Williams John L (1984) Properties of 1,3-dialkylimidazolium chloride-aluminum chloride ionic liquids. 2. Phase transitions, densities, electrical conductivities, and viscosities. *The Journal of Physical Chemistry* 88 (12):2614-2621. doi:10.1021/j150656a038
35. Abbott AP, Capper G, Davies DL, Rasheed RK, Tambyrajah V (2001) Novel ambient temperature ionic liquids for zinc and zinc alloy electrodeposition. *Transactions of the Institute of Metal Finishing* 79:204-206
36. Abbott AP, Capper G, Davies DL, Rasheed R (2004) Ionic liquids based upon metal halide/substituted quaternary ammonium salt mixtures. *Inorganic Chemistry* 43 (11):3447-3452. doi:10.1021/ic049931s
37. Hsiu SI, Huang JF, Sun IW, Yuan CH, Shiea J (2002) Lewis acidity dependency of the electrochemical window of zinc chloride-1-ethyl-3-methylimidazolium chloride ionic liquids. *Electrochimica Acta* 47 (27):4367-4372. doi:10.1016/s0013-4686(02)00509-1
38. Lin YF, Sun IW (1999) Electrodeposition of zinc from a mixture of zinc chloride and neutral aluminum chloride-1-methyl-3-ethylimidazolium chloride molten salt. *Journal of the Electrochemical Society* 146 (3):1054-1059. doi:10.1149/1.1391720

39. Wilkes JS, Zaworotko MJ (1992) Air and water stable 1-ethyl-3-methylimidazolium based ionic liquids. *Journal of the Chemical Society, Chemical Communications* (13):965-967. doi:10.1039/C39920000965
40. Fuller J, Carlin RT, De Long HC, Haworth D (1994) Structure of 1-ethyl-3-methylimidazolium hexafluorophosphate: model for room temperature molten salts. *Journal of the Chemical Society, Chemical Communications* (3):299-300. doi:10.1039/C39940000299
41. Chauvin Y, Mussmann L, Olivier H (1996) A Novel Class of Versatile Solvents for Two-Phase Catalysis: Hydrogenation, Isomerization, and Hydroformylation of Alkenes Catalyzed by Rhodium Complexes in Liquid 1,3-Dialkylimidazolium Salts. *Angewandte Chemie International Edition in English* 34 (23-24):2698-2700. doi:10.1002/anie.199526981
42. Papageorgiou N, Athanassov Y, Armand M, Bonhôte P, Pettersson H, Azam A, Grätzel M (1996) The Performance and Stability of Ambient Temperature Molten Salts for Solar Cell Applications. *Journal of The Electrochemical Society* 143 (10):3099-3108. doi:10.1149/1.1837171
43. D. Holbrey J, R. Seddon K (1999) The phase behaviour of 1-alkyl-3-methylimidazolium tetrafluoroborates; ionic liquids and ionic liquid crystals. *Journal of the Chemical Society, Dalton Transactions* (13):2133-2140. doi:10.1039/A902818H
44. Ngo HL, LeCompte K, Hargens L, McEwen AB (2000) Thermal properties of imidazolium ionic liquids. *Thermochimica Acta* 357–358 (0):97-102. doi:[http://dx.doi.org/10.1016/S0040-6031\(00\)00373-7](http://dx.doi.org/10.1016/S0040-6031(00)00373-7)
45. Noda A, Hayamizu K, Watanabe M (2001) Pulsed-Gradient Spin-Echo <sup>1</sup>H and <sup>19</sup>F NMR Ionic Diffusion Coefficient, Viscosity, and Ionic Conductivity of Non-Chloroaluminate Room-Temperature Ionic Liquids. *The Journal of Physical Chemistry B* 105 (20):4603-4610. doi:10.1021/jp004132q
46. Zhou Z-B, Matsumoto H, Tatsumi K (2005) Structure and Properties of New Ionic Liquids Based on Alkyl- and Alkenyltrifluoroborates. *ChemPhysChem* 6 (7):1324-1332. doi:10.1002/cphc.200500094
47. McEwen AB, Ngo HL, LeCompte K, Goldman JL (1999) Electrochemical Properties of Imidazolium Salt Electrolytes for Electrochemical Capacitor Applications. *Journal of The Electrochemical Society* 146 (5):1687-1695. doi:10.1149/1.1391827
48. Zhang S, Sun N, He X, Lu X, Zhang X (2006) Physical Properties of Ionic Liquids: Database and Evaluation. *Journal of Physical and Chemical Reference Data* 35 (4):1475-1517
49. Dzyuba SV, Bartsch RA (2002) Expanding the polarity range of ionic liquids. *Tetrahedron Letters* 43 (26):4657-4659. doi:[http://dx.doi.org/10.1016/S0040-4039\(02\)00858-4](http://dx.doi.org/10.1016/S0040-4039(02)00858-4)
50. Bonhôte P, Dias A-P, Papageorgiou N, Kalyanasundaram K, Grätzel M (1996) Hydrophobic, Highly Conductive Ambient-Temperature Molten Salts†. *Inorganic Chemistry* 35 (5):1168-1178. doi:10.1021/ic951325x
51. MacFarlane DR, Golding J, Forsyth S, Forsyth M, Deacon GB (2001) Low viscosity ionic liquids based on organic salts of the dicyanamide anion. *Chemical Communications* (16):1430-1431. doi:10.1039/B103064G
52. Fernandez A, Garcia J, Torrecilla JS, Olié M, Rodriguez F (2008) Volumetric, transport and surface properties of bmim MeSO<sub>4</sub> and emim EtSO<sub>4</sub> ionic liquids as a function of temperature. *Journal of Chemical and Engineering Data* 53 (7):1518-1522. doi:10.1021/jc8000766
53. Carda-Broch S, Berthod A, Armstrong DW (2003) Solvent properties of the 1-butyl-3-methylimidazolium hexafluorophosphate ionic liquid. *Anal Bioanal Chem* 375 (2):191-199. doi:10.1007/s00216-002-1684-1
54. Cooper EI, O'Sullivan In: 8th International Symposium on Molten salts, Pennington, NJ, 1992. The Electrochemical Society, p 386



55. Yoshida Y, Muroi K, Otsuka A, Saito G, Takahashi M, Yoko T (2004) 1-Ethyl-3-methylimidazolium Based Ionic Liquids Containing Cyano Groups: Synthesis, Characterization, and Crystal Structure. *Inorganic Chemistry* 43 (4):1458-1462. doi:10.1021/ic035045q
56. Fredlake CP, Crosthwaite JM, Hert DG, Aki SNVK, Brennecke JF (2004) Thermophysical Properties of Imidazolium-Based Ionic Liquids. *Journal of Chemical & Engineering Data* 49 (4):954-964. doi:10.1021/je034261a
57. Tokuda H, Hayamizu K, Ishii K, Susan MABH, Watanabe M (2004) Physicochemical Properties and Structures of Room Temperature Ionic Liquids. 1. Variation of Anionic Species. *The Journal of Physical Chemistry B* 108 (42):16593-16600. doi:10.1021/jp047480r
58. Huddleston JG, Visser AE, Reichert WM, Willauer HD, Broker GA, Rogers RD (2001) Characterization and comparison of hydrophilic and hydrophobic room temperature ionic liquids incorporating the imidazolium cation. *Green Chemistry* 3 (4):156-164. doi:10.1039/B103275P
59. Suarez P, A.Z., Einloft S, Dullius J, E.L., de Souza R, F., Dupont J (1998) Synthesis and physical-chemical properties of ionic liquids based on 1-*n*-butyl-3-methylimidazolium cation. *J Chim Phys* 95 (7):1626-1639
60. Dzyuba SV, Bartsch RA (2002) Influence of Structural Variations in 1-Alkyl(aralkyl)-3-Methylimidazolium Hexafluorophosphates and Bis(trifluoromethylsulfonyl)imides on Physical Properties of the Ionic Liquids. *ChemPhysChem* 3 (2):161-166. doi:10.1002/1439-7641(20020215)3:2<161::AID-CPHC161>3.0.CO;2-3
61. Crosthwaite JM, Muldoon MJ, Dixon JK, Anderson JL, Brennecke JF (2005) Phase transition and decomposition temperatures, heat capacities and viscosities of pyridinium ionic liquids. *The Journal of Chemical Thermodynamics* 37 (6):559-568. doi:<http://dx.doi.org/10.1016/j.jct.2005.03.013>
62. Froba AP, Kremer H, Leipertz A (2008) Density, refractive index, interfacial tension, and viscosity of ionic liquids EMIM EtSO<sub>4</sub>, EMIM NTf<sub>2</sub>, EMIM N(CN)<sub>2</sub>, and OMA NTf<sub>2</sub> in dependence on temperature at atmospheric pressure. *Journal of Physical Chemistry B* 112 (39):12420-12430. doi:10.1021/jp804319a
63. Morgan D, Ferguson L, Scovazzo P (2005) Diffusivities of Gases in Room-Temperature Ionic Liquids: Data and Correlations Obtained Using a Lag-Time Technique. *Industrial & Engineering Chemistry Research* 44 (13):4815-4823. doi:10.1021/ie048825v
64. Kitaoka S, Nobuoka K, Ishikawa Y (2005) Ionic liquids for tetraarylporphyrin preparation. *Tetrahedron* 61 (32):7678-7685. doi:<http://dx.doi.org/10.1016/j.tet.2005.05.097>
65. Fuller J, Carlin RT, Osteryoung RA (1997) The Room Temperature Ionic Liquid 1-Ethyl-3-methylimidazolium Tetrafluoroborate: Electrochemical Couples and Physical Properties. *Journal of The Electrochemical Society* 144 (11):3881-3886. doi:10.1149/1.1838106
66. Katayama Y, Dan S, Miura T, Kishi T (2001) Electrochemical Behavior of Silver in 1-Ethyl-3-methylimidazolium Tetrafluoroborate Molten Salt. *Journal of The Electrochemical Society* 148 (2):C102-C105. doi:10.1149/1.1341243
67. Nakagawa H, Izuchi S, Kuwana K, Nukuda T, Aihara Y (2003) Liquid and Polymer Gel Electrolytes for Lithium Batteries Composed of Room-Temperature Molten Salt Doped by Lithium Salt. *Journal of The Electrochemical Society* 150 (6):A695-A700. doi:10.1149/1.1568939
68. Barisci JN, Wallace GG, MacFarlane DR, Baughman RH (2004) Investigation of ionic liquids as electrolytes for carbon nanotube electrodes. *Electrochemistry Communications* 6 (1):22-27. doi:<http://dx.doi.org/10.1016/j.elecom.2003.09.015>
69. Endres F, MacFarlane D, Abbot A (2007) Electrodeposition from Ionic Liquids. Wiley vch
70. Hallett JP, Welton T (2011) Room-Temperature Ionic Liquids: Solvents for Synthesis and Catalysis. 2. *Chem Rev* 111:3508-3576
71. Welton T (2004) Ionic liquids in catalysis. *Coordination Chemistry Reviews* 248 2459-2477

72. Wasserscheid P, Welton T (2003) *Ionic liquid in Synthesis*. Wiley-VCH
73. Tsuda T, Hussey CL (2007) *Electrochemical Applications of Room-Temperature Ionic Liquids*. The Electrochemical Society Interface spr:42
74. Robinson J, Osteryoung RA (1980) The Electrochemical Behavior of Aluminum in the Low Temperature Molten Salt System n Butyl Pyridinium Chloride: Aluminum Chloride and Mixtures of This Molten Salt with Benzene. *Journal of The Electrochemical Society* 127 (1):122-128. doi:10.1149/1.2129601
75. Welch BJ, Osteryoung RA (1981) Electrochemical studies in low temperature molten salt systems containing aluminium chloride. *Journal of Electroanalytical Chemistry and Interfacial Electrochemistry* 118 (0):455-466. doi:[http://dx.doi.org/10.1016/S0022-0728\(81\)80561-X](http://dx.doi.org/10.1016/S0022-0728(81)80561-X)
76. Lai PK, Skyllas-Kazacos M (1988) Electrodeposition of aluminium in aluminium chloride/1-methyl-3-ethylimidazolium chloride. *Journal of Electroanalytical Chemistry and Interfacial Electrochemistry* 248 (2):431-440. doi:[http://dx.doi.org/10.1016/0022-0728\(88\)85103-9](http://dx.doi.org/10.1016/0022-0728(88)85103-9)
77. Liao Q, Pitner WR, Stewart G, Hussey CL, Stafford GR (1997) Electrodeposition of aluminum from the aluminum chloride-1-methyl-3-ethylimidazolium chloride room temperature molten salt plus benzene. *Journal of the Electrochemical Society* 144 (3):936-943. doi:10.1149/1.1837510
78. Abbott AP, Eardley CA, Farley NRS, Griffith GA, Pratt A (2001) Electrodeposition of aluminium and aluminium/platinum alloys from AlCl<sub>3</sub>/benzyltrimethylammonium chloride room temperature ionic liquids. *Journal of Applied Electrochemistry* 31 (12):1345-1350. doi:10.1023/a:1013800721923
79. Endres F, Bukowski M, Hempelmann R, Natter H (2003) Electrodeposition of nanocrystalline metals and alloys from ionic liquids. *Angewandte Chemie-International Edition* 42 (29):3428-3430. doi:10.1002/anie.200350912
80. Lipsztajn M, Osteryoung RA (1985). *Inorg Chem* 24:716-719
81. Piersma BJ, Ryan DM, Schumacher ER, Reichel TL (1996). *J Electrochem Soc* 143:908-913
82. Chen PY, Lin YF, Sun JW (1999). *J Electrochem Soc* 146:3290-3294
83. Pitner WR, Hussey CL (1997). *J Electrochem Soc* 144:3095
84. Habboush DA, Osteryoung RA (1984). *Inorg Chem* 23:1726-1734
85. Lipsztajn M, Osteryoung RA (1985). *Inorg Chem* 24:3492
86. Jeng EG-S, Sun I-W (1997). *J Electrochem Soc* 144:2369-2374
87. Wilkes JS, Zaworotko MJ (1992). *Chem Commun*:965-967
88. Fuller J, Carlin RT, De Long HC, Haworth D (1994). *J Chem Soc*:299-300
89. Papageorgiou N, Athanassov Y, Armand M, Bonhote P, Pettersson H, Azam A, Gratzel M (1996). *J Electrochem Soc* 143:3099-3108
90. Lin Y-F, Su I-W (1999). *Electrochim Acta* 44:2771
91. Chen P-Y, Lin M-C, Sun I-W (2000). *J Electrochem Soc* 147:3350
92. Chen P-Y, Sun I-W (2001). *Electrochim Acta* 46:1169
93. Abbott AP, Capper G, McKenzie KJ, Ryders KS (2007). *J Electroanal Chem* 599:288
94. Chen P-Y, Sun I-W (1999). *Electrochim Acta* 45:441
95. Murase K, Nitta K, Hirato T, Awakura Y (2001). *J Appl Electrochem* 31:1089
96. Zein El Abedin S, Saad AY, Farag HK, Boressinko N, Liu QX, Endres F (2007). *Electrochem Acta* 52:2746
97. Rostovshchikova TN, Smirnov VV, Kozhevnikov VM, Yavsin DA, Zabelin MA, Yassievich IN, Gurevich SA (2005). *Appl Catal A: General* 256:70
98. Chen P-Y, Sun I-W (2000). *Electrochim Acta* 45:3163
99. Huang J-F, Sun I-W (2002). *Electrochem Soc* 149:E348
100. Abbott AP, Capper G, Davies DL, Rasheed RK (2004). *Chem Eur J* 10:3769
101. Tai C-C, Su F-Y, Sun I-W (2005). *Electrochem Acta* 50:5504

102. Su F-Y, Huang J-F, Sun I-W (2004). *J Electrochem Soc* 151:C811
103. Hsiu S-I, Tai C-C, Sun I-W (2006). *Electrochim Acta* 51:2607
104. Lassègues J-C, Grondin J, Cavagnat D, Johansson P (2009) Reply to the "Comment on 'New Interpretation of the CH Stretching Vibrations in Imidazolium-Based Ionic Liquids'". *The Journal of Physical Chemistry A* 114 (1):687-688. doi:10.1021/jp909770s
105. Dominguez-Vidal A, Kaun N, Ayora-Cañada MJ, Lendl B (2007) Probing Intermolecular Interactions in Water/Ionic Liquid Mixtures by Far-infrared Spectroscopy. *The Journal of Physical Chemistry B* 111 (17):4446-4452. doi:10.1021/jp068777n
106. He P, Liu HT, Li ZY, Liu Y, Xu XD, Li JH (2004) Electrochemical deposition of silver in room-temperature ionic liquids and its surface-enhanced Raman scattering effect. *Langmuir* 20 (23):10260-10267. doi:10.1021/la0484801
107. Dieter KM, Dymek CJ, Heimer NE, Rovang JW, Wilkes JS (1988) Ionic structure and interactions in 1-methyl-3-ethylimidazolium chloride-aluminum chloride molten salts. *Journal of the American Chemical Society* 110 (9):2722-2726. doi:10.1021/ja00217a004
108. He P, Liu H, Li Z, Li J (2005). *J Electrochem Soc* 152:E146
109. Yang M-H, Sun I-W (2003). *J Appl Electrochem* 33:1077
110. Zein El Abedin S, Moustafa E, Hempelmann R, Natter H, Endres F (2005). *Electrochem Commun* 7:1111
111. Zein El Abedin S, Moustafa E, Hempelmann R, Natter H, Endres F (2006). *Chem Phys Chem* 7:1535
112. Brausch N, Metlen A, Wasserscheid P (2004). *Chem Commun* 13:1552
113. NuLi Y, Yang J, Wang P (2006). *Appl Surf Sci* 252:8086
114. Wang P, NuLi Y, Wang J, Feng Z (2006). *Surf Coat Technol* 201:3783
115. Feng Z, NuLi Y, Wang J, Yang J (2006). *J Electrochem Soc* 135:C689
116. NuLi Y, Yang J, Wu R (2005). *Electrochem Commun* 7:1105
117. Katayama Y, Morita T, Yamagata M, Miura T (2003). *Electrochemistry* 71:1033
118. Howlett PC, MacFarlane DR, Hollenkamp AF (2004). *Electrochem Solid-State Lett* 7:A97
119. Zein El Abedin S, Welz-Biermann U, Endres F (2005). *Electrochem Commun* 7:941
120. Mukhopadhyay I, Aravinda CL, Borissov D, Freyland W (2005). *Electrochim Acta* 50:1275
121. Tsai M-C, Zhuang D-X, Chen P-Y (2010) Electrodeposition of macroporous silver films from ionic liquids and assessment of these films in the electrocatalytic reduction of nitrate. *Electrochimica Acta* 55 (3):1019-1027. doi:10.1016/j.electacta.2009.09.070
122. Tsai T-H, Thiagarajan S, Chen S-M (2010) Green Synthesis of Silver Nanoparticles Using Ionic Liquid and Application for the Detection of Dissolved Oxygen. *Electroanalysis* 22 (6):680-687. doi:10.1002/elan.200900410
123. An J, Wang D, Luo Q, Yuan X (2009) Antimicrobial active silver nanoparticles and silver/polystyrene core-shell nanoparticles prepared in room-temperature ionic liquid. *Materials Science and Engineering: C* 29 (6):1984-1989. doi:<http://dx.doi.org/10.1016/j.msec.2009.03.015>
124. Xu XH, Hussey CL (1992) ELECTRODEPOSITION OF SILVER ON METALLIC AND NONMETALLIC ELECTRODES FROM THE ACIDIC ALUMINUM CHLORIDE-1-METHYL-3-ETHYLIMIDAZOLIUM CHLORIDE MOLTEN-SALT. *Journal of the Electrochemical Society* 139 (5):1295-1300. doi:10.1149/1.2069399
125. A. Zell C, Endres F, Freyland W (1999) Electrochemical insitu STM study of phase formation during Ag and Al electrodeposition on Au(111) from a room temperature molten salt. *Physical Chemistry Chemical Physics* 1 (4):697-704. doi:10.1039/A808941H
126. Endres F, Freyland W (1998) Electrochemical Scanning Tunneling Microscopy Investigation of HOPG and Silver Electrodeposition on HOPG from the Acid Room-Temperature Molten Salt

- Aluminum Chloride–1-Methyl-3-butyl-imidazolium Chloride. *The Journal of Physical Chemistry B* 102 (50):10229-10233. doi:10.1021/jp9824048
127. Abbott AP, Nandhra S, Postlethwaite S, Smith EL, Ryder KS (2007) Electroless deposition of metallic silver from a choline chloride-based ionic liquid: a study using acoustic impedance spectroscopy, SEM and atomic force microscopy. *Physical Chemistry Chemical Physics* 9 (28):3735-3743. doi:10.1039/b703954a
128. Abbott AP, El Ttaib K, Frisch G, Ryder KS, Weston D (2012) The electrodeposition of silver composites using deep eutectic solvents. *Physical Chemistry Chemical Physics* 14 (7):2443-2449. doi:10.1039/c2cp23712a
129. Bomparola R, Caporali S, Lavacchi A, Bardi U (2007) Silver electrodeposition from air and water-stable ionic liquid: An environmentally friendly alternative to cyanide baths. *Surface & Coatings Technology* 201 (24):9485-9490. doi:10.1016/j.surfcoat.2007.04.008
130. Basile A, Bhatt AI, O'Mullane AP, Bhargava SK (2011) An investigation of silver electrodeposition from ionic liquids: Influence of atmospheric water uptake on the silver electrodeposition mechanism and film morphology. *Electrochimica Acta* 56 (7):2895-2905. doi:10.1016/j.electacta.2010.12.083
131. Serizawa N, Katayama Y, Miura T (2009) EQCM Measurement of Ag(I)/Ag Reaction in an Amide-Type Room-Temperature Ionic Liquid. *Journal of the Electrochemical Society* 156 (11):D503-D507. doi:10.1149/1.3223669
132. Fukui R, Katayama Y, Miura T (2011) The Influence of Potential on Electrodeposition of Silver and Formation of Silver Nanoparticles in Some Ionic Liquids. *Journal of the Electrochemical Society* 158 (9):D567-D572. doi:10.1149/1.3610202
133. Reyna-Gonzalez JM, Torriero AAJ, Siriwardana AI, Burgar IM, Bond AM (2011) Extraction of silver(I) from aqueous solutions in the absence and presence of copper(II) with a methimazole-based ionic liquid. *Analyst* 136 (16):3314-3322. doi:10.1039/c1an15103g
134. Köddermann T, Fumino K, Ludwig R, Canongia Lopes JN, Pádua AAH (2009) What Far-Infrared Spectra Can Contribute to the Development of Force Fields for Ionic Liquids Used in Molecular Dynamics Simulations. *ChemPhysChem* 10 (8):1181-1186. doi:10.1002/cphc.200900144
135. Ispas A, Poelleth M, Khanh Hoa Tran B, Bund A, Janek J (2011) Electrochemical deposition of silver from 1-ethyl-3-methylimidazolium trifluoromethanesulfonate. *Electrochimica Acta* 56 (28):10332-10339. doi:10.1016/j.electacta.2011.04.060
136. Suryanto BHR, Gunawan CA, Lu X, Zhao C (2012) Tuning the electrodeposition parameters of silver to yield micro/nano structures from room temperature protic ionic liquids. *Electrochimica Acta* 81:98-105. doi:10.1016/j.electacta.2012.07.066
137. Grishina EP, Pimenova AM, Ramenskaya LM (2009) Electrochemical Properties of the System of Ag-1-Butyl-3-Methylimidazolium Bromide Low-Temperature Ionic Liquid-Silver Bromide. *Russian Journal of Electrochemistry* 45 (12):1358-1362. doi:10.1134/s1023193509120076
138. Tai CC, Su FY, Sun IW (2005) Electrodeposition of palladium-silver in a Lewis basic 1-ethyl-3-methylimidazolium chloride-tetrafluoroborate ionic liquid. *Electrochimica Acta* 50 (28):5504-5509. doi:10.1016/j.electacta.2005.03.045
139. Dobbs W, Suisse J-M, Douce L, Welter R (2006) Electrodeposition of silver particles and gold nanoparticles from ionic liquid-crystal precursors. *Angewandte Chemie-International Edition* 45 (25):4179-4182. doi:10.1002/anie.200600929
140. Yeh FH, Tai CC, Huang JF, Sun IW (2006) Formation of porous silver by electrochemical alloying/dealloying in a water-insensitive zinc chloride-1-ethyl-3-methyl imidazolium chloride ionic liquid. *Journal of Physical Chemistry B* 110 (11):5215-5222. doi:10.1021/jp0552527
141. Kazeminezhad I, Barnes AC, Holbrey JD, Seddon KR, Schwarzacher W (2007) Templated electrodeposition of silver nanowires in a nanoporous polycarbonate membrane from a

nonaqueous ionic liquid electrolyte. *Applied Physics a-Materials Science & Processing* 86 (3):373-375. doi:10.1007/s00339-006-3783-x

142. El Abedin SZ, Endres F (2009) Electrodeposition of nanocrystalline silver films and nanowires from the ionic liquid 1-ethyl-3-methylimidazolium trifluoromethylsulfonate. *Electrochimica Acta* 54 (24):5673-5677. doi:10.1016/j.electacta.2009.05.005

143. Iida M, Baba C, Inoue M, Yoshida H, Taguchi E, Furusho H (2008) Ionic liquids of bis(alkylethylenediamine)silver(I) salts and the formation of silver(0) nanoparticles from the ionic liquid system. *Chemistry (Weinheim an der Bergstrasse, Germany)* 14 (16):5047-5056. doi:10.1002/chem.200701764

144. Bhatt AI, Bond AM (2008) Electrodeposition of silver from the 'distillable' ionic liquid, DIMCARB in the absence and presence of chemically induced nanoparticle formation. *Journal of Electroanalytical Chemistry* 619:1-10. doi:10.1016/j.jelechem.2008.02.029

145. Fu C, Zhou H, Wu H, Chen J, Kuang Y (2008) Research on electrochemical properties of nonaqueous ionic liquid microemulsions. *Colloid and Polymer Science* 286 (13):1499-1504. doi:10.1007/s00396-008-1921-z

146. Brooks NR, Schaltin S, Van Hecke K, Van Meervelt L, Fransaer J, Binnemans K (2012) Heteroleptic silver-containing ionic liquids. *Dalton Transactions* 41 (23):6902-6905. doi:10.1039/C2DT30725A

147. Schaltin S, Brooks NR, Stappers L, Van Hecke K, Van Meervelt L, Binnemans K, Fransaer J (2012) High current density electrodeposition from silver complex ionic liquids. *Physical Chemistry Chemical Physics* 14 (5):1706-1715. doi:10.1039/c2cp22987k

148. Chen P, Sun I (1999) Electrochemical study of copper in a basic 1-ethyl-3-methylimidazolium tetrafluoroborate room temperature molten salt. *Electrochimica Acta* 45:441-450

149. Murase K, Nitta K, Hirato T, Awakura Y (2001) Electrochemical behaviour of copper in trimethyl-n-hexylammonium bis((trimethyl)sulfonyl)amide, an ammonium imide type room temperature molten salt. *Journal of Applied Electrochemistry* 31:1389-1094

150. Abedin SZE, Saad AY, Farag HK, Borisenko N, Liu QX, Endres F (2007) Electrodeposition of Selenium, Indium and Copper in an air and water stable ionic liquids at variable temperatures. *Electrochimica Acta* 52:2746-2754

151. Leong T, Sun I, Deng M, Wu C, Chen P (2008) Electrochemical study of copper in 1-Ethyl-3-Methylimidazolium Dicyanamide room temperature ionic liquid. *Journal of the Electrochemical Society* 4:F55-F60

152. Brooks NR, Schaltin S, Hecke KV, Meervelt LV, Binnemans K, Fransaer J (2011) Copper(i)-containing Ionic Liquids for High-Rate Electrodeposition. *Chem Eur J* 17:5054-5059

153. Abbot AP, Ttaib KL, Frisch G, Mackenzie KJ, Ryder KL (2009) Electrodeposition of copper composites from deep eutectic solvents based choline chloride. *Phys Chem Chem Phys* 11:4269-4277

154. Ben Assaker I, Dhahbi M (2011) Electrochemical study and electrodeposition of copper in the hydrophobic tri-n-octylmethylammonium chloride ionic liquid media. *Journal of Molecular Liquids* 161 (1):13-18. doi:10.1016/j.molliq.2011.03.018

155. Hsieh Y-T, Leong T-I, Huang C-C, Yeh C-S, Sun IW (2010) Direct template-free electrochemical growth of hexagonal CuSn tubes from an ionic liquid. *Chemical Communications* 46 (3):484-486. doi:10.1039/b919298k

156. Chen P-Y, Deng M-J, Zhuang D-X (2009) Electrochemical codeposition of copper and manganese from room-temperature N-butyl-N-methylpyrrolidinium bis(trifluoromethylsulfonyl)imide ionic liquid. *Electrochimica Acta* 54 (27):6935-6940. doi:10.1016/j.electacta.2009.07.016

157. Jiang T, Brym MJC, Dube G, Lasia A, Brisard GM (2006) Electrodeposition of aluminium from ionic liquids: Part I - electrodeposition and surface morphology of aluminium from aluminium chloride (AlCl<sub>3</sub>)-1-ethyl-3-methylimidazolium chloride ( EMIm Cl) ionic liquids. *Surface & Coatings Technology* 201 (1-2):1-9. doi:10.1016/j.surfcoat.2005.10.046
158. Jiang T, Brym MJC, Dube G, Lasia A, Brisard GM (2006) Electrodeposition of aluminium from ionic liquids: Part II - studies on the electrodeposition of aluminum from aluminum chloride (AlCl<sub>3</sub>) - trimethylphenylammonium chloride (TMPAC) ionic liquids. *Surface & Coatings Technology* 201 (1-2):10-18. doi:10.1016/j.surfcoat.2005.12.024
159. Liu K-r, Liu Q, Han Q, Tu G-f (2011) Electrodeposition of Al on AZ31 magnesium alloy in TMPAC-AlCl<sub>3</sub> ionic liquids. *Transactions of Nonferrous Metals Society of China* 21 (9):2104-2110. doi:10.1016/s1003-6326(11)60980-1
160. Liu QX, El Abedin SZ, Endres F (2006) Electroplating of mild steel by aluminium in a first-generation ionic liquid: A green alternative to commercial Al-plating in organic solvents. *Surface & Coatings Technology* 201 (3-4):1352-1356. doi:10.1016/j.surfcoat.2006.01.065
161. Caporali S, Fossati A, Lavacchi A, Perissi I, Tolstogousov A, Bardi U (2008) Aluminium electroplated from ionic liquids as protective coating against Steel corrosion. *Corrosion Science* 50 (2):534-539. doi:10.1016/j.corsci.2007.08.001
162. Bardi U, Caporali S, Craig M, Giorgetti A, Perissi I, Nicholls JR (2009) Electrodeposition of aluminium film on P90 Li-Al alloy as protective coating against corrosion. *Surface and Coatings Technology* 203 (10-11):1373-1378. doi:<http://dx.doi.org/10.1016/j.surfcoat.2008.11.003>
163. Caporali S, Fossati A, Bardi U (2010) Oxidative post-treatments for enhanced corrosion resistance of aluminium electrodeposited from ionic liquids. *Corrosion Science* 52 (1):235-241. doi:<http://dx.doi.org/10.1016/j.corsci.2009.09.009>
164. Ali MR, Nishikata A, Tsuru T (1997) Electrodeposition of aluminum-chromium alloys from AlCl<sub>3</sub>-BPC melt and its corrosion and high temperature oxidation behaviors. *Electrochimica Acta* 42 (15):2347-2354. doi:[http://dx.doi.org/10.1016/S0013-4686\(96\)00418-5](http://dx.doi.org/10.1016/S0013-4686(96)00418-5)
165. Perre E, Nyholm L, Gustafsson T, Taberna P-L, Simon P, Edstrom K (2008) Direct electrodeposition of aluminium nano-rods. *Electrochemistry Communications* 10 (10):1467-1470. doi:10.1016/j.elecom.2008.07.032
166. Pomfret MB, Brown DJ, Epshteyn A, Purdy AP, Owirutsky JC (2008) Electrochemical Template Deposition of Aluminum Nanorods Using Ionic Liquids. *Chemistry of Materials* 20 (19):5945-5947. doi:10.1021/cm801983w
167. Gandhi T, Raja KS, Misra M (2008) Room temperature electrodeposition of aluminum antimonide compound semiconductor. *Electrochimica Acta* 53 (24):7331-7337. doi:10.1016/j.electacta.2008.04.014
168. Abbott AP, Qiu F, Abood HMA, Ali MR, Ryder KS (2010) Double layer, diluent and anode effects upon the electrodeposition of aluminium from chloroaluminate based ionic liquids. *Physical Chemistry Chemical Physics* 12 (8):1862-1872. doi:10.1039/b917351j
169. El Abedin SZ, Giridhar P, Schwab P, Endres F (2010) Electrodeposition of nanocrystalline aluminium from a chloroaluminate ionic liquid. *Electrochemistry Communications* 12 (8):1084-1086. doi:10.1016/j.elecom.2010.05.034
170. Pradhan D, Reddy RG (2009) EFFECT OF ELECTRODE SURFACE MODIFICATION ON DENDRITIC DEPOSITION OF ALUMINUM ON Cu SUBSTRATE USING EMIC-ALCl<sub>3</sub> IONIC LIQUID ELECTROLYTES. *Energy Technology Perspectives: Conservation, Carbon Dioxide Reduction and Production from Alternative Sources*.
171. El Abedin SZ, Moustafa EM, Hempelmann R, Natter H, Endres F (2005) Additive free electrodeposition of nanocrystalline aluminium in a water and air stable ionic liquid. *Electrochemistry Communications* 7 (11):1111-1116. doi:10.1016/j.elecom.2005.08.010



172. Rocher NM, Izgorodina EI, Ruether T, Forsyth M, MacFarlane DR, Rodopoulos T, Horne MD, Bond AM (2009) Aluminium Speciation in 1-Butyl-1-Methylpyrrolidinium Bis(trifluoromethylsulfonyl)amide/AlCl<sub>3</sub> Mixtures. *Chemistry-a European Journal* 15 (14):3435-3447. doi:10.1002/chem.200801641
173. Moustafa EM, El Abedin SZ, Shkurankov A, Zschippang E, Saad AY, Bund A, Endres F (2007) Electrodeposition of Al in 1-butyl-1-methylpyrrolidinium bis(trifluoromethylsulfonyl)amide and 1-ethyl-3-methylimidazolium bis(trifluoromethylsulfonyl)amide ionic liquids: In situ STM and EQCM studies. *Journal of Physical Chemistry B* 111 (18):4693-4704. doi:10.1021/jp0670687
174. El Abedin SZ, Moustafa EM, Hempelmann R, Natter H, Endres F (2006) Electrodeposition of nano- and microcrystalline aluminium in three different air and water stable ionic liquids. *Chemphyschem* 7 (7):1535-1543. doi:10.1002/cphc.200600095
175. Berg RW (2007) Raman Spectroscopy and Ab-Initio Model Calculations on Ionic Liquids. *Monatshefte für Chemie* 138:1045-1075
176. Umebayashi Y, Fujimori T, Sukizaki T, Asada M, Fujii K, Kanzaki R, Ishiguro S-i (2005) Evidence of Conformational Equilibrium of 1-Ethyl-3-methylimidazolium in Its Ionic Liquid Salts: Raman Spectroscopic Study and Quantum Chemical Calculations. *J Phys Chem A* 109: 8976-8982
177. Talaty ER, Raja S, Storhaug VJ, Do1lle A, Carper WR (2004) Raman and Infrared Spectra and ab Initio Calculations of C2-4MIM Imidazolium Hexafluorophosphate Ionic Liquids. *J Phys Chem B* 108:13177-13184
178. Liu Z, Huang S, Wang W (2004) A Refined Force Field for Molecular Simulation of Imidazolium-Based Ionic Liquids. *J Phys Chem B* 2004 108:12978-12989
179. Heimer NE, Sesto RED, Meng Z, Wilkes JS, Carper WR (2006) Vibrational spectra of imidazolium tetrafluoroborate ionic liquids. *Journal of Molecular Liquids* 124:84-95
180. Palomar J, Ferro VR, Gilarranz MA, Rodriguez JJ (2007) Computational approach to nuclear magnetic resonance in 1-Alkyl-3-methylimidazolium ionic liquids. *J Phys Chem B* 111:168-180
181. Umebayashi Y, Fujimori T, Sukizaki T, Asada M, Fujii K, Kanzaki R, Ishiguro S-i (2005) Evidence of Conformational Equilibrium of 1-Ethyl-3-methylimidazolium in Its Ionic Liquid Salts: Raman Spectroscopic Study and Quantum Chemical Calculations. *The Journal of Physical Chemistry A* 109 (40):8976-8982. doi:10.1021/jp053476j
182. Kemper V, Kirchner B (2010) The role of hydrogen atoms in interactions involving imidazolium-based ionic liquids. *Journal of Molecular Structure* 972 (1–3):22-34. doi:<http://dx.doi.org/10.1016/j.molstruc.2010.02.003>
183. KIEFER J, FRIES J, LEIPERTZ A (2007) Experimental Vibrational Study of Imidazolium-Based Ionic Liquids: Raman and Infrared Spectra of 1-Ethyl-3-methylimidazolium Bis(trifluoromethylsulfonyl)imide and 1-Ethyl-3-methylimidazolium Ethylsulfate. *APPLIED SPECTROSCOPY* 61 (12):1306-1311
184. Dhumal NR, Kim HJ, Kiefer J (2011) Electronic Structure and Normal Vibrations of the 1-Ethyl-3-methylimidazolium Ethyl Sulfate Ion Pair. *J Phys Chem A* 115: 3551–3558
185. Fujii K, Fujimori T, Takamuku T, Kanzaki R (2006) Conformational Equilibrium of Bis(trifluoromethanesulfonyl) Imide Anion of a Room-Temperature Ionic Liquid: Raman Spectroscopic Study and DFT Calculations. *J Phys Chem B* 110 (16):8179-8183
186. Fujii K, Seki S, Fukuda S, Kanzaki R, Takamuku T, Umebayashi Y, Ishiguro S-i (2007) Anion Conformation of Low-Viscosity Room-Temperature Ionic Liquid 1-Ethyl-3-methylimidazolium Bis(fluorosulfonyl) Imide. *J Phys Chem B* 111:12829-12833
187. Martinelli A, Matic A, Johansson P, Jacobsson P, Borjesson L, Fernicola A, Panero S, Scrosati B, Ohno H (2010) Conformational evolution of TFSI- in protic and aprotic ionic liquids. *J Raman Spectrosc* 42:522-528

188. Johansson P, Gejji SP, Tegenfeldt J, Lindgren J (1998) The imide ion: potential energy surface and. *Electrochim Acta* 43:1375-1379
189. Rey I, Johansson P, Lindgren J, Lassègues JC, Grondin J, Servant L (1998) Spectroscopic and Theoretical Study of (CF<sub>3</sub>SO<sub>2</sub>)<sub>2</sub>N<sup>-</sup> (TFSI<sup>-</sup>) and (CF<sub>3</sub>SO<sub>2</sub>)<sub>2</sub>NH (HTFSI). *The Journal of Physical Chemistry A* 102 (19):3249-3258. doi:10.1021/jp980375v
190. Shigeto S, Hamaguchi H-o (2006) Evidence for mesoscopic local structures in ionic liquids: CARS signal spatial distribution of Cnmim[PF<sub>6</sub>] (n=4,6,8). *Chemical Physics Letters* 427 (4–6):329-332. doi:<http://dx.doi.org/10.1016/j.cplett.2006.07.004>
191. Lassègues J-C, Grondin J, Cavagnat D, Johansson P (2009) New Interpretation of the CH Stretching Vibrations in Imidazolium-Based Ionic Liquids. *The Journal of Physical Chemistry A* 113 (23):6419-6421. doi:10.1021/jp903160r
192. Matsumoto H (2005) Electrochemical Windows of Room-Temperature Ionic Liquids. In: *Electrochemical Aspects of Ionic Liquids*. John Wiley & Sons, Inc., pp 35-54. doi:10.1002/0471762512.ch4
193. Zhao Y, Truhlar D (2008) The M06 suite of density functionals for main group thermochemistry, thermochemical kinetics, noncovalent interactions, excited states, and transition elements: two new functionals and systematic testing of four M06 functionals and 12 other functionals. *Theor Chem Account* 119 (5-6):525-525. doi:10.1007/s00214-007-0401-8
194. Grondin J, Lassegues J-C, Cavagnat D, Buffeteau T, Johansson P, Holomb R (2011) Revisited vibrational assignments of imidazolium-based ionic liquids. *J Raman Spectrosc* 42:733–743
195. Noack K, Schulz PS, Paape N, Kiefer J, Wasserscheid P, Leipertz A (2010) The role of the C2 position in interionic interactions of imidazolium based ionic liquids: a vibrational and NMR spectroscopic study. *Phys Chem Chem Phys* 12:14153-14161
196. Lassegues J-C, Grondin J, Cavagnat D, Johansson P (2009) New Interpretation of the CH Stretching Vibrations in Imidazolium-Based Ionic Liquids. *J Phys Chem A* 113 (23):6419–6421
197. Wulf A, Fumino K, Ludwig R (2009) Comment on “New Interpretation of the CH Stretching Vibrations in Imidazolium-Based Ionic Liquids”. *The Journal of Physical Chemistry A* 114 (1):685-686. doi:10.1021/jp9080146
198. Herstedt M, Henderson WA, Smirnov M, Ducasse L, Servant L, Talaga D, Lassègues JC (2006) Conformational isomerism and phase transitions in tetraethylammonium bis(trifluoromethanesulfonyl)imide Et<sub>4</sub>N<sup>+</sup>TFSI<sup>-</sup>. *Journal of Molecular Structure* 783 (1–3):145-156. doi:<http://dx.doi.org/10.1016/j.molstruc.2005.08.028>
199. Fumino K, Wulf A, Ludwig R (2008) Strong, Localized, and Directional Hydrogen Bonds Fluidize Ionic Liquids. *Angewandte Chemie International Edition* 47 (45):8731-8734. doi:10.1002/anie.200803446
200. Fumino K, Wulf A, Ludwig R (2008) The Cation–Anion Interaction in Ionic Liquids Probed by Far-Infrared Spectroscopy. *Angewandte Chemie International Edition* 47 (20):3830-3834. doi:10.1002/anie.200705736
201. Wulf A, Fumino K, Ludwig R (2010) Spectroscopic Evidence for an Enhanced Anion–Cation Interaction from Hydrogen Bonding in Pure Imidazolium Ionic Liquids. *Angewandte Chemie International Edition* 49 (2):449-453. doi:10.1002/anie.200905437
202. Buffeteau T, Grondin J, Danten Y, Lassègues J-C (2010) Imidazolium-Based Ionic Liquids: Quantitative Aspects in the Far-Infrared Region. *The Journal of Physical Chemistry B* 114 (22):7587-7592. doi:10.1021/jp102087m
203. Buffeteau T, Grondin J, Lassègues J-C (2010) Infrared Spectroscopy of Ionic Liquids: Quantitative Aspects and Determination of Optical Constants. *Applied Spectroscopy* 64 (1):112-119. doi:10.1366/000370210790572089



204. Lassegues J-C, Grondin J, Talaga D (2006) Lithium solvation in bis(trifluoromethylsulfonyl)imide-based ionic liquids. *Phys Chem Chem Phys* 8:5629-5632
205. Kassègues J-C, Grondin J, Aupetit C, Johansson P (2009) Spectroscopic identification of the lithium ion transporting species in LiTFSI-doped ionic liquids. *J Phys Chem A* 113:305-314
206. Umebayashi Y, Mitsugi T, Fukuda S, Fujimori T, Fujii K, Kanzaki R, Takeuchi M, Ishiguro S-I (2007) Lithium ion solvation in room temperature ionic liquids involving bis(trifluoromethylsulfonyl) Imide anions studied by Raman spectroscopy and DFT calculations *J; PHys Chem B* 111:13028-13032
207. Duluard S, Grondin J, Bruneel J-L, Pianet I, Grélard A, Campet G, M6H. D, J-C. L (2008) Lithium solvation and diffusion in the 1-butyl-3-methylimidazolium bis(trifluoromethanesulfonyl)imide ionic liquid. *J Raman Spectrosc* 39:627-632
208. Zhang Q-G, Wang N-N, Yu Z-W (2010) The Hydrogen Bonding Interactions between the Ionic Liquid 1-Ethyl-3-Methylimidazolium Ethyl Sulfate and Water. *J Phys Chem B* 114:4747–4754
209. Sarkar S, Pramanik R, Ghatak C, Setua P, Sarkar N (2010) Probing the Interaction of 1-Ethyl-3-methylimidazolium Ethyl Sulfate ([Emim][EtSO<sub>4</sub>]) with Alcohols and Water by Solvent and Rotational Relaxation. *J Phys Chem B* 114:2779–2789
210. Miki H, Hayashi S, Kikura H, Hamaguchi H-o (2006) Raman spectra indicative of unusual water structure in crystals formed from a room-temperature ionic liquid. *J Raman Spectrosc* 37:1242–1243
211. Fujisawa T, Fukuda M, Terazima M (2006) Raman Spectroscopic Study on Solvation of Diphenylcyclopropanone and Phenol Blue in Room Temperature Ionic Liquids. *J Phys Chem A* 110: 6164-6172
212. Stricker M, Oelkers B, Rosenau CP, Sundermeyer J (2013) Copper(I) and Silver(I) Bis(trifluoromethanesulfonyl)imide and Their Interaction with an Arene, Diverse Olefins, and an NTf<sub>2</sub>--Based Ionic Liquid. *Chemistry – A European Journal* 19 (3):1042-1057. doi:10.1002/chem.201201740
213. Eiden P, Liu Q, El Abedin SZ, Endres F, Krossing I (2009) An Experimental and Theoretical Study of the Aluminium Species Present in Mixtures of AlCl<sub>3</sub> with the Ionic Liquids BMP Tf<sub>2</sub>N and EMIm Tf<sub>2</sub>N. *Chemistry-a European Journal* 15 (14):3426-3434. doi:10.1002/chem.200801616
214. Sakar S, Mandal S, Ghatak C, Rao VG, Ghosh S, Sarkar N (2012) Photoinduced electron transfer in an imidazolium ionic liquid and its binary mixtures with water, methanol and 2-propanol: Appearance of Marcus-type of inversion. *J Phys Chem B* 116:1335
215. Noack K, Leipertz A, Kiefer J (2012) Molecular interactions and macroscopic effects in binary mixtures of an imidazolium ionic liquid with water, methanol, and ethanol. *Journal of Molecular Structure* 1018:45-53
216. Gale RJ, Osteryoung RA (1980). *Electrochim Acta* 25:1527
217. Nanjundiah C, McDevitt SF, Kock VR (1997). *J Electrochem Soc* 144:3392
218. Kornyshev AA (2007) Double-Layer in Ionic Liquids: Paradigm Change? *The Journal of Physical Chemistry B* 111 (20):5545-5557. doi:10.1021/jp067857o
219. Oldham KB (2008) A Gouy–Chapman–Stern model of the double layer at a (metal)/(ionic liquid) interface. *Journal of Electroanalytical Chemistry* 613 (2):131-138. doi:<http://dx.doi.org/10.1016/j.jelechem.2007.10.017>
220. Baldelli S (2005) Probing Electric Fields at the Ionic Liquid–Electrode Interface Using Sum Frequency Generation Spectroscopy and Electrochemistry. *The Journal of Physical Chemistry B* 109 (27):13049-13051. doi:10.1021/jp052913r
221. Baldelli S (2008) Surface Structure at the Ionic Liquid–Electrified Metal Interface. *Accounts of Chemical Research* 41 (3):421-431. doi:10.1021/ar700185h

222. Peñalber CY, Baldelli S (2012) Observation of Charge Inversion of an Ionic Liquid at the Solid Salt–Liquid Interface by Sum Frequency Generation Spectroscopy. *The Journal of Physical Chemistry Letters* 3 (7):844-847. doi:10.1021/jz3000917
223. Baldelli S (2012) Interfacial Structure of Room-Temperature Ionic Liquids at the Solid–Liquid Interface as Probed by Sum Frequency Generation Spectroscopy. *The Journal of Physical Chemistry Letters* 4 (2):244-252. doi:10.1021/jz301835j
224. Santos VO, Alves MB, Carvalho MS, Suarez PAZ, Rubim JC (2006) Surface-Enhanced Raman Scattering at the Silver Electrode/Ionic Liquid (BMIPF6) Interface†. *The Journal of Physical Chemistry B* 110 (41):20379-20385. doi:10.1021/jp0643348
225. Yuan Y-X, Niu T-C, Xu M-M, Yao J-L, Gu R-A (2010) Probing the adsorption of methylimidazole at ionic liquids/Cu electrode interface by surface-enhanced Raman scattering spectroscopy. *Journal of Raman Spectroscopy* 41 (5):516-523. doi:10.1002/jrs.2480
226. Egerton RF (2005) *Physical Principles of Electron Microscopy. An Introduction to TEM, SE; and AEM.* Springer Science+Business Media, Inc., New York
227. Williams DB, Carter CB (1996) *Transmission Electron Microscopy: A Textbook for Materials Science : Basics, Diffraction, Imaging, Spectrometry.* Springer,
228. Cullity B (1956) *Elements of X-ray diffraction.* Addison-Wesley Publishing Company, Inc., Reading
229. Fischer-Cripps AC (2011) *Nanoindentation. Mechanical Engineering Series.* Springer, New York and London
230. Fumino K, Wittler K, Ludwig R (2012) The Anion Dependence of the Interaction Strength between Ions in Imidazolium-Based Ionic Liquids Probed by Far-Infrared Spectroscopy. *The Journal of Physical Chemistry B* 116 (31):9507-9511. doi:10.1021/jp306173t
231. Endo T, Kato T, Nishikawa K (2010) Effects of Methylation at the 2 Position of the Cation Ring on Phase Behaviors and Conformational Structures of Imidazolium-Based Ionic Liquids. *The Journal of Physical Chemistry B* 114 (28):9201-9208. doi:10.1021/jp104123v
232. Umebayashi Y, Mitsugi T, Fujii K, Seki S, Chiba K, Yamamoto H, Canongia Lopes JN, Pádua AIAH, Takeuchi M, Kanzaki R, Ishiguro S-i (2009) Raman Spectroscopic Study, DFT Calculations and MD Simulations on the Conformational Isomerism of N-Alkyl-N-methylpyrrolidinium Bis-(trifluoromethanesulfonyl) Amide Ionic Liquids. *The Journal of Physical Chemistry B* 113 (13):4338-4346. doi:10.1021/jp9009146
233. Holomb R, Martinelli A, Albinsson I, Lassègues JC, Johansson P, Jacobsson P (2008) Ionic liquid structure: the conformational isomerism in 1-butyl-3-methyl-imidazolium tetrafluoroborate ([bmim][BF4]). *Journal of Raman Spectroscopy* 39 (7):793-805. doi:10.1002/jrs.1912
234. Wulf A, Fumino K, Ludwig R, Taday PF (2010) Combined THz, FIR and Raman Spectroscopy Studies of Imidazolium-Based Ionic Liquids Covering the Frequency Range 2–300 cm<sup>−1</sup>. *ChemPhysChem* 11 (2):349-353. doi:10.1002/cphc.200900680
235. Jeon Y, Sung J, Kim D, Seo C, Cheong H, Ouchi Y, Ozawa R, Hamaguchi H-o (2008) Structural Change of 1-Butyl-3-methylimidazolium Tetrafluoroborate + Water Mixtures Studied by Infrared Vibrational Spectroscopy. *The Journal of Physical Chemistry B* 112 (3):923-928. doi:10.1021/jp0746650
236. Lassègues JC, Grondin J, Holomb R, Johansson P (2007) Raman and ab initio study of the conformational isomerism in the 1-ethyl-3-methyl-imidazolium bis(trifluoromethanesulfonyl)imide ionic liquid. *Journal of Raman Spectroscopy* 38 (5):551-558. doi:10.1002/jrs.1680
237. N.Gobout, Salahub DR, Andzelm J, Winner E (1992). *Can J Chem* 70:560
238. Holbrey JD, Reichert WM, Swatloski RP, Broker GA, Pitner WR, Seddon KR, Rogers RD (2002) Efficient, halide free synthesis of new, low cost ionic liquids: 1,3-dialkylimidazolium salts

- containing methyl- and ethyl-sulfate anions. *Green Chemistry* 4 (5):407-413.  
doi:10.1039/b204469b
239. Yang JZ, Wang B, Zhang QG, Tong J (2007) Study on solid-liquid phase equilibria in ionic liquid - 1. The solubility of alkali chloride (MCl) in ionic liquid EMISE. *Fluid Phase Equilibria* 251 (1):68-70.  
doi:10.1016/j.fluid.2006.10.018
240. Chen PY, Sun IW (1999) Electrochemical study of copper in a basic 1-ethyl-3-methylimidazolium tetrafluoroborate room temperature molten salt. *Electrochimica Acta* 45 (3):441-450. doi:10.1016/s0013-4686(99)00275-3
241. Murase K, Nitta K, Hirato T, Awakura Y (2001) Electrochemical behaviour of copper in trimethyl-n-hexylammonium bis((trifluoromethyl)sulfonyl)amide, an ammonium imide-type room temperature molten salt. *Journal of Applied Electrochemistry* 31 (10):1089-1094.  
doi:10.1023/a:1012255601793
242. Leong TI, Sun IW, Deng MJ, Wu CM, Chen PY (2008) Electrochemical study of copper in the 1-ethyl-3-methylimidazolium dicyanamide room temperature ionic liquid. *Journal of the Electrochemical Society* 155 (4):F55-F60. doi:10.1149/1.2840627
243. Greef R, Peat R, Peter L, Pletcher D, Robinson J (1990) *Instrumental Methods in Electrochemistry*. Ellis Horwood Limited, Chichester
244. O'Bockris JOM, Reddy AKN (1970) *Modern Electrochemistry*, vol 1. Plenum Press, New York
245. Fukui R, Katayama Y, Miura T (2010) The Influence of Potential Under Diffusion-Controlled Region on Electrodeposition of Silver in an Amide-Type Ionic Liquid. In: Fox DM, Mizuhata M, DeLong HC, Mantz RA, Trulove PC (eds) *Molten Salts and Ionic Liquids 17*, vol 33. ECS Transactions, vol 7. pp 555-561. doi:10.1149/1.3484813
246. Chiappe C, Malvaldi M, Melai B, Fantini S, Bardi U, Caporali S (2010) An unusual common ion effect promotes dissolution of metal salts in room-temperature ionic liquids: a strategy to obtain ionic liquids having organic-inorganic mixed cations. *Green Chemistry* 12 (1):77-80.  
doi:10.1039/B919111A
247. Chiappe C, Malvaldi M (2010) Highly concentrated "solutions" of metal cations in ionic liquids: current status and future challenges. *Physical Chemistry Chemical Physics* 12 (37):11191-11196.  
doi:10.1039/c001796e
248. Murase K, Nitta K, Hirato T, Awakura Y (2000) Electrochemical behavior of copper in ammonium imide type room temperature molten salt. *Second International Conference on Processing Materials for Properties*.
249. Vainikka T, Lloyd D, Murtomaki L, Manzanares JA, Kontturi K (2013) Electrochemical study of copper chloride complexes in the RTIL 1-butyl-1-methylpyrrolidinium bis(trifluoromethylsulfonyl)imide. *Electrochimica Acta* 87:739-748.  
doi:10.1016/j.electacta.2012.09.062
250. Katsyuba SA, Zvereva EE, Vidiš A, Dyson PJ (2006) Application of Density Functional Theory and Vibrational Spectroscopy Toward the Rational Design of Ionic Liquids. *The Journal of Physical Chemistry A* 111 (2):352-370. doi:10.1021/jp064610i
251. Nanjundiah C, Osteryoung RA (1983) Electrochemical Studies of Cu(I) and Cu(II) in an Aluminum Chloride-N-(n-Butyl)Pyridinium Chloride Ionic Liquid. *Journal of The Electrochemical Society* 130 (6):1312-1318. doi:10.1149/1.2119944
252. Jahn HA, Teller E (1937) Stability of Polyatomic Molecules in Degenerate Electronic States. I. Orbital Degeneracy. *Proceedings of the Royal Society of London Series A - Mathematical and Physical Sciences* 161 (905):220-235. doi:10.1098/rspa.1937.0142
253. Abbott AP, El Ttaib K, Frisch G, McKenzie KJ, Ryder KS (2009) Electrodeposition of copper composites from deep eutectic solvents based on choline chloride. *Physical Chemistry Chemical Physics* 11 (21):4269-4277. doi:10.1039/b817881j

254. Zhao H, Chang J, Boika A, Bard AJ (2013) Electrochemistry of High Concentration Copper Chloride Complexes. *Analytical Chemistry* 85 (16):7696-7703. doi:10.1021/ac4016769
255. Laher TM, Hussey CL (1983) Copper(I) and copper(II) chloro complexes in the basic aluminum chloride-1-methyl-3-ethylimidazolium chloride ionic liquid. *Inorganic Chemistry* 22 (22):3247-3251. doi:10.1021/ic00164a016
256. Rodopoulos T, Smith L, Horne MD, Ruether T (2010) Speciation of Aluminium in Mixtures of the Ionic Liquids C(3)mpip NTf2 and C(4)mpyr NTf2 with AlCl3: An Electrochemical and NMR Spectroscopy Study. *Chemistry-a European Journal* 16 (12):3815-3826. doi:10.1002/chem.200902753
257. Wells AF (1984) *Structural Inorganic Chemistry*. 5th edn. Oxford Press, Oxford
258. Bozzini B, Tondo E, Bund A, Ispas A, Mele C (2011) Electrodeposition of Au from EMIm TFSA room-temperature ionic liquid: An electrochemical and Surface-Enhanced Raman Spectroscopy study. *Journal of Electroanalytical Chemistry* 651 (1):1-11. doi:10.1016/j.jelechem.2010.11.015
259. Liu B, Yu X-Y, Zhu Z, Hua X, Yang L, Wang Z (2014) In situ chemical probing of the electrode-electrolyte interface by ToF-SIMS. *Lab on a Chip* 14 (5):855-859. doi:10.1039/C3LC50971K
260. Deng M-J, Chen P-Y, Leong T-I, Sun IW, Chang J-K, Tsai W-T (2008) Dicyanamide anion based ionic liquids for electrodeposition of metals. *Electrochemistry Communications* 10 (2):213-216. doi:10.1016/j.elecom.2007.11.026
261. Brooks NR, Schaltin S, Van Hecke K, Van Meervelt L, Binnemans K, Fransaer J (2011) Copper(I)-Containing Ionic Liquids for High-Rate Electrodeposition. *Chemistry-a European Journal* 17 (18):5054-5059. doi:10.1002/chem.201003209
262. Schaltin S, Brooks NR, Binnemans K, Fransaer J (2011) Electrodeposition from Cationic Cuprous Organic Complexes: Ionic Liquids for High Current Density Electroplating. *Journal of the Electrochemical Society* 158 (1):D21-D27. doi:10.1149/1.3512905
263. Rodriguez V, Grondin J, Adamietz F, Danten Y (2010) Local structure in ionic liquids investigated by hyper-Rayleigh scattering. *J Phys Chem B* 114:15057-15065
264. Lee C, Yang W, Parr RG (1988) Development of the Colle-Salvetti correlation-energy formula into a functional of the electron density. *Phys Rev B* 37:785-789
265. Yokozeki A, Kasprzak DJ, Shiflett MB (2007) Thermal effect on C-H stretching vibrations of the imidazolium ring in ionic liquids. *Physical Chemistry Chemical Physics* 9 (36):5018-5026. doi:10.1039/B706497G



## 1 Annex 1

### 1.1 Density Functional Theory (DFT) calculations

DFT calculations were performed by using the Gaussian 03 program. For both the pure ionic liquids of [EMIM] [TFSI] and [EMIM] [EtSO<sub>4</sub>], double cation-anion pair models (IP<sub>2</sub>) were used, as shown in Figures A1.1 and A1.2 respectively. Past calculations have shown that the data calculated by using the IP<sub>2</sub> model are in better agreement with the experimental Raman and IR spectra than those calculated by using a single cation-anion pair model (IP) [263].

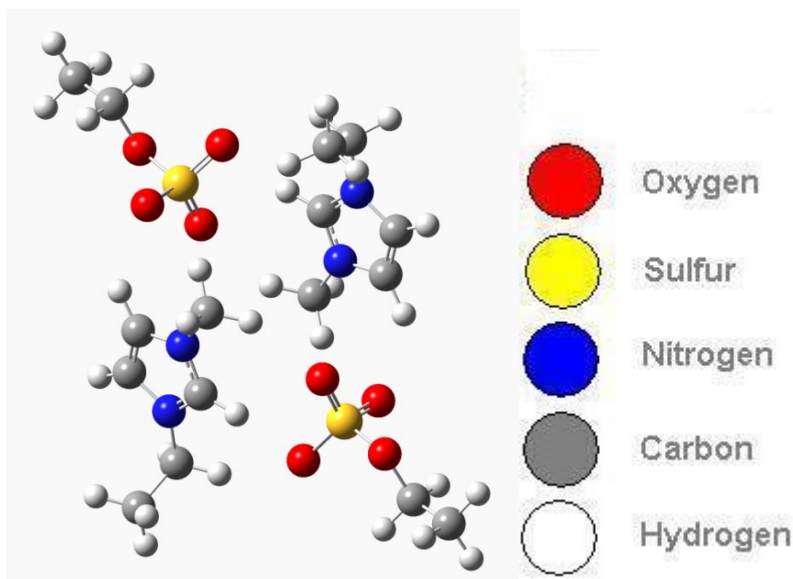


Figure A1.1: Double cation-anion pair model (IP<sub>2</sub>) for the [EMIM] [EtSO<sub>4</sub>] ionic liquid.

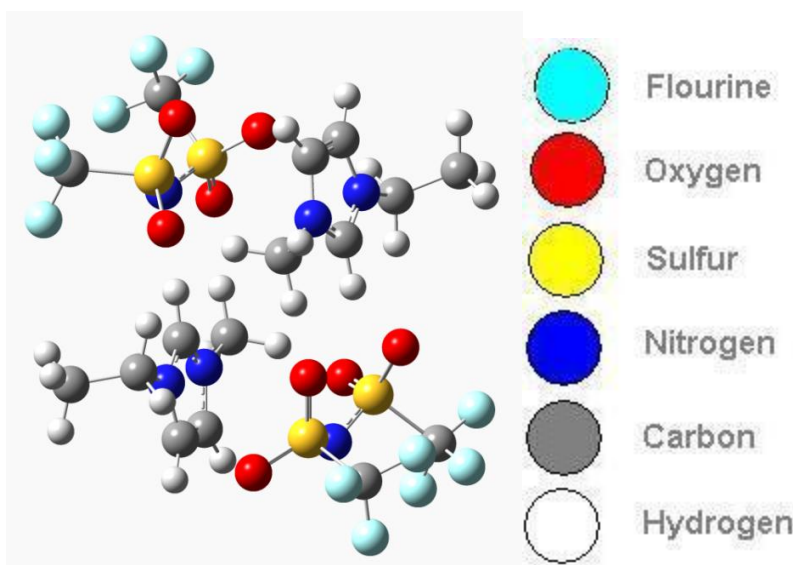


Figure A1.2: Double cation-anion pair model (IP<sub>2</sub>) for the [EMIM] [TFSI] ionic liquid.

For [EMIM] [EtSO<sub>4</sub>] – CuCl<sub>2</sub> solutions, two different models were used for the DFT calculation. The first model was a Cu ion bidentately coordinated by two EtSO<sub>3</sub><sup>−</sup> anions and two EMIM cations, as shown in Figure A1.3. The second model was a Cu ion bidentately coordinated by two EtSO<sub>3</sub><sup>−</sup> anions, two chloride anions and two EMIM cations, as shown in Figure A1.4. The frequency calculations were performed by using the Lee-Yang-Parr correlation functional (B3LYP) [264]. The basis set 6-31+ G(d,p) was used for the O, N, C and Cl atoms, while the basis set MQZVP was used for the heavier S and Cu atoms. Besides the standard harmonic wavenumber calculations, anharmonic wavenumber calculations were also carried out for the C-H region in the pure [EMIM] [EtSO<sub>4</sub>] and [EMIM] [EtSO<sub>4</sub>] – CuCl<sub>2</sub> solutions in order to determine the wavenumbers of the overtone and combinational bands [194].

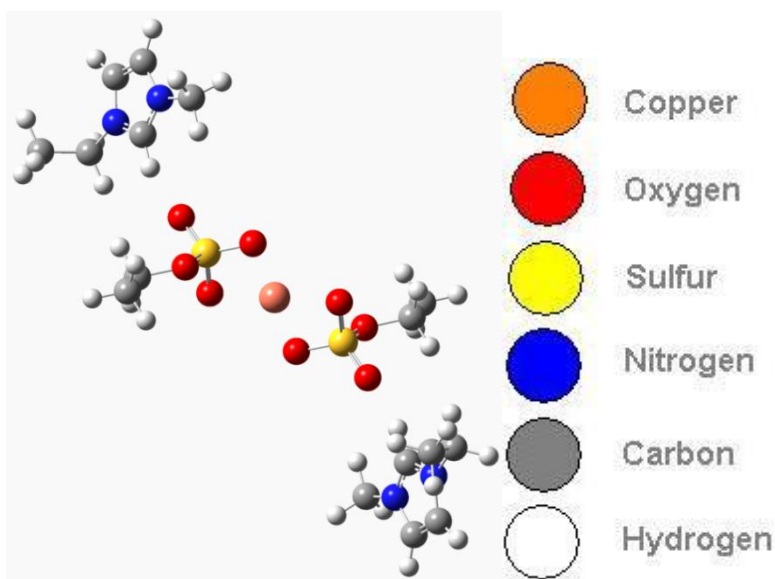


Figure A1.3: A copper ion is bidentately coordinated by two EtSO<sub>3</sub><sup>−</sup> anions and two EMIM cations.

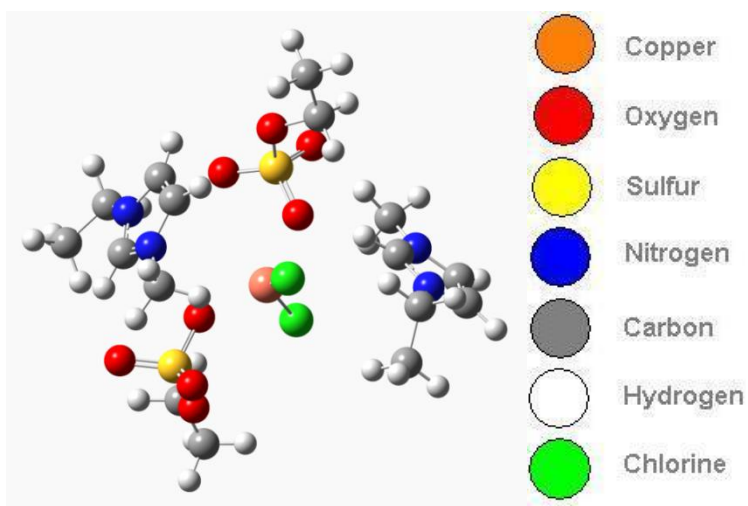


Figure A1.4: A copper ion is bidentately coordinated by two EtSO<sub>3</sub><sup>−</sup> anions, two chloride anions and two EMIM cations.

For the [EMIM] [TFSI] – AgTFSI solution, a model where the  $\text{Ag}^+$  cation is bidentately coordinated by three [TFSI] anions and two EMIM cations was used for the DFT calculations, as shown in Figure A1.4. The frequency calculations were performed by using the Lee-Yang-Parr correlation functional (B3LYP) [264]. Several basis sets were used in order to best describe the properties of the atoms making up [EMIM] [TFSI} and AgTFSI. The O, N, and C atoms were described by using the basis set 6-31+ G(d,p), the F atoms were described by using the basis set 6-311+ G(d,p), the S atoms were described by using the basis set WQZVP and the Ag atom was described by using the basis set DGDZVP.

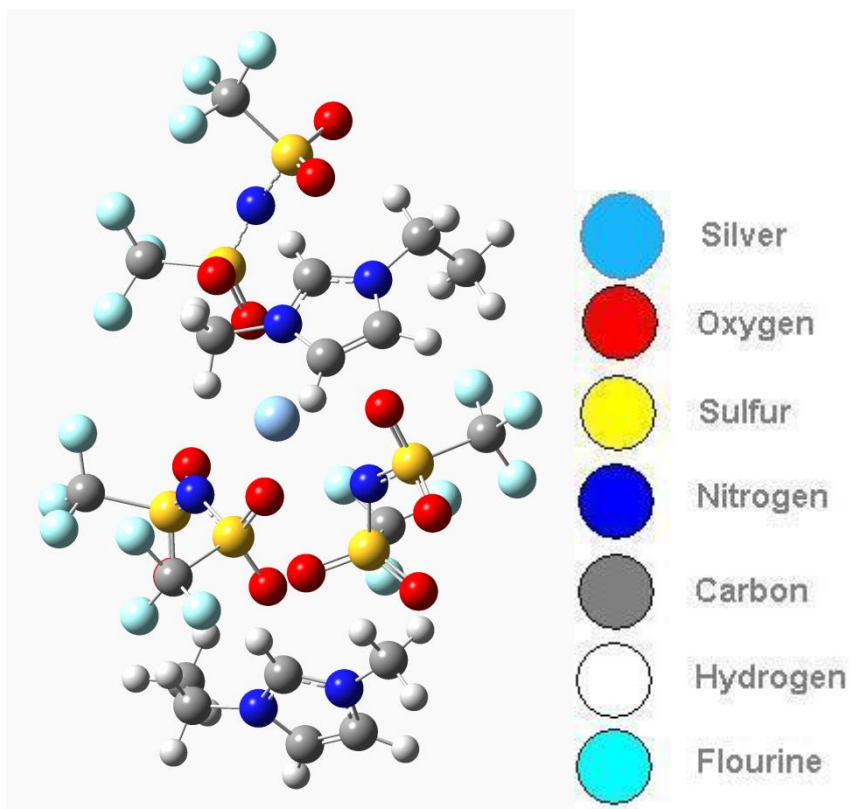


Figure A1.5: A silver ion is tridentately coordinated by two  $\text{TFSI}^-$  anions and two EMIM cations.



## 1.2 Full assignment

The tables showing the full assignment for the [EMIM] [TFSI] and [EMIM] [EtSO<sub>4</sub>] pure ionic liquids and the solutions of CuCl<sub>2</sub> + [EMIM] [EtSO<sub>4</sub>] and AgTFSI + [EMIM] [TFSI] are shown below.

### 1.2.1 Pure [EMIM] [EtSO<sub>4</sub>]

Table A1.1: Assignments of the vibrational bands of [EMIM] [EtSO<sub>4</sub>] in the 200 to 1600 cm<sup>-1</sup> region obtained from the experimental IR and Raman spectra in conjunction with the theoretical DFT calculated spectra based on the structure in Figure A1.1.

Experimental Bands (cm <sup>-1</sup> )		DFT calculated bands (cm <sup>-1</sup> )		Intensity		Assignment
IR	Raman	EMIM	EtSO <sub>4</sub>	IR	Raman	
245	245		250.0	1.8	0.5	Rock. (ρ) CH <sub>3</sub> (ethyl, anion)
300	295	300-303		6.9	0.5	Rock. (ρ) CH <sub>3</sub> , CH <sub>2</sub> (cation)
337	342		337.5	18.7	7.9	Bend. (δ) O-C-C(CH <sub>3</sub> ) (anion)
418	416		404.0-414.7	26.6	0.5	Bend. (δ) O-S-O (SO <sub>3</sub> )
		429-433		10.1	1.0	Bend. (δ) CNCH <sub>3</sub> , CNCH <sub>2</sub>
567	566		555-556	25.7	6.0	Bend. (δ) O-S-O (SO <sub>3</sub> ) ⊗ Bend. (δ) C <sub>(CH<sub>2</sub>)</sub> -O-S(SO <sub>3</sub> )
579	578		569-571	92.4	2.3	Bend. O-S-O (SO <sub>3</sub> ) ⊗ Twist. (τ) (SO <sub>3</sub> )
	598		600	5.4	10.9 P	Sym. Str. (ν <sub>s</sub> ) NCH <sub>2</sub> ; (ν) NCH <sub>3</sub> ⊗ Bend. (δ) N-C-C ⊗ Bend. (δ) C-N-C (ring)
621			618.0	150.5	2.6	Sym. Bend. (δ <sub>s</sub> ) SO <sub>3</sub> ⊗ Bend. (δ) (CH <sub>2</sub> )C-O-S(SO <sub>3</sub> )
650{		636.7-637.8		20.6	1.2	Vib. (γ) NCH <sub>3</sub> ; Twist. (τ) C-N, C-C (ring)
	648	660-662.4		47.2	1.0	Vib. (γ) NCH <sub>2</sub> ; Twist. (τ) C-N, C-C (ring)
	702	705		11.0	4.9	Asym. Str. (ν <sub>a</sub> ) NCH <sub>2</sub> , NCH <sub>3</sub> ⊗ Bend. (δ) N-C-C ⊗ Bend. (δ) C-N-C (ring)
734	734	751.5		106.2	2.1	Vib. (γ) C <sub>(4,5)</sub> H ⊗ (γ) C <sub>(2)</sub> H
766	766		771.7-773.2	427.0	31.2 P	Str. (ν) O-S (SO <sub>3</sub> ) ⊗ Bend. (δ) O-C-C(CH <sub>3</sub> )
805	805	805-811		6.6	0.7	Rock. (ρ) CH <sub>2</sub> , CH <sub>3</sub> (ethyl, cation)
			821.1	0.4	0.7	Rock. (ρ) CH <sub>2</sub> , CH <sub>3</sub> (ethyl, anion)
850		882.1-899.7		151.0	8.4	p.p. Vib. (γ) C <sub>(4,5)</sub> H ⊗ (γ) C <sub>(2)</sub> H
916			925.9-927.4	304.9	2.1	Bend. (δ) C(CH <sub>2</sub> )CH(CH <sub>3</sub> ) (anion)
960	960	964.2		6.9	15.2	Str. (ν) C-C (ethyl, cation)
1020	1020		1029.6	764.8	0.	p.p. Asym Str. (ν <sub>a</sub> ) C(CH <sub>2</sub> )-O-S(SO <sub>3</sub> )
			1032.1	0.2	61.4 P	p.p. Asym Str. (ν <sub>a</sub> ) S-O(SO <sub>3</sub> )
		1032.8-1033.8				Str. (ν) C-N (ring); Bend. (δ) C-N-C (ring)
		1048		18.0	18.4	Str. (ν) C-N (ring); Bend. (δ) C-N-C (ring)
1061	1061		1068.2	51.4	28.0	Str. (ν) O-C(CH <sub>2</sub> )-C(CH <sub>3</sub> )
1095	1091	1105.5		5.3	12.1 P	Rock. (ρ) CH <sub>3</sub> (ethyl, cation)
1109	1109	1121.3		22.8	3.2 P	Rock. (ρ) CH <sub>3</sub> (methyl, cation) ⊗ Bend. (δ) C <sub>(4,5)</sub> H
		1129.6		10.7	9.7	Rock. (ρ) CH <sub>3</sub> (ethyl, anion)
		1132-1134		4.2	9.1	Bend. (δ) C <sub>(4,5)</sub> H ⊗ Bend. (δ) C <sub>(2)</sub> H
		1140		3.9	8.7	Rock. (ρ) CH <sub>2</sub> (ethyl, cation) ⊗ Bend. (δ) C <sub>(4,5)</sub> H ⊗ Bend. (δ) C <sub>(2)</sub> H
1172	1175	1163.8-1173.9		35.5	4.8	Rock. (ρ) CH <sub>3</sub> (methyl, cation) ⊗ Bend. (δ) C <sub>(4,5)</sub> H ⊗ Bend. (δ) C <sub>(2)</sub> H
			1183.0	4.5	1.3	Rock. (ρ) CH <sub>2</sub> (ethyl, anion)
1225	1224		1221.9-1223.3	853.7	13.2	p.p. Asym Str. (ν <sub>a</sub> ) S-O (SO <sub>3</sub> ) ⊗ Rock.(ρ) CH <sub>2</sub> (ethyl, anion)

1246	1252		1239.3-1247.1	606.0	8.7	i.p. Asym Str. ( $\nu_a$ ) S-O ( $\text{SO}_3$ ) $\otimes$ Bend. ( $\delta$ ) $\text{C}_{(4,5)}\text{H}$ $\otimes$ Bend. ( $\delta$ ) $\text{C}_{(2)}\text{H}$
		1276-1322.4		21.3	13.9	Bend. ( $\delta$ ) $\text{C}_{(4,5)}\text{H}$ $\otimes$ Bend. ( $\delta$ ) $\text{C}_{(2)}\text{H}$ $\otimes$ Rock. ( $\rho$ ) $\text{CH}_2$ (ethyl, cation)
1337	1337	1358.2-1361.		29.8	51.9 P	Str. ( $\nu_{ip}$ ) C-N (ring) $\otimes$ Str. ( $\nu_{ip}$ ) C-N ( $\text{CH}_{2(3)}$ )
1360		1389.6-1399.4		20.1	2.4	Wagg. ( $\omega$ ) $\text{CH}_2$ (cation)
			1395.4	3.9	0.4	Wagg. ( $\omega$ ) $\text{CH}_2$ $\otimes$ Sym. Bend. ( $\delta_s$ ) CH ( $\text{CH}_3$ )
1387	1387	1417.5		5.0	18.0 P	Asym. Str. ( $\nu_a$ ) $\text{C}_{(2,5)}\text{N}$ $\otimes$ Sym. Bend. ( $\delta_s$ ) CH ( $\text{CH}_3$ )
		1426.3-1456.9		22.0	62.1	Bend. ( $\delta$ ) CH ( $\text{CH}_3$ , $\text{CH}_2$ ) $\otimes$ Str. ( $\nu$ ) C-N
			1423	28.9	5.0	Sym. Bend. ( $\delta_s$ ) CH ( $\text{CH}_3$ )
1434	1420	1467.4-1468.5		25.5	40.6	Sym. Bend. ( $\delta_s$ ) CH ( $\text{CH}_3$ )
			1486.5	12.7	19.5	Asym. Bend. ( $\delta_{as}$ ) CH ( $\text{CH}_3$ )
1454	1454	1490.7-1500.8	1505.5	23.5	69.7	Asym. Bend. ( $\delta_{as}$ ) CH ( $\text{CH}_3$ , $\text{CH}_2$ )
1464		1507.6-1521.7	1529.7	51.6	66.1	Bend. ( $\delta$ ) H-C-H ( $\text{CH}_2$ , $\text{CH}_3$ )
1574	1568	1596.9-1615.4		124.3	12.8	Str. ( $\nu$ ) $\text{C}_{(2)}\text{N}$ $\otimes$ ( $\nu$ ) C-C (ring) $\otimes$ Bend. ( $\delta$ ) $\text{C}_{(2,4,5)}\text{H}$

Frequency calculation B3LYP; Basis set 6-31+G(d,p) for O, N, C, & Cl; Basis set MQZVP for S.  
Rocking ( $\rho$ ), Bending ( $\delta$ ), Stretching ( $\nu$ ), Wagging ( $\omega$ ), Twisting ( $\tau$ ), Vibration ( $\nu$ ), In Phase (i.p.), Out of Phase (o.p.)

Table A1.2: Assignments of the vibrational bands of [EMIM] [EtSO<sub>4</sub>] in the 2700-3200 cm<sup>-1</sup> C-H region obtained from the experimental IR and Raman spectra in conjunction with the anharmonic calculation of the spectra using DFT calculation, based on the structure in Figure A1.1.

Experimental bands (cm <sup>-1</sup> )		DFT calculated bands, $\nu_{\text{harm}}$ (cm <sup>-1</sup> )		Intensity		Assignment
IR	Raman	EMIM	EtSO <sub>4</sub>	IR	Raman	
2830	2840	EthSO <sub>4</sub>	3047	64.6	258.9	Sym. Str. ( $\nu_s$ ) C-H ( $\text{CH}_2$ )
2900	2896	EthSO <sub>4</sub>	3090.2	13	134.8	Asym. Str. ( $\nu_a$ ) C-H ( $\text{CH}_2$ )
2943	2940	EthSO <sub>4</sub>	3044	51.8	245.8	Sym. Str. ( $\nu_s$ ) C-H ( $\text{CH}_3$ )
2981	2970	EthSO <sub>4</sub>	3114.6	61.6	191	Asym. Str. ( $\nu_a$ ) C-H ( $\text{CH}_3$ )
		EMIM	3050-3078	137.5	1009	Sym. Str. ( $\nu_s$ ) C-H ( $\text{CH}_2$ , $\text{CH}_3$ )
		EMIM	3129-3158	37.6	194	Asym. Str. ( $\nu_a$ ) C-H ( $\text{CH}_3$ ) (ethyl)
3040 (Shoulder)		EMIM	3150-3183	47.6	266.6	Asym. Str. ( $\nu_a$ ) C-H ( $\text{CH}_3$ ) (methyl)
3105	3105	EMIM		n.c.	n.c.	2R1
						2R2
						R1+R2, 2(R1, R2)- (R1+R2) <sup>c</sup>
3150	3160	EMIM	3264.6-3268.4	265.7	154.9	Asym. Str. ( $\nu_a$ ) $\text{C}_{(4,5)}$ H (HCCH) str. $\nu\text{C}_2\text{H}$
			3275.0-3280.6	337	179.3	Str. ( $\nu$ ) $\text{C}_2\text{H}$
			3307.8-3309	6.1	181.1 P	Sym. Str. ( $\nu_s$ ) $\text{C}_{(4,5)}$ H (HCCH) <sup>a, b</sup>

<sup>a, b</sup> This is assigned to the ( $\nu$ ) i.p.  $\text{C}_{(4,5)}$  H, ( $\nu$ )  $\text{C}_{(2)}\text{H}$  and ( $\nu$ ) o.p.  $\text{C}_{(4,5)}$  H modes. <sup>c</sup> is assigned to overtones and combination of the ring modes in Fermi resonance Lassègues et al. [265].  
Rocking ( $\rho$ ), Bending ( $\delta$ ), Stretching ( $\nu$ ), Wagging ( $\omega$ ), Twisting ( $\tau$ ), Vibration ( $\nu$ ), In Phase (i.p.), Out of Phase (o.p.)

### 1.2.2 Pure [EMIM] [TFSI]

Table A1.3: Assignments of the vibrational bands of [EMIM] [TFSI] in the 200 to 1600  $\text{cm}^{-1}$  region obtained from the experimental IR and Raman spectra in conjunction with the theoretical DFT calculated spectra based on the structure in Figure A1.2.

Experimental bands ( $\text{cm}^{-1}$ )		DFT calculated bands, $\nu_{\text{harm}}$ ( $\text{cm}^{-1}$ )		Intensity		Assignment
IR	Ram.	EMIM	TFSI	IR	Raman	
206			199.3-201.7	3.8	0.3	Rock. ( $\rho$ ) $\text{CF}_3$ , $\text{SO}_2$ ; Rock. ( $\rho$ ) $\text{CH}_2$ , $\text{CH}_3$ (ethyl)
225		209.6-213.1		1.5	0.7	Rock. ( $\rho$ ) $\text{CH}_3$ ; Rock. ( $\rho$ ) $\text{CF}_3$ , $\text{SO}_2$
		237.5, 243.8		9.7	2.2	Bend. ( $\delta$ ) $\text{CNCH}_3$ (out of plane)
	245		266.7, 269.7	1.2	10.9	Sym. Rock. ( $\rho_s$ ) $\text{CF}_3$ ; Rock. ( $\rho$ ) $\text{SO}_2$
	279		273.8, 275.3	4.5	2.2	Asym. Rock. ( $\rho_a$ ) $\text{CF}_3$
288	287	299.1-304.1		8.0	5.5	Rock. ( $\rho$ ) methyl & ethyl; Bend. ( $\delta$ ) $\text{SO}_2$
	296		314.2, 314.9	2.4	16.4	Sym. Bend. ( $\delta_s$ ) $\text{CF}_3$
314	311		322.7, 324.5	1.7	3.7	Asym. Bend. ( $\delta_{as}$ ) $\text{CF}_3$
324	328		341.9, 343.1	1.0	6.1	Sym. Bend. ( $\delta_s$ ) N-S- $\text{CF}_3$
333, 341	339	374.8, 384.4		1.8	3.3	Bend. ( $\delta$ ) ( $\text{CNCH}_2$ ) of ethyl (out of plane)
363	397		396.5-424.6	14.2	3.3	Bend. ( $\delta$ ) $\text{SO}_2$
408	405	426.8-436.9		11.7	2.4	Bend. ( $\delta$ ) $\text{CNCH}_3$ , $\text{CNCH}_2$
517	513		506.2, 507.5	121.3	0.2	Sym. Bend. ( $\delta_s$ ) $\text{SO}_2$
531	534		525.7, 527.6	13.8	0.9	Asym. Bend. ( $\delta_{as}$ ) $\text{CF}_3$ ; Bend. ( $\delta$ ) $\text{SO}_2$
553	551		543.3, 543.4	7.0	4.0	Asym. Bend. ( $\delta_{as}$ ) $\text{CF}_3$
	556		552.6, 552.9	3.6	3.1	Asym. Bend. ( $\delta_{as}$ ) $\text{CF}_3$
573	571		566.0, 567.2	73.9	3.3	Bend. ( $\delta$ ) O-S-O; Asym. Bend. ( $\delta_{as}$ ) $\text{CF}_3$
	589		573.8, 574.0	119.2	2.0	Bend. ( $\delta$ ) S-N-S; Bend. ( $\delta$ ) O-S-O
603	597	594.4-597.8		299.7	9.3	Sym. Str. ( $\nu_s$ ) $\text{NCH}_2$ ; $\text{NCH}_3 \otimes$ Bend. ( $\delta$ ) N-C-C $\otimes$ ( $\delta$ ) C-N-C (ring)
						Bend. ( $\delta$ ) O-S-O
620	625	630.8, 631.7		13.0	0.4	Vib. ( $\gamma$ ) $\text{NCH}_3$ ; Twist. ( $\tau$ ) C-N, C-C (ring)
653	649		644.3	176.4	0.3	Bend. ( $\delta$ ) S-N-S, F-C-F
			647.3	86.0	1.4	Bend. ( $\delta$ ) S-N-S, F-C-F $\otimes$ ( $\gamma\text{NCH}_2, \tau\text{CN}, \text{CC}_{\text{ring}}$ )
		662.1, 663.9		54.1	1.3	( $\gamma\text{NCH}_2, \tau\text{CN}, \text{CC}_{\text{ring}}$ )
703	701	707.3, 708.3		10.0	3.1	Asym. Str. ( $\nu_a$ ) $\text{NCH}_2$ , $\text{NCH}_3 \otimes$ Bend. ( $\delta$ ) N-C-C $\otimes$ ( $\delta$ ) C-N-C (ring)
743			729.1, 732.4	115.2	59.9	Sym. Str. ( $\nu_s$ ) S-N-S; Sym. Bend. ( $\delta_s$ ) $\text{CF}_3$ ; $\gamma\text{C}_{(4,5)}\text{H} \otimes \gamma\text{C}_{(2)}\text{H}$
	741	742.8, 744.4		88.8	2.1	$\gamma\text{C}_{(4,5)}\text{H} \otimes \gamma\text{C}_{(2)}\text{H}$

			754.7,755.4	3.6	1.4	Sym. Bend. ( $\delta_s$ ) $\text{CF}_3$ ; Str. ( $\nu$ ) C-S
764			777.0,781.9	106.7	1.1	Sym. Bend. ( $\delta_s$ ) $\text{CF}_3$ ; Bend. ( $\delta$ ) N-S; Str. ( $\nu$ ) N-S
792	792	814.1,815.1		5.5	0.7	Rock. ( $\delta$ ) $\text{CH}_3, \text{CH}_2$ (ethyl, cation)
845	861	855.2-903.7		49.9	3.8	o.p. Vib. ( $\gamma$ ) $\text{C}_{(4,5)}\text{H} \otimes (\gamma) \text{C}_{(2)}\text{H}$
960	959	964.2,965.3		5.1	16.9	Str. ( $\nu$ ) C-C (ethyl)
	1024					
1036	1031	1038.4-1047.7		16.9	20.7	Str. ( $\nu$ ) C-N (ring); Bend. ( $\delta$ ) C-N-C (ring)
1059			1052.2-1060.1	412.1	2.1	Asym. Str. ( $\nu_a$ ) S-N-S; Bend. ( $\delta$ ) $\text{CF}_3$
	1089	1103.0,1103.7		7.2	15.2	Rock. ( $\rho$ ) $\text{CH}_3$ (ethyl) $\otimes$ Bend. ( $\delta$ ) $\text{C}_{(4)}\text{H}$
		1112.7,1112.8		29.8	3.9	Rock ( $\rho$ ) $\text{CH}_3$ (methyl); Bend. ( $\delta$ ) $\text{C}_{(4)}\text{H} \otimes (\delta) \text{C}_{(2)}\text{H}$
	1109	1121.6-1129.4		186.9	45.8	Rock. ( $\rho$ ) $\text{CH}_3$ (methyl); Bend. ( $\delta$ ) $\text{C}_{(4,5)}\text{H}$ ; Bend. ( $\delta$ ) $\text{CF}_3$
1141	1136	1134.3-1147.0		32.3	14.4	Rock. ( $\rho$ ) methyl, ethy $\otimes$ Bend. ( $\delta$ ) $\text{C}_{(4,5)}\text{H} \otimes (\delta) \text{C}_{(2)}\text{H}$ ; Sym. Str. ( $\nu_s$ ) O-S-O; Asym. Str. ( $\nu_a$ ) S-N-S
1194		1162.1,1162.2		6.9	1.8	Rock. ( $\rho$ ) methyl
1227	1242	1163.3-1195.9	1163.3,1177.0	2351.1	15.2	Asym. Str. ( $\nu_a$ ) C-F; Bend. ( $\delta$ ) $\text{C}_{(4,5)}\text{H} \otimes (\delta) \text{C}_{(2)}\text{H}$
1296	1297		1210.2,1222.7	707.1	4.5	Str. ( $\nu$ ) S-N-S; Bend. ( $\delta$ ) $\text{CF}_3$ ; Bend. ( $\delta$ ) $\text{C}_{(4,5)}\text{H} \otimes (\delta) \text{C}_{(2)}\text{H}$
			1226.6,1228.4	56.1	38.6	Sym. Str. ( $\nu_s$ ) O-S-O; Sym. Bend. ( $\delta_s$ ) $\text{CF}_3$
		1278.4-1327.1		145.3	21.4	Bend. ( $\delta$ ) $\text{C}_{(4,5)}\text{H} \otimes (\delta) \text{C}_{(2)}\text{H} \otimes$ Rock. ( $\rho$ ) $\text{CH}_2$ (ethyl); Rock. $\text{CH}_3$ (methyl)
			1334.4	89.2	10.6	o.p. Asym. Str. ( $\nu_a$ ) O-S-O; i.p. Str. ( $\nu_{i.p.}$ ) C-N (ring); ( $\nu_{i.p.}$ ) C-N ( $\text{CH}_{2(3)}$ )
			1341.7-1352.5	964.8	10.5	i.p. Asym. Str. ( $\nu_a$ ) O-S-O; i.p. Str. ( $\nu_{i.p.}$ ) C-N (ring); ( $\nu_{i.p.}$ ) C-N ( $\text{CH}_{2(3)}$ )
1334	1335	1357.5,1359.4		45.8	30.6	i.p. Str. ( $\nu_{i.p.}$ ) C-N (ring); ( $\nu_{i.p.}$ ) C-N ( $\text{CH}_{2(3)}$ )
1354		1398.9,1402.7		22.9	2.6	Wagg. ( $\omega$ ) $\text{CH}_2$ (ethyl, methyl)
1392	1388	1420.8,1421.5		6.2	13.8	Asym. Str. ( $\nu_a$ ) $\text{C}_{(2,5)}\text{N} \otimes$ Sym. Bend. ( $\delta_s$ ) C-H ( $\text{CH}_3$ )
		1429.4,1431.1		17.5	30.9	Bend. ( $\delta$ ) C-H ( $\text{CH}_3, \text{CH}_2$ ) $\otimes$ Str. ( $\nu$ ) C-N
1434	1422	1453.5,1457.0		6.1	39.9	Bend. ( $\delta$ ) C-H ( $\text{CH}_3, \text{CH}_2$ ) $\otimes$ Str. ( $\nu$ ) C-N
		1463.6,1464.3		16.9	27.6	Sym. Bend. ( $\delta_s$ ) C-H ( $\text{CH}_3$ )
1456	1453	1496.7-1522.3		61.4	71.8	Asym. Bend. ( $\delta_{as}$ ) C-H ( $\text{CH}_3, \text{CH}_2$ )
1462						
1472						
1574	1571	1602.7-1616.8		130.9	16.3	Str. ( $\nu$ ) $\text{C}_{(2)}\text{N} \otimes$ Str. ( $\nu$ ) C-C (ring) $\otimes$ Bend. ( $\delta$ ) $\text{C}_{(2,4,5)}\text{H}$ )
Frequency calculation B3LYP; Basis set 6-31+G(d,p) for O, N & C; Basis set 6-311+ G(d,p) for F; Basis set WQZVP for S. Rocking ( $\rho$ ), Bending ( $\delta$ ), Stretching ( $\nu$ ), Wagging ( $\omega$ ), Twisting ( $\tau$ ), Vibration ( $\gamma$ ), In Phase (i.p.), Out of Phase (o.p.)						

### 1.2.3 [EMIM] [EtSO<sub>4</sub>] + CuCl<sub>2</sub> solution

Table A1.4: Assignments of the vibrational bands of [EMIM] [EtSO<sub>4</sub>] + CuCl<sub>2</sub> solution in the 200 to 1600 cm<sup>-1</sup> region obtained from the experimental IR and Raman spectra in conjunction with the theoretical spectra calculated using DFT calculation based on the structure in Figure A1.4.

Experimental bands (cm <sup>-1</sup> )		DFT calculated bands, ν <sub>harm</sub> (cm <sup>-1</sup> )		Intensity		Assignment
IR	Raman	EMIM	EtSO <sub>4</sub>	IR	Raman	
245	245		251.6,253.9	0.3	2.5	Rock. (ρ) CH <sub>3</sub> (ethyl, anion)
300	295	292.5,294.1		1.3	0.6	Rock. (ρ) CH <sub>3</sub> , CH <sub>2</sub> (cation)
315	315		325.9	14.0	0.0	Asym. Str. (ν <sub>a</sub> ) O-Cu-O; Bend. (δ) C-C-O (ethyl, anion)
			333.6, 334.8	8.9	5.0	Sym. Str. (ν <sub>s</sub> ) O-Cu-O; Bend. (δ) C-C-O (ethyl, anion)
337	342		351.6	85.4	0.0	Asym. Str. (ν <sub>a</sub> ) SO <sub>2</sub> -Cu-SO <sub>2</sub> ; Bend. (δ) C-C-O (ethyl, anion)
418	416		370.5	0.0	3.0	Bend. (δ) O-S-O; Bend. (δ) S-O-C
			377.7	23.2	0.0	Asym. Str. (ν <sub>a</sub> ) O-Cu-O; Bend. (δ) S-O-C, Bend. (δ) O-S-O
		378.9,379.1,427.9,428.4		4.8	6.4	Bend. (δ) CNCH <sub>3</sub> , CNCH <sub>2</sub>
435	~445		471	0.0	25.0	i.p. Str. (ν <sub>i.p.</sub> ) SO <sub>2</sub> ; Bend. (δ) S-O-C
			486.5	171.2	0.0	o.p. Str. (ν <sub>o.p.</sub> ) SO <sub>2</sub> ; Bend. (δ) S-O-C
567	566		544.5	0.0	16.2	i.p. Bend. (δ <sub>i.p.</sub> ) SO <sub>2</sub> ; C-C-O (ethyl)
			555.3	39.1	0.0	o.p. Bend. (δ <sub>o.p.</sub> ) SO <sub>2</sub> ; C-C-O (ethyl)
579	578		577.6	0.0	14.0	Bend. (δ) SO <sub>3</sub> ; Bend. (δ) O-S-O
			585.1	88.5	0.0	Bend. (δ) SO <sub>3</sub> ; Bend. (δ) O-S-O; Bend. (δ) S-O-C
	598	594.6,594.7		3.0	10.7	Sym. Str. (ν <sub>s</sub> ) NCH <sub>2</sub> ; (ν) NCH <sub>3</sub> ⊗ Bend. (δ) N-C-C ⊗ Bend. (δ) C-N-C (ring)
621	620	633.5		7.0	0.4	Vib. (γ) NCH <sub>3</sub> ; Twist. (τ) C-N, C-C (ring)
			646.6	411.2	0.0	Sym. Bend. (δ <sub>s</sub> ) SO <sub>3</sub> ⊗ Bend. (δ) (CH <sub>2</sub> )C-O-S(SO <sub>3</sub> )
650	648	663.2,663.5		35.2	2.3	Vib. (γ) NCH <sub>3</sub> ; Twist. (τ) C-N, C-C (ring)
			665.6	1.1	34.0	Asym. Bend. (δ <sub>a</sub> ) SO <sub>3</sub> ⊗ Bend. (δ) (CH <sub>2</sub> )C-O-S(SO <sub>3</sub> )
704	702	702.5,702.6		14.1	4.6	Asym. Str. (ν <sub>a</sub> ) NCH <sub>2</sub> , NCH <sub>3</sub> ⊗ Bend. (δ) N-C-C ⊗ Bend. (δ) C-N-C (ring)
734	734	758.2,758.3		75.3	0.2	Vib. (γ) C <sub>(4,5)</sub> H ⊗ (γ) C <sub>(2)</sub> H
766	766		793.45	4.5	34.0	Rock. (ρ) CH <sub>3</sub> (ethyl, anion); Sym. Str. (ν <sub>s</sub> ) O-Cu-O
			793.51	51.1	2.9	Rock. (ρ) CH <sub>3</sub> (ethyl, anion); Asym. Str. (ν <sub>a</sub> ) O-Cu-O
805	805	803.1,803.5		4.3	0.4	Rock. (ρ) CH <sub>2</sub> , CH <sub>3</sub> (ethyl, anion)
			824.8,825.2	1.7	0.4	Rock. (ρ) CH <sub>2</sub> , CH <sub>3</sub> (ethyl, anion)
850		874.4-877.5		37.8	2.0	o.p. γC <sub>(4,5)</sub> H ⊗ γC <sub>(2)</sub> H
916	916		939.1	484.9	0.0	o.p. Asym. Str. (ν <sub>a</sub> ) C-O-S; Rock. (δ) CH <sub>3</sub> (ethyl, anion)
			942.1	4.1	4.1	i.p. Asym. Str. (ν <sub>s</sub> ) C-O-S; Rock. (δ) CH <sub>3</sub> (ethyl, anion)
960	960	962.2,962.5		7.7	14.7	Str. (ν) C-C (ethyl, cation)
990			990	960.1	0.0	o.p. Rock. (ρ) CH <sub>3</sub> (ethyl, anion); Asym str. (ν <sub>a</sub> ) C-O-S
			1001	0.4	7.5	i.p. Asym. Str. (ν <sub>a</sub> ) O-C-C (ethyl, anion); Rock. (ρ) CH <sub>3</sub> (ethyl, anion)

1020	1020		1024.8	204.9	0.0	o.p. Sym. Str. ( $\nu_s$ ) O-C-C (ethyl, anion); Asym. Str. ( $\nu_a$ ) SO <sub>2</sub> -Cu-SO <sub>2</sub> ; Rock. ( $\rho$ ) CH <sub>3</sub> (ethyl, anion)
1045			1028.6	0.1	11.0	Rock. ( $\rho$ ) CH <sub>3</sub> (ethyl, anion); Sym. Str. ( $\nu_s$ ) O-C-C (ethyl, anion); Sym. Str. ( $\nu_s$ ) SO <sub>2</sub> -Cu-SO <sub>2</sub>
		1037.2-1043.0		16.0	33.4	Str. ( $\nu$ ) C-N (ring); Bend. ( $\delta$ ) C-N-C (ring); Rock. ( $\rho$ ) methyl, ethyl (cation)
1061	1061		1057	0.1	21.4	i.p. Asym. Str. ( $\nu_a$ ) S-O (SO <sub>3</sub> ); Sym. Str. ( $\nu_s$ ) S-O-C; Rock. ( $\rho$ ) CH <sub>3</sub> (ethyl, anion)
			1066.9	265.4	0.0	o.p. Asym. Str. ( $\nu_s$ ) S-O (SO <sub>3</sub> ); Sym. Str. ( $\nu_s$ ) S-O-C; Rock. ( $\rho$ ) CH <sub>3</sub> (ethyl, anion)
1095	1091	1102.5,1102.9		8.8	11.1	Rock. ( $\rho$ ) CH <sub>3</sub> (ethyl, cation)
1109	1109	1109.2,1109.3		4.4	3.9	Rock. ( $\rho$ ) CH <sub>3</sub> (methyl, cation)
			1124.7,1124.9	16.8	18.1	Rock. ( $\rho$ ) CH <sub>3</sub> (ethyl, anion)
		1128.6,1129.0		10.4	9.5	Bend. ( $\delta$ ) C <sub>4,5</sub> H
		1137.6,1137.7		2.1	13.1	Rock. ( $\rho$ ) CH <sub>2</sub> , CH <sub>3</sub> (ethyl, cation); Bend. ( $\delta$ ) C <sub>(4,5)</sub> H ⊗ ( $\delta$ ) C <sub>(2)</sub> H
		1154.7,1154.9		0.2	1.1	Rock. ( $\rho$ ) (methyl, cation)
			1174.7,1174.8	12.5	2.2	Rock. ( $\rho$ ) CH <sub>2</sub> , CH <sub>3</sub> (ethyl, anion)
1172	1175	1189.4,1189.5		256.0	8.0	Bend. ( $\delta$ ) C <sub>4,5</sub> H; ( $\delta$ ) C <sub>2</sub> H
1225	1224	1272.9-1273.2		52.3	25.4	Bend. ( $\delta$ ) C <sub>(4,5)</sub> H ⊗ ( $\delta$ ) C <sub>(2)</sub> H ⊗ Rock. ( $\rho$ ) CH <sub>2</sub> (ethyl, cation)
1298			1291.7,1295.3	637.9	32.8	Rock. ( $\rho$ ) (ethyl, anion)
1246	1252		1305.7	543.3	0.0	Rock. ( $\rho$ ) CH <sub>2</sub> (ethyl, anion), Str. ( $\nu_s$ ) S-O
			1314.3	0.0	176.5	Rock. ( $\rho$ ) CH <sub>2</sub> (ethyl, anion), Str. ( $\nu_s$ ) S-O
		1320.7,1321.0		1.1	5.7	Bend. ( $\delta$ ) C <sub>(4,5)</sub> H ⊗ ( $\delta$ ) C <sub>(2)</sub> H ⊗ Rock. ( $\rho$ ) CH <sub>2</sub> (ethyl, cation)
1337	1337	1351.4,1351.7		20.5	53.9	Str. ( $\nu_{ip}$ ) C-N (ring) ⊗ Str. ( $\nu_{ip}$ ) C-N (CH <sub>2(3)</sub> )
1360		1388.2,1388.5		23.9	1.6	Wagg. ( $\omega$ ) CH <sub>2</sub> (ethyl, cation)
			1403.1,1403.5	9.3	3.3	Rock. ( $\rho$ ) ethyl (anion)
1387	1387	1421.1,1421.3		6.2	40.3	Bend. ( $\delta$ ) CH (CH <sub>3</sub> , CH <sub>2</sub> ) ⊗ Str. ( $\nu$ ) C-N
			1430.7,1431.0	28.1	9.9	Asym. Bend. ( $\delta_{as}$ ) CH (CH <sub>3</sub> , anion)
		1431.5,1431.9		11.6	11.7	Bend. ( $\delta$ ) CH (CH <sub>3</sub> , CH <sub>2</sub> ) ⊗ Str. ( $\nu$ ) C-N
		1444.9,1445.1		7.2	67.2	Bend. ( $\delta$ ) CH (CH <sub>3</sub> , CH <sub>2</sub> ) ⊗ Str. ( $\nu$ ) C-N
1434	1420	1466.0,1466.2		15.4	21.5	Asym. Bend. ( $\delta_a$ ) CH (CH <sub>3</sub> , anion)
			1486.9,1487.0	10.8	21.1	Asym. Bend. ( $\delta_a$ ) CH (CH <sub>3</sub> , anion)
1454	1454	1494.6-1497.3		68.1	74.0	Asym. Bend. ( $\delta_a$ ) CH (CH <sub>3</sub> , CH <sub>2</sub> , cation)
			1504.0,1504.2	8.8	19.7	Asym. Bend. ( $\delta_a$ ) CH (CH <sub>3</sub> , CH <sub>2</sub> , anion)
		1510.9,1511.5		22.0	1.8	Asym. Bend. ( $\delta_a$ ) CH (CH <sub>3</sub> , CH <sub>2</sub> , cation)
1464		1515.3,1515.9		18.5	34.9	Asym. Bend. ( $\delta_a$ ) CH (CH <sub>3</sub> , CH <sub>2</sub> , cation)
			1519.9,1520.1	8.5	6.8	Asym. Bend. ( $\delta_a$ ) CH (CH <sub>3</sub> , CH <sub>2</sub> , anion)

1574	1568	1604.6-1612.4		160.3	18.5	Str. (v) C <sub>(2)</sub> N ⊗ (v) C-C (ring) ⊗ Bend. (δ) C <sub>(2,4,5)</sub> H
Frequency calculation B3LYP; Basis set 6-31+G(d,p) for O, N, C, & Cl; Basis set MQZVP for S & Cu. Rocking (ρ), Bending (δ), Stretching (v), Wagging (ω), Twisting (τ), Vibration (γ), In Phase (i.p.), Out of Phase (o.p.) Vibrational transition values in <i>italic</i> are associated with the complex formation experimentally observed Experimental values in <b>bolded</b> are associated with the new bands due to addition of CuCl <sub>2</sub>						

Table A1.5: Assignments of the vibrational bands of [EMIM] [EtSO<sub>4</sub>] + CuCl<sub>2</sub> solution in the 2700-3200 cm<sup>-1</sup> C-H region obtained from the experimental IR and Raman spectra in conjunction with DFT calculation based on the structure in Figure A1.4.

Experimental bands (cm <sup>-1</sup> )		Species	DFT calculated bands, V <sub>harm</sub> (cm <sup>-1</sup> )	Intensity		Assignment
IR	Raman			IR	Raman	
2830	2840	EtSO <sub>4</sub>	3082.5,3082.8	25.6	95.4	Sym. Str. (v <sub>s</sub> ) C-H (CH <sub>2</sub> , ethyl)
2900	2896	EtSO <sub>4</sub>	3157.1,3157.1	33.9	16.2	Asym. Str. (v <sub>a</sub> ) C-H (CH <sub>2</sub> , ethyl)
2943	2940	EtSO <sub>4</sub>	3061.8,3061.8	9.5	360.3	Sym. Str. (v <sub>s</sub> ) C-H (CH <sub>3</sub> , ethyl)
2981	2970	EtSO <sub>4</sub>	3135.0-3136.6	16.2	348	Asym. Str. (v <sub>a</sub> ) C-H (CH <sub>2</sub> , CH <sub>3</sub> , ethyl)
		EMIM	3060.9,3061.1	8.7	309.1	Sym. Str. (v <sub>s</sub> ) C-H (CH <sub>3</sub> , ethyl)
		EMIM	3081.7,3082.0	13.3	368.3	Sym. Str. (v <sub>s</sub> ) (CH <sub>3</sub> , methyl)
		EMIM	3091.6,3091.8	14.1	186.7	Sym. Str. (v <sub>s</sub> ) C-H (CH <sub>2</sub> , ethyl)
		EMIM	3129.8,3130.0	3.9	96.9	Asym. Str. (v <sub>a</sub> ) C-H (CH <sub>2</sub> , CH <sub>3</sub> , ethyl)
		EMIM	3151.8,3151.9	12.7	16.4	Asym. Str. (v <sub>a</sub> ) C-H (CH <sub>2</sub> , CH <sub>2</sub> , ethyl)
3040		EMIM	3165.2,3165.3	1.1	126.2	Asym. Str. (v <sub>a</sub> ) C-H (CH <sub>2</sub> , methyl)
			3188.4,3188.9	4.2	186.2	Asym. Str. (v <sub>a</sub> ) C-H (CH <sub>3</sub> , methyl)
3105	3105	EMIM				Fermi Resonance
						2R1
						2R2
						R1+R2 2{R1,R2}-(R1+R2) <sup>c</sup>
3150	3160	EMIM	3272.3,3273.2	393.7	320.9	Str. (v) C <sub>2</sub> H
			3296.2,3296.3	30.6	96.1	Asym. Str. (v <sub>a</sub> ) C <sub>4,5</sub> H
			3313.1,3313.2	21.6	128	Sym. Str. (v <sub>s</sub> ) C <sub>(4,5)</sub> H (HCCH) <sup>a, b</sup>
<sup>a, b</sup> This is assigned to the (v) i.p. C <sub>(4,5)</sub> H, (v) C <sub>(2)</sub> H and (v) o.p. C <sub>(4,5)</sub> H modes. <sup>c</sup> is assigned to overtones and combination of the ring modes in Fermi resonance Lassègues et al. [265]. Rocking (ρ), Bending (δ), Stretching (v), Wagging (ω), Twisting (τ), Vibration (γ), In Phase (i.p.), Out of Phase (o.p.)						

### 1.2.4 [EMIM] [TFSI] + AgTFSI solution

Table A1.6: Assignments of the vibrational bands of [EMIM] [TFSI] + AgTFSI solution in the 200 to 1600  $\text{cm}^{-1}$  region obtained from the experimental IR and Raman spectra in conjunction with the theoretical spectra calculated using DFT calculation based on the structure in Figure A1.5.

Experimental bands ( $\text{cm}^{-1}$ )		DFT calculated bands, $\nu_{\text{harm}}$ ( $\text{cm}^{-1}$ )		Intensity		Assignment
IR	Raman	EMIM	TFSI	IR	Raman	
			195.5- 203.3	4.2	1.7	Rock. ( $\rho$ ) $\text{CF}_3$ , $\text{SO}_2$ ; Rock. ( $\rho$ ) $\text{CH}_2$ ; $\text{CH}_3$ (ethyl)
		204.7- 211.6		3.1	1.0	Rock. ( $\rho$ ) $\text{CH}_3$ ; Rock. ( $\rho$ ) $\text{CF}_3$ , $\text{SO}_2$
		235.5,240. 3		4.7	2.0	Bend. ( $\delta$ ) $\text{CNCH}_3$ (out of plane)
	245		266.4,269. 2	1.4	10.4	Sym. Rock. ( $\rho_s$ ) $\text{CF}_3$ ; Rock. ( $\rho$ ) $\text{SO}_2$
	279		273.1,273. 5	4.3	7.0	Asym. Rock. ( $\rho_a$ ) $\text{CF}_3$ ; Rock. ( $\rho$ ) $\text{SO}_2$
			274.7- 297.6	5.8	9.3	Wagg. ( $\omega$ ) C-F ( $\text{CF}_3$ ); Str. ( $\nu$ ) C-S
	287	299.2- 303.5		5.0	6.6	Rock. ( $\rho$ ) methyl & ethyl; Bend. ( $\delta$ ) $\text{SO}_2$
	296		312.9,316. 4	3.2	19.1	Sym. Bend. ( $\delta_s$ ) $\text{CF}_3$
	311		320.4,332. 1	4.4	8.3	Asy. Bend. ( $\delta_{as}$ ) $\text{CF}_3$
	328		338.5,349. 0	1.8	8.6	Sym. Bend. ( $\delta_s$ ) N-S- $\text{CF}_3$
	339	372.1,376. 4		1.3	3.4	Bend. ( $\delta$ ) ( $\text{CNCH}_2$ ) of ethyl (out of plane)
	397		392.5 - 426.6	26.3	7.7	Bend. ( $\delta$ ) $\text{SO}_2$ ; ( $\delta$ ) $\text{CF}_3$ ; Bend. ( $\delta$ ) $\text{CNCH}_3$ , $\text{CNCH}_2$
408	405	436.2- 436.7		5.2	1.6	Bend. ( $\delta$ ) $\text{CNCH}_3$ , $\text{CNCH}_2$
			444.5	7.1	1.5	Bend. ( $\delta$ ) O-S-N; ( $\delta$ ) O-S-O; ( $\delta$ ) F-C-F
517	513		504.6- 508.6	214.8	0.7	Sym. Bend. ( $\delta_s$ ) $\text{SO}_2$
531	534		526.0- 527.3	18.1	7.8	Asym. Bend. ( $\delta_{as}$ ) $\text{CF}_3$ , Bend. ( $\delta$ ) $\text{SO}_2$
553	551		543.5- 546.4	8.2	6.9	Asym. Bend. ( $\delta_{as}$ ) $\text{CF}_3$
	556		552.2- 554.2	6.3	5.6	Asym. Bend. ( $\delta_{as}$ ) $\text{CF}_3$
573	571		565.2- 568.0	138.0	5.7	Bend. ( $\delta$ ) O-S-O; Asym. Bend. ( $\delta_{as}$ ) $\text{CF}_3$
	589		572.0- 574.4	80.4	2.9	Bend. ( $\delta$ ) S-N-S; Bend. ( $\delta$ ) O-S-O
			580.2- 593.9	428.0	1.3	Bend. ( $\delta$ ) O-S-O
			595.2	55.4	4.1	Bend. ( $\delta$ ) O-S-O; Sym. Str. ( $\nu_s$ ) $\text{NCH}_2$ , $\text{NCH}_3$ $\otimes$ Bend. ( $\delta$ ) N-C-C $\otimes$ ( $\delta$ ) C-N-C (ring)
603	597	597.4- 597.7		7.1	6.9	Sym. Str. ( $\nu_s$ ) $\text{NCH}_2$ , $\text{NCH}_3$ $\otimes$ Bend. ( $\delta$ ) N-C-C $\otimes$ ( $\delta$ ) C-N-C (ring)
620	625	633.3,634. 5		34.8	0.8	Vib. ( $\gamma$ ) $\text{NCH}_3$ ; Twist. ( $\tau$ ) C-N, C-C (ring)
653	649		643.0- 653.7	328.0	4.8	Bend. ( $\delta$ ) S-N-S, F-C-F
		659.6,660. 1		37.4	0.6	Vib. ( $\gamma$ ) $\text{NCH}_3$ ; Twist. ( $\tau$ ) C-N, C-C (ring)



703	701	704.1,704.9		10.1	3.3	Asym. Str. ( $\nu_a$ ) NCH <sub>2</sub> , NCH <sub>3</sub> ⊗ Bend. ( $\delta$ ) N-C-C ⊗ ( $\delta$ ) C-N-C (ring)
743	741		732.3-734.3	145.2	100.5	Sym. Str. ( $\nu_s$ ) S-N-S; Sym. Bend. ( $\delta_s$ ) CF <sub>3</sub>
		741.5,756.7,757.2		104.9	1.8	Vib. ( $\gamma$ ) C <sub>(4,5)</sub> H ⊗ ( $\gamma$ ) C <sub>(2)</sub> H
			756.2,757.0	3.0	2.4	Sym. Bend. ( $\delta_s$ ) CF <sub>3</sub> ; Str. ( $\nu$ ) C-S
<b>747</b>	<b>753</b>					
764			776.4,783.6	159.6	2.6	Sym. Bend. ( $\delta_s$ ) CF <sub>3</sub> ; Bend. ( $\delta$ ) N-S; Str. ( $\nu$ ) N-S
792	792	808.6,809.2		9.5	0.7	Rock. ( $\rho$ ) CH <sub>3</sub> , CH <sub>2</sub> (ethyl, cation)
	<b>804</b>					
845	861	854.0-904.2		60.9	4.2	o.p. Vib. ( $\gamma$ ) C <sub>(4,5)</sub> H ⊗ ( $\gamma$ ) C <sub>(2)</sub> H
960	959	965.2,965.9		3.6	9.4	Str. ( $\nu$ ) C-C (ethyl)
<b>1015</b>			1019.9	312.1	0.7	Asym. Str. ( $\nu_a$ ) S-N-S
	1024					
1036	1031	1035.3-1050.5		18.4	26.1	Str. ( $\nu$ ) C-N (ring); Bend. ( $\delta$ ) C-N-C (ring)
1059			1056.2-1059.2	323.9	1.5	Asym. Str. ( $\nu_a$ ) S-N-S; Bend. ( $\delta$ ) CF <sub>3</sub>
	1089	1105.2,1106.2		19.5	6.7	Rock. ( $\rho$ ) CH <sub>3</sub> (ethyl) ⊗ Bend. ( $\delta$ ) C <sub>(4)</sub> H
		1111.9,1114.0		22.1	5.4	Rock. ( $\rho$ ) CH <sub>3</sub> (methyl); Bend. ( $\delta$ ) C <sub>(4)</sub> H ⊗ ( $\delta$ ) C <sub>(2)</sub> H
			1116.8-1118.0	817.0	11.0	Sym. Bend. ( $\delta_s$ ) CF <sub>3</sub> ; Str. C-F; Sym. Str. ( $\nu_s$ ) O-S-O; ⊗ Bend. ( $\delta$ ) C <sub>(4,5)</sub> H ⊗ ( $\delta$ ) C <sub>(2)</sub> H
	1109	1124.2-1138.2		605.9	80.4	Rock. ( $\rho$ ) CH <sub>3</sub> (methyl); Bend. ( $\delta$ ) C <sub>(4,5)</sub> H; Bend. ( $\delta$ ) CF <sub>3</sub>
1141	1136	1140.4-1147.1		57.1	7.3	Rock. ( $\rho$ ) methyl, ethyl ⊗ Bend. ( $\delta$ ) C <sub>(4,5)</sub> H ⊗ ( $\delta$ ) C <sub>(2)</sub> H; Sym. Str. ( $\nu_s$ ) O-S-O; Asym. Str. ( $\nu_a$ ) S-N-S
1194		1162.3,1163.5		12.6	1.4	Rock. ( $\rho$ ) methyl
1227	1242	1172.6-1201.0	1172.6-1201.0	3609.1	30.1	Asym. Str. ( $\nu_a$ ) C-F; Bend. ( $\delta$ ) C <sub>(4,5)</sub> H ⊗ ( $\delta$ ) C <sub>(2)</sub> H
1296	1297		1216.4,1223.6	415.4	10.4	Str. ( $\nu$ ) S-N-S; Bend. ( $\delta$ ) CF <sub>3</sub> ; Bend. ( $\delta$ ) C <sub>(4,5)</sub> H ⊗ ( $\delta$ ) C <sub>(2)</sub> H
			1224.1,1229.4	62.2	60.4	Sym. Str. ( $\nu_s$ ) O-S-O; Sym. Bend. ( $\delta_s$ ) CF <sub>3</sub>
			1231.7	578.7	6.8	Asym. Str. ( $\nu_a$ ) S-N-S; Bend. ( $\delta$ ) C <sub>(4,5)</sub> H ⊗ ( $\delta$ ) C <sub>(2)</sub> H
		1279.7-1326.8		512.3	36.5	Bend. ( $\delta$ ) C <sub>(4,5)</sub> H ⊗ ( $\delta$ ) C <sub>(2)</sub> H ⊗ Rock. ( $\rho$ ) CH <sub>2</sub> (ethyl); Rock. ( $\rho$ ) CH <sub>3</sub> (methyl); Asym. Str. ( $\nu_a$ ) O-S-O
			1348.0	59.4	18.4	Asym. Str. ( $\nu_a$ ) O-S-O; i.p. Str. ( $\nu_{ip}$ ) C-N (ring); ( $\nu_{i.p.}$ ) C-N (CH <sub>2(3)</sub> )
1334	1335	1353.2-1355.4		595.0	27.0	i.p. Str. ( $\nu_{i.p.}$ ) C-N (ring); ( $\nu_{i.p.}$ ) C-N (CH <sub>2(3)</sub> )
			1364.7-1370.3	840.7	39.7	Asym. Str. ( $\nu_a$ ) O-S-O
1354		1392.0,1394.3		26.7	3.1	Wagg. ( $\omega$ ) CH <sub>2</sub> (ethyl, methyl)
<b>1371</b>						
1392	1388	1420.6,1423.2		3.0	24.9	Asym. Str. ( $\nu_a$ ) C <sub>(2,5)</sub> N ⊗ Sym. Bend. ( $\delta_s$ ) C-H (CH <sub>3</sub> )
		1430.74,1431.6		16.8	14.3	Bend. ( $\delta$ ) C-H (CH <sub>3</sub> , CH <sub>2</sub> ) ⊗ Str. ( $\nu$ ) C-N
1434	1422	1454.8,1455.6		6.4	49.9	Bend. ( $\delta$ ) C-H (CH <sub>3</sub> , CH <sub>2</sub> ) ⊗ Str. ( $\nu$ ) C-N
		1468.0,1470.8		20.2	16.5	Sym. Bend. ( $\delta_s$ ) C-H (CH <sub>3</sub> )

1456	1453	1494.7- 1519.9		98.2	96.3	Asym. Bend. ( $\delta_{as}$ ) C-H ( $\text{CH}_3$ , $\text{CH}_2$ )
1462						
1472						Bend. ( $\delta$ ) H-C-H
1574	1571	1601.6- 1616.5		127.0	16.9	Str. ( $\nu$ ) $\text{C}_{(2)}\text{N}$ $\otimes$ Str. ( $\nu$ ) C-C (ring) $\otimes$ Bend. ( $\delta$ ) $\text{C}_{(2,4,5)}\text{H}$
Frequency calculation B3LYP; Basis set 6-31+G(d,p) for O, N & C; Basis set 6-311+ G(d,p) for F; Basis set WQZVP for S. Basis set DGDZVP for Ag. Rocking ( $\rho$ ), Bending ( $\delta$ ), Stretching ( $\nu$ ), Wagging ( $\omega$ ), Twisting ( $\tau$ ), Vibration ( $\gamma$ ), In Phase (i.p.), Out of Phase (o.p.) Vibrational transition values in <i>italic</i> are associated with the complex formation experimentally observed Experimental values in <b>bolded</b> are associated with the new bands due to addition of AgTFSI						